博士論文

Volcanic geology, petrology and geochemistry of a juvenile arc sequence in northern Zambales ophiolite: Implications for subduction initiation along Philippine Sea Plate margins

（北部サンバレスオフィオライトの未成熟島弧の火山地質学，岩石学及び地球化学：フィリピン海プレート縁辺部に沿った沈み込み開始に関する示唆）

金沢大学大学院自然科学研究科
自然システム学専攻

学籍番号: 1524062012
氏名: アメリカス・デチャベス・ペレス
主任指導教員名: 海野　進

June 2018

Table of Contents

List of Figures

Abstract

In terrestrial planets, the transition from a stagnant lid regime to the present mode dominated by plate forces necessitates the initiation of subduction zones. Initiation of Cenozoic subduction zones in the oceanic domain is marked by a distinct volcanic sequence that reflects progressive depletion of the mantle wedge source and addition of diverse slab-derived components. This study provides field, petrologic and geochemical evidence for oceanic accretion and juvenile arc magmatism along the western margin of the Philippine Sea Plate as recorded by the Coto (45 Ma) and Acoje (44-43 Ma) volcanic sections of the Zambales ophiolite (Luzon island, Philippines).

We report the discovery of low-calcium, high-silica boninite in Zambales ophiolite. Olivine–orthopyroxene microphyric high-silica boninite, olivine–clinopyroxene–phyric low-silica boninite and boninitic basalt occur as lapilli fall deposits and pillow flows in the upper volcanic unit of the juvenile arc section (Barlo locality, Acoje Block) of Zambales ophiolite. This upper volcanic unit in turn overlies a lower volcanic unit consisting of basaltic andesite, andesite to dacitic lavas and explosive eruptives (subaqueous pahoehoe and lobate sheet flows, agglutinate, and spatter deposits) forming a low-silica boninite series. The overall volcanic stratigraphy of the extrusive sequence at Barlo resembles Holes U1439 and U1442 drilled by IODP Expedition 352 in the Izu-Ogasawara (Bonin) trench slope. Zambales boninite and boninite series volcanics are marked low trace element abundances relative to mid ocean ridge basalt (MORB) with fluid mobile element enrichment and heavy rare earth element (HREE) depletion comparable with boninite from Troodos and Oman. Trace element ratios suggest that aqueous fluids are the dominant slab components in Zambales boninite. A low-silica boninite primary magma composition is determined which yield pressure-temperatures estimates (1243° C, 0.34 GPa) indicative of shallow sub-arc melting. Based on middle and heavy rare earth element (REE) abundances, primary Zambales LSB magma can be modelled as second-stage melts of a mantle source that previously underwent 8% anhydrous fractional melting.

Basaltic andesite and gabbroic dikes of the Coto Block have primitive mantle-normalized immobile element abundances that are more depleted than MORB and depleted back-arc basin basalts (BABB) with Ti/V ratios (17-21) that overlap with proto-arc basalts (or forearc basalt) from IODP Expeditions 352 and 351. Volcanic sections of the Zambales ophiolite likewise show decreasing Ti/V ratios from Coto Block dikes to Acoje

Block boninite; indicating increasingly oxidized sub-arc environment that is interpreted to be the result of progressive source oxidation by slab-derived fluids.

The presence of protoarc basalts in Coto Block (45 Ma), boninite and boninite series volcanics in Barlo, Acoje Block (44 Ma) and simultaneous and post-boninite moderate-Fe arc tholeiites in Sual and Subic, Acoje Block (44-43 Ma) demonstrate that the observed subduction initiation stratigraphy in the Izu-Ogasawara-Mariana forearc is present in Zambales ophiolite as well. Paleolatitudes derived from tilt-corrected sites in the Acoje Block place the juvenile arc of northern Zambales ophiolite in the western margin of the Philippine Sea Plate (PSP). In this scenario, the origin of Philippine Sea Plate proto-arc basalts and boninites (IBM and Zambales) would be in a doubly-vergent subduction initiation setting. A doubly vergent subduction initiation (SI) geometry based on the Zambales ophiolite provides another boundary condition for refined geodynamic models of incipient subduction along PSP margins. Placed in its proper geodynamic context, Zambales ophiolite can address scientific objectives of several IODP drilling proposals in the IBM region (e.g. the origin of the felsic middle crust and the nature of forearc Moho).

1. Introduction

Plate tectonics posits that the Earth's surface forms part of a dynamic thin outer shell (lithosphere) that moves rigidly and coherently. When two plates meet, density difference causes one to descend beneath the other forming a subduction zone. As the surface manifestation of a convecting mantle, subduction zones play a fundamental role in material transfer from the surface to the deep interior and vice versa. Water, carbon dioxide and volatiles trapped in the hydrated oceanic crust are introduced to the mantle in subduction zones. The breakdown of hydrous minerals in the subducting slab promotes mantle melting; producing magmas that are recycled back to the surface during volcanic eruptions (Tatsumi & Eggins, 1995). Volcanism reflects asthenospheric upwelling, and together with surface deformation and impact crater density are criteria used to infer the tectonic activity and the presence of internal convection in planetary bodies (Cattermole, 1989).

1.1 The first subduction zones

In a survey of the 30 largest "planetoids" (referring to planets, asteroids and satellites), Stern et al. (2018) notes that only 9 are tectonically active. These include 3 terrestrial planets (Earth, Venus and Mars), 4 satellites (Io, Ganymede Enceladus, Titan) and 2 medium-sized icy bodies (Triton and Pluto). That is *plate tectonics* is uncommon and that *stagnant lid tectonics* is the dominant style of heat loss in planetary bodies. In a stagnant lid regime, a planetary body can lose heat in a variety of ways; thru heat pipe magmatism (Io), drips & plumes (Venus), and delamination & upwelling (Mars). These mechanisms reflect progressive phases coincident with cooling and thickening of the lid lithosphere leading to a terminal stagnant lid stage with ultra-stable and -thick lithosphere exemplified by the Moon and Mercury. Since Earth is the only tectonically active planetoid with plate tectonics *sensu stricto* (Stern et al., 2018); there must be a point early in Earth's history when the stagnant lid regime transitioned into the present mode dominated by plate forces. This necessitates the initiation of the first subduction zones. Numerical models show that plate tectonics or mantle overturn in terrestrial planets can be triggered by narrow plumes impinging on weakened crust inducing gravitational instability and slab descent (Crameri & Tackley, 2016; Gerya et al., 2015). The presence of coronae with arcuate trenches in Venus is regarded as an observational evidence for plume-induced subduction initiation (Davaille et al., 2017). Internally driven mechanisms such as plume-induced subduction initiation,

however, are distinct from end-member models of Cenozoic subduction initiation which rely on pre-existing zones of weakness such as fracture zones and transform faults (induced subduction initiation) or require lithospheric collapse (spontaneous subduction initiation) (Stern, 2004). In an updated review, Stern & Gerya (2017) includes plume head margin collapse as a spontaneous SI subtype. This addition is based on the temporal association of several mantle plume pulses, including the Late Cretaceous Caribbean Large Igneous Province (CLIP), and succeeding arc volcanism with oppositely-dipping slab polarities (Whattam & Stern, 2015). The 3-D thermo-mechanical models of plume-induced subduction initiation (PISI) by Baes et al. (2016) show that plume head size and significant age difference (> 10 Ma) between the subducting slab and overriding plate are needed for sustained PISI. More importantly, this work demonstrates that PISI can both operate in Precambrian Earth with higher upper mantle temperatures, and in modern settings (e.g Cretaceous Carribean SI).

1.2 Eocene Western Pacific intra-oceanic subduction initiation

Although nearly half of subduction zones are young (< 60 Ma, i.e. initiated during the Cenozoic) (Gurnis et al., 2004), their inception in the oceanic domain is one fundamental issue yet to be fully deciphered. Thus, it is regarded as a high priority scientific target (Challenge No. 11) of the International Ocean Discovery Program (IODP) for 2013 to 2023. Understanding this volcanic and tectonic process is hampered by its transient nature, with few examples in the geologic record including submarine active and paleo-forearcs and onshore supra-subduction ophiolites. In testing subduction initiation models, the Izu–Ogasawara (Bonin)–Mariana (IBM) forearc region remains as one of the most appropriate locality; this is due to its temporally distinct volcanic record of oceanic accretion and juvenile arc magmatism immediately following the onset of subduction. After the subduction of Pacific Plate beneath the Philippine Sea Plate commenced at 52 Ma, magmatism progressed from 52–48 Ma mid-ocean ridge basalt (MORB)-like proto-arc basalts (or forearc basalts) to 48–44 Ma boninite and boninite-series volcanics followed by 45–35 Ma arc tholeiites and calc–alkaline lavas (Ishizuka et al., 2011; Kanayama et al., 2012; Reagan et al., 2010). The widespread occurrence of subduction initiation rock suites along the eastern margin of the Philippine Sea Plate is summarized in Fig.1a. Basalts of similar composition and age range to proto-arc basalts dredged along the Mariana and Bonin

trench slopes were found at IODP Expedition 351 Site U1438 in the Amami Sankaku Basin (Arculus et al., 2015; Ishizuka et al., 2018). This indicates that the Oligocene Kyushu–Palau Ridge (KPR) intra-oceanic arc is built upon an igneous basement that formed part of the earliest seafloor spreading event related to subduction initiation. The subsequent late Oligocene opening of the Shikoku–Parece Vela Basin resulted in its present configuration with Site U1438 in the back-arc side of KPR. Based on dredging and dive observations in the forearc trench slope, proto-arc basalts are found at deeper depths relative to boninites which occur upslope and subaerially at Chichijima (type locality) and Mukojima island groups (Ishizuka et al., 2011; Kanayama et al., 2012; Umino & Nakano, 2007). The hypothesis that proto-arc basalt lies stratigraphically below boninite has been verified by IODP Expedition 352 based on four sites drilled in the trench-side slope of the Bonin Ridge (Reagan et al., 2015). Both spontaneous and induced initiation have been replicated in numerical models of incipient subduction at the IBM. Earlier models with imposed plate velocities generally focused on initiation across a preexisting weak zone, and combined with melting models could reproduce the observed proto-arc basalt–boninite stratigraphy (Hall et al., 2003; Leng et al., 2012). Subsequently, spontaneous subduction initiation has been shown to be plausible; with compositional density contrast being provided by the thickened middle crust of relic Cretaceous arc terranes (Leng & Gurnis, 2015). So far, neither spontaneous nor induced subduction initiation models can unequivocally be attributed to the incipient subduction that produced the IBM forearc and the mechanism remains elusive (Keenan & Encarnación, 2016).

1.3 Motivation and objective

Here an alternative approach to exploring subduction initiation processes in the Western Pacific region is presented. Following Stern et al. (2012), this study focuses on the middle Eocene Zambales ophiolite in the Philippines as an archetype supra-subduction ophiolite of the region (Dilek & Furnes, 2011), offering a ~3,200 km^2 exposure of Eocene supra-subduction oceanic lithosphere. Most of the Jurassic to Cretaceous ophiolites that form basement complexes in eastern Philippines are increasingly recognized as complementary features to Cretaceous terranes in the northern Philippine Sea Plate (e.g. Amami Plateau, Daito Ridge) possibly sharing a common history as the overriding plate prior to initiation of subduction (Deschamps & Lallemand, 2002; Lallemand, 2016) (Fig.1a). Therefore, juxtaposed Eocene ophiolites are potential targets to investigate subduction

initiation as a plate-scale process. Regional tectonic reconstructions predict the interaction of a pre-Eocene ocean basin located east of Eurasia and the western margin of the Philippine Sea Plate (Wu et al., 2016; Zahirovic et al., 2014).

Coincidentally, aside from the IBM forearc region, the Dasol–Barlo locality in northern Zambales ophiolite is where middle Eocene boninitic rocks are also reported (Evans et al., 1991; Florendo & Hawkins, 1992; Hawkins, 2003; Hawkins & Evans, 1983). The first unambiguous report of boninite (low-Ca type) occurrence in the Barlo locality is given Florendo & Hawkins (1992). Light rare earth element (LREE) depleted chondrite-normalized REE patterns of Dasol–Sual boninites are shown in Hawkins (2003). In both studies, petrological characteristics of said boninites are meagerly discussed and neither geochemical data nor sampling localities are given. The significance of Zambales ophiolite in addressing the early arc history of the Philippine Sea Plate has been recognized since the early 1990s (Pearce et al., 1992; Stern & Bloomer, 1992) yet this connection remains unexplored. Pearce et al. (1992) explicitly states that "*Acoje Block represents early subduction magmatism and maybe the best analogue for the Izu-Bonin outer arc high; while the Coto Block which probably formed in a proto-forearc setting as suggested Geary et al. (1989) is a possible candidate for crust created before or at the start of subduction*".

Motivated by how the ophiolite concept progressed through studies of the IBM forearc (e.g. Ishizuka et al., 2014), this study aims to test the "subduction initiation rule" (Whattam & Stern, 2011) in the volcanic sections of the Zambales ophiolite and to evaluate subduction initiation and boninite petrogenesis in a regional geodynamic context. These objectives are addressed through (1) geochemical study of spreading-stage dikes in the Coto Block and (2) field, petrologic, and geochemical characterization of a juvenile arc section in the Acoje Block.

2. Geologic background

Located in western Luzon, the structurally coherent Zambales ophiolite is the largest fossil oceanic lithosphere in the Philippines (Fig. 1b). The ophiolite spans the entire Zambales mountain range from 16° N to 14.7° N where it partly underlies stratovolcanoes of the Luzon Arc including Mt. Pinatubo. It consists of three structurally bounded massifs, namely Masinloc, Cabangan and San Antonio, which each preserve complete ophiolite internal stratigraphy. The ophiolite is flanked by the Central Valley Basin (CVB) to the east

and West Luzon Basin to the west. Late Eocene to late Miocene Aksitero and Moriones Formations of the CVB record the transition from a hemipelagic, deep marine setting to shallower environment dominated by ophiolite-derived sedimentation signaling the uplift of the ophiolite. While sedimentary sequences west of the ophiolite, Cabaluan and Sta. Cruz Formations, indicate that large-scale uplift, transport from equatorial positions and terrane docking have transpired by the Pliocene (Fuller et al., 1989; Karig et al., 1986; Pubellier et al., 2004; Schweller et al., 1984). The identity of what Zambales ophiolite "docked with" is still unknown. Sporadic chert slivers with late Jurassic–early Cretaceous radiolarian fauna are found in the westernmost margin of the ophiolite (Queaño et al., 2017a). Radiolarian bearing-cherts with similar age range are associated with disrupted ophiolitic fragments in northern Luzon; this highlights the existence of a shear zone (West Luzon shear zone) west of the ophiolite (Karig, 1983; Queaño et al., 2017b). The Zambales ophiolite is probably docked with the composite of the following— (1) fragments an ocean basin that predates the South China Sea (prior to 2016 there is consensus that this fully consumed ocean basin is the proto-South China Sea), the vestiges of which are the Mesozoic cherts in the West Luzon Shear Zone and (2) northern extension of the Palawan microcontinental block. Based on the presence of distinct bottom-simulating reflectors, Arfai et al. (2011) speculates that West Luzon Basin west of Zambales ophiolite is partly underlain by continental basement.

Petrologic, geochemical and isotopic studies reveal that Zambales ophiolite represents two distinct mantle-crust sequences – the 45.1 Ma Coto Block with transitional MORB affinity and 44.2–43.7 Ma Acoje Block with island arc characteristics (Encarnación et al., 1999; Encarnación et al., 1993; Geary et al., 1989; Hawkins & Evans, 1983; Yumul, 1990). The existence of a NNE–SSW trending structural boundary previously characterized by Hawkins and Evans (1983) as a left-lateral fault between Acoje and Coto Blocks within the Masinloc massif is supported by gravity and magnetic data with anomaly contrasts which extend at depth (Salapare et al., 2015). Although the juvenile arc character of Acoje Block and the supra-subduction origin of Zambales ophiolite are clear, the crustal nature and tectonic environment of Acoje and Coto blocks remain unresolved. Acoje Block as defined by Yumul et al. (1990) consists of the northern Masinloc massif and the San Antonio massif while the Coto Block consists of the southern Masinloc massif and the Cabangan massif (Fig. 1b). The present disposition of Acoje Block is postulated to be the result of southward translation of San Antonio massif with respect to northern Masinloc massif (Yumul et al., 1998). Crustal

thickness estimates, based on SW–NE transects of the northern Masinloc massif, are up to 9.5 km for the mantle section and 7 km for the lower crustal section. The fertile to moderately depleted Acoje mantle section is comprised of harzburgite and lherzolite with spinel Cr# [Cr/(Cr+Al)] ranging from 0.18 to 0.56, generally increasing towards the mantle–crust transition zone. Harzburgites from the uppermost mantle section are strongly depleted in light and middle rare earth elements (LREEs and MREEs) with equilibration temperature and oxygen fugacity estimates of 730° C and 1.9 $\Delta\log(fO_2)$ units above the FMQ buffer, respectively (Evans & Hawkins, 1989; Tamayo, 2001; Yumul, 1989). From the residual mantle section, the mantle–crust transition zone passes through interlayered ultramafic cumulates and dunite to layered cumulate gabbronorite. The Acoje transition zone hosts podiform chromite deposits (Cr# = 0.71–0.77) and Ni–Cu sulfides both of which are PGE-bearing (Bacuta et al., 1990). Refractory transition zone dunites, characterized by spinel Cr# greater than 0.6, are interpreted to be of cumulate origin (Abrajano et al., 1989). The Acoje Block lower crustal section is dominated by cumulate gabbronorites with olivine–clinopyroxene–orthopyroxene–plagioclase crystallization sequence. Coexisting plagioclase and clinopyroxene in gabbronorite are calcic (anorthite content [Ca/(Ca+Na+K)] = 89–94) and magnesian (Mg# [Mg/(Mg+Fe)] = 0.80–0.87). In addition to petrological criteria discussed above, the arc affinity of Acoje Block has been demonstrated using immobile element-based geochemical fingerprinting of volcanic and hypabyssal rocks, as well as constituent clinopyroxene (Yumul, 1996). On a regional scale, the ophiolite appears to have a domal structure with a north-south trending axis. The volcanic section of Acoje Block in the northern Masinloc massif dips northwest and is unconformably overlain by middle to late Miocene sedimentary sequences.

3. Volcanic geology

Based on observations around the Barlo massive sulfide mine, two volcanic units with distinct lithofacies are distinguished in the Acoje Block extrusive sequence—a dominantly pyroclastic lower basaltic andesite-andesite unit overlain by an upper boninite unit with minor boninitic basalts. Here and in the succeeding sections, we use the term boninite as per the recommended IUGS criterion (Le Maitre, 2002). Pillow lavas that qualify as boninite based on MgO and TiO_2 contents but with less than 52 wt% SiO_2 are classified as boninitic basalts, equivalent to the "basaltic boninite" of Reagan et al. (2015). Structural

measurements of bedding planes in 136 locations constrain the gross structure of the crustal sequence, consisting of a NE-SW trending doubly-plunging anticline forming a dome structure and NW-plunging anticline (Fig. 2). Estimated thickness of the upper unit and lower volcanic units are 680 and 520 meters, respectively. Structural data, field observations, and locality coordinates are summarized in Appendix 1.

South of Barlo mine, boninite dike swarms with conjugate intrusive directions change into a succession of submarine explosive volcanic deposits. In order of ascending stratigraphic level, the lower basaltic andesite-andesite unit consists of tuff breccia with block-sized pyroclasts (Fig. 3j), subaqueous pahoehoe lava flows with ropy wrinkles and stretched vesicles on lobe crust (Umino et al., 2002; Umino et al., 2000) (Fig. 3i), moderately welded agglutinate, welded scoria and spatter deposits marginal to a NW-SE trending fissure vent, and an uppermost fall-out deposit of glassy lapilli tuff (Fig. 3h). In places, tuff breccia is cut by NE-dipping boninite dikes. The dominant occurrence of flat pahoehoe lobes suggest the pre-existence of subhorizontal topography (Umino et al., 2002). The volcanic facies recognized in the upper section of the lower volcanic unit (agglutinate, scoria and spatter deposits surrounding fissure vent) are characteristic of intermittent submarine Strombolian to Hawaiian fire fountaining (Head & Wilson, 2003).

NW-dipping boninite tuff breccia and pillow lavas of the upper unit (Figs. 3b, c) overlie hyaloclastite (Fig. 3d), spatter deposits and pillow lavas (Fig. 3e) of the lower basaltic andesite-andesite unit at an exposure north of Mt. Sol. A dacite sill directly above glassy dacite pillow lavas in the lower unit has a *presumed* whole-rock K-Ar age of 44.1 $\pm$ 3.0 Ma (Fuller et al., 1989). Pillow lavas of the upper and lower unit show distinct morphological features based on vertical (*V*) and horizontal (*H*) axes measurements after the method of Walker (1992) (Fig. 4). Pillow lavas of the lower unit (Fig. 3e) are marked by lower aspect ratios (n=92, median H=0.53 m, median V=0.34 m) compared to boninitic basalts of the upper unit (Fig. 3f) which are elongate (n=15, median H=0.74 m, median V=0.32 m). SW of Barlo mine, NE-dipping pillow lavas of the upper unit (Fig. 3f) are overlain by middle-late Eocene radiolarian-bearing claystone (Schweller et al., 1984). Further southwest in a synclinal area with upright structures preserved, a ~30 meter-high boninite pillow volcano is recognized (Fig. 3g). It consists of flattened flow lobes in the summit with pillow lavas dipping downslope along its flanks. This volcanic construct is one of several discrete boninitic volcanic edifices rising above the lower unit. Elsewhere, these pillow lavas are cut

by SW-dipping dikes with glassy margins and overlain by glassy boninite lapilli tuff fall deposit (Fig. 3a).

4. Sampling and analytical methods

4.1 Acoje Block (Barlo) whole-rock dataset

A total of 152 samples were collected during the 2016 mapping campaign. For this study, a subset of 44 samples located along NW–SE transects of the Acoje Block volcanic sequence at Barlo were selected for whole-rock geochemical analyses and screened through visual and microscopic assessment of secondary alteration. The location of samples is shown in the geologic map in Fig. 2. Rock slabs were cut to remove altered surfaces. Initially, slabs were crushed coarsely to manually separate low temperature secondary minerals such as quartz and calcite. The coarse crushing step was followed by rinsing with deionized water and drying in an oven at 110 °C for at least 12 hours. An iron mortar and an agate mill were used for fine crushing and grinding, respectively. Ignition loss is taken as the normalized lost weight after ignition of ground rock powder at 900 °C for four hours. Major element compositions were determined by X-ray fluorescence (XRF) spectrometry using a PANanalytical Axios spectrometer at the Geological Survey of Japan. Glass beads were fused using a Tokyo Kagaku bead sampler (TK-4500) at a 1:10 dilution ratio as mixtures of 0.5 g (±0.0002) rock powder and 5 g (±0.001) lithium tetraborate alkali flux ($Li_2B_4O_7$, Merck Spectromelt A10). Precision, measured as percent relative standard deviation (%RSD), was also better than 2% based on repeated measurements of JB-2, BIR-1 and BHVO-2; accuracy is better than 2%. Trace element (REE, V, Cr, Ni, Li, Be, Rb, Sr, Y, Zr, Nb, Cs, Ba, Hf, Ta, Pb, Th and U) concentrations were determined by inductively coupled plasma mass spectrometry (ICP-MS) using an Agilent 7900 instrument also located at GSJ/AIST. Samples were digested for at least 48 hours on a hotplate using screw top Teflon beakers with a mixture of HF and HNO3 at 5:1 ratio. Dissolution procedures were performed in a Class 1000 clean laboratory. 12 international standards (BIR-1, BRR-1, JB-2, JB-3, JA-1, JGb-1, JA-2, BCR-1, AGV-1, JB-1a, BHVO-2 and BE-N-1) were used to construct calibration lines. JB-2 and JB-3 solutions at similar dilution levels were used as external standards. Reproducibility is better than 2 % for REEs and better than 3 % for the rest of the trace elements except for Ta (6.5 %) and Be (3.6 %). Mean percent error is generally within 5 to 10 % relative to the preferred values of Jochum et al. (2016) and Dulski (2001).

Major element compositions of constituent mineral phases were determined with a JEOL-8800R electron microprobe at Kanazawa University using a 3 μm probe diameter, 20 nA probe current and 20 kV accelerating voltage. Natural (Kurose olivine and clinopyroxene) and synthetic mineral standards were used for calibration and data were corrected using the ZAF method.

Representative mineral chemistry data are listed in Table 1. Results of whole-rock major and trace element analyses are given in Table 2 with total Fe represented as Fe_2O_3. In succeeding discussions, all samples are normalized to 100 % volatile free with total Fe recalculated as FeO* to enable comparison with compiled datasets. A collection of previously published and unpublished major element composition of lavas and dikes from the volcanic sections of the Zambales ophiolite (Tarlac, Barlo, Sual and Subic) utilized in the discussion are compiled in Appendix 2.

Additional whole-rock geochemical data for Acoje Block samples (Barlo and Sual localities) from separate sampling campaigns (2015 and 2018) can be found in Table 5 with corresponding analytical methods in section 4.3.

4.2 Acoje Block (Barlo) glass and melt inclusion dataset

Twelve boninitic glasses and nineteen spinel grains were selected for in-situ analyses of water content, major and trace element compositions. The boninitic glasses include high-silica boninite, low-silica boninite and low-silica boninite series subtypes from at least 8 localities; while the spinel grains were separated from detrital sand collected marginal to boninitic basalt outcrops. Most of the glass samples are groundmass glasses (*n*=8) and quenched pillow rims (*n*=2). In addition, groundmass glasses with abundant quenched crystals (*n*=2) were also selected to assess the effect of crystallinity on water content. Crushed glass separates and spinel grains were first sonicated in deionized water prior to mounting and polishing. Water concentrations were determined via Fourier transform infrared (FT-IR) micro-reflectance spectroscopy using the FT-IR system, consisting of a JASCO FT/IR-660 Plus spectrometer and a JASCO IRT-30 microscope, housed at the Earthquake Research Institute (ERI), University of Tokyo. Adapting the method of Yasuda (2014), a vacuum FT-IR setup for noise reduction and a narrow-band mercury-cadmium-telluride (MCT) detector for signal-to-noise ratio enhancement were used. From the measured raw reflectance values, a 25-point moving average and 4th order polynomial curve fitting (range: 2000 to 5500 cm^{-1}) were applied. The reflectance value of the fitted

curve at 3650 cm^{-1} is defined as the $R_{baseline}$ value. ΔR is then taken as the absolute value of the difference between $R_{baseline}$ and the corresponding reflectance value at 3650 cm^{-1} which is characterized by local minima in the 25-point moving averaged reflectance spectra. Step-wise determination of $\Delta R/R_{baseline}$ ratios is illustrated in Appendix 3. Water contents were derived from $\Delta R/R_{baseline}$ values using the empirical calibrations of Yasuda (2014) based on synthesized basaltic, andesitic and dacitic glasses. The appropriate calibration was chosen by visual inspection of the raw reflectance spectra in the 800 to 1300 cm^{-1} region.

Major and trace element compositions (REEs, V, Cr, Co, Ni, Li, B, Sc, Rb, Sr, Y, Zr, Nb, Cs, Ba, Hf, Ta, Pb, Th and U) of boninitic glasses and spinel-hosted melt inclusions were determined at Kanazawa University following established protocols reported in Umino et al. (2015) and Umino et al. (2018). Following Noguchi et al. (2004), broad beam diameters were used in the microprobe analyses (30 μm for glass and 25 μm for melt inclusions). Prior to point analyses, X-ray Mg-Ca-Al-Ti-Fe compositional mapping was employed to check for Fe loss in the melt inclusion-spinel host grain interface. Five of the nineteen spinel grains bear melt inclusions, and only two grains have inclusions that were large enough for microanalyses. In the LA-ICPMS analyses, a typical cycle consists of single measurements of standards NIST 612 and BCR-2g followed by 4–6 sample measurements with each glass being analysed 3 times. Laser ablation beam diameter for glasses and melt inclusions are 100 μm and 40 μm, respectively. CaO determined by EPMA is used as internal standard.

Water contents, major and trace element compositions of boninitic glasses and spinel hosted melt inclusions from Barlo are summarized in Table 3.

4.3 Coto Block dataset

During the March 2018 reconnaissance sampling campaign, samples were collected from the dike section of the Coto Block along Bulsa River (Fig. 1b). This sampling locality (Sitio Balogbalog) corresponds to the southernmost "dike-sill" and "gabbro-diabase" sampling sites of Geary et al. (1989). At this locality, planar intrusives with sharp contacts both have NE and NW strike orientations (Fig. 5a-d). Comparison of structural data from 1:50,000 quadrangle maps and the sedimentary carapace of the ophiolite (the Eocene Aksitero Formation) immediately east of the sampling sites enables structural correction to the paleohorizontal direction. Using the pole of the sedimentary carapace bedding orientations, the dominant NW and subordinate NE striking intrusives are characterized as

sheeted dikes (Fig. 5a) and minor late-stage mafic dikes (Fig. 5c), respectively. Younger mafic dikes intrude plagiogranites and gabbro (Fig. 5b-c), thus the sampled igneous stratigraphic level is estimated to be the root zone of the sheeted dike complex. Texturally, the sampled dikes range from fine grained basaltic andesite (Fig. 5e), diabase with characteristic subophitic texture (Fig. 5f) and fine to medium grained gabbro with tabular, euhedral-subhedral plagioclase and altered clinopyroxene (Fig. 5g-h). As noted by Geary & Kay (1983), greenschist facies alteration minerals are prevalent including blue-green actinolite and yellowish epidote+chlorite.

Whole-rock and trace element compositions of Coto Block dikes and Acoje Block lavas and dikes from 2015 and 2018 sampling campaigns were analysed at Kanazawa University. Rock powders were prepared following the sample preparation procedures of Tani et al. (2005). Loss on ignition (LOI) values were determined by a two-step process. First, powders were dried in an oven for 2 hours at 105° C to remove moisture (H_2O^-) followed by ignition in a muffle furnace for 4 hours at 900° C. Preparation of glass beads and instrumental setup of the Rigaku ZSX Primus II X-ray fluorescence spectrometer is similar to that Kusano et al. (2014). Accuracies of both the 2015 and 2018 runs based on GSJ standards and JA-2, JA-3 and Jb-1b are generally better than 5%. Repeat analyses of inter-laboratory sample NK during the 2018 run show a precision (% RSD) that is better than 1% except for Na_2O. Whole-rock trace element concentrations (Li, Sc, Ti, V, Cr, Co, Ni, Rb, Sr, Y, Zr, Nb, Cs, Ba, Hf, Ta, Pb, Th, U and REEs) were determined by LA-ICPMS on flux-free fused glasses (A. Tamura et al., 2015). Rock powders of standards JB-2, BHVO-2, BIR-1 and JA-2 were fused as glass in a similar way and were analysed as unknowns. A typical cycle consists of single measurements of standards NIST 610 and BCR-2g followed by 4–6 sample measurements with each glass being analysed 3 times with a laser ablation beam diameter of 60 μm. CaO determined by XRF is used as internal standard. The fused glasses are fairly homogeneous with percent relative standard deviation (% RSD) that is less than 5%, except for the following elements– Cr, Ni, Rb, Nb, Cs, U and Pb. With the exception of Pb, B, Cs and Cr, all trace elements have a mean percent error that is better than 15% relative to the preferred JB-2, BHVO-2, BIR-1 and JA-2 values of Jochum et al. (2016). Whole-rock and trace element compositions of Coto Block dikes and additional Acoje Block lavas and dikes from Barlo, Sual and Subic localities are given in Tables 4 and 5, respectively.

5. Textures and phase chemistry

Zambales high-silica boninite is mostly aphyric and consists of subhedral olivine microphenocrysts (Mg# [Mg/(Mg+Fe^{2+})] = 0.88–0.91), abundant elongate enstatite microphenocrysts (Mg# = 0.86–0.89, $Wo_{2.6–4.9}En_{82–86}$) with augite ± pigeonite overgrowth (Mg# = 0.67–0.84, $Wo_{31-44}En_{34-57}$), and chromian spinel (Cr# [Cr/(Cr+Al)] = 0.69–0.84, Mg# =0.53–0.69) set in a glassy groundmass with feathery quench clinopyroxene (Figs. 6a-d). This assemblage corresponds to "Type II boninite" of Umino (1986) in samples described from the type locality at Chichijima, Ogasawara (Bonin) Archipelago in southern Japan. Unlike low-Ca, high-silica boninites from Ogasawara, clinoenstatite has not been identified so far. Comparative mineral chemistry of Zambales and Ogasawara boninite is shown in Fig. 7. Olivine, orthopyroxene and spinel compositions of Zambales and Ogasawara boninite are almost identical except for a limited range of olivine Mg#, which is most likely due to a small number of samples analyzed (two for olivine and four for spinel), and lower spinel Cr# in Zambales boninite (Taylor et al., 1994; Umino, 1986; Yajima & Fujimaki, 2001). NiO contents of olivine range from 0.18–0.41 wt% and plot on fractionation trends from the mantle olivine array. Subhedral olivine microphenocrysts in high-silica boninite (ZM2-100A) is zoned with magnesian cores. The range of spinel Cr# of Zambales boninite overlap with Acoje podiform chromitites and transition zone dunites. Enstatite microphenocrysts with sieve texture and reverse zoning are recognized together with embayed quartz xenocrysts (Figs. 6e-g). Reversely zoned enstatite has oscillatory-zoned magnesian rims (Mg# = 0.86–0.87) with resorbed and dissolved cores (Mg# = 0.68–0.77). Similar xenocrystic quartz and sieve-textured enstatite have also been noted in Ogasawara boninite (Watanabe & Kuroda, 2000). Glassy olivine-phyric and olivine-clinopyroxene-phyric low-silica boninite varieties are also present (Figs. 6h-i). Hypocrystalline boninite pillow lavas consist of olivine, usually altered and replaced by chlorite and carbonate minerals, subhedral clinopyroxene phenocrysts, elongate orthopyroxene and plagioclase microphenocrysts.

Highly phyric boninitic basalt has a phenocryst assemblage of olivine replaced by calcite, zeolite and clay minerals, euhedral to subhedral augite (Mg# = 0.82–0.90, $Wo_{41-43}En_{48-53}$) with oscillatory and sector zoning, and rare corroded enstatite (Mg# = 0.85–0.88, Wo_3En_{82-84}) with reverse zoning. Chromian spinel (Cr# = 0.62–0.71) occurs near phenocryst margins and as inclusions in olivine. Peculiar zoning relationship of augite and enstatite demonstrates that

some pyroxenes are xenocrysts in nature. Groundmass consists of less than 0.3 mm long plagioclase microlites with swallow-tail terminations, spherulitic clinopyroxene and altered interstitial glass totally replaced by clay minerals. Acicular zeolite occurs as vesicle fillings. We note that such textures have been described in samples reported as boninite by Evans et al. (1991). Lower-unit basaltic andesite and andesite pillows and lapilli tuff are marked by the presence of abundant plagioclase laths as glomerocrysts and sparse cpx±opx microphenocrysts with two-pyroxene intergrowths in a glassy groundmass with plagioclase microlites and magnetite (Figs. 6j-k).

6. Whole-rock and glass geochemistry

6.1 Acoje Block (Barlo) whole-rock dataset

The Acoje Block extrusive section at Barlo is predominantly composed of basaltic andesite and andesite. Loss on ignition (LOI) values are generally between 4 and 7 wt% and total alkalis are less than 3 wt% (Table 2). Cs, Rb, K, Li, Ba and Mn in some dikes and pillow lavas, especially those collected nearest to the massive sulfide mine, are highly scattered and plot away from general fractionation trends shown by the majority of samples. The rest of the samples show variations in the major element and trace element compositions consistent with fractional crystallization and are deemed as primary. Pillow lava, tuff breccia and lapilli tuff of the upper volcanic unit and dikes from the uppermost section of the dike-sill complex are primitive with > 8 wt% MgO and < 0.5 wt% TiO_2, satisfying the IUGS criteria for boninite (Le Maitre, 2002). Pillow lavas that qualify as boninite based on MgO and TiO_2 contents but with < 52 wt% SiO_2 are classified as boninitic basalts. Following the classification of Kanayama et al. (2013) and Reagan et al. (2015) both high-silica (HSB) and low-silica (LSB) boninite subtypes are recognized (Fig. 8). This compositional division is consistent with petrographic observations, with HSB having olivine with orthopyroxene microphenocrysts and LSB with olivine or olivine with clinopyroxene phenocrysts. Boninitic samples previously described at Barlo are actually from the dike section and lower section of the upper unit and with sampling having being limited to Balincaguin River and the periphery of Barlo VMS mine (Evans et al., 1991; Hawkins & Evans, 1983; Tamayo, 2001; Yumul, 1990). Besides the low-silica boninite and boninitic basalt samples from previous studies with altered equivalents having more than 3.5 wt % Na_2O+K_2O, 3–5 wt % LOI and possibly up to 4 wt% SiO_2 enrichment, this is the first report of pristine high-silica boninite

in Zambales ophiolite. Boninite from Zambales (n=14) have CaO/Al_2O_3 ratios less than 0.76, mostly within 0.63–0.71 with FeO*/MgO ratios <1 (Mg# values from 63 to 73). Ni and Cr contents are high, ranging from 72 μg/g to 292 μg/g and 145 μg/g to 727 μg/g, respectively. Boninitic basalts (n=3) are primitive as well with 12.4–13.6 wt% MgO and 712–1113 μg/g Cr.

Pillow lava and lapilli tuff of the lower volcanic unit and dikes from the deeper section of the dike-sill complex are andesitic in composition with 55.5–63.5 wt% SiO_2, 2.4–7.1 wt% MgO and 0.31–0.47 wt% TiO_2 (Fig. 8). These andesites (n=26) are magnesian with Mg# mostly within 0.47 and 0.54, CaO/Al_2O_3 ratios < 0.63, FeO*/MgO ratios > 1.16 and Ni and Cr contents are also low at 8–58 μg/g and 3–47 μg/g, respectively. MgO and SiO_2 compositions of lower unit volcanics and corresponding dikes lie above the island arc basalt (B)–basaltic andesite (BA)–andesite (A)–dacite (D) discriminant line of Pearce and Robinson (2010) and follow a curvilinear fractionation trend from low-silica boninite; thus, are recognized here as forming a low-silica boninite differentiation series (Fig. 6). Dacitic pillow lavas represent the differentiated end of the LSB series. A gap between andesitic boninite-series volcanics with < 60 wt% SiO_2 and dacite (62–63 wt%) is present. A single dike (B-47 d4) that cross cuts the LSB-series dikes is the only sample with >0.5 wt% TiO_2. Although the pervasive clay alteration of samples from the Barlo massive sulfide mine hinders the direct characterization of the host rocks, the massive sulfide deposit is most likely hosted by the lower volcanic unit and possibly up to the lowermost section of the upper unit based on stratigraphic relationships and comparison of field and core descriptions (Paringit, 1977). The occurrence of massive sulfide-bearing horizons at Barlo is also consistent with massive sulfide mineralization in Oman, Troodos and Bonin Ridge which occur either below or within the boninitic volcanic section (Ishizuka et al., 2014; Umino et al., 2009).

Trace element compositions of Zambales boninite and boninite series volcanics are marked by low abundances relative to MORB (Fig. 9). Extended trace element patterns arranged after Pearce and Parkinson (1993) show the dominance of slab-derived components with notable enrichment in fluid-mobile elements (Cs, Rb, Ba, U, K, Pb, Sr, Li, Na) and depletion of high field strength elements (Nb, Ta). Hf shows a positive anomaly relative to Sm while Ti shows a negative anomaly relative to Y. In contrast with samples from Ogasawara that exhibit characteristic U-shaped chondrite-normalized rare earth element (REE) patterns, Zambales boninite and boninite-series volcanics exhibit spoon-shaped REE patterns with heavy REEs (HREE) at 5–15 times chondrite values and weak negative Eu

anomaly (Eu/Eu* = 0.9). Boninitic basalts are more depleted in middle and heavy REEs with just three to five times the chondrite values. Excluding moderately altered samples, chondrite normalized La/Ce ($[La/Ce]_N$) ratios of Zambales and Ogasawara boninite are both <1. The range of $[Sm/Yb]_N$ ratios, as measure of middle REE depletion relative to heavy REE, however, are distinct at 0.06–0.09 for Zambales and 0.02–0.05 for Ogasawara. The effect of fractionation in Zambales samples is shown as increasing trace element abundances relative to a glassy olivine–phyric LSB (ZM2-107) with 12.4 wt% MgO. The evolved dacitic samples does not differ significantly with just twice the normalized REE abundances of the most primitive sample. Trace element pattern of a single dike (B-47 d4) with > 0.5 wt% TiO_2 is visibly different with muted fluid-mobile element enrichment without a negative Ti anomaly, and smooth, concave downward LREE-depletion (Fig. 9).

6.2 Acoje Block (Barlo) glass and melt inclusion dataset

Compared to their bulk-rock counterparts, the anhydrous boninitic glasses are marked by lower MgO and higher Al_2O_3, CaO, FeO*/MgO at similar SiO_2 values (Table 3). The essential trace element characteristics of bulk-rock boninites are reflected by the glass samples. Extended trace element patterns show that boninitic glasses possess faithful records of large ion lithophile elements (LILE) enrichment (Fig. 9). Although there is considerable scatter in Yb vs. LILE (K_2O, Rb, Sr) variation diagrams caused by the fractionated nature of LSB-series glass and variable crystallinity in HSB glasses (Fig. 10), there is a positive correlation in HSB and LSB glasses suggesting that this variation is magmatic.

Spinel-hosted melt inclusions from Zambales analyzed in this study consists of variolitic orthopyroxene crystals, quenched glass and vesicles (Fig. 10, Appendix 3). Elemental maps show uniform Fe content throughout the inclusion as well as the absence of anomalous Fe enrichment in inclusions rims. Based on normalized compositions, Zambales melt inclusions can be classified as low-silica boninite subtype. CaO and normalized trace element patterns define two melt inclusion (MI) groups— type I MIs with 11.5 wt% CaO and severe LREE/HREE depletion and Type II MIs with 9.5 wt % CaO and chondrite-normalized REE patterns is similar to LSB glass.

The water contents of both HSB (n=13) and LSB (n=3) glasses are low at 1.03±0.22 wt % and 1.07±0.12 wt %, respectively (Fig. 11). Groundmass glass of highly crystalline samples have higher water contents and varies from 1.4 to 3 wt %. LSB series glasses have decreasing H_2O contents with decreasing MgO illustrating the effect of fractional crystallization. H_2O/Ce

ratios of boninite glasses and fractionated LSB-series glasses are tightly clustered at 7000±1000. Boninitic melt inclusions (Type I and II) are characterized by uniform H_2O contents (2.6±0.17 wt %) and are higher than matching LSB glass. Type I and II boninitic melt inclusions have distinct H_2O/Ce ratios at 24,000 and 40,000. The degassed nature of boninitic glasses is inferred based on decreasing H_2O/Ce ratios of Type II LSB melt inclusions and LSB glass at similar Ce concentrations.

6.3 Acoje Block volcanic stratigraphy

The volcanic sequence at Barlo, based on observed local stratigraphic relationships, is LSB series volcanics– boninitic basalt–LSB–HSB from base to top (Fig. 3). This volcanic stratigraphy is remarkably similar to Holes U1439 and U1442 of IODP Exp. 352. Both the Barlo extrusive section and Holes U1439 and U1442 are marked by an abundance of LSB relative to HSB (Reagan et al., 2015). In contrast, the onshore boninite sequence at Ogasawara is dominated by 48–46 Ma HSB and HSB series volcanics interbedded with minor LSB (Maruberiwan Formation), which are overlain by 45 Ma LSB and calc-alkaline andesite–dacite (Mikazukiyama Formation) (Kanayama et al., 2012; Taylor et al., 1994; Umino, 1986). Several dikes in the Subic crustal section in the southern San Antonio massif have compositions like Barlo boninitic basalts (Yumul et al., 2000), albeit their petrographic characteristics have not been described. This raises the possibility that boninite is present in other volcanic sections of the Acoje Block as well. The rest of the volcanic sections of the Zambales ophiolite (Coto volcanic section in Tarlac, Sual dikes north of Barlo, and Subic dikes and pillow lavas in the south) are dominated by basalts and basaltic andesites with greater than 0.5 wt% TiO_2 which can be classified as moderate-Fe tholeiites (Pearce & Robinson, 2010). The tholeiite dike (B-47 d4) that cross cuts low-silica boninite dikes in the deeper dike swarm section at Barlo is similar in composition and correlatable with 44.0±3.0 Ma dikes in the Sual crustal section located NE of Barlo, suggesting that tholeiites are coeval or slightly younger than the Barlo extrusive section.

7. Discussion

7.1 Low-pressure fractionation and magma mixing

Early experimental studies of primitive boninite produced andesitic primary liquids and led to the initial characterization of boninite as a primary magma (Kuroda et al., 1978).

Subsequent detailed petrologic analyses resulted in the recognition of the importance of low-pressure fractionation and magma mixing processes to account for the compositional variation of boninite and boninite series volcanics (Dobson et al., 2006; Taylor et al., 1994; Umino, 1986). Meijer (1980) introduced the concept of the boninite series to describe cogenetic bronzite andesite, dacite and rhyolite formed through the differentiation of boninite, analogous to tholeiitic and calc-alkaline magma series. Figure 8 shows oxide vs. SiO_2 variation diagrams of Zambales boninite and boninite series volcanics. Also shown are boninite and boninite series volcanics from Ogasawara (Kanayama et al., 2012; Nagaishi, 2008; Taylor et al., 1994; Umino & Nakano, 2007; Yajima & Fujimaki, 2001) and Holes U1439 and U1442 of IODP Expedition 352 (Haugen, 2017; Reagan et al., 2015). MgO, TiO_2, CaO and Al_2O_3 contents of HSB and LSB form subparallel trends suggesting distinct parental magma compositions and fractionation paths. Parental HSB is characterized by higher MgO, lower TiO_2, Al_2O_3 and CaO at a given SiO_2 than LSB. HSB is marked by the abundance of orthopyroxene and, in some localities, the presence of clinoenstatite. Umino (1986) describes the crystallization sequence at Chichijima as chromian spinel, olivine, clinoenstatite, enstatite and augite. The HSB differentiation series is best exemplified by samples from Ogasawara and Site 786, ODP Leg 125 (Arculus et al., 1992). Boninite from other notable Western Pacific localities such as the Mariana Trench (Bloomer & Hawkins, 1987; Dietrich et al., 1978), Cape Vogel, Papua New Guinea (G. A. Jenner, 1981; König et al., 2010), Nepoui, New Caledonia (Cameron, 1989; Cluzel et al., 2016) and Hahajima seamount (Y. B. Li et al., 2013) are all high-silica sub type (Fig. 12). Zambales HSB show limited compositional variation with most of the samples collected in an area north of Mt. Sol, possibly from a single volcanic edifice. On the other hand, LSB crystallization sequence is controlled by olivine and clinopyroxene fractionation (Kostopoulos & Murton, 1992; Natland, 1982). LSB differentiation series is typified by suites from northern Zambales, Holes U1439 and U1442 of Expedition 352 and Hole 458, ODP Leg 60 (Meijer, 1982; Sharaskin, 1982). Other LSB and LSB series localities include Facpi Formation in Guam (Reagan & Meijer, 1984), northern Tonga Trench and active Tonga arc (Cooper et al., 2010; Falloon et al., 2007; Falloon & Crawford, 1991; Resing et al., 2011), Tethyan ophiolites such as Troodos (Cameron, 1985; König et al., 2008; Osozawa et al., 2012; Pearce & Robinson, 2010) and Oman (Ishikawa et al., 2002; Kusano et al., 2017; Kusano et al., 2014; Nagaishi, 2008) and Paleozoic ophiolites in the Appalachians namely Betts Cove and Thetford Mines (Bedard, 1999; Coish, 1989;

Laurent & Hébert, 1989). Ediacaran boninitic rocks reported from Khaintaishir and Erdene Uul ophiolites in western Mongolia (Buriánek et al., 2017; Gianola et al., 2017) are possibly low-silica boninite series volcanics (Fig. 12).

Using spinel-hosted melt inclusions reported by Umino et al. (2018) as parental magma compositions, isobaric fractional crystallization paths of residual liquids at +1 Δlog(FMQ) are modeled using rhyoliteMELTS v.1.2.0 (Ghiorso & Gualda, 2015). The compositions of primary spinel-hosted boninitic melt inclusions from Ogasawara (2.1–3.4 wt% H_2O) and Guam (3.8 wt% H_2O) are in accord with experimental glasses formed by melting synthetic Troodos harzburgite and depleted Tinaquillo lherzolite at 1.5 GPa (Falloon & Danyushevsky, 2000) (Fig. 8). The range of whole-rock HSB compositions can be reproduced by low pressure (1–2 kb) fractional crystallization of parental Ogasawara HSB magmas at lower water content (1 wt%). TiO_2 and CaO contents of Zambales HSB are in the upper end of Ogasawara HSB compositions and can alternatively be produced by fractionation from a parental composition straddling the HSB and LSB boundary of Reagan et al. (2015). Given a primary LSB magma composition identical to a spinel-hosted melt inclusion from Guam, low pressure (1–2 kb) fractional crystallization at lower water content (1 wt%) can likewise account for the major element variation of Zambales LSB and LSB series volcanics. The modeled early crystallization of cpx relative to opx and the onset of plagioclase crystallization following cpx at ~57 wt% SiO_2 is reflected in the modal compositions of Zambales LSB and LSB-series volcanics (Fig. 6j-k). The occurrence of differentiated LSB series volcanics in the base of the volcanic pile suggests that initial LSB magmas underwent protracted crystal fractionation in magma chambers at depth. Influx of primitive HSB perturbed sub-volcanic magma chambers and likely induced magma mixing. The presence of reversely zoned enstatite microphenocrysts in Zambales HSB, attest to high-level magma mixing between an olivine+orthopyroxene saturated HSB magma and a preexisting LSB series andesitic magma. Zambales HSB slightly deviate from the modeled Ogasawara HSB fractionation paths and lie on a mixing line with potential HSB and LSB-series end member components having SiO_2 contents that does not vary significantly at 58 and 57 wt % respectively.

The markedly divergent fractionation paths followed by boninite and boninite series volcanics from Barlo (Fig. 8) and basalts–basaltic andesites from various volcanic sections of the Zambales ophiolite are shown in the MgO, TiO_2 and FeO*/MgO vs SiO_2 variation

diagrams (Fig. 13). Zambales LSB and LSB series volcanics follow fractionation paths of hydrous primitive arc magmas (Grove et al., 2012). Moderate-Fe tholeiitic basalts and basaltic andesites from the rest of the volcanic sections of Zambales ophiolite (Evans et al., 1991; Geary et al., 1989; Hawkins & Evans, 1983; Tamayo, 2001; Yumul, 1990), including the Coto Block dikes sampled in this study, and proto-arc basalts from the Izu–Ogasawara–Mariana forearc (Arculus et al., 2015; Ishizuka et al., 2011; Reagan et al., 2010, 2015) exhibit large FeO*/MgO ratio variation at a restricted SiO_2 interval and define a slope steeper than the discriminant line of Miyashiro (1974). The variation of Coto Block dikes and lavas can be explained by the onset of clinopyroxene and plagioclase following spinel and olivine assuming primary proto-arc basalts from Mariana and Ogasawara trench slopes as parental magmas at pressures of 1kb and water content of 0.2 wt % H_2O (Fig. 13).

7.2 Shallow slab contributions to a less depleted mantle source

Although there is a general consensus on boninite petrogenesis (Crawford et al., 1989; Pearce et al., 1992), the requisite sub-arc conditions ideal for boninite generation span a range that may involve heterogeneous mantle wedge sources (depleted lherzolite to harzburgite) and the addition of diverse slab-derived components. Here, we highlight the peculiar trace element characteristics of Zambales boninite; geochemical modeling will be in the next sub-section. Fig. 9 shows MORB and chondrite-normalized trace element patterns of Zambales boninite and boninite-series volcanics (bulk-rock and glasses) together with boninite suites from Ogasawara, Holes U1439 and U1442 of IODP Expedition 352, Troodos and Oman ophiolites, Nepoui (New Caledonia) and Cape Vogel (Papua New Guinea). Boninite from Zambales, Oman and Troodos ophiolites all show spoon-shaped chondrite normalized REE patterns with heavy REEs that are 5–9 times chondrite values.

Based on lower spinel Cr#s and higher HREE abundances of the most primitive sample, Zambales boninite is derived from a mantle source that is less depleted than Ogasawara boninite (Fig. 9). The less depleted nature of the Zambales mantle wedge source can be further examined using spinel Cr#–spinel Mg# and olivine Fo–spinel Cr# systematics of residual peridotites in the mantle section the ophiolite. A compilation of residual peridotite mineral chemistry data from Zambales (Bacuta, 1989; Evans, 1983; Tamayo, 2001; Yumul, 1990), Oman (Hanghoj et al., 2010; Kanke & Takazawa, 2014; Miura et al., 2012) and the Izu–Ogasawara–Mariana forearc (Ishii, 1992; Morishita et al., 2011; Parkinson & Pearce, 1998; Zanetti et al., 2006) is shown in Fig. 14. Also shown in the background is the contoured

abyssal peridotite dataset of Warren (2016); this depiction is preferred over a simple field as it shows potentially significant petrological details such as the bimodal spinel Cr# population in harzburgite and its coincidence with pMELTS (Ghiorso et al., 2002) modeled fractional melting residues of DMM source at 1 GPa and degrees of melting (F) prior to clinopyroxene exhaustion. The range of spinel Cr#s in fertile to moderately depleted residual peridotites from Acoje ranges from 0.18 to 0.56, coinciding with abyssal harzburgites. This range is distinct from Coto Block, Fizh Block (northern Oman), and Conical and Torishima seamounts (IBM forearc) peridotites with spinel Cr#s that range from 0.36 to 0.63, 0.24 to 0.78 and 0.31 to 0.81, respectively (Fig. 14). Although overlapping in spinel Cr#s, IBM forearc peridotites record diverse oxygen fugacities (Conical Seamount: FMQ -1.1 to FMQ +0.4 log units, Torishima Seamount: FMQ +0.8. to FMQ +1.6 log units) and are products of varying degrees of partial melting (Conical Seamount: 15–20%, Torishima Seamount: 20–25%) (Parkinson & Pearce, 1998). A harzburgite from Acoje Block (PH98-16, spinel Cr#=0.310) possess characteristics that are indicative of a supra-subduction environment, i.e. low olivine-spinel equilibration tempeatures (780^{o} C) and calculated oxygen fugacities higher than abyssal peridotites (FMQ +1.9 log units) (Tamayo Jr., 2001), and can be modeled as residues of less than18% fractional melting of a DMM source (Fig. 14). The point I wish to raise here is that like IBM forearc peridotites, the Acoje and Coto mantle sections of the Zambales ophiolite record different melting histories. Based on spinel Cr#–spinel Mg# and olivine Fo–spinel Cr# systematics, it can be inferred that Acoje Block peridotites are possible residues of pre-subduction mantle and are the potential sources of Barlo boninites.

Superimposed on the depleted character of boninite are slab-derived components whose nature can be explored using normalized trace element diagrams and trace element ratios with varying compatibilities. The magnitude of hydrous fluid mobile element enrichment in boninite from Ogasawara, Zambales, Oman and Troodos ophiolites are comparable. LREE enrichment is most prominent in Nepoui and Cape Vogel boninites. All boninite suites except for Nepoui and Cape Vogel have elevated Ba/Th ratios (Fig. 15a). Ba is strongly partitioned into aqueous fluids relative to Th, thus is a good proxy for the addition of subduction components released at shallow depths – sz1, Ba-only component of Pearce et al. (2005) (Keppler, 2017; Ribeiro et al., 2015). Increasing Ba/Th ratio is mirrored by Sr/Nd ratio for Zambales, Oman and Troodos boninite (Fig. 15b). Ogasawara, Cape Vogel and Nepoui follow a vertical Th/Yb vector towards sediments – “component 1” of Elliott

(2003). We interpret this decoupling as an indicator of increasing contributions from a deep subduction component that is usually characterized as either sediment melt and/or siliceous fluid (Pearce et al., 2005). Zambales boninite and boninite-series volcanics have U/Th ratio (0.62–0.77) much higher than Cape Vogel boninites (0.20–0.29). High U/Th ratio is associated with saline and oxidizing fluids, while a low U/Th ratio points to the transport of silica-rich fluids (Keppler, 2017). Zambales and Cape Vogel boninites both have a uniform La/Th ratio of 0.2. In the La/Th vs. Sm/La diagram of Plank (2005), Zambales, Oman, and Troodos boninites lie on a mixing line between sediments with Th/La ratio of 0.30–0.35 and a mantle source more refractory than MORB with a Sm/La ratio of 1.75. Ogasawara, Cape Vogel and Nepoui boninites may lie on the mixing line between sediments with a Th/La ratio of 0.1 and 0.2 and a highly depleted mantle source with a Sm/La ratio greater than 2. An alternative explanation is that the low Sm/La ratios of Ogasawara, Cape Vogel and Nepoui boninites dominantly reflect LREE enrichment which masks mixing relationship. The shared characteristics of Zambales, Oman, and Troodos boninites are further exemplified by subchondritic bulk Earth Nb/Ta ratios with low Zr/Hf and Zr/Sm ratios (< 30) characteristic of depleted mantle (Münker et al., 2003; Weyer et al., 2003; Zanetti et al., 2006) (Figs. 15c,d). The high Zr/Sm ratios (> 40) of Ogasawara, Cape Vogel and Nepoui boninites have been ascribed to the presence of residual amphibole in the slab (Cluzel et al., 2016; Foley et al., 2002; König et al., 2010; Pearce et al., 1992). In summary, trace element ratios show that aqueous fluids are the dominant slab components in Zambales boninite and boninite series volcanics with very minor contribution from slab melts (Umino et al., 2015). This is corroborated by the enriched Pb and Sr isotopic compositions of the Acoje Block uppermost crustal differentiates and cumulate ultramafic samples that do not show an inverse relationship with Nd isotopic compositions (Encarnación et al., 1999).

7.3 Primary magma estimates and sub-arc P–T conditions

To infer the sub-arc pressure–temperature conditions of Zambales boninites, primary magma compositions of a glassy olivine–phyric low-silica boninite (ZM2-107, MgO= 12.28 wt%) and an olivine–orthopyroxene microphyric high-silica boninite (ZM2-100A, MgO=8.98 wt%) are estimated using the olivine addition method of Takahashi (1986) and Tamura et al. (2011). Rather than assuming ferric iron over total iron ratios, $Fe^{3+}/(Fe^{2+} + Fe^{3+})$ ratios are solved iteratively using equation 7 of Kress & Carmichael (1991) at $\Delta\log(FMQ)=0$ and an initial guess of temperature. Compositionally dependent Fe–Mg partition coefficients

between olivine and liquid are approximated using an empirical relationship between $K_D(Fe/Mg)^{ol\text{-}liq}$ and mol% (MgO+0.33FeO) of experimental liquids derived by Tamura et al. (2000). Starting from an initial olivine composition, equilibrium olivine and liquid are calculated assuming $Fe^{3+}/(Fe^{2+} + Fe^{3+})$ ratios of 0.14 and 0.16 and $K_D(Fe/Mg)^{ol\text{-}liq}$ values of 0.32-0.33 and 0.30-0.32 for low-silica and high-silica boninite. The $Fe^{3+}/(Fe^{2+} + Fe^{3+})$ ratios used here are slightly lower than those determined by Brounce et al. (2015) for LSB-series glasses using micro-X-ray absorption near-edge structure (μ-XANES) spectroscopy (Site 458: 0.2, 0.24–0.25 ; Guam: 0.21–0.22). Calculations of equilibrium olivine and liquid are repeated until an equilibrium olivine NiO value of approximately 0.4 wt% on the mantle olivine array (Takahashi, 1986) is reached. The method described above enables the estimation of primary Zambales LSB ($Fo_{91.7}$) and HSB ($Fo_{91.8}$) magmas by adding 6% and 11% olivine, respectively. NiO and MnO compositions of olivine in Zambales boninite and calculated equilibrium olivine are shown in Fig. 16. Note that the NiO contents of equilibrium olivine are congruent with actual LSB and HSB olivine; however, only Zambales LSB can satisfy both NiO and MnO equilibrium olivine fractionation paths. The DMM and abyssal peridotite olivine compositions are shown to highlight the refractory nature of the Zambales boninite source. Zambales primary LSB and HSB magma compositions are listed in Table 6 and shown in Fig. 8 with bulk-rock boninite and boninitic melt inclusions. The primary Zambales LSB magma estimate has 14.6 wt MgO compared to the primary boninitic melt inclusion from Guam with 15.1 wt MgO; thus, the primary LSB estimate is regarded as more accurate than the HSB estimate. Trace element compositions of Zambales primary boninite magmas are likewise estimated using the amount of olivine added and the olivine–liquid partition coefficients of Kelemen, et al. (2004). Following Umino et al. (2015), the water content of the primary LSB magma is reconstructed using H_2O/Ce ratios of primitive spinel-hosted boninitic (LSB) melt inclusions. As shown in Fig. 11, LSB glasses and type II melt inclusions are marked by contrasting H_2O/Ce ratios at similar Ce concentrations; since H_2O and Ce are relatively incompatible, the contrasting H_2O/Ce ratios can be attributed solely to degassing. The water content of the primary LSB magma can therefore be estimated by assuming a H_2O/Ce ratio identical to type II LSB melt inclusion. A ratio H_2O/Ce of 24,000 in primitive melt inclusions amounts to a restored H_2O content of 3.17 wt %. The choice type II melt inclusion is further justified by its chondrite-normalized REE patterns comparable to LSB glass. So far, all melt inclusions sampled from Zambales are LSB-type, this hinders estimation of the

water content of primary HSB magma. Consequently, at this point P-T estimates for Zambales HSB are not given.

In consistency with recently published boninite pressure (P)–temperature (T) estimates by Umino et al. (2018), P–T conditions of Zambales primary LSB magma are determined in the same manner by simultaneously solving the olivine–liquid geothermometer (Equation 4) of Putirka et al. (2007) the olivine–orthopyroxene–liquid geothermobarometer (Equation 42) of Putirka (2008). The estimated equilibration temperature–pressure, assuming an oxygen fugacity (fO_2) of Δlog(FMQ)=+1, are 1273° C and 0.34 GPa. P-T conditions of primary Eocene boninite magmas in the Philippine Sea Plate are shown in Fig. 17. Boninites record shallow juvenile sub-arc melting conditions that are less than 1 GPa. Low-silica boninites from Zambales, Guam and Oman have lower olivine and orthopyroxene saturation temperatures than Ogasawara (Umino et al., 2014, 2018). Varying genetic pressure–temperature conditions indicate melting of heterogeneous mantle sources, i.e. ascent of refractory harzburgite source for Ogasawara high-silica boninite (Umino et al., 2018). Zambales LSB lie in an upwelling adiabatic path similar to Guam LSB, with mantle potential temperature (T_P) in excess of 1300° C, within the ambient mantle T_p range. Putirka (2016) estimate a modern MORB (ambient) T_p range of 1330–1450° C. The determined P-T condition for Zambales LSB is very shallow (0.34 GPa). This is interpreted as a record of last equilibration in the uppermost mantle just below the Acoje lower crust cumulates with estimated crystallization pressures of 0.2–0.3 GPa (Abrajano et al., 1989). Using PRIMELT3 (Herzberg & Asimow, 2015), the primary magma composition and olivine liquidus temperature of a depleted (proto-arc) basalt (PAB) from the Coto Block that precedes boninite from the Acoje Block can likewise be estimated. The olivine liquidus temperature of a depleted PAB from Coto Block lies in the adiabatic upwelling path of Mariana Trench PAB with a T_p of ~1370 ˚C.

7.4 Second-stage melting

The primitive nature of boninite permits the straightforward identification of components that control its trace element characteristics (Fig. 9). MORB-normalized multi-element patterns of boninites can be broken down into two pertinent features namely enrichment of large ion lithophile elements (LILE) and depletion of middle and heavy rare earth elements (REE) which are controlled by fluxes from the subducting slab and the

degree of depletion of the mantle wedge source. Geochemical models of boninite petrogenesis focus on quantifying these components. Using trace element compositions of amphibolite and quartzose rocks found in the metamorphic sole of the Oman, Ishikawa et al. (2005) estimated the composition of hydrous fluids released by the subducting slab at amphibolite-facies P-T conditions. The proportion of fluids involved was approximated by matching the fluid mobile element (e.g. Rb, Ba, B, Pb, Li) concentrations of a mantle melt plus fluid composite to fluid mobile element concentrations of Oman low-silica boninite. This approach was extended by Kusano et al. (2017) to document the progressive contributions of slab-derived fluids to incipient arc (V2) magmas represented by lower V2 arc tholeiite and upper V2 boninite. The use of natural samples in Oman contrasts with the approach used by Kimura (2017) and Li et al. (2013) to constrain the nature of slab liquid involved in the generation of high-silica boninite dredged from the Hahajima Seamount in the Izu-Ogasawara forearc. The Arc Basalt Simulator (ABS) of Kimura (2017) uses thermal structures of worldwide subduction zones to determine proportion and phase relations of dehydrating materials in the subducting slab, as well as the depth of dehydration; this enables the construction of an open-system flux melting model for arc magmas. Extensive parameters such as amount of slab liquid added, depletion of mantle wedge source and degree of melting are then matched to a primary arc magma composition. To model Hahajima Seamount boninite, the thermal structure of present-day SW Japan is used as an analogue for a hot subduction zone characteristic of incipient subduction. Shallow mantle wedge conditions of boninite generation (0.8 GPa) estimated using this model are consistent with Umino et al. (2018), albeit at lower temperatures (1314° C). This discrepancy can be attributed to the composition of candidate primary magma with 16.34% MgO. Unless the thermal structure of model incipient subduction zones such as those of Leng et al. (2012) are incorporated in this forward geochemical model, contributions from the subducting slab persist as model-dependent parameters. In lieu of adopting such assumptions in case of a fossil oceanic lithosphere such as Zambales, the depleted character of the mantle wedge source expressed by middle and heavy REEs remain as robust constraints of F (degree of melting) that can be modeled given an appropriate mantle source.

Here, fractional melting residues of a DMM source (Warren, 2016; Workman & Hart, 2005) are regarded as potential sources of boninite in a second-stage, sub-arc hydrous

melting episode. In the spinel-field fractional melting model of Warren (2016), Acoje Block harzburgites (Tamayo Jr., 2001) are residues of 8-12% melting while and IBM forearc harzburgites (Parkinson & Pearce, 1998) are residues of melting in excess of 16% (Fig. 18). Using hydrous melting partition coefficients of Green et al. (2000) and variable residual mineral modes generated from pMELTS (Kimura, 2017), the middle and heavy REE concentrations of primary boninite and proto-arc basalt magmas are matched by visual fitting to modeled modal batch melts with F (degree of melting) as the intensive variable. These parameters therefore model the composition of instantaneous melts of a heterogeneous mantle wedge source at similar degrees of second-stage melting. We find that 10% modal batch melting of a DMM residue previously depleted by 8% fractional melting, represented by Acoje harzburgite PH98-17, will yield MREE-HREEs comparable to Zambales primary LSB magma. A residual source produced by higher degrees of stage 1 fractional melting (12%) or higher degrees of second-stage batch melting cannot account for the Zambales LSB composition. Compared to Zambales, Ogawasawara high-silica boninites can be produced by modal batch melting of a more refractory source (14% fractional melting) at similar degrees of second-stage melting (10%). Batch melting of depleted fractional melting residues greater than 16% will produce melts that are too depleted in HREE to match Ogasawara HSB. Using a new set partition coefficients suitable to clinopyroxene–poor to –absent peridotites (Lee et al., 2007) will result in even more HREE-depleted melts. The composition of Coto PAB that predates Acoje LSB calls for a relatively fertile source that underwent 2% fractional melting. The modelled residual compositions of second stage modal melting are also significant. A more depleted Acoje harzburgite (PH98-16) can be modelled as residue of second-stage melting. In a similar way, batch melting residue of a source that previously underwent 14% fractional melting satisfies the refractory REE abundances of IBM forearc peridotites. This suggest a possible multi-stage melting relationship between heterogeneous mantle wedge sources and sequential source depletion of proto-arc basalt and boninite.

7.5 Subduction initiation origin of Zambales ophiolite

The 45 Ma crustal section of the Coto Block has a composition transitional to mid-ocean ridge basalt (MORB) and island arc tholeiite (IAT). On the basis of immobile element-based trace element discrimination diagrams, Coto Block dikes and lavas from Tarlac are robustly characterized as distinct from Mariana Trough back-arc basin basalts (Geary et al.,

1989). Decreasing REEs, TiO_2, Zr and Y in Coto volcanics, dikes in the Coto mantle section to Acoje volcanics document the progressive depletion of the mantle source in Zambales mantle wedge (Yumul, 1990). Succeeding zircon U–Pb geochronology established the 1–2 Myr age difference between Coto and Acoje blocks (Encarnación et al., 1993). Thus, combined geochemical and age constraints preclude a back-arc basin origin for Coto Block as forwarded by Hawkins and Evans (1983), and are more compatible with a proto-forearc setting as originally suggested by Geary et al. (1989).

Coto Block lavas and dikes from this study (n=19) have Ti/V ratios that overlap with IBM proto-arc basalt. (Fig. 19). Volcanic sections of Zambales ophiolite are also marked by decreasing Ti/V ratios from proto-arc basalt to boninite. Vanadium (V) partitioning experiments show that V is compatible (K_d is >1) with olivine, orthopyroxene and clinopyroxene at reducing conditions (0 to -12 log (fO_2) units above FMQ buffer). However, in oxidizing conditions (0 to +12 log (fO_2) units above FMQ buffer) V behaves incompatibly (K_d is <1) (Canil, 1999; Mallmann & O'Neill, 2009). The sub-arc mantle is generally considered to be more oxidized than MORB sources (Evans et al., 2012; Frost & McCammon, 2008). Since V is incompatible in oxidizing conditions, it will partition into the melt; leading to higher V concentrations in the melt and lower whole-rock Ti/V ratios. This is best exemplified by Expedition 352 and Zambales boninites, with Ti/V ratios less than 10. Proto-arc basalt and MORB have distinct Ti/V ratios, mostly between 16-20 and 24-33 respectively. These indicate an environment that is getting more oxidized and we interpret this as the reflection of the progressive source oxidation by slab-derived fluids. Another manifestation of the oxidized nature of the mantle wedge is the higher proportion of Fe^{2+}(oxidized iron) relative to Fe^{3+} in arc magmas. In the IBM forearc, this is expressed by the temporal increase of $Fe^{3+}/ (Fe^{2+} + Fe^{3+})$ ratios from proto-arc basalt to boninite (Brounce et al., 2015).

The corresponding Ti_8 and Si_8 values of the Coto Block are comparable with proto-arc basalts from the Bonin Ridge, Mariana Trench slope, Hole U1430 of IODP Exp. 351 and Hole 1440 of IODP Exp. 352 (Arculus et al., 2015; Ishizuka et al., 2011; Reagan et al., 2010, 2015) (Fig. 20). Si_8 and Ti_8 values of Coto Block basalts are also distinct from Celebes Sea Basin and West Philippine Basin MORB (Pearce et al., 2005; Savov et al., 2006; Serri et al., 1991; Spadea et al., 1996; Zakariadze, 1981). In addition, the primitive mantle-normalized fluid immobile trace element abundances of Coto Block dikes from this study are exceptionally low as well, and more depleted compared to MORB, depleted back-arc basin basalts (BABB) (Hickey-

Vargas et al., 2018) and Celebes Sea Basin basalts (Fig. 21). Coto Block lavas and dikes are probably from a source that is slightly oxidized and more depleted than typical MORB.

From observations in the field, oceanic accretion can be inferred from the Coto crustal section based on a well-developed sheeted dike complex, in contrast to the mutually intrusive dikes of the Acoje crustal section. With the recognition of boninite and boninite-series volcanics (Barlo), simultaneous and post-boninite moderate-Fe arc tholeiites (Barlo-Sual, Subic) in the crustal section of Acoje Block, it is apparent that the subduction initiation chemostratigraphy (Ishizuka et al., 2011; Whattam & Stern, 2011) is present in the Zambales ophiolite as well. Although stratigraphic relationships of individual volcanic sections may be obfuscated by emplacement-related tectonic deformation, by considering available age constraints, the crustal sections of the Zambales ophiolite represent proto-arc accretion and juvenile arc sections supplied by separate magma plumbing systems as observed in IODP Exp. 352 sites (Reagan et al., 2015).

7.6 Doubly-vergent subduction initiation along Philippine Sea Plate margins

Previous attempts to ascertain the provenance of Zambales ophiolite focused on its characterization as a marginal basin and thus linked it to the surrounding Eocene marginal basins such as the Celebes Sea Basin and Molucca Sea Basin. In the most comprehensive petrological and geochemical study of Philippine ophiolites, Tamayo et al. (2004) notes the strong subduction geochemical imprint of Zambales ophiolite and placed it as a marginal basin between Celebes Sea Basin and the western margin of the Philippine Sea Plate. The difficulty in reconstructing the Paleogene tectonic configuration of the southeast Asian region, specifically the spreading history of the oceanic domain east of Sundaland and west of the Philippine Sea Plate, stems from the fact that this region has been fully consumed along convergent margins east of southeastern Eurasia (Zahirovic et al., 2014). This gap was addressed by Wu et al. (2016) through the novel use of structural unfolding of subducted slabs imaged by seismic tomography. In their preferred model (model 1b), unfolding of subducted slabs beneath southern Eurasia reveals that the Philippine Sea Plate was bordered by Cretaceous oceanic crust (the East Asian Sea) in its western margin. Paleomagnetic data derived from sites in the Philippine Sea Plate shows northward translation concomitant with clockwise rotation (Hall et al., 1995; Richter & Ali, 2015; Yamazaki et al., 2010) (Fig. 22a). Eocene to Miocene sites from Luzon indicate similar

northward migration; thus, the island can be regarded as the western promontory of the Philippine Sea Plate (Queano et al., 2007). The subequatorial position of Luzon during the middle Eocene is further supported by paleomagnetic data from pillow lavas forming the basement of Luzon Central Cordillera (K-Ar age: 45.49±2.27 Ma) that yield a paleolatitude of 6.3±3 °S (Queaño et al., 2009; Sajona, 1995). East of Luzon and forming the greater part of Philippine Sea Plate, the West Philippine Basin (WPB) is characterized as a back-arc basin formed between opposing subduction zones (Deschamps & Lallemand, 2002). Pre-Eocene subduction south of WPB possibly generated the Mesozoic arc terranes in the Philippine Sea Plate including Amami Plateau and Daito ridge as well as the Cretaceous ophiolites in eastern Philippines (Lallemand, 2016). Initiation of a long-lived subduction east of WPB produced the Izu-Ogasawara (Bonin)-Mariana (IBM) forearc above a west-dipping subduction zone (Ishizuka et al., 2011). It is in this context that we re-evaluate the origin of Zambales ophiolite.

Tilt-corrected inclination data from sites in the 44 Ma Acoje Block equates to equatorial paleolatitudes (Fuller et al., 1991). Adopting southerly paleolatitudes in consonance with the modelled Luzon translation history of Wu et al. (2016), we make the case for the subduction initiation origin of the Zambales ophiolite in the leading edge of the northwestward-moving, clockwise-rotating Philippine Sea Plate. In this scenario, the origin of Philippine Sea Plate boninites (IBM and Zambales) would be in a doubly-vergent subduction initiation setting (Fig. 10b). In contrast with IBM, incipient subduction that produced Zambales ophiolite proto-arc basalts, boninites and arc tholeiites within 3 Ma is rather short-lived and alludes to rapid emplacement. The timing of the proposed subduction initiation in the western margin of Philippine Sea Plate is yet to be constrained. The late Oligocene to early Miocene onset of true basinal sedimentation in the Central Valley Basin provides a minimum docking age between Zambales ophiolite and eastern Luzon (Bachman et al., 1983). The GPlates-based reconstruction presented here, using unfolded slab data (Wu et al., 2016), is essentially similar to the Philippine Sea Plate evolutionary models of Deschamps and Lallemand (2003). Although it is beyond the scope of this study to identify the nature of a pre-existing structural boundary as a transform fault or strike-slip extension of a subduction zone, we note that both Zambales and IBM are orthogonal to the West Philippine Basin spreading center and the Cretaceous arc terranes in the overriding plate. Contrary to a subduction initiation origin, Lallemand (2016) posits

that proto-arc basalts (or forearc basalts) formed in short lived Eocene oceanic basins (e.g. Kita-Daito and Minami-Daito basins) bounded by the Cretaceous arc terranes. We believe that this might be the case for Eocene ophiolites in eastern Philippines (e.g. Angat ophiolite) but not for the Zambales ophiolite. The early Eocene age (48.1±0.5 Ma) of Angat ophiolite does not necessarily prove an affinity with Zambales as suggested by Encarnación et al. (1993), rather it simply demonstrates that basement complexes in the Philippine Mobile Belt consists of juxtaposed geochemically distinct Eocene and Cretaceous ophiolites (ophiolite belts 1B and 1C of Tamayo et al., 2004) (Fig. 1a). Slightly older Eocene ages (e.g. 50.83±3.35 Ma) were obtained by subsequent whole-rock K-Ar and SHRIMP zircon U-Pb dating of ophiolitic samples from eastern Luzon (Sajona, 1995; Tani et al., 2015). In addition, these Cretaceous and Eocene ophiolites are associated with Eocene volcano-sedimentary arc sequences (Caraballo, Maybangain, Anawan and Payo Formations) (Billedo et al., 1996; David et al., 1997). This differs sharply with the deep-marine, isolated environment deduced from the Eocene sedimentary carapace of the Zambales ophiolite (Schweller & Karig, 1982).

Although current terrestrial subduction is dominantly asymmetric, it is interesting to note that two-sided subduction is what is essentially produced in 2-D and 3-D models of mantle convection (Gerya et al., 2008; Wada & King, 2015). Likewise, we discern that doubly-vergent SI geometry or subduction initiation with oppositely-dipping subduction zones along its margins is characteristic of 3-D thermo-mechanical models of plume-induced subduction initiation (Baes et al., 2016; Gerya et al., 2015). Plume-induced subduction initiation was first recognized by Whattam and Stern (2015) to describe the temporal association of late Cretaceous plume-related oceanic plateaus in Central America that was followed by arc volcanism with oppositely dipping slab dispositions. In the case of the Eocene Western Pacific, a mantle plume centered on the Manus Basin had originally been invoked by Macpherson and Hall (2001) to account for an inferred thermal anomaly in IBM boninite mantle source, implicitly connecting the initiation of the IBM arc to the presence of a mantle plume. Isotopic studies are in agreement that a mantle plume is likely associated with the oceanic plateaus and bathymetric highs emplaced at the same time as the opening of the West Philippine Basin (Hickey-Vargas et al., 2006; Ishizuka et al., 2013); however, thermal anomalies in excess of the ambient mantle are not reflected in mantle potential temperature estimates of proto-arc basalt from the IBM forearc (Umino et al., 2018). A causative link between a mantle plume and the doubly-vergent SI configuration along

Philippine Sea Plate margins is yet to be established. We speculate that the location of Philippine Sea Plate (PSP) in the nexus of Pacific, Indo-Australian and Eurasian plates and their long-term Cenozoic plate motion makes doubly-vergent subduction initiation along its margins feasible. The northwestward translation and clockwise rotation of the Philippine Sea Plate starting in the early Eocene had to be accommodated by the adjoining oceanic domain east of southern Eurasia (e.g. East Asian Sea); hence, its interaction with the oceanic leading edge of the Philippine Sea Plate is expected (Wu et al., 2016; Zahirovic et al., 2016) and likely led to incipient subduction (Fig. 22). The dynamics of sustained double-vergent subduction is examined by Holt et al. (2017) but doubly-vergent subduction initiation is yet to be explored by numerical modelling. Field and petrologic data presented here demonstrate that models of subduction initiation based on the IBM forearc are currently simplistic. Geodynamic models of subduction initiation should be based on robust geologic data and a doubly-vergent SI configuration based on the Zambales ophiolite provides another boundary condition for refined models of SI along PSP margins. We advocate that geodynamic models of subduction initiation along Philippine Sea Plate margins incorporate a pre-Eocene, N/NE-dipping subduction zone (the proto West Philippine Trench of Faccenna et al., 2010) associated with Cretaceous terranes forming the overriding plate, doubly-vergent subduction initiation along its margins as well as the interplay of plate forces and mantle upwelling (e.g. Oki-Daito plume of Ishizuka et al. 2013) during incipient subduction (Fig. 22b).

8. Summary

The extrusive sequence in the juvenile arc section of the Zambales ophiolite in Luzon Island in the Philippines consists of boninite and boninite-series volcanics. This makes northern Zambales ophiolite the lone middle Eocene boninite locality in the Philippine Sea plate apart from the Ogasawara islands, Guam and their submarine equivalent in the IBM forearc.

Zambales boninite and boninite series volcanics are marked by low trace element abundances relative to mid-ocean ridge basalt with hydrous fluid mobile element enrichment and heavy rare earth element depletion, which is comparable with boninite from Troodos and Oman. Trace element ratios suggest that aqueous fluids released from shallow sub-arc depths are the dominant slab components in Zambales boninite. Based on

lower spinel Cr#s and higher HREE abundances of the most primitive sample, Zambales boninite is derived from a mantle source that is less depleted than Ogasawara boninite. A primary LSB composition derived using the olivine addition method yield olivine orthopyroxene saturation temperature of 1243° C at 0.34 GPa. This is very shallow depth is regarded as a record of last equilibration in the uppermost mantle.

Basaltic andesite and gabbroic dikes of the Coto Block have primitive mantle normalized abundances that more depleted than MORB and depleted back-arc basin basalts (BABB) with Ti/V ratios (17-21) similar to proto-arc basalts (or forearc basalt) from IODP Expeditions 352 and 351. Volcanic sections of the Zambales ophiolite likewise show decreasing Ti/V ratios from Coto Block dikes to Acoje Block boninite; indicating increasingly oxidized sub-arc environment that is interpreted to be the result of progressive source oxidation by slab-derived fluids. Subduction initiation stratigraphy deduced from diving, dredging and drilling programs in the Izu–Ogasawara (Bonin)–Mariana forearc is recognized in the Zambales ophiolite as well.

The temporal variation from proto-arc basalt to boninite and post-boninite arc tholeiite is represented by the Coto (45 Ma), Barlo (44 Ma) and Sual– Subic (44–43 Ma) volcanic sections of Zambales ophiolite. Incipient subduction associated with the juvenile arc in the northern Zambales ophiolite likely involved the unfolded East Asian Sea crust as the subducting slab and the westernmost margin of Philippine Sea plate as the overriding plate. By studying the Zambales ophiolite, it can be shown that subduction initiation is a plate-scale process.

To address Eocene western Pacific subduction initiation, it is essential to consider not just the Izu–Ogasawara–Mariana forearc but also geologic constraints from the entire Philippine Sea plate. Doubly vergent subduction initiation deduced from the rock record is a testable mechanism that can be explored by geodynamic modeling. Placed its proper geodynamic context, Zambales ophiolite can address scientific objectives of several IODP drilling proposal in the IBM region. The origin of the felsic middle crust can be addressed by vertical and horizontal traverses of the upper and lower crustal sections of the Acoje Block. While the ForeArc Mohole to Mantle proposal can be addressed by the Coto and Acoje mantle sections.

9. Acknowledgements.

This work was funded by a Ministry of Education, Culture, Sports, Science and Technology (MEXT) PhD scholarship. The field expedition to the Zambales ophiolite was supported by a 2016 Fukada Geological Institute Grant-in-Aid to Americus Perez. This work was also supported by JSPS KAKENHI grant no. 25400446 and donated funds from JAPEX to Susumu Umino, in addition to grant no. 25287133 to Osamu Ishizuka. We thank Ferdinand Jumawan, Alexer Mapa, Betchaida Payot, Juan Miguel Guotana and Efren Gadot for their assistance during the March 2015 reconnaissance and May 2016 field campaigns. We are grateful to Kiyo Yamanobe (GSJ) and Akihiro Tamura, Yusuke Soda, Makoto Miura and Nguyen Khac Du (Kanazawa) for their help during geochemical analyses.

I would like to thank Professor Susumu Umino for his guidance and patience. I am grateful to Dr. Osamu Ishizuka for the analytical support and cruise opportunities. Initial discussions of the PhD proposal with Dr. Kenichiro Tani is acknowledged. FT-IR analyses in ERI-University of Tokyo were performed in collaboration with Dr. Atsushi Yasuda. I would also like to thank Dr. Graciano P. Yumul Jr., Dr. Carla B. Dimalanta and Dr. Decibel Faustino-Eslava for their support and encouragement. I thank my emergency funding agency, my family, for tolerating a jobless 30-year-old. To Dr. Rodolfo A. Tamayo, Jr.† and Dr. Betchaida D. Payot, this one's for the team.

10. References

Abrajano, T. A., Pasteris, J. D., & Bacuta, G. C. (1989). Zambales ophiolite, Philippines I. Geology and petrology of the critical zone of the Acoje massif. *Tectonophysics*, *168*(1), 65–100. https://doi.org/10.1016/0040-1951(89)90369-7

Arculus, R. J., Ishizuka, O., Bogus, K. A., Gurnis, M., Hickey-Vargas, R., Aljahdali, M. H., Bandini-Maeder, A.N., Barth, A.P., Brandl, P.A., Drab, L., do Monte Guerra, R., Hamada, M., Jiang, F., Kanayama, K., Kender, S., Kusano, Y., Li, H., Loudin, L.C., Maffione, M., Marsaglia, K.M., McCarthy, A., Meffre, S., Morris, A., Neuhaus, M., Savov, I.P., Sena, C., Tepley III, F.J., van der Land, C., Yogodzinski, G.M., Zhang, Z. (2015). A record of spontaneous subduction initiation in the Izu-Bonin-Mariana arc. *Nature Geoscience*, *8*(9), 728–733. https://doi.org/10.1038/ngeo2515

Arculus, R. J., Pearce, J. A., Murton, B., & van der Laan, S. (1992). Igneous stratigraphy and major element geochemistry of Holes 786A and 786B. In P. Fryer, J. A. Pearce, L. B. Stokking, J. R. Ali, R. J. Arculus, R. Balloti, … B. J. Murton (Eds.), *Proc. ODP Sci. Results* (pp. 143–169). College Station, TX (Ocean Drilling Program): Ocean Drilling Program. https://doi.org/doi:10.2973/odp.proc.sr.125.137.1992

Bachman, S. B., Lewis, S. D., & Schweller, W. J. (1983). Evolution of a Forearc Basin, Luzon Central Valley, Philippines. *AAPG Bulletin*, *67*(7), 1143–1162.

Bacuta, G. (1989). *The Zambales Ophiolite Complex, Philippines: Chromite and platinum-group element mineralization*. Ph.D. Thesis, Cornell University.

Bacuta, G. C., Kay, R. W., Gibbs, A. K., & Lipin, B. R. (1990). Platinum-group element abundance and distribution in chromite deposits of the Acoje Block, Zambales Ophiolite Complex, Philippines. *Journal of Geochemical Exploration*, *37*(1), 113–145. https://doi.org/10.1016/0375-6742(90)90086-P

Baes, M., Gerya, T., & Sobolev, S. V. (2016). 3-D thermo-mechanical modeling of plume-induced subduction

initiation. *Earth and Planetary Science Letters*, *453*, 193–203. https://doi.org/10.1016/J.EPSL.2016.08.023
Barrat, J. A., Zanda, B., Moynier, F., Bollinger, C., Liorzou, C., & Bayon, G. (2012). Geochemistry of CI chondrites: Major and trace elements, and Cu and Zn Isotopes. *Geochimica et Cosmochimica Acta*, *83*, 79–92. https://doi.org/10.1016/j.gca.2011.12.011
Bedard, J. H. (1999). Petrogenesis of Boninites from the Betts Cove Ophiolite, Newfoundland, Canada: Identification of Subducted Source Components. *Journal of Petrology*, *40*(12), 1853–1889. https://doi.org/10.1093/petroj/40.12.1853
Billedo, E., Stephan, J. F., Delteil, J., Bellon, H., Sajona, F. G., & Feraud, G. (1996). The pre-Tertiary ophiolitic complex of Northeastern Luzon and the Polilio Group of Islands, Philippines. *Journal of the Geological Society of the Philippines*, *51*(3&4), 95–114.
Blenkinsop, T. G. (2012). Visualizing structural geology: From Excel to Google Earth. *Computers & Geosciences*, *45*, 52–56. https://doi.org/10.1016/j.cageo.2012.03.007
Bloomer, S. H., & Hawkins, J. W. (1987). Petrology and geochemistry of boninite series volcanic rocks from the Mariana trench. *Contributions to Mineralogy and Petrology*, *97*(3), 361–377. https://doi.org/10.1007/BF00371999
Boyden, J. A., Müller, R. D., Gurnis, M., Torsvik, T. H., Clark, J. A., Turner, M., Ivey-Law, H., Watson, R.J., Cannon, J. S. (2011). Next-generation plate-tectonic reconstructions using GPlates. In C. Baru & G. R. Keller (Eds.), *Geoinformatics: Cyberinfrastructure for the Solid Earth Sciences* (pp. 95–114). Cambridge: Cambridge University Press. https://doi.org/DOI: 10.1017/CBO9780511976308.008
Brounce, M., Kelley, K. A., Cottrell, E., & Reagan, M. K. (2015). Temporal evolution of mantle wedge oxygen fugacity during subduction initiation. *Geology*, *43*(9), 775–778. https://doi.org/10.1130/G36742.1
Buriánek, D., Schulmann, K., Hrdličková, K., Hanžl, P., Janoušek, V., Gerdes, A., & Lexa, O. (2017). Geochemical and geochronological constraints on distinct Early-Neoproterozoic and Cambrian accretionary events along southern margin of the Baydrag Continent in western Mongolia. *Gondwana Research*, *47*, 200–227. https://doi.org/10.1016/J.GR.2016.09.008
Cameron, W. E. (1985). Petrology and origin of primitive lavas from the Troodos ophiolite, Cyprus. *Contributions to Mineralogy and Petrology*, *89*(2–3), 239–255. https://doi.org/10.1007/BF00379457
Cameron, W. E. (1989). Contrasting boninite–tholeite associations from New Caledonia. In A. J. Crawford (Ed.), *Boninites and Related Rocks* (pp. 314–338). London: Unwin-Hyman.
Canil, D. (1999). Vanadium partitioning between orthopyroxene, spinel and silicate melt and the redox states of mantle source regions for primary magmas. *Geochimica et Cosmochimica Acta*, *63*(3–4), 557–572. https://doi.org/10.1016/S0016-7037(98)00287-7
Carter, L. B., Skora, S., Blundy, J. D., De Hoog, J. C. M., & Elliott, T. (2015). An Experimental Study of Trace Element Fluxes from Subducted Oceanic Crust. *Journal of Petrology*, *56*(8), 1585–1606. https://doi.org/10.1093/petrology/egv046
Cattermole, P. (1989). *Planetary Volcanism A Study of Volcanic Activity in the Solar System*. West Sussex, England: Ellis Horwood Limited.
Cluzel, D., Ulrich, M., Jourdan, F., Meffre, S., Paquette, J.-L., Audet, M.-A., Secchiari, A., Maurizot, P. (2016). Early Eocene clinoenstatite boninite and boninite-series dikes of the ophiolite of New Caledonia; a witness of slab-derived enrichment of the mantle wedge in a nascent volcanic arc. *Lithos*, *260*, 429–442. https://doi.org/10.1016/j.lithos.2016.04.031
Coish, R. . (1989). Boninitic lavas in Appalachian ophiolites: a review. In A. J. Crawford (Ed.), *Boninites and Related Rocks* (pp. 264–287). Unwin-Hyman.
Cooper, L. B., Plank, T., Arculus, R. J., Hauri, E. H., Hall, P. S., & Parman, S. W. (2010). High-Ca boninites from the active Tonga Arc. *Journal of Geophysical Research: Solid Earth*, *115*(10), B10206. https://doi.org/10.1029/2009JB006367
Crameri, F., & Tackley, P. J. (2016). Subduction initiation from a stagnant lid and global overturn: new insights from numerical models with a free surface. *Progress in Earth and Planetary Science*, *3*(1), 1–19. https://doi.org/10.1186/s40645-016-0103-8
Crawford, A. J., Falloon, T. J., & Green, D. H. (1989). Classification, petrogenesis and tectonic setting of boninites. In A. J. Crawford (Ed.), *Boninites and Related Rocks* (pp. 1–49). London: Unwin-Hyman.
Davaille, A., Smrekar, S. E., & Tomlinson, S. (2017). Experimental and observational evidence for plume-induced subduction on Venus. *Nature Geoscience*, *10*(5), 349–355. https://doi.org/10.1038/ngeo2928
David, S., Stephan, J.-F., Delteil, J., Müller, C., Butterlin, J., Bellon, H., & Billedo, E. (1997). Geology and tectonic history of Southeastern Luzon, Philippines. *Journal of Asian Earth Sciences*, *15*(4–5), 435–452. https://doi.org/10.1016/S0743-9547(97)00027-5
Deschamps, A., & Lallemand, S. (2002). The West Philippine Basin: An Eocene to early Oligocene back arc

basin opened between two opposed subduction zones. *Journal of Geophysical Research: Solid Earth*, *107*(B12), EPM 1-1-EPM 1-24. https://doi.org/10.1029/2001JB001706

Deschamps, A., & Lallemand, S. (2003). Geodynamic setting of Izu-Bonin-Mariana boninites. *Geological Society, London, Special Publications*, *219*(1), 163–185. https://doi.org/10.1144/GSL.SP.2003.219.01.08

Dietrich, V., Emmermann, R., Oberhänsli, R., & Puchelt, H. (1978). Geochemistry of basaltic and gabbroic rocks from the West Mariana basin and the Mariana trench. *Earth and Planetary Science Letters*, *39*(1), 127–144. https://doi.org/10.1016/0012-821X(78)90149-8

Dilek, Y., & Furnes, H. (2011). Ophiolite genesis and global tectonics: Geochemical and tectonic fingerprinting of ancient oceanic lithosphere. *Bulletin of the Geological Society of America*, *123*(3–4), 387–411. https://doi.org/10.1130/B30446.1

Dobson, P. F., Blank, J. G., Maruyama, S., & Liou, J. G. (2006). Petrology and geochemistry of boninite-series volcanic rocks, Chichi-Jima, Bonin Islands, Japan. *International Geology Review*, *48*(8), 669–701. https://doi.org/10.2747/0020-6814.48.8.669

Dulski, P. (2001). Reference materials for geochemical studies: New analytical data by ICP-MS and critical discussion of reference values. *Geostandards Newsletter*, *25*(1), 87–125. https://doi.org/10.1111/j.1751-908X.2001.tb00790.x

Elliott, T. (2003). Tracers of the slab. In J. Eiler (Ed.), *Inside the Subduction Factory* (Vol. 138, pp. 23–45). Washington, D. C.: American Geophysical Union. https://doi.org/10.1029/138gm03

Encarnación, J., Mukasa, S. B., & Evans, C. A. (1999). Subduction components and the generation of arc-like melts in the Zambales ophiolite, Philippines: Pb, Sr and Nd isotopic constraints. *Chemical Geology*, *156*(1–4), 343–357. https://doi.org/10.1016/S0009-2541(98)00190-9

Encarnación, J. P., Mukasa, S. B., & Obille, E. C. (1993). Zircon U-Pb geochronology of the Zambales and Angat Ophiolites, Luzon, Philippines: Evidence for an Eocene arc-back arc pair. *Journal of Geophysical Research: Solid Earth*, *98*(B11), 19991–20004. https://doi.org/10.1029/93JB02167

Evans, C. A. (1983). *Petrology and geochemistry of the transition from mantle to crust beneath an island arc-backarc pair: Implications from the Zambales Range Ophiolite, Luzon, Philippines*. Ph.D. Thesis, University of California San Diego.

Evans, C. A., Casteneda, G., & Franco, H. (1991). Geochemical complexities preserved in the volcanic rocks of the Zambales Ophiolite, Philippines. *Journal of Geophysical Research: Solid Earth*, *96*(B10), 16251–16262. https://doi.org/10.1029/91JB01488

Evans, C., & Hawkins, J. W. (1989). Compositional heterogeneities in upper mantle peridotites from the Zambales Range Ophiolite, Luzon, Philippines. *Tectonophysics*, *168*(1), 23–41. https://doi.org/10.1016/0040-1951(89)90367-3

Evans, K. A., Elburg, M. A., & Kamenetsky, V. S. (2012). Oxidation state of subarc mantle. *Geology*, *40*(9), 783–786. https://doi.org/10.1130/G33037.1

Faccenna, C., Becker, T. W., Lallemand, S., Lagabrielle, Y., Funiciello, F., & Piromallo, C. (2010). Subduction-triggered magmatic pulses: A new class of plumes? *Earth and Planetary Science Letters*, *299*(1–2), 54–68. https://doi.org/10.1016/J.EPSL.2010.08.012

Falloon, T. J., & Crawford, A. J. (1991). The petrogenesis of high-calcium boninite lavas dredged from the northern Tonga ridge. *Earth and Planetary Science Letters*, *102*(3–4), 375–394. https://doi.org/10.1016/0012-821X(91)90030-L

Falloon, T. J., Danyushevsky, L. V., Crawford, T. J., Maas, R., Woodhead, J. D., Eggins, S. M., Bloomer, S.H., Wright, D.J., Zlobin, S.K., Stacey, A. R. (2007). Multiple mantle plume components involved in the petrogenesis of subduction-related lavas from the northern termination of the Tonga Arc and northern Lau Basin: Evidence from the geochemistry of arc and backarc submarine volcanics. *Geochemistry, Geophysics, Geosystems*, *8*(9), 45. https://doi.org/10.1029/2007GC001619

Falloon, T. J., & Danyushevsky, L. V. (2000). Melting of refractory mantle at 1.5, 2 and 2.5 GPa under anhydrous and H2O-undersaturated conditions: Implications for the petrogenesis of high-Ca boninites and the influence of subduction components on mantle melting. *Journal of Petrology*, *41*(2), 257–283. https://doi.org/10.1093/petrology/41.2.257

Florendo, F. F., & Hawkins, J. W. (1992). Comparison of the geochemistry of volcanic rocks of the Zambales Ophiolite, northern Luzon, Philippines: Implications for tectonic setting. *Acta Geologica Taiwanica: Science Reports of the National Taiwan University*, *30*, 172–176.

Foley, S., Tiepolo, M., & Vannucci, R. (2002). Growth of early continental crust controlled by melting of amphibolite in subduction zones. *Nature*, *417*(6891), 837–840. https://doi.org/10.1038/nature00799

Frost, D. J., & McCammon, C. A. (2008). The Redox State of Earth's Mantle. *Annual Review of Earth and Planetary Sciences*, *36*(1), 389–420. https://doi.org/10.1146/annurev.earth.36.031207.124322

Fuller, M., Haston, R., & Almasco, J. (1989). Paleomagnetism of the Zambales ophiolite, Luzon, northern

Philippines. *Tectonophysics*, *168*(1), 171–203. https://doi.org/10.1016/0040-1951(89)90375-2
Fuller, M., Haston, R., Lin, J. L., Richter, B., Schmidtke, E., & Almasco, J. (1991). Tertiary paleomagnetism of regions around the South China Sea. *Journal of Southeast Asian Earth Sciences*, *6*(3–4), 161–184. https://doi.org/10.1016/0743-9547(91)90065-6
Gale, A., Dalton, C. A., Langmuir, C. H., Su, Y., & Schilling, J. G. (2013). The mean composition of ocean ridge basalts. *Geochemistry, Geophysics, Geosystems*, *14*(3), 489–518. https://doi.org/10.1029/2012GC004334
Geary, E. E., & Kay, R. W. (2013). (1983). Petrological and Geochemical Documentation of Ocean Floor Metamorphism in the Zambales Ophiolite, Philippines. In D. E. Hayes (Ed.), *The Tectonic and Geologic Evolution of Southeast Asian Seas and Islands: Part 2* (pp. 139–156). Washington, D. C.: American Geophysical Union (AGU). https://doi.org/doi:10.1029/GM027p0139
Geary, E. E., Kay, R. W., Reynolds, J. C., & Kay, S. M. (1989). Geochemistry of mafic rocks from the Coto Block, Zambales ophiolite, Philippines: trace element evidence for two stages of crustal growth. *Tectonophysics*, *168*(1), 43–63. https://doi.org/10.1016/0040-1951(89)90368-5
Gerya, T. V., Connolly, J. A. D., & Yuen, D. A. (2008). Why is terrestrial subduction one-sided? *Geology*, *36*(1), 43–46. https://doi.org/10.1130/G24060A.1
Gerya, T. V., Stern, R. J., Baes, M., Sobolev, S. V., & Whattam, S. A. (2015). Plate tectonics on the Earth triggered by plume-induced subduction initiation. *Nature*, *527*(7577), 221–225. https://doi.org/10.1038/nature15752
Ghiorso, M. S., & Gualda, G. A. R. (2015). An H2O-CO2 mixed fluid saturation model compatible with rhyolite-MELTS. *Contributions to Mineralogy and Petrology*, *169*(53), 1–30. https://doi.org/10.1007/s00410-015-1141-8
Ghiorso, M. S., Hirschmann, M. M., Reiners, P. W., & Kress, V. C. (2002). The pMELTS: A revision of MELTS for improved calculation of phase relations and major element partitioning related to partial melting of the mantle to 3 GPa. *Geochemistry, Geophysics, Geosystems*, *3*(5), 1–35. https://doi.org/10.1029/2001GC000217
Gianola, O., Schmidt, M. W., Jagoutz, O., & Sambuu, O. (2017). Incipient boninitic arc crust built on denudated mantle: the Khantaishir ophiolite (western Mongolia). *Contributions to Mineralogy and Petrology*, *172*(11–12), 92. https://doi.org/10.1007/s00410-017-1415-4
Green, T., Blundy, J., Adam, J., & Yaxley, G. (2000). SIMS determination of trace element partition coefficients between garnet, clinopyroxene and hydrous basaltic liquids at 2–7.5 GPa and 1080–1200°C. *Lithos*, *53*(3–4), 165–187. https://doi.org/10.1016/S0024-4937(00)00023-2
Grove, T. L., Till, C. B., & Krawczynski, M. J. (2012). The Role of H2O in Subduction Zone Magmatism. *Annual Review of Earth and Planetary Sciences*, *40*(1), 413–439. https://doi.org/10.1146/annurev-earth-042711-105310
Gurnis, M., Hall, C., & Lavier, L. (2004). Evolving force balance during incipient subduction. *Geochemistry, Geophysics, Geosystems*, *5*(7). https://doi.org/10.1029/2003GC000681
Hall, C. E., Gurnis, M., Sdrolias, M., Lavier, L. L., & Müller, R. D. (2003). Catastrophic initiation of subduction following forced convergence across fracture zones. *Earth and Planetary Science Letters*, *212*(1–2), 15–30. https://doi.org/10.1016/S0012-821X(03)00242-5
Hall, R., Ali, J. R., Anderson, C. D., & Baker, S. J. (1995). Origin and motion history of the Philippine Sea Plate. *Tectonophysics*, *251*(1–4), 229–250. https://doi.org/10.1016/0040-1951(95)00038-0
Hall, R., Fuller, M., Ali, J. R., & Anderson, C. D. (1995). The Philippine Sea Plate: Magnetism and reconstructions (pp. 371–404). American Geophysical Union. https://doi.org/10.1029/GM088p0371
Hanghoj, K., Kelemen, P. B., Hassler, D., & Godard, M. (2010). Composition and Genesis of Depleted Mantle Peridotites from the Wadi Tayin Massif, Oman Ophiolite; Major and Trace Element Geochemistry, and Os Isotope and PGE Systematics. *Journal of Petrology*, *51*(1–2), 201–227. https://doi.org/10.1093/petrology/egp077
Haugen, E. (2017). *Magmatic Evolution of Early Subduction Zones: Geochemical Modeling and Chemical Stratigraphy of Boninite and Fore Arc Basalt from the Bonin Fore Arc"*. M.Sc. Thesis, Utah State University. Retrieved from http://digitalcommons.usu.edu/etd/5934
Hawkins, J. W. (2003). *Geology of supra-subduction zones-Implications for the origin of ophiolites*. *Geological Society of America Special Papers* (Vol. 373). Geological Society of America. https://doi.org/10.1130/0-8137-2373-6.227
Hawkins, J. W., & Evans, C. A. (1983). Geology of the Zambales Range, Luzon, Philippine Islands: Ophiolite Derived from an Island Arc-Back Arc Basin Pair. In D. E. Hayes (Ed.), *The Tectonic and Geologic Evolution of Southeast Asian Seas and Islands: Part 2, Geophyical Monograph Series Vol. 27* (pp. 95–123). Washington, D.C.: American Geophysical Union.

https://doi.org/https://doi.org/10.1029/GM027p0095
Head, J. W., & Wilson, L. (2003). Deep submarine pyroclastic eruptions: theory and predicted landforms and deposits. *Journal of Volcanology and Geothermal Research*, *121*(3–4), 155–193. https://doi.org/10.1016/S0377-0273(02)00425-0
Herzberg, C., & Asimow, P. D. (2015). PRIMELT3 MEGA.XLSM software for primary magma calculation: Peridotite primary magma MgO contents from the liquidus to the solidus. *Geochemistry, Geophysics, Geosystems*, *16*(2), 563–578. https://doi.org/10.1002/2014GC005631
Hickey-Vargas, R., Yogodzinski, G. M., Ishizuka, O., McCarthy, A., Bizimis, M., Kusano, Y., Savov, I.P., Arculus, R. (2018). Origin of depleted basalts during subduction initiation and early development of the Izu-Bonin-Mariana island arc: Evidence from IODP expedition 351 site U1438, Amami-Sankaku basin. *Geochimica et Cosmochimica Acta*, *229*, 85–111. https://doi.org/10.1016/J.GCA.2018.03.007
Hickey-Vargas, R., Savov, I. P., Bizimis, M., Ishii, T., & Fujioka, K. (2006). Origin of Diverse Geochemical Signatures in Igneous Rocks from the West Philippine Basin: Implications for Tectonic Models (pp. 287–303). Washington, D. C.: American Geophysical Union. https://doi.org/10.1002/9781118666180.ch14
Holt, A. F., Royden, L. H., & Becker, T. W. (2017). The dynamics of double slab subduction. *Geophysical Journal International*, *209*(1), 250–265. https://doi.org/10.1093/gji/ggw496
Ishii, T. (1992). Petrological studies of peridotites from diapiric serpentinite seamounts in the Izu-Ogasawara-Mariana forearc, Leg 125. *Proceedings of the Ocean Drilling Program, Scientific Results*, *125*, 445.
Ishikawa, T., Fujisawa, S., Nagaishi, K., & Masuda, T. (2005). Trace element characteristics of the fluid liberated from amphibolite-facies slab: Inference from the metamorphic sole beneath the Oman ophiolite and implication for boninite genesis. *Earth and Planetary Science Letters*, *240*(2), 355–377. https://doi.org/10.1016/j.epsl.2005.09.049
Ishikawa, T., Nagaishi, K., & Umino, S. (2002). Boninitic volcanism in the Oman ophiolite: Implications for thermal condition during transition from spreading ridge to arc. *Geology*, *30*(10), 899–902. https://doi.org/10.1130/0091-7613(2002)030<0899:BVITOO>2.0.CO;2
Ishizuka, O., Hickey-Vargas, R., Arculus, R. J., Yogodzinski, G. M., Savov, I. P., Kusano, Y., McCarthy, A., Brandl, A.P., Sudo, M. (2018). Age of Izu – Bonin – Mariana arc basement. *Earth and Planetary Science Letters*, *481*, 80–90. https://doi.org/10.1016/j.epsl.2017.10.023
Ishizuka, O., Tani, K., & Reagan, M. K. (2014). Izu-Bonin-Mariana Forearc Crust as a Modern Ophiolite Analogue. *Elements*, *10*(2), 115–120. https://doi.org/10.2113/gselements.10.2.115
Ishizuka, O., Tani, K., Reagan, M. K., Kanayama, K., Umino, S., Harigane, Y., Sakamoto, I., Miyajima, Y., Yuasa, M., Dunkley, D. J. (2011). The timescales of subduction initiation and subsequent evolution of an oceanic island arc. *Earth and Planetary Science Letters*, *306*(3–4), 229–240. https://doi.org/10.1016/j.epsl.2011.04.006
Ishizuka, O., Taylor, R. N., Ohara, Y., & Yuasa, M. (2013). Upwelling, rifting, and age-progressive magmatism from the Oki-Daito mantle plume. *Geology*, *41*(9), 1011–1014. https://doi.org/10.1130/G34525.1
Ishizuka, O., Umino, S., Taylor, R. N., & Kanayama, K. (2014). Evidence for hydrothermal activity in the earliest stages of intraoceanic arc formation: Implications for ophiolite-hosted hydrothermal activity. *Economic Geology*, *109*(8), 2159–2177. https://doi.org/10.2113/econgeo.109.8.2159
Jenner, F. E., & O'Neill, H. S. C. (2012). Analysis of 60 elements in 616 ocean floor basaltic glasses. *Geochemistry, Geophysics, Geosystems*, *13*(1), Q02005. https://doi.org/10.1029/2011GC004009
Jenner, G. A. (1981). Geochemistry of high-Mg andesites from Cape Vogel, Papua New Guinea. *Chemical Geology*, *33*(1–4), 307–332. https://doi.org/10.1016/0009-2541(81)90106-6
Jochum, K. P., Weis, U., Schwager, B., Stoll, B., Wilson, S. A., Haug, G. H., Andreae, M.O., Enzweiler, J. (2016). Reference Values Following ISO Guidelines for Frequently Requested Rock Reference Materials. *Geostandards and Geoanalytical Research*, *40*(3), 333–350. https://doi.org/10.1111/j.1751-908X.2015.00392.x
Kanayama, K., Kitamura, K., & Umino, S. (2013). New geochemical classification of global boninites. In *IAVCEI 2013 Scientific Assembly* (p. 99). Kagoshima, Japan.
Kanayama, K., Umino, S., & Ishizuka, O. (2012). Eocene volcanism during the incipient stage of Izu–Ogasawara Arc: Geology and petrology of the Mukojima Island Group, the Ogasawara Islands. *Island Arc*, *21*(4), 288–316. https://doi.org/10.1111/iar.12000
Kanke, N., & Takazawa, E. (2014). A kilometre-scale highly refractory harzburgite zone in the mantle section of the northern Oman Ophiolite (Fizh Block): implications for flux melting of oceanic lithospheric mantle. *Geological Society, London, Special Publications*, *392*(1), 229 LP-246. Retrieved from http://sp.lyellcollection.org/content/392/1/229.abstract
Karig, D. E. (1983). Accreted terranes in the northern part of the Philippine archipelago. *Tectonics*, *2*(2), 211–236. https://doi.org/10.1029/TC002i002p00211

Karig, D. E., Lagoe, M. B., Snow, J. K., Schweller, W. J., & Bacuta, G. C. (1986). Stratigraphy along the Cabaluan River and geologic relations on the west flank of the Zambales Range, Luzon, Philippines. *The Philippine Geologist*, *30*(3), 1–20.

Keenan, T. E., & Encarnación, J. (2016). Unclear causes for subduction. *Nature Geoscience*, *9*(5), 338–338. https://doi.org/10.1038/ngeo2703

Kelemen, P. B., Yogodzinski, G. M., & Scholl, D. W. (2004). Along-strike variation in the aleutian island arc: Genesis of high Mg# andesite and implications for continental crust. In *Geophysical Monograph Series* (Vol. 138, pp. 223–276). American Geophysical Union (AGU). https://doi.org/10.1029/138GM11

Keppler, H. (2017). Fluids and trace element transport in subduction zones. *American Mineralogist*. https://doi.org/10.2138/am-2017-5716

Kimura, J.-I. (2017). Modeling chemical geodynamics of subduction zones using the Arc Basalt Simulator version 5. *Geosphere*, *13*(4), GES01468.1. https://doi.org/10.1130/GES01468.1

König, S., Münker, C., Schuth, S., & Garbe-Schönberg, D. (2008). Mobility of tungsten in subduction zones. *Earth and Planetary Science Letters*, *274*(1–2), 82–92. https://doi.org/10.1016/j.epsl.2008.07.002

König, S., Münker, C., Schuth, S., Luguet, A., Hoffmann, J. E., & Kuduon, J. (2010). Boninites as windows into trace element mobility in subduction zones. *Geochimica et Cosmochimica Acta*, *74*(2), 684–704. https://doi.org/10.1016/j.gca.2009.10.011

Kostopoulos, D. K., & Murton, B. J. (1992). Origin and distribution of components in boninite genesis: significance of the OIB component. *Geological Society, London, Special Publications*, *60*(1), 133–154. https://doi.org/10.1144/GSL.SP.1992.060.01.08

Kress, V. C., & Carmichael, I. S. E. (1991). The compressibility of silicate liquids containing Fe2O3 and the effect of composition, temperature, oxygen fugacity and pressure on their redox states. *Contributions to Mineralogy and Petrology*, *108*(1–2), 82–92. https://doi.org/10.1007/BF00307328

Kuroda, N., Shiraki, K., & Urano, H. (1978). Boninite as a possible calc-alkalic primary magma. *Bulletin Volcanologique*, *41*(4), 563–575. https://doi.org/10.1007/BF02597387

Kusano, Y., Hayashi, M., Adachi, Y., Umino, S., & Miyashita, S. (2014). Evolution of volcanism and magmatism during initial arc stage: constraints on the tectonic setting of the Oman Ophiolite. *Geological Society, London, Special Publications*, *392*(1), 177–193. https://doi.org/10.1144/SP392.9

Kusano, Y., Umino, S., Kobayashi, J., Mizukami, T., Okuno, M., & Arai, S. (2014). Quantitative analysis of major elements in igneous rocks with X-ray fluorescence spectrometer "ZSX primus II" using a 1:10 dilution glass bead. *The Science Reports of the Kanazawa University*, *58*, 31–44.

Kusano, Y., Umino, S., Shinjo, R., Ikei, A., Adachi, Y., Miyashita, S., & Arai, S. (2017). Contribution of slab-derived fluid and sedimentary melt in the incipient arc magmas with development of the paleo-arc in the Oman Ophiolite. *Chemical Geology*, *449*, 206–225. https://doi.org/10.1016/j.chemgeo.2016.12.012

Lallemand, S. (2016). Philippine Sea Plate inception, evolution, and consumption with special emphasis on the early stages of Izu-Bonin-Mariana subduction. *Progress in Earth and Planetary Science*, *3*(1), 1–26. https://doi.org/10.1186/s40645-016-0085-6

Laurent, R., & Hébert, R. (1989). The volcanic and intrusive rocks of the Québec Appalachian ophiolites (Canada) and their island-arc setting. *Chemical Geology*, *77*(3–4), 287–302. https://doi.org/10.1016/0009-2541(89)90079-X

Le Maitre, R. W. (2002). *Igneous rocks : a classification and glossary of terms : recommendations of the International Union of Geological Sciences, Subcommission on the Systematics of Igneous Rocks*. (R. W. Le Maitre, Ed.) (2nd ed.). Cambridge, New York, Melbourne: Cambridge University Press. https://doi.org/https://doi.org/10.1017/CBO9780511535581

Lee, C.-T. A., Harbert, A., & Leeman, W. P. (2007). Extension of lattice strain theory to mineral/mineral rare-earth element partitioning: An approach for assessing disequilibrium and developing internally consistent partition coefficients between olivine, orthopyroxene, clinopyroxene and basaltic melt. *Geochimica et Cosmochimica Acta*, *71*(2), 481–496. https://doi.org/10.1016/J.GCA.2006.09.014

Leng, W., & Gurnis, M. (2015). Subduction initiation at relic arcs. *Geophysical Research Letters*, *42*(17), 7014–7021. https://doi.org/10.1002/2015GL064985

Leng, W., Gurnis, M., & Asimow, P. (2012). From basalts to boninites: The geodynamics of volcanic expression during induced subduction initiation. *Lithosphere*, *4*(6), 511–523. https://doi.org/10.1130/L215.1

Li, Y.-B., Kimura, J.-I., Machida, S., Ishii, T., Ishiwatari, A., Maruyama, S., Qiu, H.-N., Ishikawa, T., Kato, Y., Haraguchi, S., Takahata, N., Hirahara, Y., Miyazaki, T. (2013). High-Mg Adakite and Low-Ca Boninite from a Bonin Fore-arc Seamount: Implications for the Reaction between Slab Melts and Depleted Mantle. *Journal of Petrology*, *54*(6), 1149–1175. https://doi.org/10.1093/petrology/egt008

Macpherson, C. G., & Hall, R. (2001). Tectonic setting of Eocene boninite magmatism in the Izu–Bonin–Mariana forearc. *Earth and Planetary Science Letters*, *186*(2), 215–230. https://doi.org/10.1016/S0012-

821X(01)00248-5
Mallmann, G., & O'Neill, H. S. C. (2009). The Crystal/Melt Partitioning of V during Mantle Melting as a Function of Oxygen Fugacity Compared with some other Elements (Al, P, Ca, Sc, Ti, Cr, Fe, Ga, Y, Zr and Nb). *Journal of Petrology*, *50*(9), 1765–1794. https://doi.org/10.1093/petrology/egp053
Meijer, A. (1980). Primitive arc volcanism and a boninite series; example from western Pacific Island arcs. In *The Tectonic and Geologic Evolution of Southeast Asian Seas and Islands* (pp. 269–282). Washington, D.C.: American Geophysical Union. https://doi.org/10.1029/GM023p0269
Meijer, A. (1982). Petrology of volcanic rocks from the fore-arc sites. *Initial Reports of the Deep Sea Drilling Project*, *60*, 709. https://doi.org/10.2973/dsdp.proc.60.138.1982
Miura, M., Arai, S., Ahmed, A. H., Mizukami, T., Okuno, M., & Yamamoto, S. (2012). Podiform chromitite classification revisited: A comparison of discordant and concordant chromitite pods from Wadi Hilti, northern Oman ophiolite. *Journal of Asian Earth Sciences*, *59*, 52–61. https://doi.org/10.1016/J.JSEAES.2012.05.008
Miyashiro, A. (1974). Volcanic rock series in island arcs and active continental margins. *American Journal of Science*. American Journal of Science. https://doi.org/10.2475/ajs.274.4.321
Morishita, T., Tani, K., Shukuno, H., Harigane, Y., Tamura, A., Kumagai, H., & Hellebrand, E. (2011). Diversity of melt conduits in the Izu-Bonin-Mariana forearc mantle: Implications for the earliest stage of arc magmatism. *Geology*, *39*(4), 411–414. https://doi.org/10.1130/G31706.1
Münker, C., Pfänder, J. A., Weyer, S., Büchl, A., Kleine, T., & Mezger, K. (2003). Evolution of planetary cores and the Earth-Moon system from Nb/Ta systematics. *Science*, *301*(5629), 84–87. https://doi.org/10.1126/science.1084662
Nagaishi, K. (2008). *Fluid transfer and magmatism in the initial stage of subduction: Inference from the Oman ophiolite*. Ph.D. Thesis, Shizuoka University, Shizuoka, Japan. Retrieved from http://ir.lib.shizuoka.ac.jp/handle/10297/6386
Natland, J. H. (1982). Crystal Morphologies and Pyroxene Compositions in Boninites and Tholeiitic Basalts from Deep Sea Drilling Project Holes 458 and 459B in the Mariana Fore-Arc Region. *Initial Reports of the Deep Sea Drilling Project, 60*, 681–707. https://doi.org/10.2973/dsdp.proc.60.137.1982
Noguchi, S., Morishita, T., & Toramaru, A. (2004). Corrections for Na-loss on micro-analysis of glasses by electron probe X-ray micro analyzer. *Japanese Magazine of Mineralogical and Petrological Sciences*, *33*, 85–95.
Osozawa, S., Shinjo, R., Lo, C.-H., Jahn, B.-M., Hoang, N., Sasaki, M., Ishikawa, M., Kano, H., Hoshi, H., Xenophontos, C., Wakabayashi, J. (2012). Geochemistry and geochronology of the Troodos ophiolite: An SSZ ophiolite generated by subduction initiation and an extended episode of ridge subduction? *Lithosphere*, *4*(6), 497–510. https://doi.org/10.1130/L205.1
Paringit, R. . (1977). Notes on the massive copper-pyrite deposits and exploration concepts applied at Barlo, Dasol, Pangasinan. *Journal of the Geological Society of the Philippines*, *31*(3), 1–6.
Parkinson, I. J., & Pearce, J. A. (1998). Peridotites from the Izu-Bonin-Mariana forearc (ODP Leg 125): evidence for mantle melting and melt-mantle interaction in a supra-subduction zone setting. *Journal of Petrology*, *39*(9), 1577–1618. https://doi.org/10.1093/petroj/39.9.1577
Pearce, J. A., & Parkinson, I. J. (1993). Trace element models for mantle melting: application to volcanic arc petrogenesis. *Geological Society, London, Special Publications*, *76*(1), 373–403. https://doi.org/doi.org/10.1144/GSL.SP.1993.076.01.19
Pearce, J. A., & Robinson, P. T. (2010). The Troodos ophiolitic complex probably formed in a subduction initiation, slab edge setting. *Gondwana Research*, *18*(1), 60–81. https://doi.org/10.1016/j.gr.2009.12.003
Pearce, J. A., Stern, R. J., Bloomer, S. H., & Fryer, P. (2005). Geochemical mapping of the Mariana arc-basin system: Implications for the nature and distribution of subduction components. *Geochemistry, Geophysics, Geosystems*, *6*(7), n/a-n/a. https://doi.org/10.1029/2004GC000895
Pearce, J. A., van der Laan, S. R., Arculus, R. J., Murton, B. J., Ishii, T., Peate, D. W., & Parkinson, I. J. (1992). Boninite and harzburgite from Leg 125 (Bonin-Mariana forearc); a case study of magma genesis during the initial stages of subduction. *Proceedings of the Ocean Drilling Program, Scientific Results*, *125*, 623–659. https://doi.org/10.2973/odp.proc.sr.125.172.1992
Plank, T. (2005). Constraints from Thorium/Lanthanum on sediment recycling at subduction zones and the evolution of the continent. *Journal of Petrology*, *46*(5), 921–944. https://doi.org/10.1093/petrology/egi005
Pubellier, M., Monnier, C., Maury, R., & Tamayo, R. (2004). Plate kinematics, origin and tectonic emplacement of supra-subduction ophiolites in SE Asia. *Tectonophysics*, *392*(1–4), 9–36. https://doi.org/10.1016/J.TECTO.2004.04.028

Putirka, K. (2016). Rates and styles of planetary cooling on Earth, Moon, Mars, and Vesta, using new models for oxygen fugacity, ferric-ferrous ratios, olivine-liquid Fe-Mg exchange, and mantle potential temperature. *American Mineralogist*, *101*(4), 819–840. https://doi.org/10.2138/am-2016-5402

Putirka, K. D. (2008). Thermometers and Barometers for Volcanic Systems. *Reviews in Mineralogy and Geochemistry*, *69*(1), 61–120. https://doi.org/10.2138/rmg.2008.69.3

Putirka, K. D., Perfit, M., Ryerson, F. J., & Jackson, M. G. (2007). Ambient and excess mantle temperatures, olivine thermometry, and active vs. passive upwelling. *Chemical Geology*, *241*(3–4), 177–206. https://doi.org/10.1016/J.CHEMGEO.2007.01.014

Queano, K. L., Ali, J. R., Milsom, J., Aitchison, J. C., & Pubellier, M. (2007). North Luzon and the Philippine Sea Plate motion model: Insights following paleomagnetic, structural, and age-dating investigations. *Journal of Geophysical Research*, *112*(B5), B05101. https://doi.org/10.1029/2006JB004506

Queaño, K. L., Ali, J. R., Pubellier, M., Yumul, G. P., & Dimalanta, C. B. (2009). Reconstructing the Mesozoic-early Cenozoic evolution of northern Philippines: Clues from palaeomagnetic studies on the ophiolitic basement of the Central Cordillera. *Geophysical Journal International*, *178*(3), 1317–1326. https://doi.org/10.1111/j.1365-246X.2009.04221.x

Queaño, K. L., Dimalanta, C. B., Yumul, G. P., Marquez, E. J., Faustino-Eslava, D. V, Suzuki, S., & Ishida, K. (2017). Stratigraphic units overlying the Zambales Ophiolite Complex (ZOC) in Luzon, (Philippines): Tectonostratigraphic significance and regional implications. *Journal of Asian Earth Sciences*, *142*, 20–31. https://doi.org/10.1016/j.jseaes.2016.06.011

Queaño, K. L., Marquez, E. J., Dimalanta, C. B., Aitchison, J. C., Ali, J. R., & Yumul, G. P. (2017). Mesozoic radiolarian faunas from the northwest Ilocos Region, Luzon, Philippines and their tectonic significance. *Island Arc*, *26*(4), e12195–n/a. https://doi.org/10.1111/iar.12195

Reagan, M. K., Ishizuka, O., Stern, R. J., Kelley, K. A., Ohara, Y., Blichert-Toft, J., Bloomer, S.H., Cash, J., Fryer, P., Hanan, B.B., Hickey-Vargas, R., Ishii, T., Kimura, J.-I., Peate, D.W., Rowe, M.C., Woods, M. (2010). Fore-arc basalts and subduction initiation in the Izu-Bonin-Mariana system. *Geochemistry, Geophysics, Geosystems*, *11*(3), Q03X12. https://doi.org/10.1029/2009GC002871

Reagan, M. K., & Meijer, A. (1984). Geology and geochemistry of early arc-volcanic rocks from Guam. *GSA Bulletin*, *95*(6), 701–713. Retrieved from http://dx.doi.org/10.1130/0016-7606(1984)95%3C701:GAGOEA%3E2.0.CO

Reagan, M. K., Pearce, J. A., Petronotis, K., Almeev, R., Avery, A. J., Carvallo, C., Chapman, T., Christeson, G.L., Ferre, E., Godard, M., Heaton, D.E., Kirchenbaur, M., Kurz, W., Kutterolf, S., Li, H.Y., Li, Y.B., Michibayashi, K., Morgan, S., Nelson, W.R., Prytulak, J., Python, M., Robertson, A.H.F., Ryan, J.G., Sager, W.W., Sakuyama, T., Shervais, J.W., Shimizu, K., Whattam, S. A. (2015). Expedition 352 summary. *Proceedings of the International Ocean Discovery Program*, *352*, 1–32. https://doi.org/doi: 10.14379/iodp.proc.352.102.2015

Reagan, M. K., Pearce, J. A., Petronotis, K., Almeev, R. R., Avery, A. J., Carvallo, C., Chapman, T., Christeson, G.L., Ferre, E., Godard, M., Heaton, D.E., Kirchenbaur, M., Kurz, W., Kutterolf, S., Li, H.Y., Li, Y.B., Michibayashi, K., Morgan, S., Nelson, W.R., Prytulak, J., Python, M., Robertson, A.H.F., Ryan, J.G., Sager, W.W., Sakuyama, T., Shervais, J.W., Shimizu, K., Whattam, S. A. (2017). Subduction initiation and ophiolite crust: new insights from IODP drilling. *International Geology Review*, *59*(11), 1439–1450. https://doi.org/10.1080/00206814.2016.1276482

Resing, J. A., Rubin, K. H., Embley, R. W., Lupton, J. E., Baker, E. T., Dziak, R. P., Baumberger, T., Lilley, M. D., Huber, J. A., Shank, T. M., Butterfield, D. A., Clague, D. A., Keller, N. S., Merle, S. G., Buck, N. J., Michael, P. J., Soule, A., Caress, D. W., Walker, S. L., Davis, R., Cowen, J. P., Reysenbach, A. L., Thomas, H. (2011). Active submarine eruption of boninite in the northeastern Lau Basin. *Nature Geoscience*, *4*(11), 799–806. https://doi.org/10.1038/ngeo1275

Ribeiro, J. M., Stern, R. J., Kelley, K. A., Shaw, A. M., Martinez, F., & Ohara, Y. (2015). Composition of the slab-derived fluids released beneath the Mariana forearc: Evidence for shallow dehydration of the subducting plate. *Earth and Planetary Science Letters*, *418*, 136–148. https://doi.org/10.1016/j.epsl.2015.02.018

Richter, C., & Ali, J. R. (2015). Philippine Sea Plate motion history: Eocene-Recent record from ODP Site 1201, central West Philippine Basin. *Earth and Planetary Science Letters*, *410*, 165–173. https://doi.org/10.1016/j.epsl.2014.11.032

Sajona, F. G. (1995). *Fusion de la croute oceanique en contexte de subduction/collision: Geochimie, geochronologie et petrologie du magmatisme Plioquaternaire de Mindanao (Philippines)*. Ph.D. Thesis, Universite de Bretagne Occidentale, Brest, France.

Salapare, R. C., Dimalanta, C. B., Ramos, N. T., Manalo, P. C., Faustino-Eslava, D. V., Queano, K. L., & Yumul, G. P. (2015). Upper crustal structure beneath the Zambales Ophiolite Complex, Luzon, Philippines inferred

from integrated gravity, magnetic and geological data. *Geophysical Journal International*, *201*(3), 1522–1533. https://doi.org/10.1093/gji/ggv094

Savov, I. P., Hickey-Vargas, R., D'Antonio, M., Ryan, J, G., & Spadea, P. (2006). Petrology and Geochemistry of West Philippine Basin Basalts and Early Palau–Kyushu Arc Volcanic Clasts from ODP Leg 195, Site 1201D: Implications for the Early History of the Izu–Bonin–Mariana Arc. *Journal of Petrology*, *47*(2), 277–299. https://doi.org/10.1093/petrology/egi075

Schweller, W. J., & Karig, D. E. (1982). Emplacement of the Zambales Ophiolite into the West Luzon Margin. In J. S. Watkins & C. L. Drake (Eds.), *AAPG Memoir 34: Studies in Continental Margin Geology* (pp. 441–454). Tulsa, Oklahoma: American Association of Petroleum Geologists.

Schweller, W. J., Roth, P. H., Karig, D. E., & Bachman, S. B. (1984). Sedimentation history and biostratigraphy of ophiolite-related Tertiary sediments, Luzon, Philippines. *Geological Society of America Bulletin*, *95*(11), 1333–1342. https://doi.org/10.1130/0016-7606(1984)95<1333:SHABOO>2.0.CO;2

Serri, G., Spadea, P., Beccaluva, L., Civetta, L., Coltorti, M. ., Dostal, J., Sajona, F. G., Vaccaro, C., Zeda, O. (1991). Petrology of igneous rocks from the Celebes Sea basement. *Proceedings of the Ocean Drilling Program, Scientific Results*, *124*, 271–296. https://doi.org/10.2973/odp.proc.sr.124.160.1991

Sharaskin, A. Y. (1982). Petrography and geochemistry of basement rocks from five Leg 60 sites. *Initial Reports of the Deep Sea Drilling Project, 60*, 647–656. https://doi.org/10.2973/dsdp.proc.60.134.1982

Shervais, J. W. (1982). TiV plots and the petrogenesis of modern and ophiolitic lavas. *Earth and Planetary Science Letters*, *59*(1), 101–118. https://doi.org/10.1016/0012-821X(82)90120-0

Spadea, P., D'Antonio, M., & Thirlwall, M. F. (1996). Source characteristics of the basement rocks from the Sulu and Celebes Basins (Western Pacific): chemical and isotopic evidence. *Contributions to Mineralogy and Petrology*, *123*(2), 159–176. https://doi.org/10.1007/s004100050148

Stern, R. J. (2004). Subduction initiation: spontaneous and induced. *Earth and Planetary Science Letters*, *226*(3), 275–292. https://doi.org/10.1016/j.epsl.2004.08.007

Stern, R. J., & Bloomer, S. H. (1992). Subduction zone infancy: examples from the Eocene Izu-Bonin-Mariana and Jurassic California arcs. *Geological Society of America Bulletin*, *104*(12), 1621–1636. https://doi.org/10.1130/0016-7606(1992)104<1621:SZIEFT>2.3.CO;2

Stern, R. J., & Gerya, T. (2017, October 27). Subduction initiation in nature and models: A review. *Tectonophysics*. https://doi.org/10.1016/j.tecto.2017.10.014

Stern, R. J., Gerya, T., & Tackley, P. J. (2018). Stagnant lid tectonics: Perspectives from silicate planets, dwarf planets, large moons, and large asteroids. *Geoscience Frontiers*, *9*(1), 103–119. https://doi.org/10.1016/j.gsf.2017.06.004

Stern, R. J., Reagan, M., Ishizuka, O., Ohara, Y., & Whattam, S. (2012). To understand subduction initiation, study forearc crust: To understand forearc crust, study ophiolites. *Lithosphere*, *4*(6), 469–483. https://doi.org/10.1130/L183.1

Takahashi, E. (1986). Origin of basaltic magmas--implications from peridotite melting experiments and an olivine fractionation model. *Bulletin of the Volcanological Society of Japan*, *30*, S17–S40.

Tamayo Jr., R. A. (2001). *Caracterisation petrologique et geochemique, origines et evolutions geodynamiques des ophiolites des Philippines*. Ph.D. Thesis, Universite de Bretagne Occidentale, Brest, France.

Tamayo, R. A., Maury, R. C., Yumul, G. P., Polvé, M., Cotten, J., Dimantala, C. B., & Olaguera, F. O. (2004). Subduction-related magmatic imprint of most Philippine ophiolites: Implications on the early geodynamic evolution of the Philippine archipelago. *Bulletin de La Societe Geologique de France*, *175*(5), 443–460. https://doi.org/10.2113/175.5.443

Tamura, A., Akizawa, N., Otsuka, R., Kanayama, K., Python, M., Morishita, T., & Arai, S. (2015). Measurement of whole-rock trace-element composition by flux-free fused glass and LA-ICP-MS: evaluation of simple and rapid routine work. *Geochemical Journal*, *49*(3), 243–258. https://doi.org/10.2343/geochemj.2.0353

Tamura, Y., Ishizuka, O., Stern, R. J., Shukuno, H., Kawabata, H., Embley, R. W., … Bloomer, S. H. (2011). Two primary basalt magma types from northwest Rota-1 volcano, Mariana arc and its mantle diapir or mantle wedge plume. *Journal of Petrology*, *52*(6), 1143–1183. https://doi.org/10.1093/petrology/egr022

Tamura, Y., Yuhara, M., & Ishii, T. (2000). Primary arc basalts from Daisen volcano, Japan: Equilibrium crystal fractionation versus disequilibrium fractionation during supercooling. *Journal of Petrology*, *41*(3), 431–448. https://doi.org/10.1093/petrology/41.3.431

Tani, K., Gabo, J. A. S., Horie, K., Ishizuka, O., Padrones, J., Payot, B., Tejada, M. L., Faustino-Eslava, D. V., Imai, A., Arai, S., Hokada, T., Yumul, Jr., G. P., Dimalanta, C. B. (2015). Temporal constraints for the tectonic development of the Philippine ophiolite belts from new zircon U-Pb ages. In *Japan Geoscience Union*

Meeting. Chiba, Japan.
Tani, K., Kawabata, H., Chang, Q., Sato, K., & Tatsumi, Y. (2005). Quantitative analyses of silicate rock major and trace elements by X-ray fluorescence spectrometer: evaluation of analytical precision and sample preparation. *Frontier Research on Earth Evolution*, *2*(2), 1–8. Retrieved from http://www.jamstec.go.jp/ifree/j/about/result/report_for_2003-2004/honbun/02_16.pdf
Tatsumi, Y., & Eggins, S. M. (1995). *Subduction Zone Magmatism*. Cambridge, M.A: Blackwell Science, Inc.
Taylor, R. N., Nesbitt, R. W., Vidal, P., Harmon, R. S., Auvray, B., & Croudace, I. W. (1994). Mineralogy, chemistry, and genesis of the boninite series volcanics, Chichijima, Bonin Islands, Japan. *Journal of Petrology*, *35*(3), 577–617. https://doi.org/10.1093/petrology/35.3.577
Umino, S. (1986). Magma mixing in boninite sequence of Chichijima, Bonin Islands. *Journal of Volcanology and Geothermal Research*, *29*(1), 125–157. https://doi.org/10.1016/0377-0273(86)90042-9
Umino, S., Kanayama, K., Kitamura, K., Tamura, A., Ishizuka, O., Senda, R., & Arai, S. (2018). Did boninite originate from the heterogeneous mantle with recycled ancient slab? *Island Arc*, *27*(1), e12221. https://doi.org/10.1111/iar.12221
Umino, S., Kitamura, K., Kanayama, K., Kusano, Y., Nagaishi, K., Ishikawa, T., & Ishizuka, O. (2014). Prolonged vs. failed subduction zone. In *Goldschimdt 2014 abstracts* (p. 2532.).
Umino, S., Kitamura, K., Kanayama, K., Tamura, A., Sakamoto, N., Ishizuka, O., & Arai, S. (2015). Thermal and chemical evolution of the subarc mantle revealed by spinel-hosted melt inclusions in boninite from the Ogasawara (Bonin) Archipelago, Japan. *Geology*, *43*(2), 151–154. https://doi.org/10.1130/G36191.1
Umino, S., Lipman, P. W., & Obata, S. (2000). Subaqueous lava flow lobes, observed on ROV dives off Hawaii. *Geology*, *28*(6), 503–506. https://doi.org/10.1130/0091-7613(2000)28<503:SLFLOO>2.0.CO;2
Umino, S., & Nakano, S. (2007). *Geology of the Chichijima Retto District. Quadrangle Series, 1:50,000*. Tsukuba, Japan: Geological Survey of Japan, AIST (in Japanese with English abstract 3p.).
Umino, S., Nakano, S., Ishizuka, O., & Komazawa, M. (2009). *Geological map of Japan 1:200,000, Ogasawara Shoto*. Tsukuba, Japan: Geological Survey of Japan, AIST (in Japanese with English abstract).
Umino, S., Obata, S., Lipman, P., Smith, J. R., Shibata, T., Naka, J., & Trusdell, F. (2002). Emplacement and inflation structures of submarine and subaerial from Hawaii (pp. 85–101). American Geophysical Union. https://doi.org/https://doi.org/10.1029/GM128p0085
Vollmer, F. (2015). Orient 3: a new integrated software program for orientation data analysis, kinematic analysis, spherical projections, and Schmidt plots. In *Geological Society of America Abstracts with Programs* (Vol. 47, p. 49). Geological Society of America.
Wada, I., & King, S. (2015). Dynamics of Subducting Slabs: Numerical Modeling and Constraints from Seismology, Geoid, Topography, Geochemistry, and Petrology. In *Treatise on Geophysics* (pp. 339–391). United Kingdom: Elsevier. https://doi.org/10.1016/B978-0-444-53802-4.00132-9
Walker, G. P. L. (1992). Morphometric study of pillow-size spectrum among pillow lavas. *Bulletin of Volcanology*, *54*(6), 459–474. https://doi.org/10.1007/BF00301392
Warren, J. M. (2016, April 1). Global variations in abyssal peridotite compositions. *Lithos*. Elsevier. https://doi.org/10.1016/j.lithos.2015.12.023
Watanabe, A., & Kuroda, N. (2000). Quartz-bearing boninite from northern Chichi-jima, Bonin Islands : Magma mixing of boninite with quartz dacite. *Geoscience Reports of Shizuoka University*, *27*, 1–9. https://doi.org/10.14945/00000365
Weyer, S., Münker, C., & Mezger, K. (2003). Nb/Ta, Zr/Hf and REE in the depleted mantle: Implications for the differentiation history of the crust - mantle system. *Earth and Planetary Science Letters*, *205*(3–4), 309–324. https://doi.org/10.1016/S0012-821X(02)01059-2
Whattam, S. A., & Stern, R. J. (2011). The 'subduction initiation rule': a key for linking ophiolites, intra-oceanic forearcs, and subduction initiation. *Contributions to Mineralogy and Petrology*, *162*(5), 1031–1045. https://doi.org/10.1007/s00410-011-0638-z
Whattam, S. A., & Stern, R. J. (2015). Late Cretaceous plume-induced subduction initiation along the southern margin of the Caribbean and NW South America: The first documented example with implications for the onset of plate tectonics. *Gondwana Research*, *27*(1), 38–63. https://doi.org/10.1016/J.GR.2014.07.011
Workman, R. K., & Hart, S. R. (2005). Major and trace element composition of the depleted MORB mantle (DMM). *Earth and Planetary Science Letters*, *231*(1–2), 53–72. https://doi.org/10.1016/j.epsl.2004.12.005
Wu, J., Suppe, J., Lu, R., & Kanda, R. (2016). Philippine Sea and East Asian plate tectonics since 52 Ma constrained by new subducted slab reconstruction methods. *Journal of Geophysical Research: Solid Earth*, *121*(6), 4670–4741. https://doi.org/10.1002/2016JB012923
Yajima, K., & Fujimaki, H. (2001). High-Ca and low-Ca boninites from Chichijima, Bonin (Ogasawara)

archipelago. *Japanese Magazine of Mineralogical and Petrological Sciences*, *30*(5), 217–236. https://doi.org/10.2465/gkk.30.217

Yamazaki, T., Takahashi, M., Iryu, Y., Sato, T., Oda, M., Takayanagi, H., Chiyonobu, S., Nishimura, A., Nakazawa, T., Ooka, T. (2010). Philippine Sea Plate motion since the Eocene estimated from paleomagnetism of seafloor drill cores and gravity cores. *Earth, Planets and Space*, *62*(6), 495–502. https://doi.org/10.5047/eps.2010.04.001

Yasuda, A. (2014). A new technique using FT-IR micro-reflectance spectroscopy for measurement of water concentrations in melt inclusions. *Earth, Planets and Space*, *66*(1), 34. https://doi.org/10.1186/1880-5981-66-34

Yumul, G. P. (1996). Varying mantle sources of supra-subduction zone ophiolites: REE evidence from the Zambales Ophiolite Complex, Luzon, Philippines. *Tectonophysics*, *262*(1), 243–262. https://doi.org/10.1016/0040-1951(96)00013-3

Yumul, G. P., Dimalanta, C. B., & Jumawan, F. T. (2000). Geology of the southern Zambales Ophiolite Complex, Luzon, Philippines. *Island Arc*, *9*(4), 542–555. https://doi.org/10.1111/j.1440-1738.2000.00300.x

Yumul Jr., G. P. (1989). Petrological characterization of the residual-cumulate sequences of the Zambales Ophiolite Complex, Luzon, Philippines. *Ofioliti*, *14*, 253–291.

Yumul Jr., G. P. (1990). *Multi-stage melting, evolving mantle sources and ophiolite generation: Constraints from the Zambales ophiolite complex, Philippines*. Ph.D. Thesis, University of Tokyo, Tokyo, Japan.

Yumul Jr., G. P., Datuin, R. T., & Manipon, J. C. (1990). Geology and geochemistry of the Cabangan-San Antonio massifs, Zambales ophiolite complex, Philippines: Tectonically juxtaposed marginal basin-island arc terranes. *Journal of the Geological Society of the Philippines*, *45*(1–4), 69–100.

Yumul Jr., G. P., Dimalanta, C. B., Faustino, D. V, & De Jesus, J. V. (1998). Translation and docking of an arc terrane: geological and geochemical evidence from the southern Zambales Ophiolite Complex, Philippines. *Tectonophysics*, *293*(3–4), 255–272. https://doi.org/10.1016/S0040-1951(98)00096-1

Zahirovic, S., Matthews, K. J., Flament, N., Müller, R. D., Hill, K. C., Seton, M., & Gurnis, M. (2016). Tectonic evolution and deep mantle structure of the eastern Tethys since the latest Jurassic. *Earth-Science Reviews*, *162*, 293–337. https://doi.org/10.1016/J.EARSCIREV.2016.09.005

Zahirovic, S., Seton, M., & Müller, R. D. (2014). The Cretaceous and Cenozoic tectonic evolution of Southeast Asia. *Solid Earth*, *5*(1), 227–273. https://doi.org/10.5194/se-5-227-2014

Zakariadze, G. S. (1981). Petrology of basalts of holes 447A, 449, and 450, South Philippine Sea transect, Deep Sea Drilling Project Leg 59. *Initial Reports of the Deep Sea Drilling Project*, *59*, 669–680. https://doi.org/doi: 10.2973/dsdp.proc.59.129.1981

Zanetti, A., D'Antonio, M., Spadea, P., Raffone, N., Vannucci, R., & Bruguier, O. (2006). Petrogenesis of mantle peridotites from the Izu-Bonin-Mariana (IBM) forearc. *Ofioliti*, *31*(2), 189–206. https://doi.org/https://doi.org/10.4454/ofioliti.v31i2.340

11.Figures

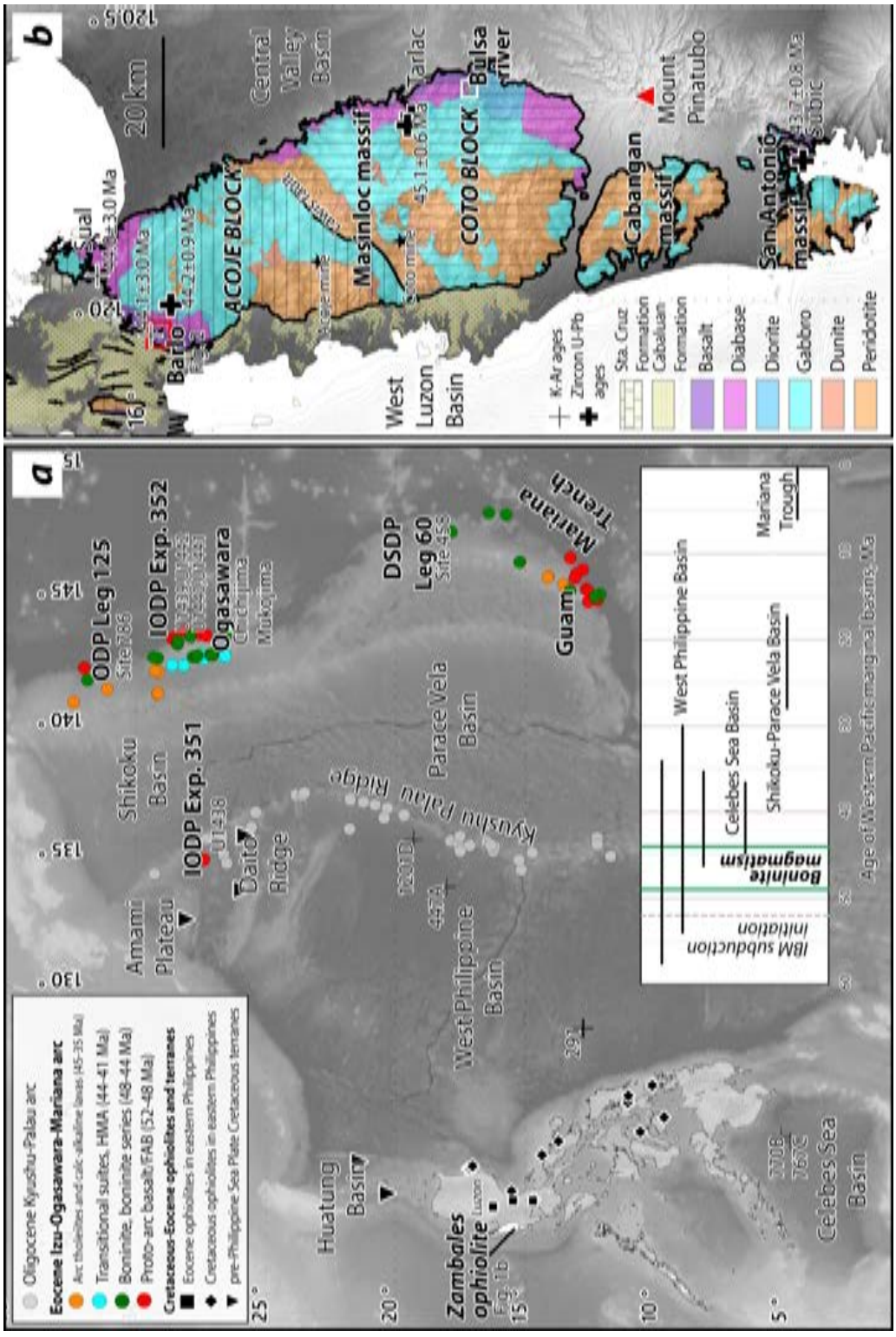

Figure 1. (a) Distribution of subduction initiation rock suites in the Philippine Sea Plate and spreading histories of associated marginal basins (Deschamps & Lallemand, 2002; Pearce et al., 1992; Reagan et al., 2017). (b) Regional geological map of the Zambales ophiolite after Yumul et al. (1990) with whole rock K-Ar and zircon U-Pb ages from Fuller et al. (1989) and Encarnacion et al. (1993). The 44–43 Ma Acoje Block consists of the northern Masinloc massif and the southernmost San Antonio massif. The enclosed region (red box) is the Barlo extrusive section mapped in this study.

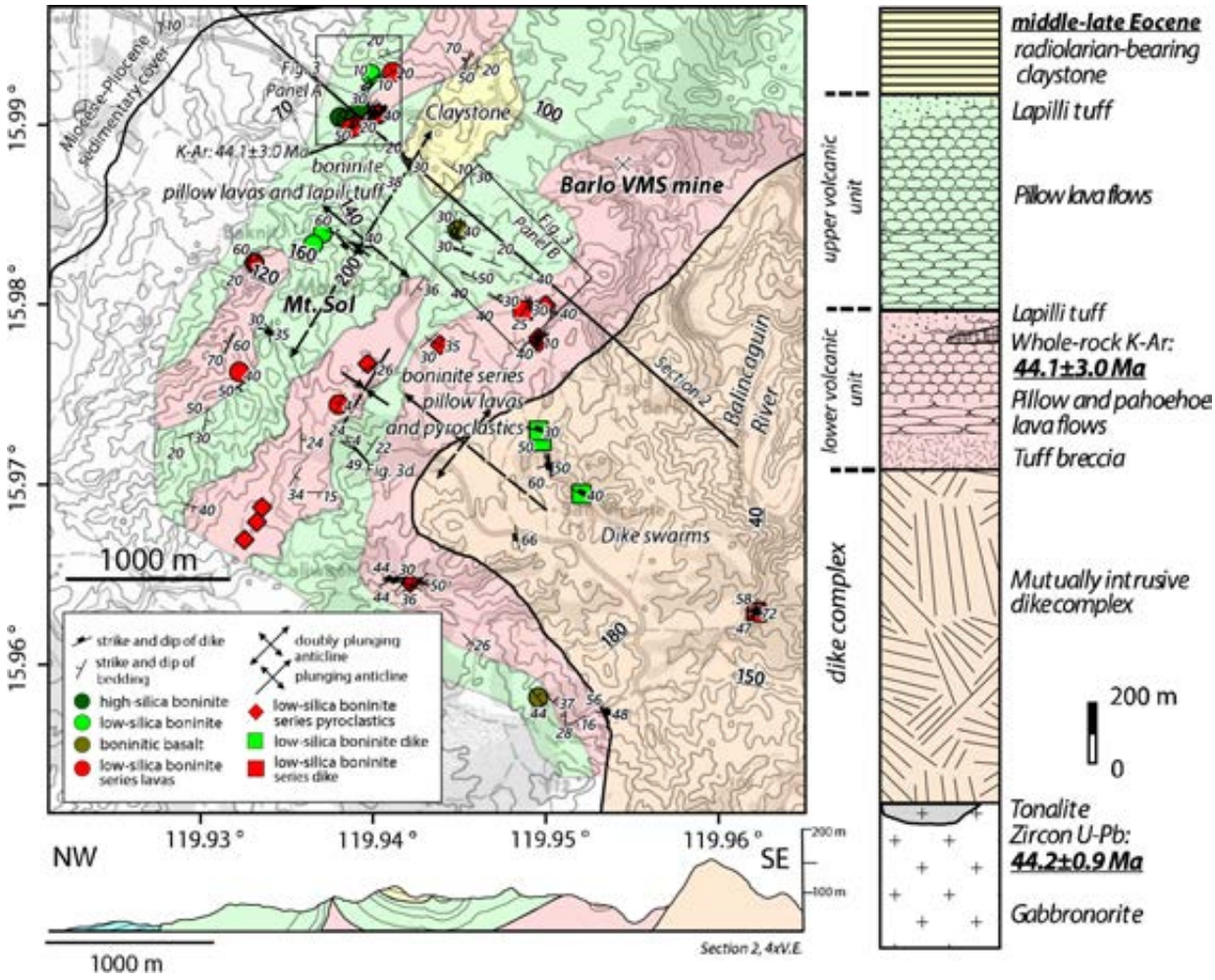

Figure 2. Geological map of Barlo and its environs. Closed symbols are samples with whole-rock geochemical data. Enclosed areas (panel A and B) are shown in Figure 3. Geologic cross-section is given along a NW-SE section line. Geologic column shows stratigraphic relationships and estimated thickness of the upper and lower volcanic unit. Biostratigraphic, whole rock K-Ar and zircon U-Pb ages are from Schweller et al. (1984), Fuller et al. (1989) and Encarnacion et al. (1993).

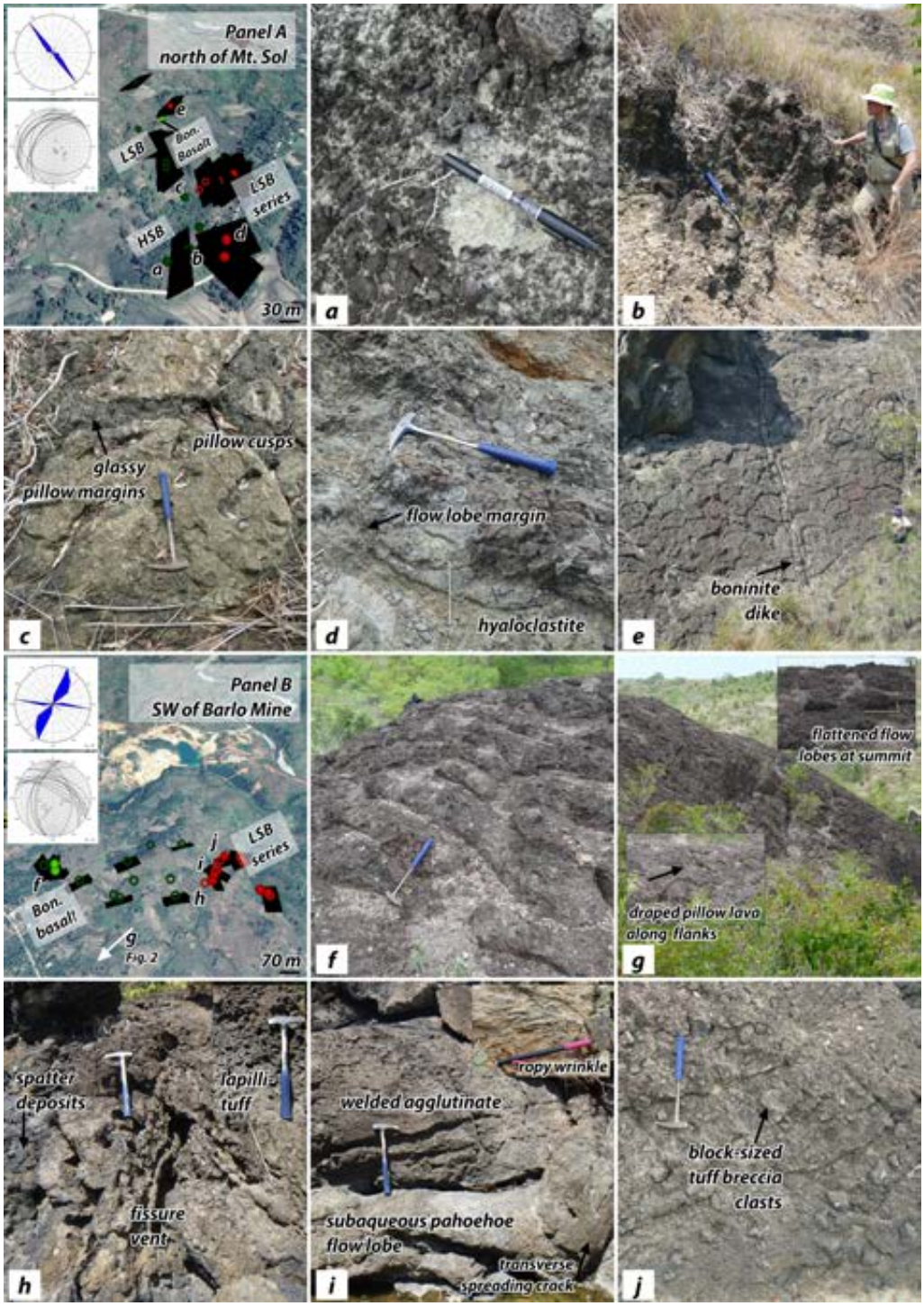

Figure 3. Representative outcrops showing distinct volcanic facies and stratigraphic relationship of the upper boninite unit and lower basaltic andesite-andesite unit. (a) High-Si boninite lapilli tuff. (b) NW-dipping high-Si boninite pillow lavas. (c) High-Si boninite pillow lava with fresh glassy margins. (d) Andesite flow lobe with basal hyaloclastite. (e) Basaltic andesite pillow lavas cut by boninite dike. (f) NE-dipping elongate boninitic basalt pillow lavas. (g) Boninite pillow volcano. (h) Fissure vent with fluidal, flattened basaltic andesite-andesite spatter deposits and lapilli tuff (inset). (i) Basaltic andesite pahoehoe flow with ropy wrinkles (inset) and transverse spreading cracks on lobe crust indicating flow direction. (j) Basaltic andesite tuff breccia with glassy matrix. Rock hammer for scale (0.42 m). Orientation poles of bedding planes (dip azimuth) are shown in lower hemisphere stereographic projection (Vollmer, 2015)*. Bedding plane orientations in GoogleEarth (Digital Globe, CNES/Astrium) images, viewed from southeast direction, are visualized using the S2K macro* (Blenkinsop, 2012)*.*

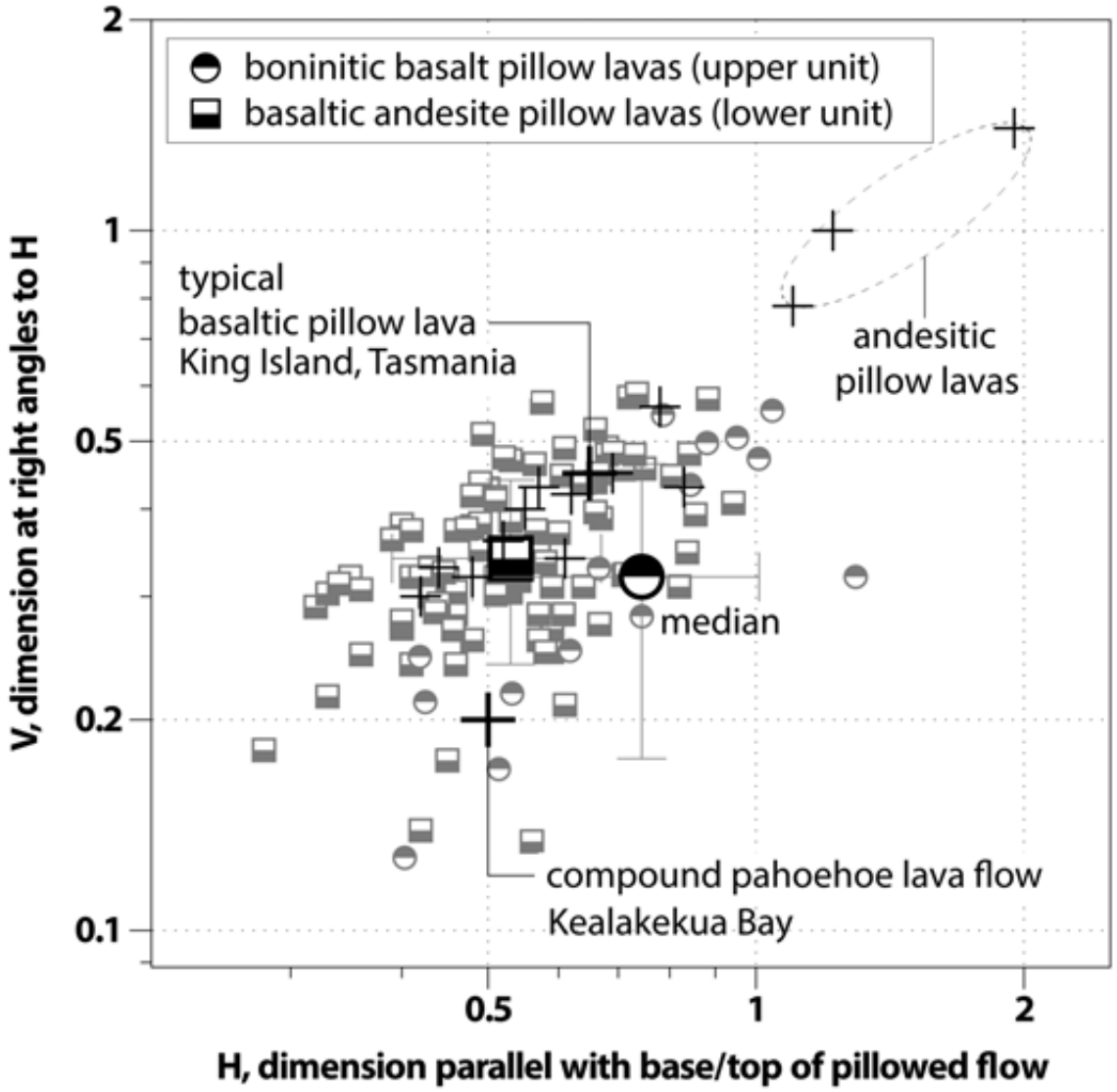

Figure 4. Horizontal and vertical dimensions of pillow lavas from the upper and lower volcanic units of the Acoje Block volcanic sequence at Barlo. Representative lava flow measurements are from Walker (1992).

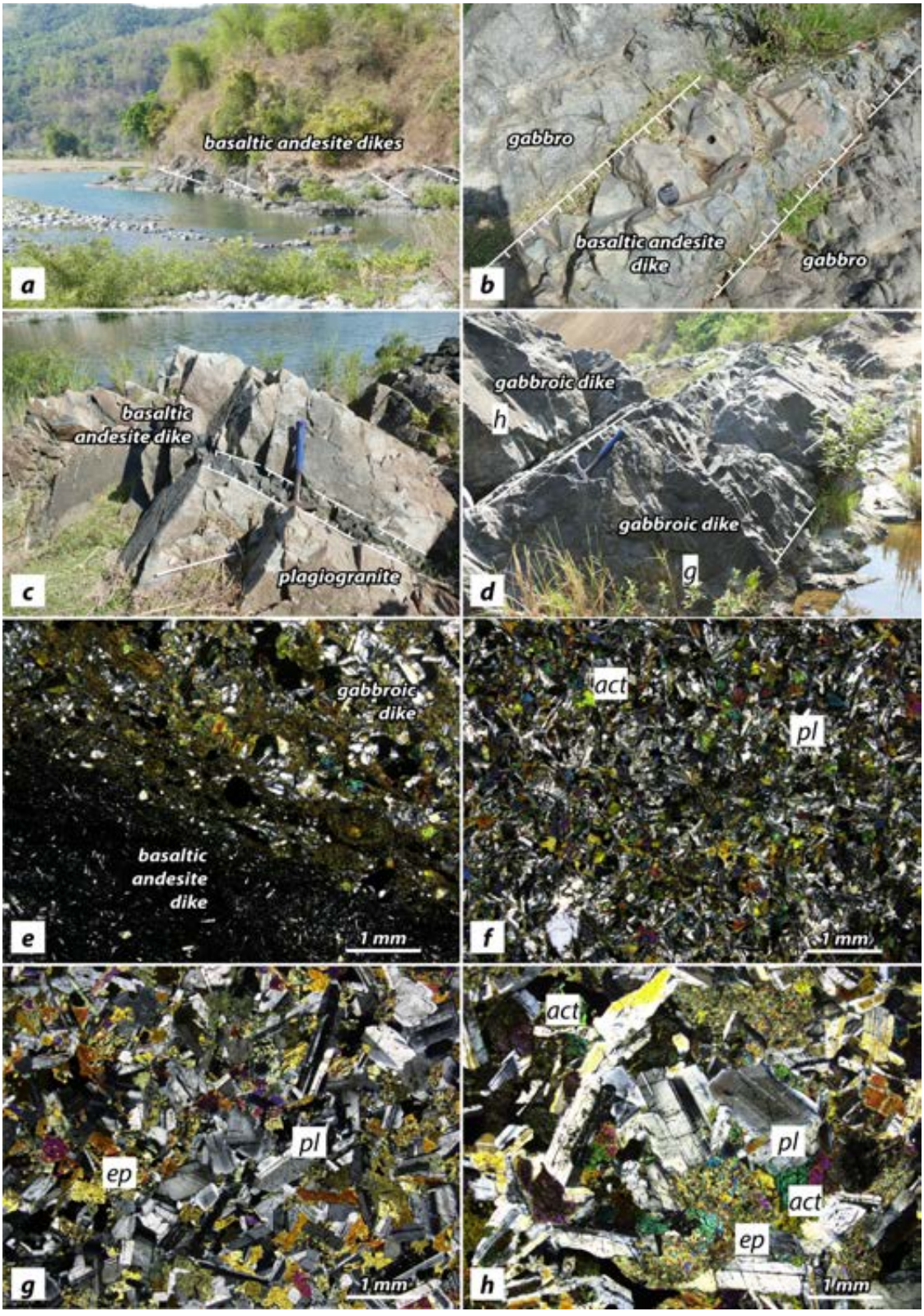

Figure 5. Field occurrence and textures of Coto Block basaltic andesite and gabbroic dikes sampled in this study.

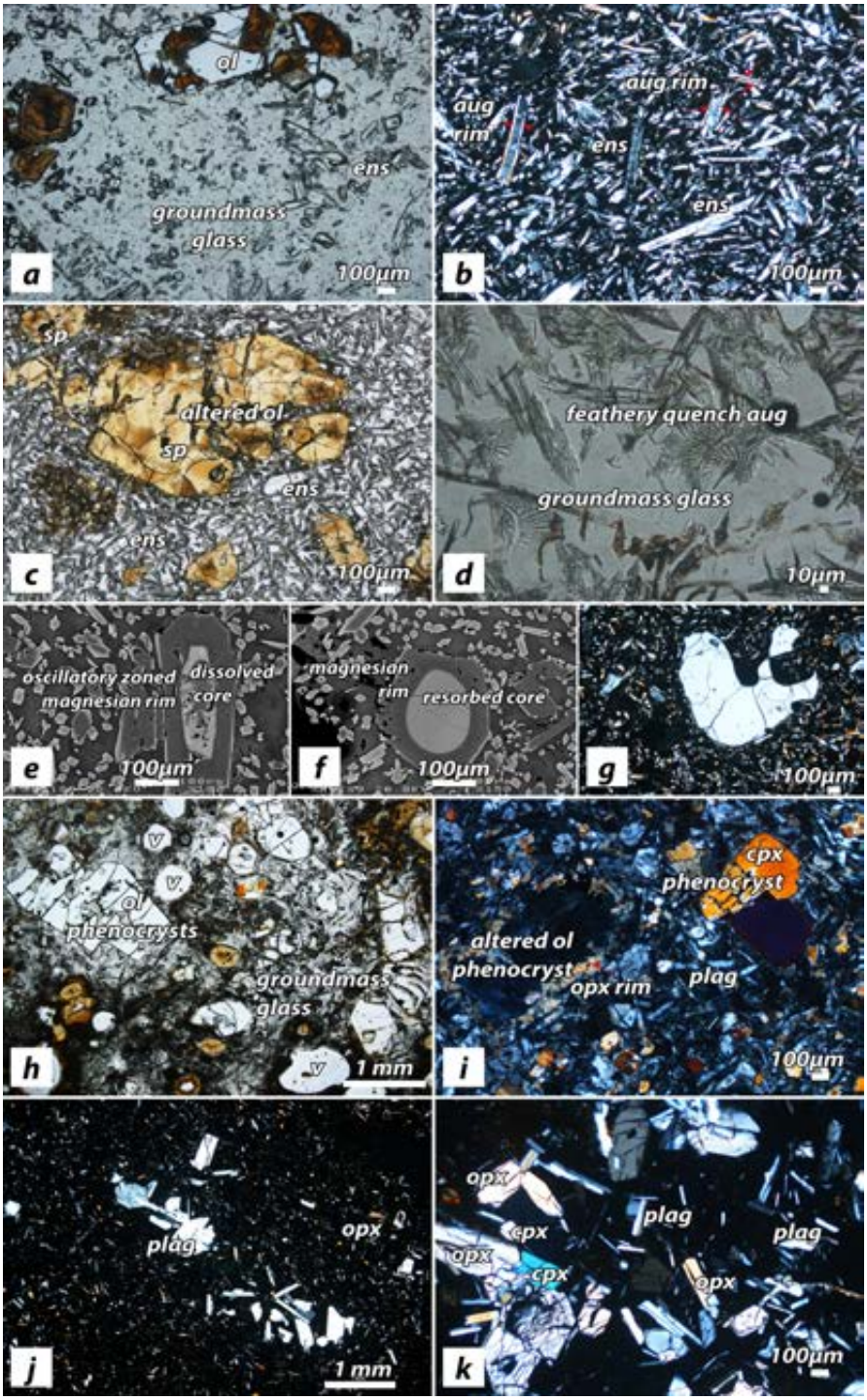

Figure 6. Microphotographs showing textures of Zambales boninite and boninite-series volcanics. (a) Fresh olivine in transparent groundmass glass, outer pillow margin, HSB. (PPL). (b) (b) Abundant elongate enstatite microphenocryts with augite rims, HSB (XPL). (c) Spinel in altered olivine microphenocryst with abundant elongate enstatite, HSB (PPL). (d) Characteristic feathery clinopyroxene in groundmass glass, HSB (PPL). (e) Oscillatory zoning in magnesian rim of enstatite xenocryst with dissolved core, HSB (BSE). (f) Reverse zoning in enstatite xenocryst with resorbed core, HSB (BSE). (g) Embayed quartz xenocryst, HSB (XPL). (h) Fresh olivine phenocryst and clinopyroxene microphenocryt in glassy groundmass, LSB (PPL). (i) Altered olivine, clinopyroxene with groundmass plagioclase, LSB (XPL). (j) Plagioclase glomerophenocrysts in glassy groundmass, glassy LSB-series andesite pillow core (XPL). (k) Plagioclase, othropyroxene and clinopyroxene microphenocrysts in LSB-series basaltic andesite tuff breccia matrix (XPL).

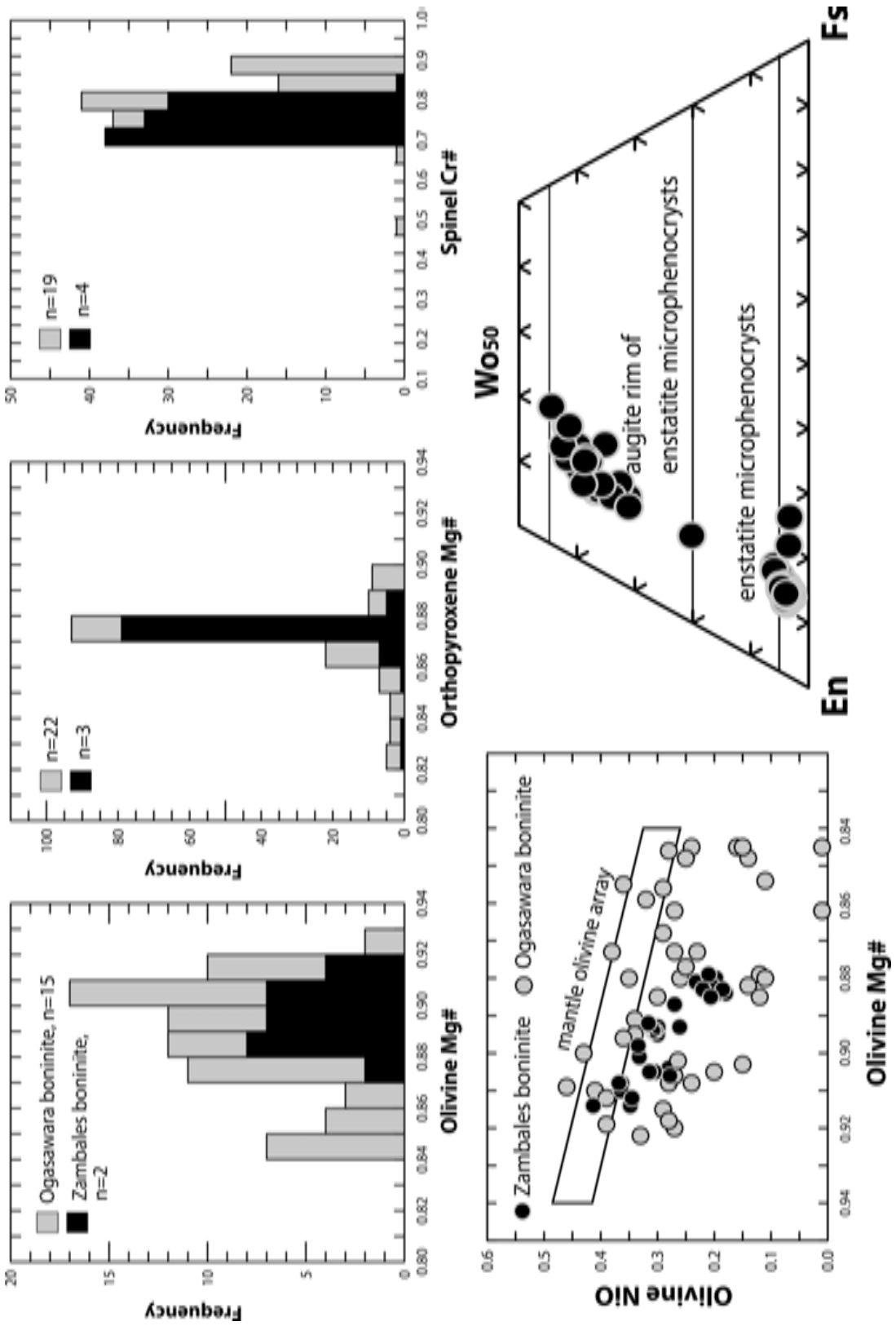

Figure 7. Comparative mineral chemistry of constituent phases (olivine, orthopyroxene, clinopyroxene and spinel) in Zambales and Ogasawara boninites. Mantle olivine array is from Takahashi (1986).

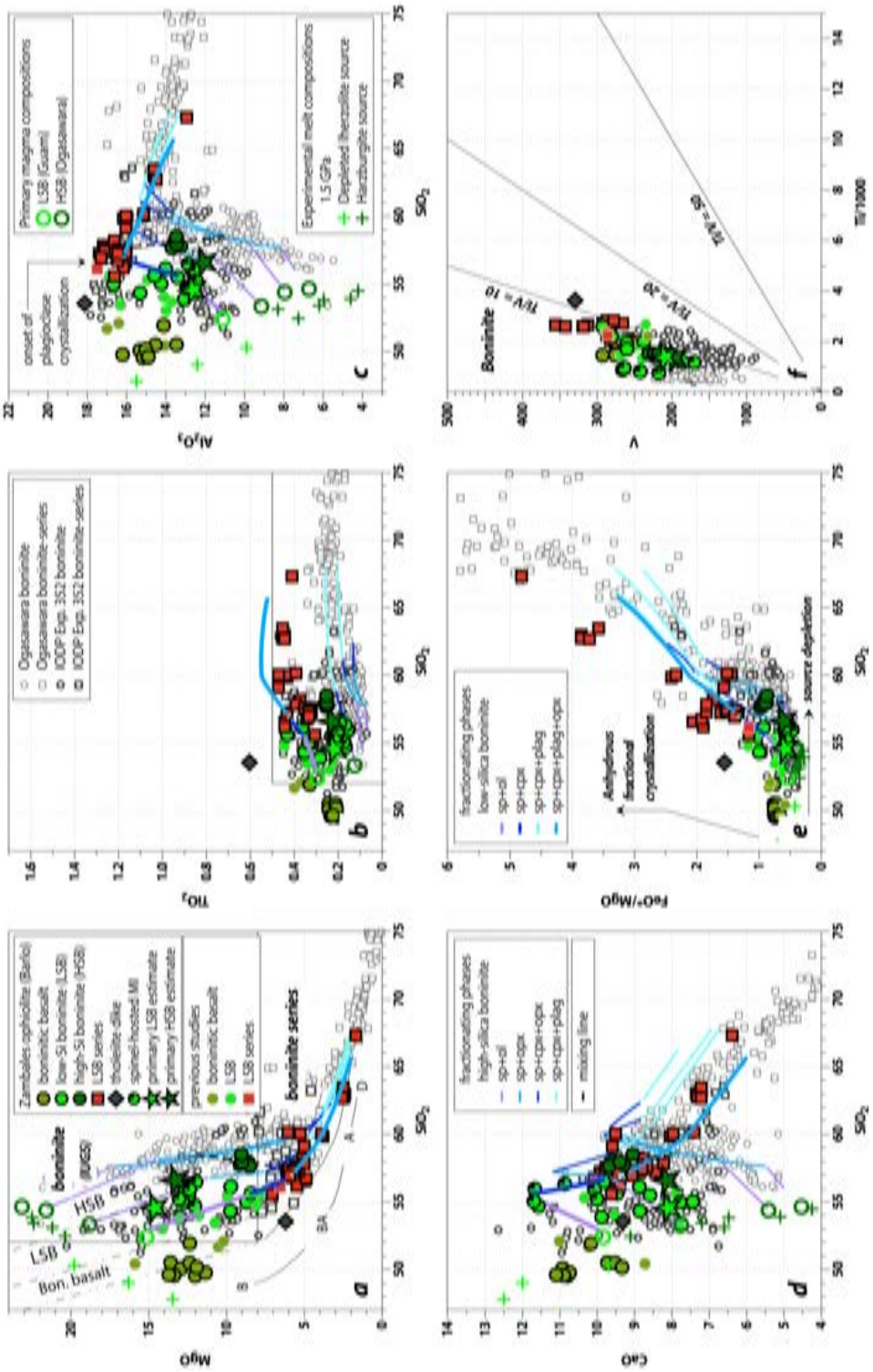

Figure 8. (a–e) MgO, TiO_2, FeO/MgO, CaO, Al_2O_3 vs. SiO_2 variation diagrams showing the distinct parental magma compositions and modeled fractional crystallization paths of high- and low-silica boninites and boninite-series volcanics. Fractional crystallization paths are modeled using rhyoliteMELTS v.1.2.0* (Ghiorso & Gualda, 2015) *at 1 kb pressure and initial fO_2 of FMQ+1. The designated primary boninite magmas given by Umino et al. (2018) are used as parental compositions with an initial H_2O content of 1 wt %. Models were run at temperature range of 1500–980 °C. Modified boninite classification after Kanayama et al. (2013) and Reagan et al. (2017). Dividing lines between boninite and basalt–andesite–dacite–rhyolite (BADR) series are from Pearce & Robinson (2010). (f) Ti-V systematics* (Shervais, 1982) *of IBM and Zambales subduction initiation rock suites is also shown.*

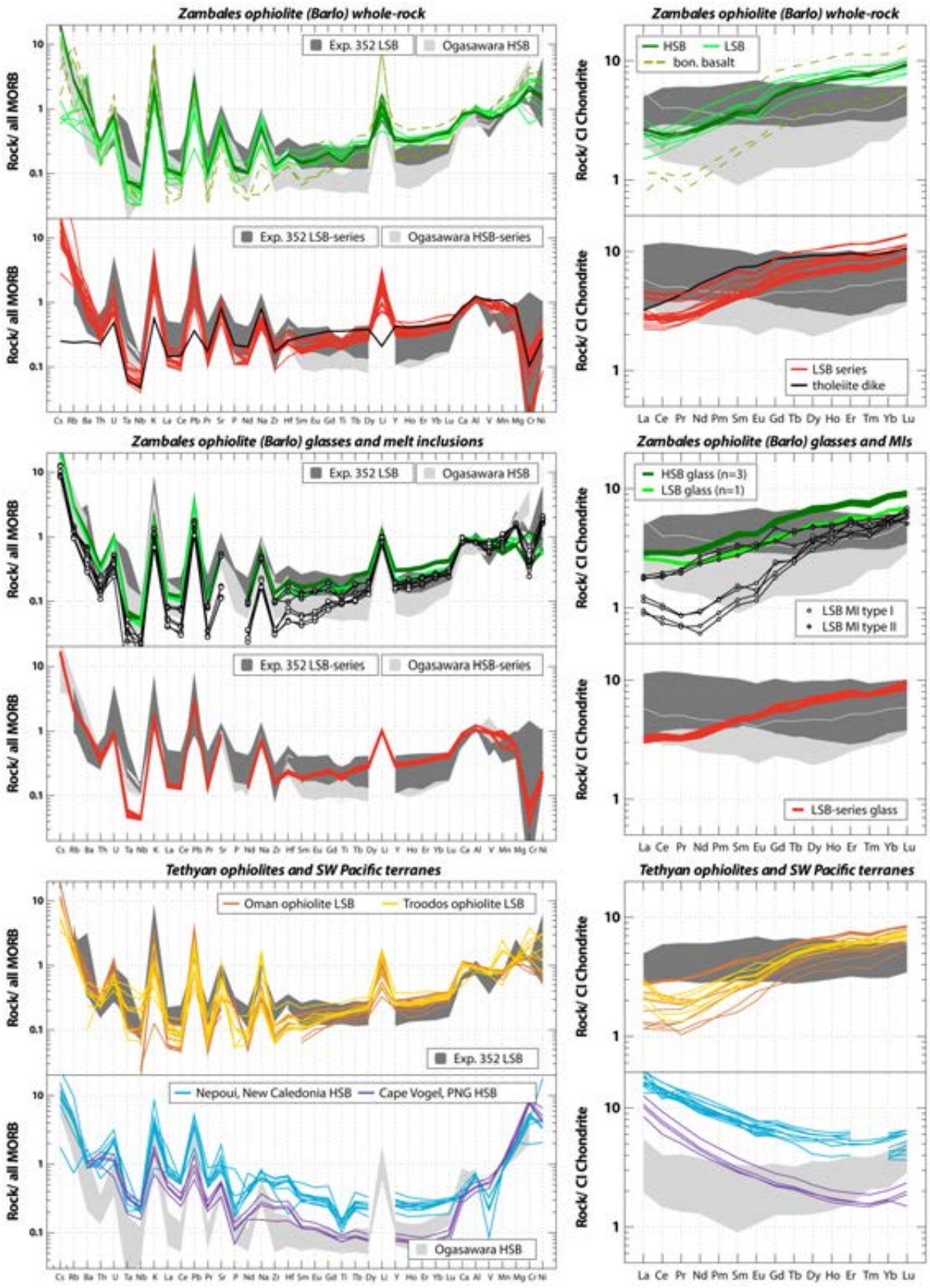

Figure 9. Extended MORB and chondrite normalized trace element patterns. Normalizing values are from Barrat et al. (2012) and Gale et al. (2013).

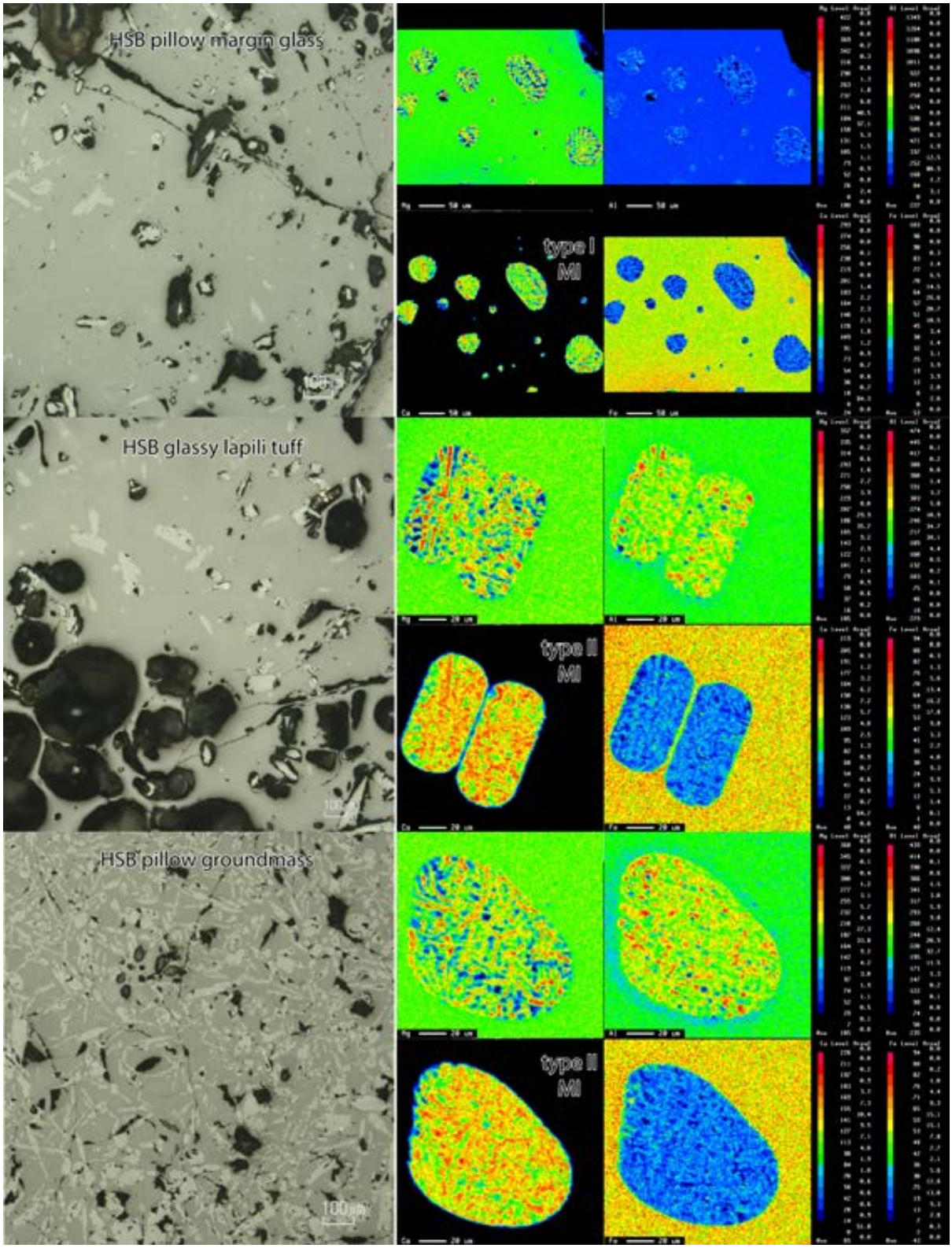

Figure 10. (Left) Reflected light microphotographs of Zambales boninitic glasses. (RIght) EPMA Mg-Al-Ca-Fe elemental maps of Zambales spinel-hosted melt inclusions. Most of the inclusions consist of variolitic pyroxene crystals, glass and vesicles.

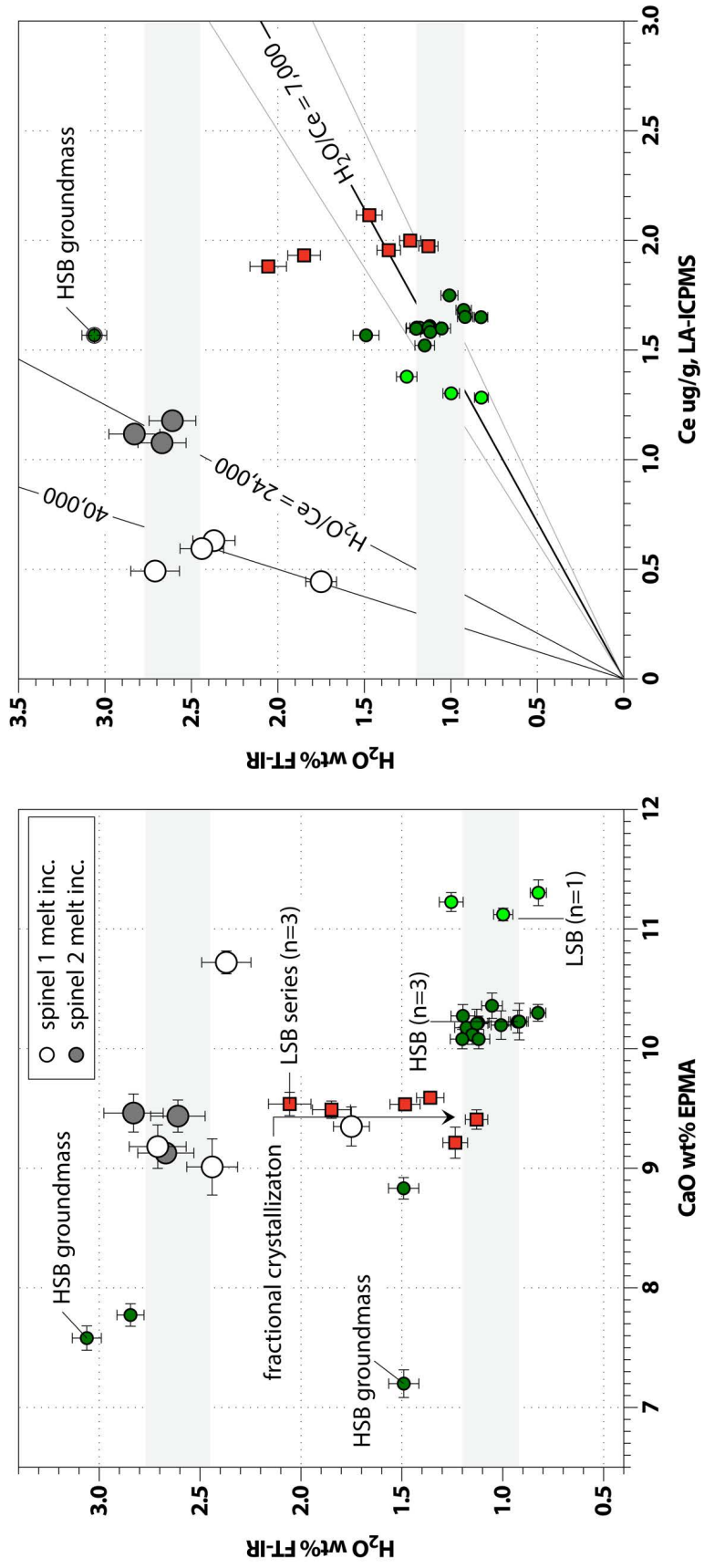

Figure 11. Water contents of Zambales boninitic glasses and melt inclusions. H_2O/Ce ratios of boninitic glasses and boninite series glasses vary within 7000±1000.

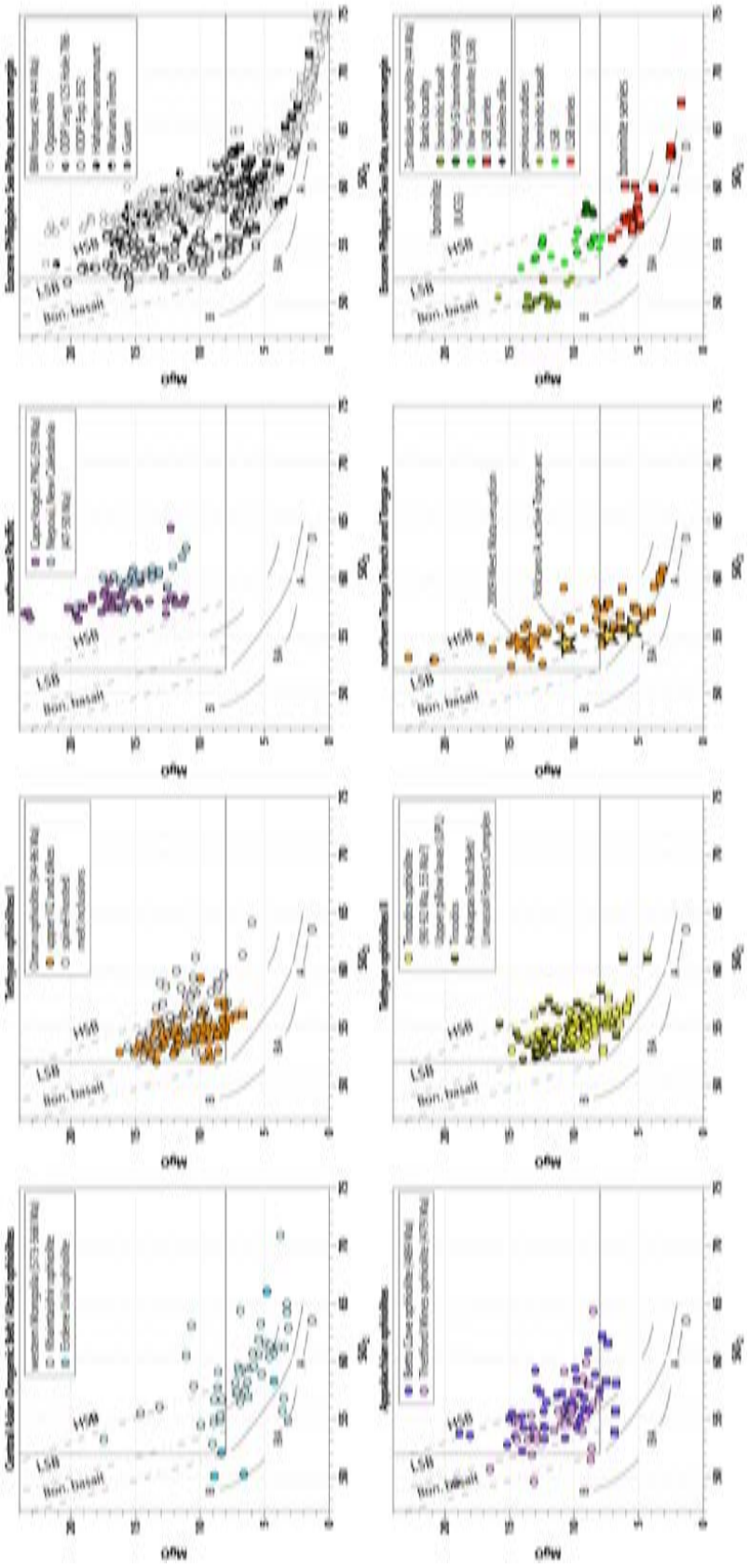

Figure 12. SiO_2-MgO systematics of worldwide boninite localities (Pre-Cambrian, Paleozoic, Mesozoic and Cenozoic ophiolites and terranes) using the proposed classification of Kanayama et al. (2013) and Reagan et al. (2017).

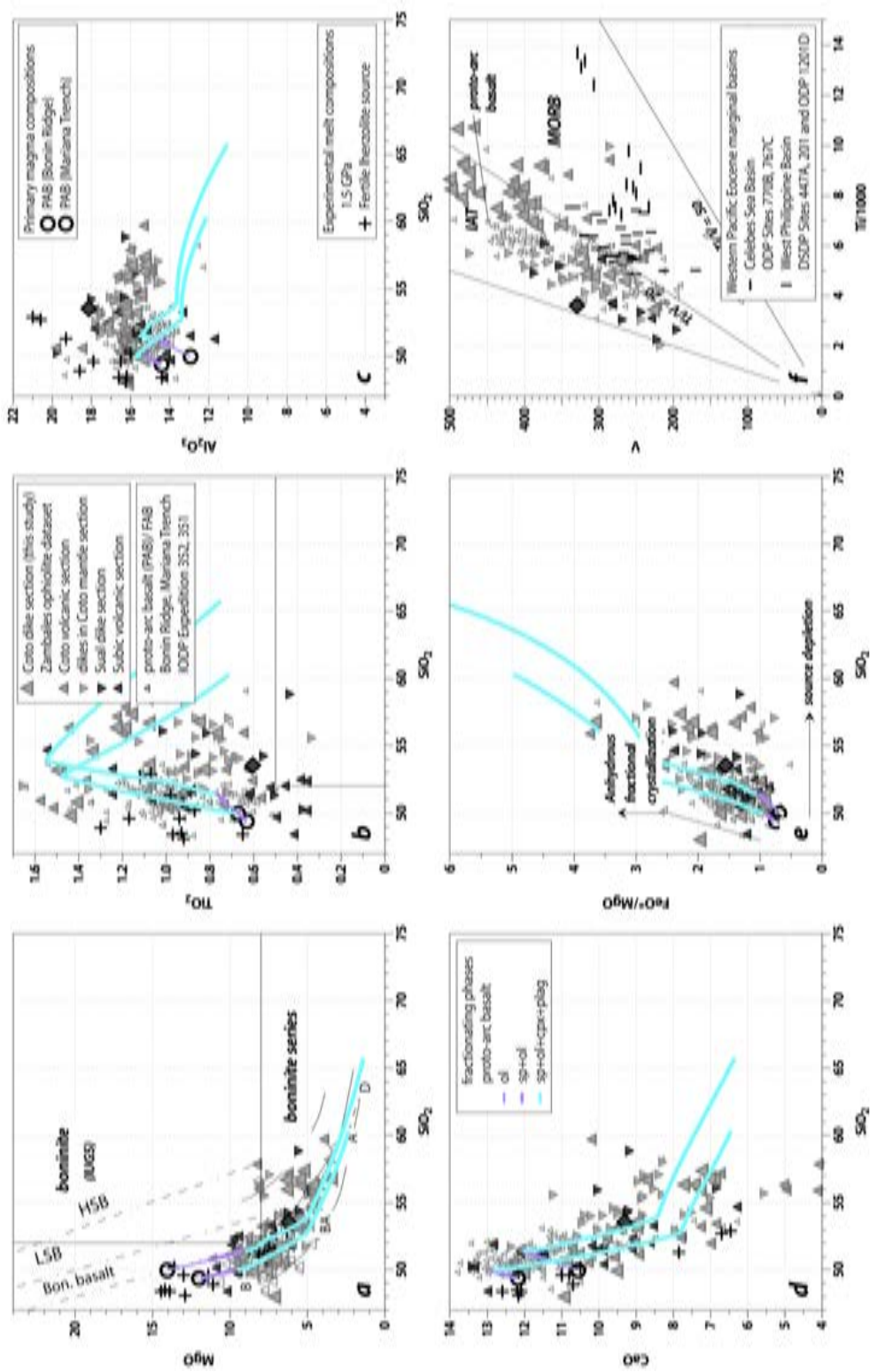

Figure 13. (a–e) MgO, TiO_2, FeO/MgO, CaO, Al_2O_3 vs. SiO_2 variation diagrams showing the distinct fractionation paths of proto-arc basalts compared to boninite and boninite-series volcanics. Fractional crystallization paths are modeled using rhyoliteMELTS v.1.2.0* (Ghiorso & Gualda, 2015) *at 1 kb pressure and initial fO_2 of FMQ+1.*

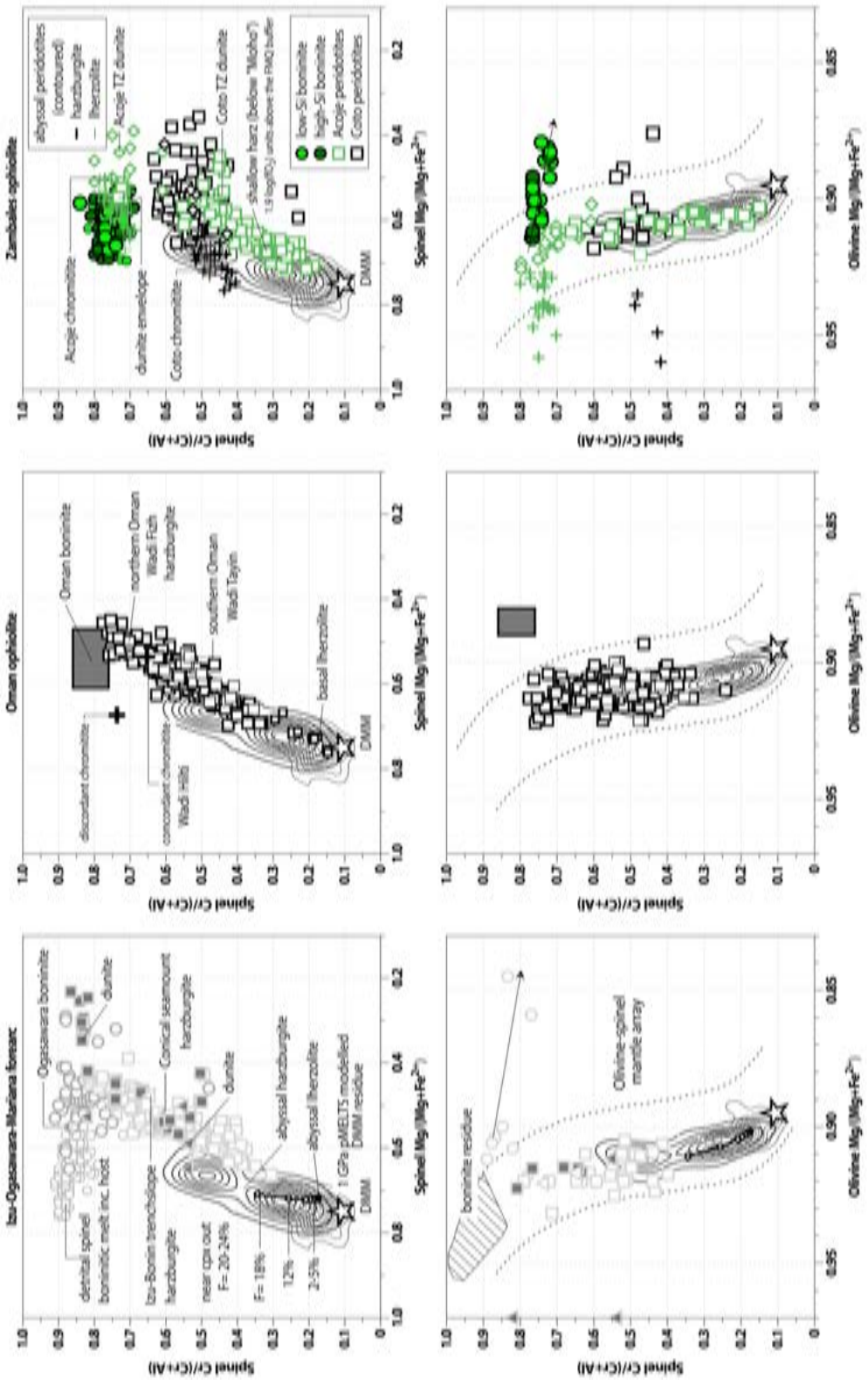

Figure 14. Spinel Cr#–spinel Mg# and olivine Fo–spinel Cr# systematics of residual peridotites from Zambales, Oman and the IBM forearc. Data sources are given in the text. Spinel Cr#s of fertile to moderately depleted residual peridotites from Acoje range from 0.18 to 0.56, coinciding with abyssal harzburgites.

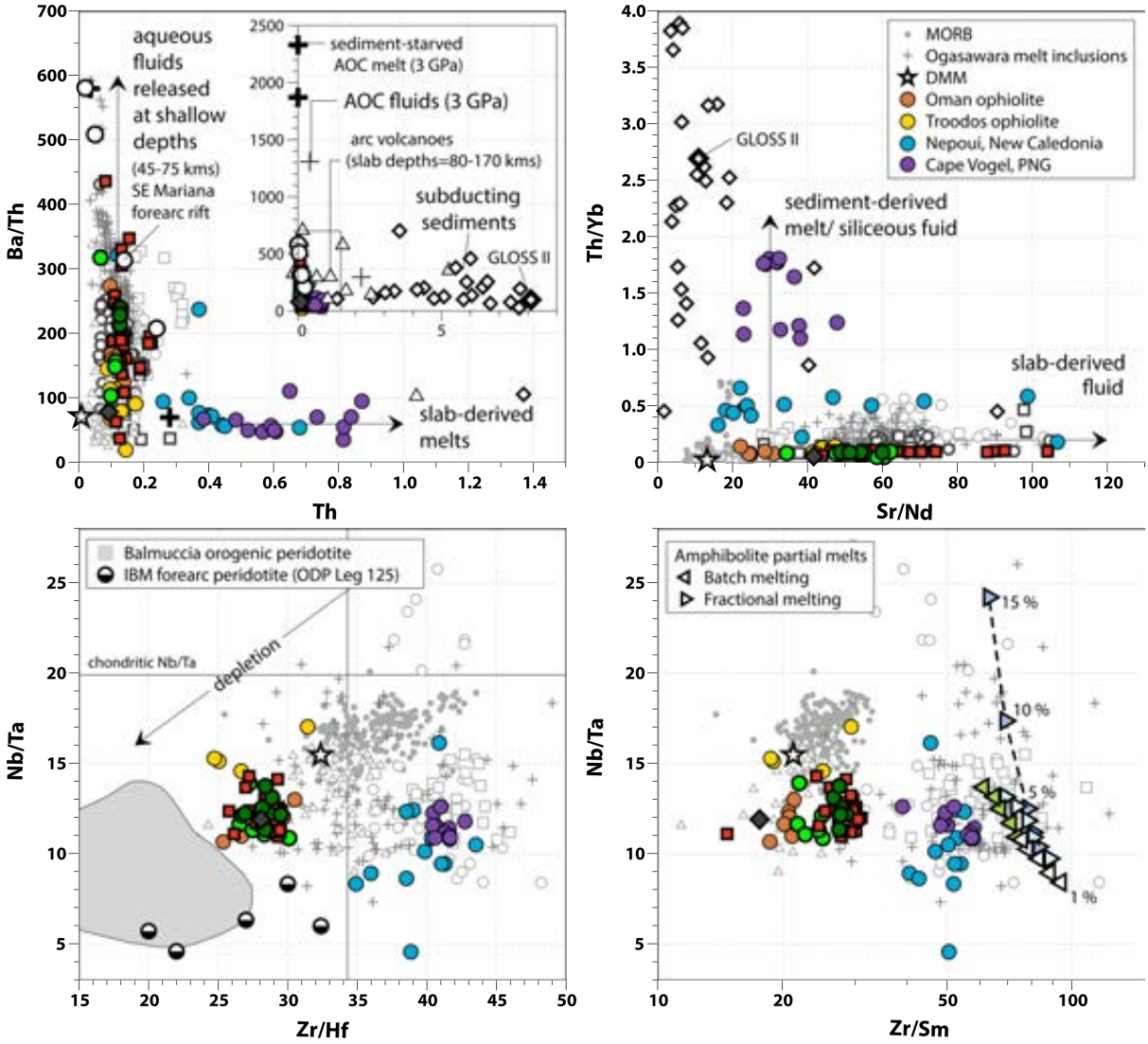

Figure 15. Trace element ratios discriminating the nature of slab-derived components in boninite and boninite-series volcanics. Zambales, Oman and Troodos boninites have distinct LILE and HFSE enrichments compared to Ogasawara, Cape Vogel and Nepoui. Data sources: Ogasawara spinel-hosted boninitic melt inclusions (Umino et al., 2018), altered oceanic crust (AOC) fluids, melts and sediments (Carter et al., 2015), aqueous fluids released at shallow depths (Ribeiro et al., 2015) *and subducting sediments and GLOSS II (Plank, 2014). Chondritic bulk Earth Nb/Ta and Zr/Hf ratios are from Münker et al. (2003). DMM and MORB compositions are from Jenner and O'Neill (2012) and Workman and Hart (2005), respectively. Symbols are the same as those in Fig. 8 except those shown in the diagram.*

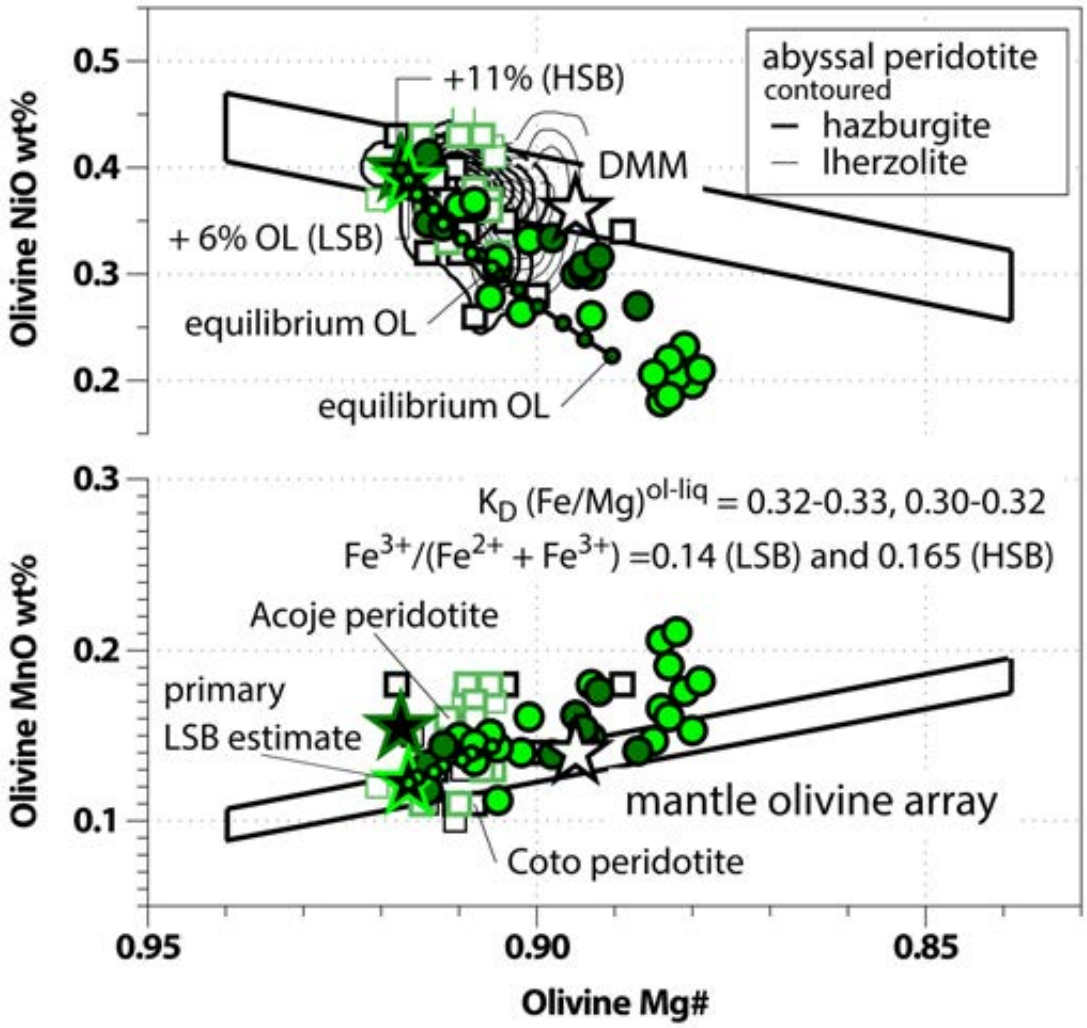

Figure 16. NiO and MnO contents of olivine in Zambales boninite. Small filled circles are hypothetical olivines in equilibrium with a liquid derived by olivine addition starting from an olivine in equilibrium with the original bulk-rock composition. Only Zambales LSB can satisfy both NiO and MnO equilibrium olivine fractionation paths.

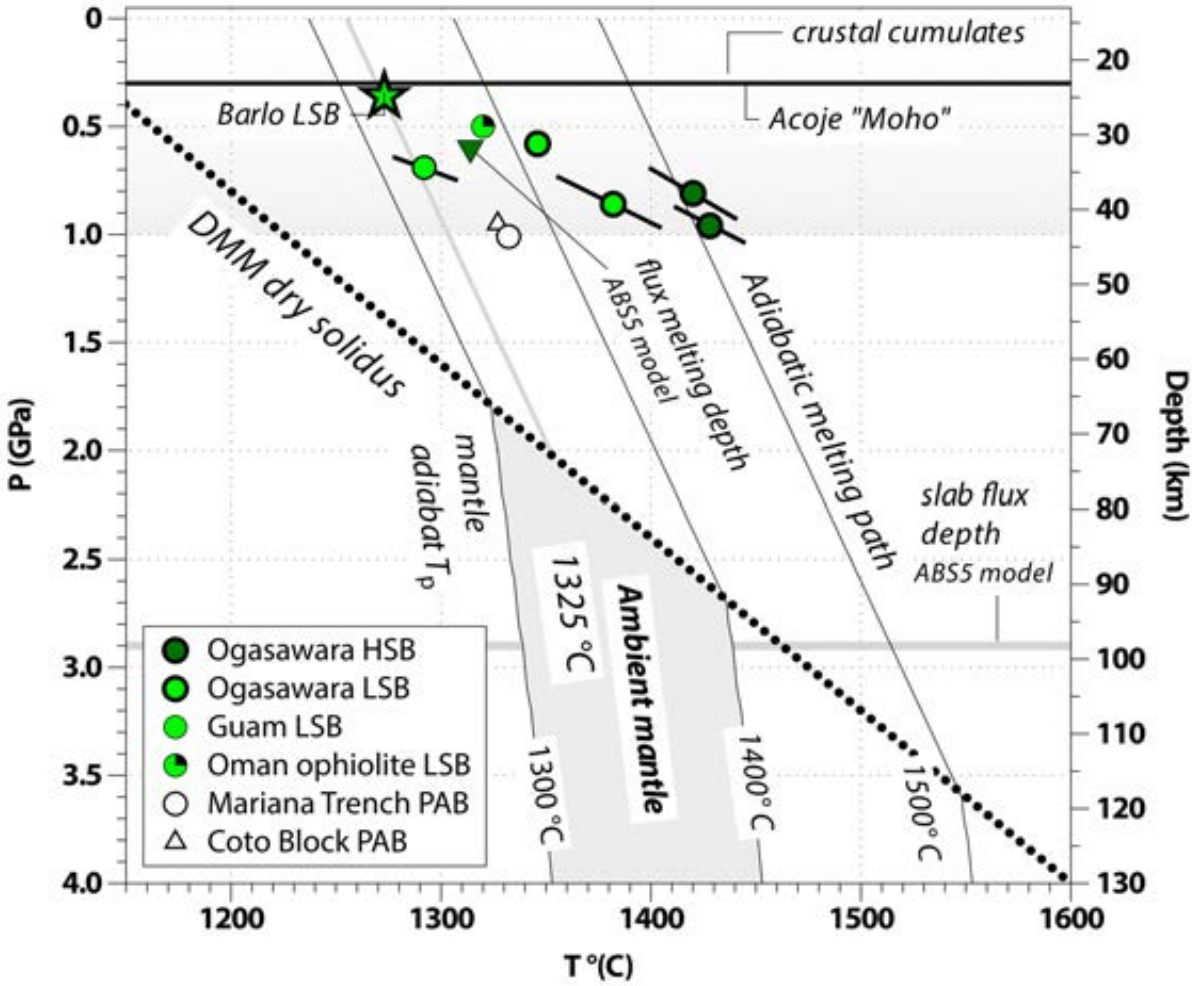

Figure 17. Pressure and temperature estimates of olivine and orthopyroxene saturation in boninites. Data sources: Umino et al. (2014, 2018) (filled circles) and this study (filled star). Boninites record shallow juvenile sub-arc melting conditions that are less than 1 GPa. Estimated depths of open-system mantle melting and slab flux generation for Izu boninites using Arc Basalt Simulator of Kimura (2017) are shown for comparison.

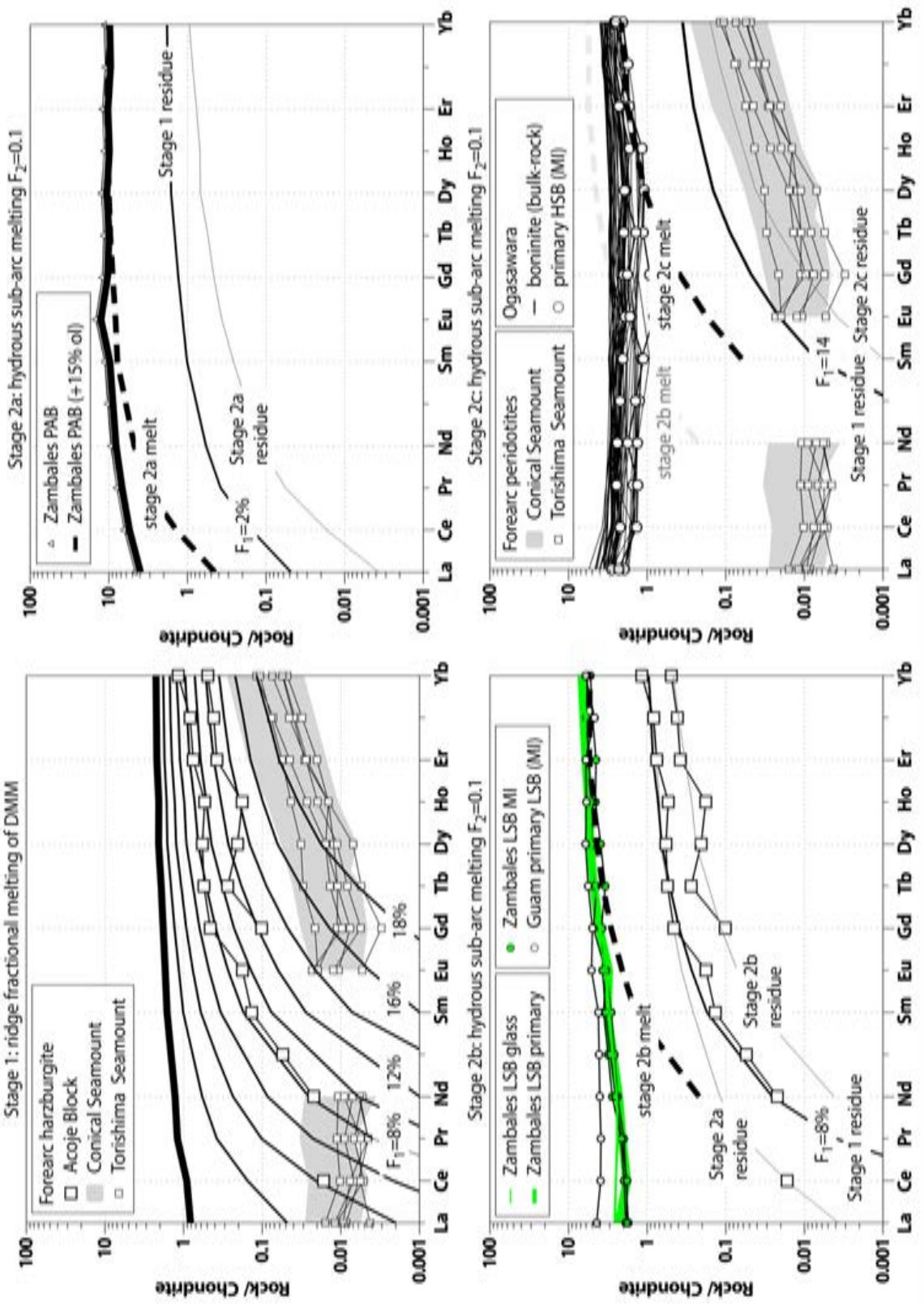

Figure 18. Second-stage hydrous batch melting models with DMM fractional melting residues as mantle wedge source.

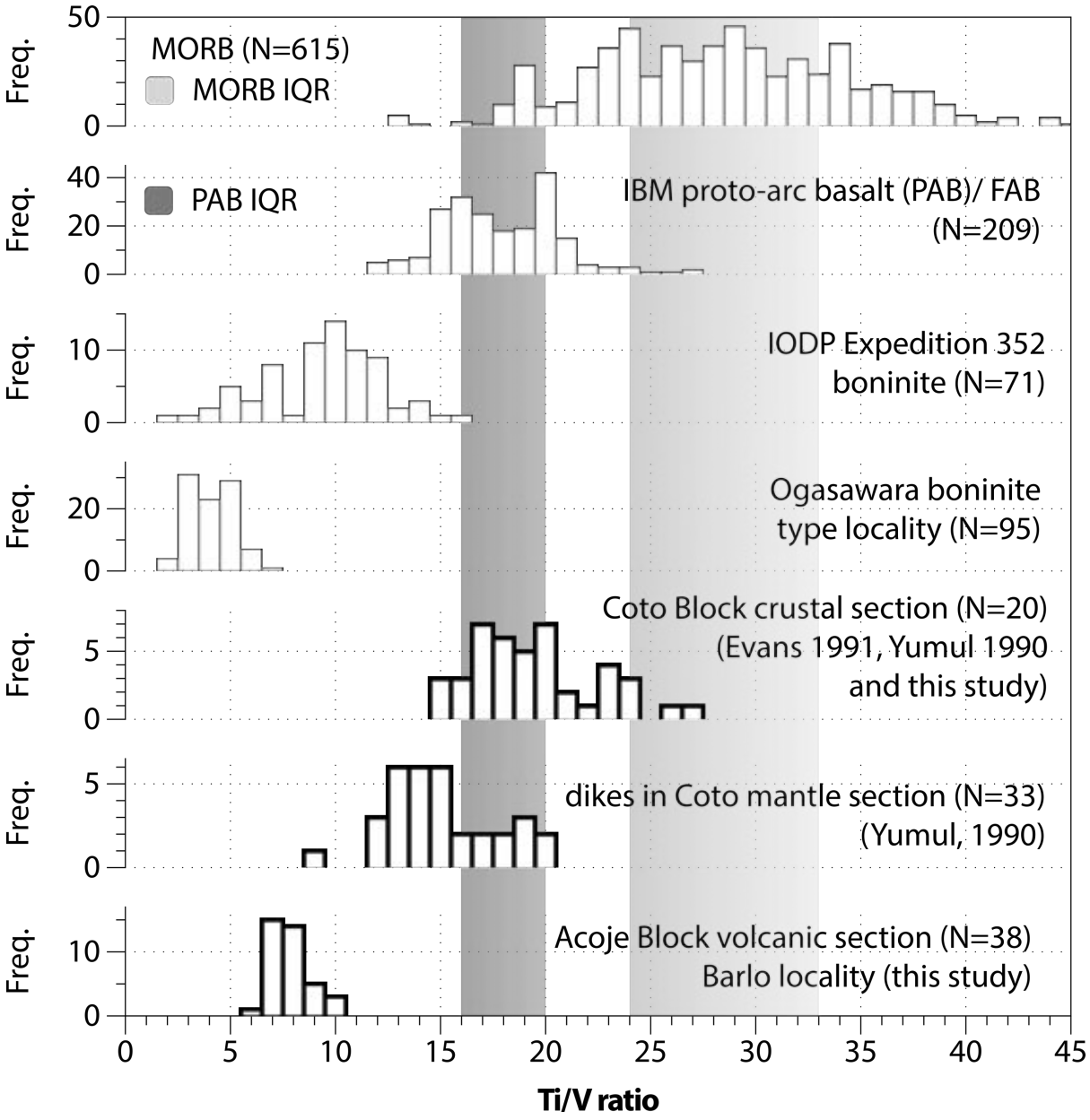

Figure 19. Temporal decrease in Ti/V ratios during incipient subduction exemplified by IBM and Zambales ophiolite proto-arc basalts and boninites that reflect progressive source oxidation by slab-derived fluids

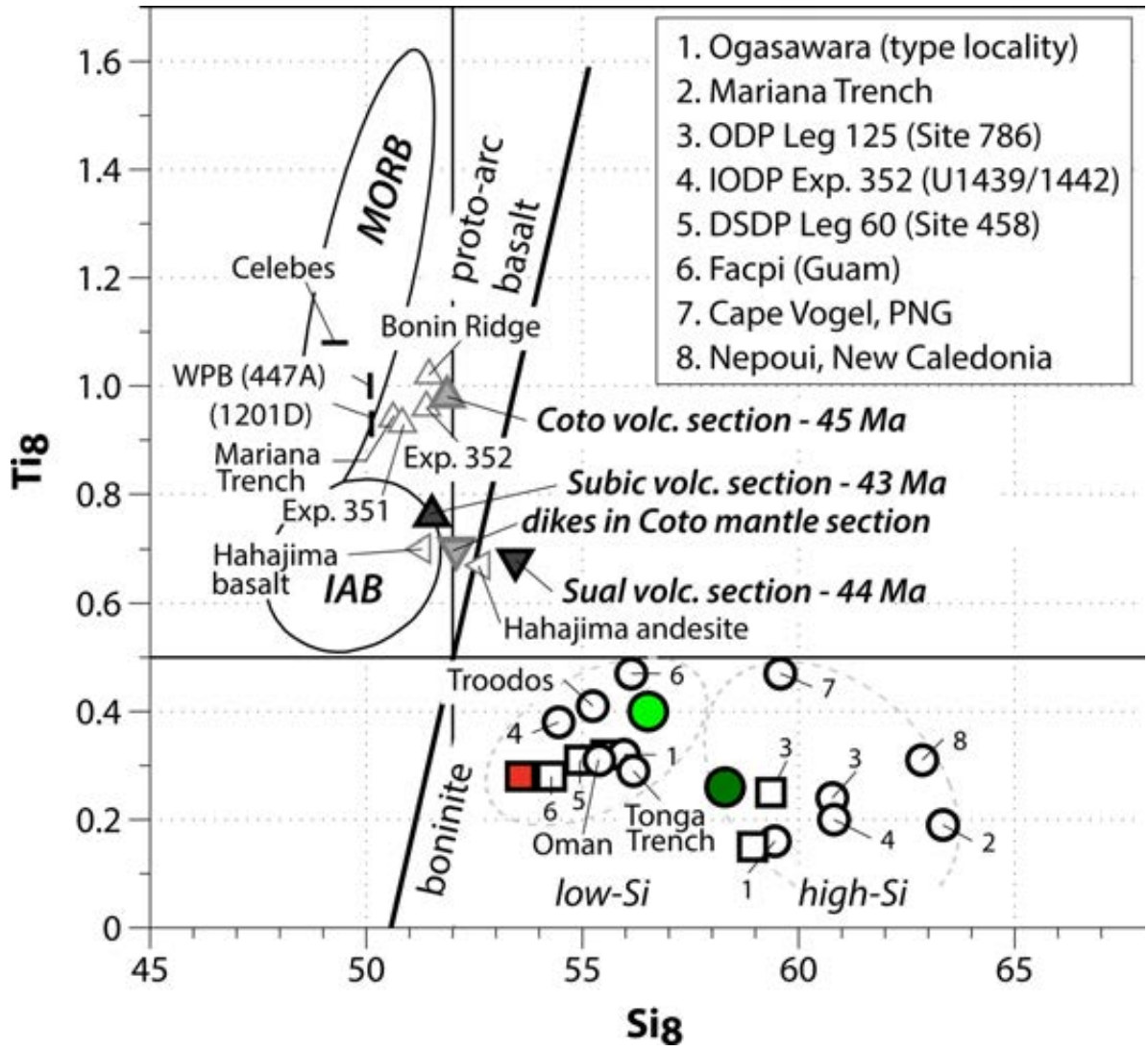

Figure 20. The 8 wt% MgO-normalized SiO2 (Si8) and TiO2 (Ti8) values of the crustal sections of Zambales ophiolite and IBM forearc showing temporal evolution from proto-arc basalt, boninite to arc tholeiite associated with subduction initiation. Also shown are Si8-Ti8 values of other notable boninite localities (Oman, Troodos, Tonga Trench). MORB and IAB fields are from Pearce and Robinson (2010). Data sources are given in the text. Symbols are the same as in Fig. 6 except those shown in the diagram.

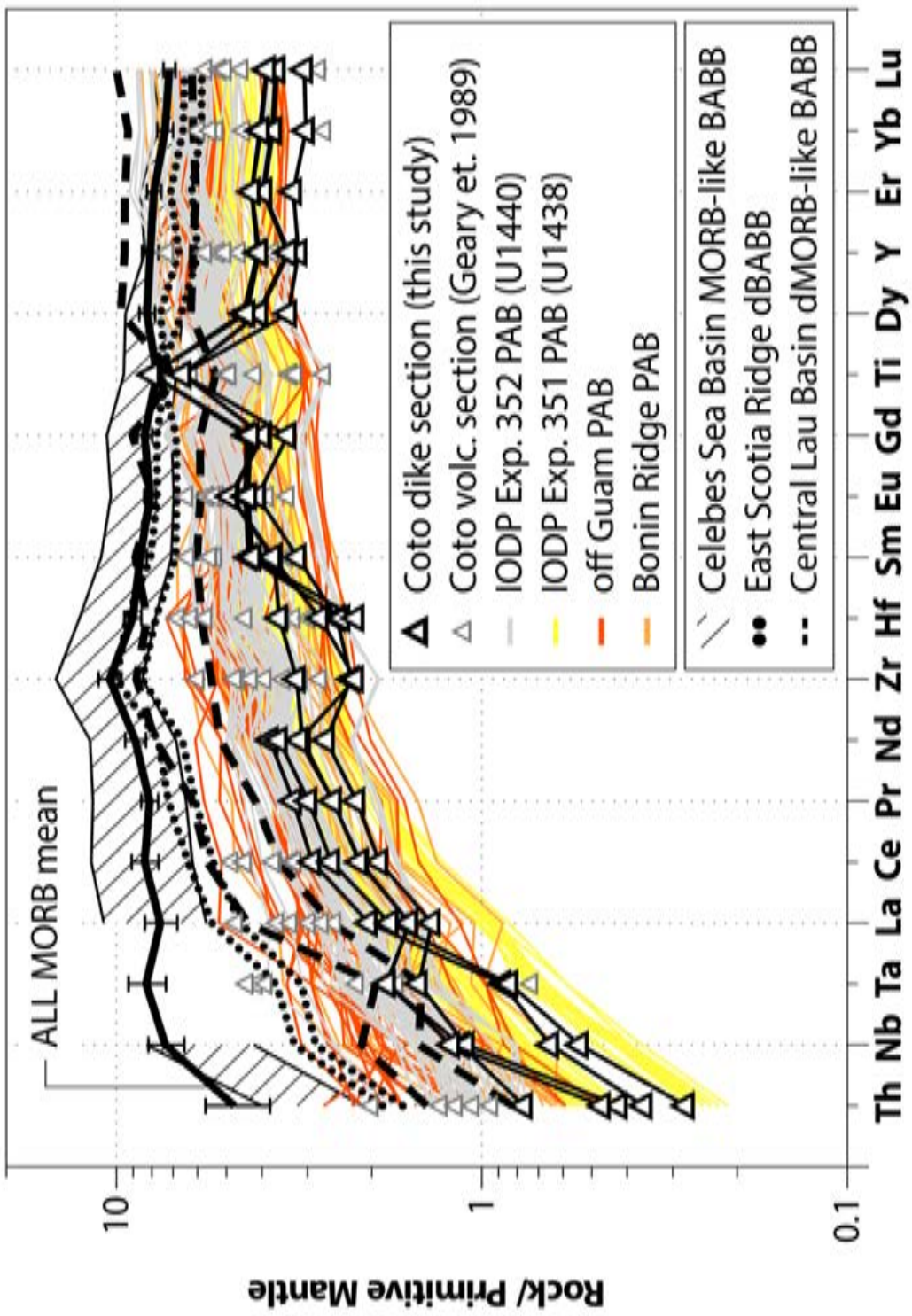

Figure 21. Primitive mantle normalized immobile element abundances of IBM proto-arc basalts (PAB) and Coto Block volcanics are similarly depleted compared to MORB. Data sources: IBM PAB (Haugen, 2017; Hickey-Vargas et al., 2018; Ishizuka et al., 2018; Reagan et al., 2010), MORB (Jenner & O'Neill, 2012), all MORB mean (Gale et al., 2013)*, Coto volcanic section (Geary et al., 1989 and this study) and Celebes Sea Basin* (Spadea et al., 1996)*.*

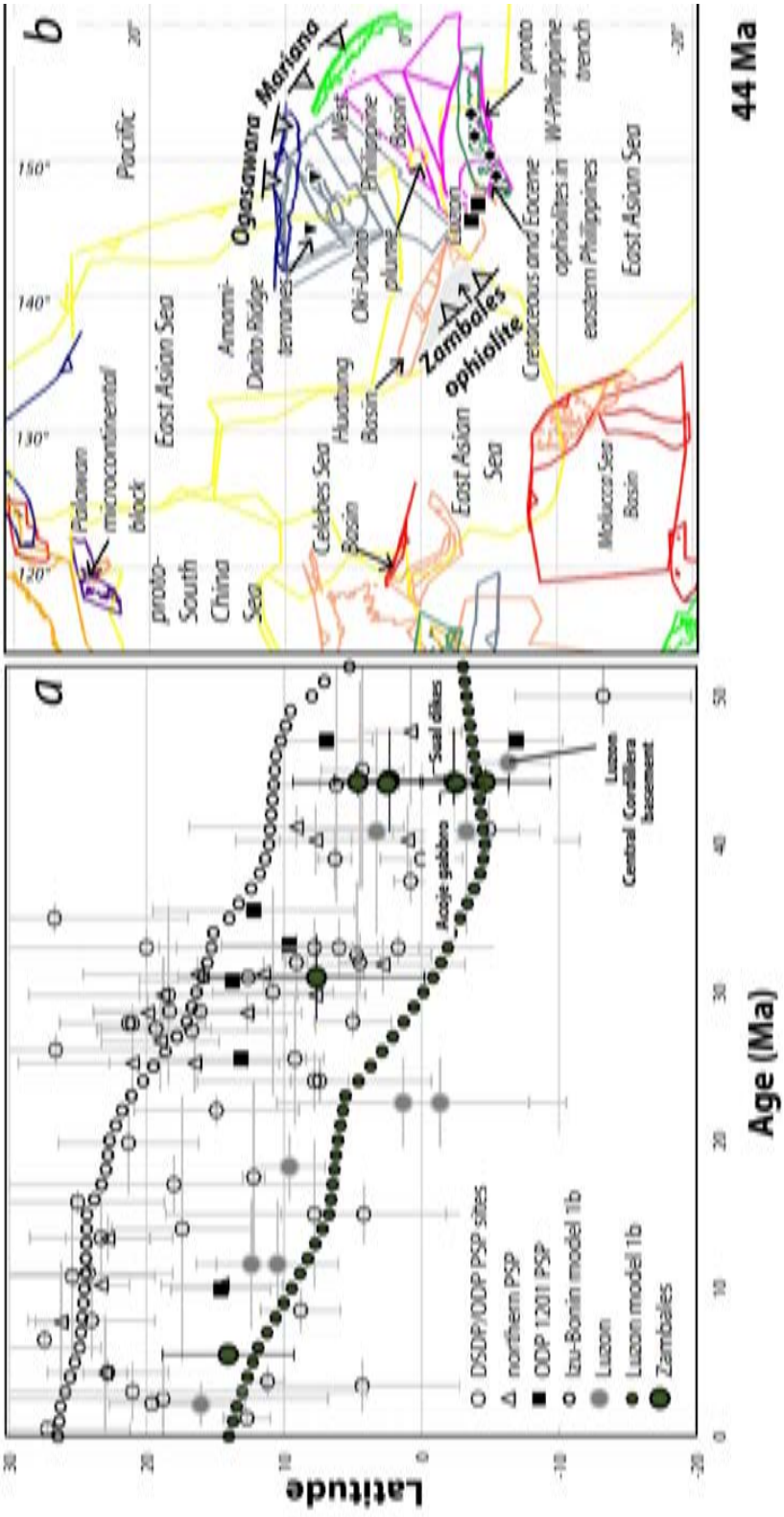

Figure 22. Paleolatitudes derived from Philippine Sea plate, Luzon and Zambales inclination data (Fuller et al., 1991; Hall et al., 1995; Queano et al., 2007; Queaño et al., 2009; Richter & Ali, 2015). (b) Tectonic reconstruction of the western Pacific region at 44Ma using GPlates (Boyden et al., 2011) *and unfolded slab data, plate polygons and the rotation files (model 1b) of Wu et al. (2016). Inverted triangles, diamonds and squares previously shown in Fig. 1b. refer to Cretaceous arc terranes in the northern Philippine Sea plate and Cretaceous–Eocene ophiolites in eastern Philippines, respectively.*

12.Tables

Table 1. Representative mineral compositions of constituent mineral phases (olivine, pyroxene, spinel) in Zambales boninite.

Table 1a. Representative microprobe analyses of olivine in Zambales boninite

Sample	ZM2-107-spot1-ol1	ZM2-107-spot1-2	ZM2-107-spot2-ol2	ZM2-107-spot4-ol1	ZM2-107-spot5-ol1A	ZM2-107-spot5-ol1B	ZM2-107-spot6-ol3	ZM2-107-spot7-ol3	ZM2-107-spot8-ol2	ZM2-107-spot8-ol3	ZM2-100A spot5 ol1	ZM2-100A spot5 ol1	ZM2-100A spot6 ol1	ZM2-100A spot6 ol1	ZM2-100A spot6 ol1	ZM2-100A spot6 ol2	ZM2-100A spot6 ol4
SiO_2	41.10	41.05	41.43	41.01	41.31	41.24	41.13	41.49	41.00	40.90	40.58	40.25	40.79	39.32	40.68	40.83	40.69
FeO	10.61	11.45	9.75	11.72	9.47	9.14	11.39	9.78	11.44	11.18	8.61	11.24	8.72	10.63	10.56	10.28	10.67
MnO	0.18	0.17	0.14	0.18	0.14	0.14	0.21	0.16	0.19	0.15	0.12	0.14	0.14	0.15	0.15	0.14	0.18
MgO	49.52	48.96	50.12	48.71	50.51	50.77	48.85	49.78	48.57	48.51	51.38	49.61	50.61	49.79	50.07	50.97	49.38
CaO	0.11	0.14	0.11	0.12	0.11	0.11	0.13	0.10	0.12	0.11	0.16	0.17	0.15	0.17	0.16	0.17	0.17
NiO	0.26	0.18	0.26	0.23	0.31	0.36	0.20	0.33	0.22	0.21	0.41	0.27	0.35	0.30	0.30	0.33	0.32
Total	101.86	101.96	101.85	102.00	101.90	101.79	101.94	101.70	101.54	101.08	101.35	101.79	100.83	100.40	101.98	102.81	101.43
Mg#	0.89	0.88	0.90	0.88	0.90	0.91	0.88	0.90	0.88	0.89	0.91	0.89	0.91	0.89	0.89	0.90	0.89
Cations (based on 4.0 oxygens)																	
Si	0.994	0.994	0.997	0.994	0.993	0.992	0.996	1.000	0.997	0.998	0.980	0.979	0.989	0.969	0.984	0.978	0.989
Fe	0.215	0.232	0.196	0.238	0.190	0.184	0.231	0.197	0.233	0.228	0.174	0.229	0.177	0.219	0.213	0.206	0.217
Mn	0.004	0.003	0.003	0.004	0.003	0.003	0.004	0.003	0.004	0.003	0.002	0.003	0.003	0.003	0.003	0.003	0.004
Mg	1.785	1.768	1.798	1.761	1.810	1.820	1.764	1.789	1.761	1.765	1.849	1.798	1.829	1.829	1.805	1.821	1.789
Ca	0.003	0.004	0.003	0.003	0.003	0.003	0.003	0.003	0.003	0.003	0.004	0.004	0.004	0.004	0.004	0.004	0.004
Ni	0.005	0.004	0.005	0.005	0.006	0.007	0.004	0.006	0.004	0.004	0.008	0.005	0.007	0.006	0.006	0.006	0.006
Total	3.007	3.005	3.003	3.005	3.007	3.008	3.003	3.000	3.003	3.002	3.020	3.020	3.010	3.031	3.016	3.021	3.010

Table 1b. Representative microprobe analyses of pyroxene in Zambales boninite

	B-7-11								
Sample	spot1-opx2	spot2-opx4	spot4-opx	spot6-opx2	spot8-opx2	spot9-opxB	spot9-opxC	spot10-opx1	spot11-opx3
Comment	opx mp	opx mp	opx mp	opx mp	opx mp	opx mp	opx mp	opx mp	opx mp
SiO_2	57.08	57.11	57.14	57.53	56.99	57.47	56.91	56.45	57.24
TiO_2	0.05	0.05	0.02	0.03	0.05	0.03	0.00	0.04	0.04
Al_2O_3	1.05	1.34	1.27	0.65	1.32	0.74	0.44	1.62	0.93
Cr_2O_3	0.34	0.71	0.51	0.40	0.63	0.26	0.11	0.82	0.60
FeO*	8.65	7.97	8.48	8.49	8.18	8.71	9.64	7.60	7.94
MnO	0.20	0.22	0.19	0.20	0.21	0.22	0.27	0.21	0.19
MgO	31.29	31.62	31.35	31.95	31.90	31.52	30.19	32.04	32.49
CaO	1.79	1.72	1.88	1.56	1.57	1.69	2.50	1.55	1.42
Na_2O	0.02	0.02	0.03	0.00	0.01	0.00	0.02	0.02	0.00
K_2O	0.00	0.01	0.01	0.00	0.00	0.00	0.00	0.01	0.00
NiO	0.06	0.05	0.04	0.08	0.07	0.07	0.02	0.09	0.08
Total	100.52	100.81	100.92	100.89	100.93	100.69	100.12	100.43	100.92
Mg#	0.87	0.88	0.87	0.87	0.87	0.87	0.85	0.88	0.88
Wo	3.44	3.31	3.61	2.97	2.99	3.23	4.81	2.97	2.69
En	83.60	84.71	83.70	84.44	84.80	83.78	80.73	85.64	85.58
Fs	12.96	11.98	12.70	12.59	12.20	12.99	14.46	11.39	11.73
Cations (based on 6.0 oxygens)									
Si	1.985	1.976	1.979	1.991	1.971	1.994	2.000	1.960	1.977
Ti	0.001	0.001	0.000	0.001	0.001	0.001	0.000	0.001	0.001
Al(4)									
Al(6)	0.043	0.055	0.052	0.026	0.054	0.030	0.018	0.066	0.038
Cr	0.009	0.019	0.014	0.011	0.017	0.007	0.003	0.022	0.016
Fe	0.251	0.231	0.246	0.246	0.237	0.253	0.283	0.220	0.229
Mn	0.006	0.007	0.006	0.006	0.006	0.006	0.008	0.006	0.006
Mg	1.622	1.631	1.619	1.649	1.645	1.630	1.581	1.658	1.673
Ca	0.067	0.064	0.070	0.058	0.058	0.063	0.094	0.058	0.053
Na	0.001	0.001	0.002	0.000	0.001	0.000	0.002	0.001	0.000
Ni	0.002	0.001	0.001	0.002	0.002	0.002	0.001	0.003	0.002
Total	3.988	3.986	3.989	3.990	3.992	3.987	3.990	3.996	3.995

mp-microphenocryst

	B-5-7								
Sample	spot2 opx2	spot4 opx2	spot5 opx4	spot6 opx1	spot6 opx2	spot7 opx1	spot7 opx7	spot9 opx2	spot1
Comment	opx mp	opx mp	opx mp	opx mp	opx mp	opx mp	opx mp	opx mp	opx mp
SiO_2	56.34	56.49	56.13	56.27	56.34	55.74	56.13	55.54	56.11
TiO_2	0.02	0.04	0.02	0.02	0.03	0.02	0.04	0.05	0.02
Al_2O_3	0.99	1.06	1.49	1.30	1.25	1.26	1.44	1.32	0.87
Cr_2O_3	0.45	0.65	0.93	0.55	0.76	0.50	0.68	0.56	0.42
FeO*	8.03	7.48	7.26	8.39	7.50	8.50	8.27	8.51	8.61
MnO	0.18	0.19	0.17	0.23	0.18	0.20	0.20	0.20	0.23
MgO	32.18	32.99	32.81	31.85	32.59	31.64	32.02	31.69	32.41
CaO	2.30	2.01	1.79	1.97	2.07	2.49	1.99	2.58	2.01
Na_2O	0.02	0.02	0.03	0.04	0.03	0.01	0.03	0.00	0.03
K_2O	0.00	0.00	0.00	0.00	0.00	0.00	0.01	0.00	0.00
NiO	0.06	0.06	0.07	0.07	0.07	0.07	0.07	0.08	0.06
Total	100.57	100.98	100.70	100.69	100.81	100.42	100.86	100.53	100.78
Mg#	0.88	0.89	0.89	0.87	0.89	0.87	0.87	0.87	0.87
Wo	4.31	3.73	3.38	3.72	3.89	4.69	3.76	4.84	3.74
En	83.93	85.41	85.96	83.88	85.13	82.83	84.07	82.70	83.78
Fs	11.75	10.86	10.67	12.40	10.98	12.48	12.18	12.46	12.48
Cations (based on 6.0 oxygens)									
Si	1.961	1.954	1.945	1.958	1.953	1.950	1.950	1.943	1.955
Ti	0.001	0.001	0.000	0.000	0.001	0.000	0.001	0.001	0.001
Al(4)									
Al(6)	0.041	0.043	0.061	0.053	0.051	0.052	0.059	0.054	0.036
Cr	0.012	0.018	0.025	0.015	0.021	0.014	0.019	0.015	0.012
Fe	0.234	0.216	0.210	0.244	0.217	0.249	0.240	0.249	0.251
Mn	0.005	0.005	0.005	0.007	0.005	0.006	0.006	0.006	0.007
Mg	1.670	1.701	1.695	1.652	1.683	1.650	1.658	1.653	1.683
Ca	0.086	0.074	0.067	0.073	0.077	0.093	0.074	0.097	0.075
Na	0.001	0.001	0.002	0.003	0.002	0.001	0.002	0.000	0.002
Ni	0.002	0.002	0.002	0.002	0.002	0.002	0.002	0.002	0.002
Total	4.012	4.015	4.012	4.009	4.012	4.017	4.011	4.021	4.022

	ZM2-100A												
Sample	spot1	spot1	spot2	spot4	spot6	spot7	spot7	spot9	spot9	spot2	spot2	spot2	spot4
	opx mp	opx mp	opx mp	opx mp	opx mp	opx mp	opx mp	opx mp	opx mp	zoned opx core	zoned opx rim	zoned opx rim	spongy opx core
SiO_2	56.52	55.63	56.31	55.76	56.05	56.31	55.22	56.53	55.60	54.23	56.10	56.63	53.28
TiO_2	0.03	0.04	0.04	0.02	0.03	0.00	0.05	0.03	0.01	0.12	0.05	0.03	0.20
Al_2O_3	1.23	1.09	1.00	1.30	1.18	1.16	1.48	0.87	0.95	1.30	1.57	0.67	1.22
Cr_2O_3	0.47	0.34	0.49	0.69	0.61	0.44	0.60	0.46	0.59	0.05	0.55	0.19	0.00
FeO*	8.04	9.40	8.25	8.29	8.40	8.46	8.85	8.37	8.11	17.81	8.55	9.05	19.98
MnO	0.17	0.22	0.24	0.24	0.19	0.21	0.24	0.22	0.19	0.40	0.20	0.27	0.39
MgO	32.06	31.51	32.30	32.06	31.34	32.22	31.11	32.40	31.93	25.56	31.52	32.05	24.19
CaO	2.25	2.12	2.05	2.32	2.55	2.07	2.59	1.96	2.00	1.75	2.01	2.27	1.63
Na_2O	0.03	0.00	0.00	0.00	0.01	0.01	0.05	0.00	0.01	0.03	0.03	0.01	0.03
K_2O	0.01	0.00	0.01	0.00	0.00	0.01	0.00	0.00	0.00	0.01	0.00	0.00	0.00
NiO	0.07	0.05	0.08	0.10	0.05	0.07	0.08	0.06	0.06	0.03	0.05	0.05	0.01
Total	100.87	100.41	100.77	100.79	100.41	100.98	100.26	100.88	99.45	101.29	100.64	101.23	100.94
Mg#	0.88	0.86	0.87	0.87	0.87	0.87	0.86	0.87	0.88	0.72	0.87	0.86	0.68
Wo	4.23	3.98	3.84	4.35	4.84	3.87	4.91	3.66	3.79	3.42	3.83	4.21	3.21
En	83.96	82.25	84.11	83.53	82.73	83.79	82.00	84.15	84.21	69.44	83.47	82.69	66.14
Fs	11.81	13.77	12.05	12.12	12.44	12.34	13.09	12.19	12.00	27.13	12.71	13.09	30.65
Cations (based on 6.0 oxygens)													
Si	1.961	1.952	1.958	1.943	1.959	1.955	1.941	1.963	1.958	1.957	1.954	1.967	1.950
Ti	0.001	0.001	0.001	0.001	0.001	0.000	0.001	0.001	0.000	0.003	0.001	0.001	0.006
Al(4)													
Al(6)	0.050	0.045	0.041	0.053	0.048	0.048	0.061	0.035	0.039	0.055	0.064	0.028	0.053
Cr	0.013	0.009	0.013	0.019	0.017	0.012	0.017	0.013	0.016	0.002	0.015	0.005	0.000
Fe	0.233	0.276	0.240	0.242	0.246	0.246	0.260	0.243	0.239	0.537	0.249	0.263	0.612
Mn	0.005	0.007	0.007	0.007	0.006	0.006	0.007	0.006	0.006	0.012	0.006	0.008	0.012
Mg	1.658	1.648	1.675	1.666	1.633	1.668	1.630	1.677	1.677	1.375	1.637	1.659	1.320
Ca	0.083	0.080	0.076	0.087	0.095	0.077	0.098	0.073	0.075	0.068	0.075	0.085	0.064
Na	0.002	0.000	0.000	0.000	0.001	0.001	0.003	0.000	0.001	0.002	0.002	0.001	0.002
Ni	0.002	0.001	0.002	0.003	0.001	0.002	0.002	0.002	0.002	0.001	0.001	0.002	0.000
Total	4.008	4.020	4.014	4.020	4.008	4.016	4.020	4.013	4.014	4.013	4.006	4.017	4.019

ZM2-100A													
Sample	spot7	spot8	spot8	spot8	spot8	spot3	spot3	spot3	spot3	sp2-	spot1	spot2	spot3
Comment	spot4 opx3 rim spongy	zoned spongy opx rim	zoned opx core	zoned opx rim	zoned opx rim	zoned opx rim	zoned opx core	zoned opx rim	zoned opx rim	zoned opx rim	augite rim	augite rim	augite rim
SiO_2	56.54	56.83	54.92	56.52	56.44	56.10	56.47	56.90	56.91	56.61	54.67	50.60	49.32
TiO_2	0.04	0.03	0.07	0.02	0.03	0.03	0.04	0.01	0.01	0.03	0.14	0.36	0.34
Al_2O_3	1.19	0.36	1.54	1.18	1.23	1.09	0.63	0.69	0.87	0.85	3.01	6.08	6.90
Cr_2O_3	0.51	0.15	0.09	0.37	0.41	0.41	0.16	0.26	0.30	0.38	0.13	0.00	0.00
FeO*	8.18	9.70	14.90	8.77	8.91	8.52	9.52	9.11	8.72	8.70	7.98	8.38	9.27
MnO	0.20	0.30	0.33	0.22	0.23	0.24	0.28	0.23	0.18	0.21	0.21	0.19	0.20
MgO	32.63	31.06	27.94	32.30	32.11	32.21	32.00	32.00	32.18	32.21	22.76	15.81	15.22
CaO	2.11	2.71	1.51	2.01	2.03	2.03	1.95	2.18	2.09	2.07	9.60	18.90	18.59
Na_2O	0.00	0.02	0.01	0.01	0.01	0.03	0.05	0.04	0.01	0.00	0.09	0.13	0.11
K_2O	0.01	0.00	0.00	0.01	0.00	0.01	0.01	0.01	0.00	0.01	0.00	0.01	0.00
NiO	0.08	0.08	0.03	0.05	0.04	0.06	0.08	0.06	0.09	0.07	0.03	0.05	0.02
Total	101.49	101.24	101.33	101.45	101.43	100.72	101.18	101.49	101.35	101.14	98.62	100.49	99.98
Mg#	0.88	0.85	0.77	0.87	0.87	0.87	0.86	0.86	0.87	0.87	0.84	0.77	0.75
Wo	3.92	5.07	2.90	3.73	3.77	3.79	3.62	4.05	3.89	3.86	20.22	39.84	39.54
En	84.24	80.78	74.73	83.55	83.27	83.79	82.60	82.73	83.43	83.49	66.66	46.38	45.06
Fs	11.84	14.15	22.37	12.72	12.95	12.43	13.78	13.22	12.68	12.66	13.12	13.79	15.40
Cations (based on 6.0 oxygens)													
Si	1.952	1.981	1.952	1.955	1.954	1.954	1.965	1.970	1.969	1.964	1.974	1.855	1.827
Ti	0.001	0.001	0.002	0.001	0.001	0.001	0.001	0.000	0.000	0.001	0.004	0.010	0.009
Al(4)											0.128	0.263	0.301
Al(6)	0.048	0.015	0.065	0.048	0.050	0.045	0.026	0.028	0.035	0.035			
Cr	0.014	0.004	0.003	0.010	0.011	0.011	0.004	0.007	0.008	0.010	0.004	0.000	0.000
Fe	0.236	0.283	0.443	0.254	0.258	0.248	0.277	0.264	0.252	0.252	0.241	0.257	0.287
Mn	0.006	0.009	0.010	0.006	0.007	0.007	0.008	0.007	0.005	0.006	0.007	0.006	0.006
Mg	1.679	1.614	1.480	1.665	1.657	1.673	1.660	1.652	1.659	1.665	1.225	0.864	0.840
Ca	0.078	0.101	0.057	0.074	0.075	0.076	0.073	0.081	0.077	0.077	0.371	0.742	0.738
Na	0.000	0.001	0.001	0.001	0.001	0.002	0.003	0.003	0.001	0.000	0.006	0.009	0.008
Ni	0.002	0.002	0.001	0.001	0.001	0.002	0.002	0.002	0.003	0.002	0.001	0.001	0.001
Total	4.010	4.013	4.016	4.015	4.018	4.020	4.014	4.010	4.013	3.960	4.008	4.017	4.017

ZM2-100A									
Sample	spot4	spot5	spot5	spot6	spot7	spot8	spot9	spot9	spot4 3
Comment	augite rim	augite rim	augite rim	augite rim	augite rim	augite rim	augite rim	augite rim	augite rim
SiO_2	52.20	52.17	49.51	49.68	51.50	48.50	49.32	51.86	47.25
TiO_2	0.29	0.23	0.35	0.35	0.27	0.52	0.37	0.21	0.42
Al_2O_3	4.54	4.00	6.81	6.37	4.59	8.15	6.28	3.97	9.59
Cr_2O_3	0.08	0.04	0.00	0.00	0.02	0.01	0.00	0.00	0.00
FeO*	7.66	7.79	9.30	8.75	8.36	9.40	9.71	7.37	11.36
MnO	0.18	0.20	0.19	0.22	0.22	0.21	0.25	0.16	0.25
MgO	18.11	19.13	14.61	15.03	18.05	13.88	15.47	17.35	12.83
CaO	17.75	16.85	19.47	19.88	17.67	19.76	18.31	19.11	18.93
Na_2O	0.11	0.10	0.13	0.15	0.14	0.19	0.13	0.15	0.15
K_2O	0.00	0.00	0.00	0.00	0.00	0.00	0.00	0.00	0.00
NiO	0.03	0.05	0.02	0.03	0.02	0.03	0.03	0.03	0.01
Total	100.93	100.56	100.39	100.46	100.82	100.63	99.87	100.23	100.81
Mg#	0.81	0.81	0.74	0.75	0.79	0.72	0.74	0.81	0.67
Wo	36.29	34.01	41.37	41.74	35.83	42.57	38.62	38.99	41.47
En	51.50	53.71	43.20	43.91	50.93	41.62	45.40	49.26	39.10
Fs	12.21	12.27	15.43	14.35	13.23	15.81	15.98	11.74	19.43
Cations (based on 6.0 oxygens)									
Si	1.891	1.895	1.830	1.834	1.876	1.793	1.833	1.899	1.757
Ti	0.008	0.006	0.010	0.010	0.007	0.014	0.010	0.006	0.012
Al(4)	0.194	0.171	0.297	0.277	0.197	0.355	0.275	0.171	0.420
Al(6)									
Cr	0.002	0.001	0.000	0.000	0.000	0.000	0.000	0.000	0.000
Fe	0.232	0.237	0.288	0.270	0.255	0.291	0.302	0.226	0.353
Mn	0.005	0.006	0.006	0.007	0.007	0.007	0.008	0.005	0.008
Mg	0.978	1.036	0.805	0.827	0.980	0.765	0.857	0.947	0.711
Ca	0.689	0.656	0.771	0.786	0.690	0.783	0.729	0.750	0.754
Na	0.007	0.007	0.009	0.011	0.010	0.013	0.010	0.011	0.011
Ni	0.001	0.001	0.001	0.001	0.001	0.001	0.001	0.001	0.000
4.007	4.016	4.017	4.023	4.023	4.022	4.024	4.015	4.027	

mp-microphenocryst

Table 1c. Representative microprobe analyses of spinel in Zambales boninite

	B-7-11								
Sample	spot1-spl2	spot1-spl8	spot2-spl1	spot2-spl2	spot4-sp4	spot4-sp6	spot7-sp1	spot8-sp4	spot8-sp7
SiO_2	0.06	0.11	0.09	0.08	0.07	0.09	0.86	0.10	0.10
TiO_2	0.14	0.15	0.13	0.12	0.11	0.10	0.21	0.09	0.15
Al_2O_3	10.30	12.98	9.47	11.40	11.08	10.46	12.51	14.29	11.18
Cr_2O_3	58.42	54.63	57.92	57.41	57.16	57.75	51.08	51.82	55.63
Fe_2O_3	5.17	5.69	4.42	4.51	5.10	4.28	7.53	5.79	5.76
FeO	12.34	12.69	16.09	13.14	14.11	14.73	15.19	15.63	15.62
MnO	0.28	0.23	0.31	0.24	0.28	0.28	0.26	0.28	0.30
MgO	13.77	13.76	11.02	13.33	12.73	12.09	11.70	11.87	11.68
CaO	0.01	0.04	0.01	0.03	0.00	0.02	0.39	0.08	0.06
Na_2O	0.00	0.02	0.00	0.00	0.00	0.00	0.01	0.00	0.00
NiO	0.12	0.12	0.07	0.11	0.11	0.10	0.12	0.09	0.08
Total	100.61	100.42	99.54	100.38	100.77	99.89	99.87	100.04	100.54
Cr#	0.79	0.74	0.80	0.77	0.78	0.79	0.73	0.71	0.77
Cr'	74.24	68.81	75.97	72.95	72.78	74.60	66.44	65.91	71.53
Al'	19.52	24.37	18.52	21.60	21.03	20.14	24.25	27.09	21.42
Fe^{3+}	6.25	6.82	5.51	5.45	6.19	5.26	9.32	7.00	7.05
Cations (based on 4.0 oxygens)									
Si	0.002	0.003	0.003	0.003	0.002	0.003	0.028	0.003	0.003
Ti	0.003	0.004	0.003	0.003	0.003	0.002	0.005	0.002	0.004
Al	0.389	0.485	0.369	0.430	0.419	0.401	0.475	0.540	0.427
Cr	1.480	1.370	1.513	1.454	1.451	1.487	1.301	1.314	1.425
Fe3+	0.125	0.136	0.110	0.109	0.123	0.105	0.182	0.140	0.140
Fe2+	0.331	0.337	0.445	0.352	0.379	0.401	0.409	0.419	0.423
Mn	0.007	0.006	0.009	0.007	0.008	0.008	0.007	0.008	0.008
Mg	0.658	0.651	0.543	0.637	0.610	0.587	0.562	0.567	0.564
Ca	0.000	0.001	0.000	0.001	0.000	0.001	0.014	0.003	0.002
Na	0.000	0.001	0.000	0.000	0.000	0.000	0.000	0.000	0.000
Ni	0.003	0.003	0.002	0.003	0.003	0.003	0.003	0.002	0.002
Total	2.998	2.998	2.998	2.998	2.998	2.998	2.988	2.998	2.997

	B-7-11			ZM2-107					
Sample	spot9-sp3	spot11-sp1	spot11-sp3	spot1-spl4	spot2-sp1	spot2-sp3	spot4-sp4	spot5-sp2	spot7-sp
SiO_2	0.22	0.08	0.15	0.06	0.06	0.05	0.06	0.05	0.05
TiO_2	0.25	0.21	0.21	0.18	0.15	0.11	0.20	0.15	0.14
Al_2O_3	14.60	12.78	13.87	13.57	11.93	11.60	13.31	11.77	12.46
Cr_2O_3	48.81	52.08	50.94	52.04	55.71	55.92	52.12	55.53	53.62
Fe_2O_3	8.28	7.11	7.83	7.23	5.70	5.58	7.45	5.60	6.87
FeO	15.43	15.27	13.66	15.32	11.98	13.99	14.51	14.68	14.47
MnO	0.28	0.28	0.26	0.27	0.25	0.29	0.31	0.32	0.29
MgO	11.97	11.83	13.04	12.26	14.06	12.79	12.67	12.38	12.59
CaO	0.13	0.19	0.21	0.00	0.00	0.00	0.00	0.01	0.00
Na_2O	0.00	0.00	0.00	0.01	0.00	0.00	0.00	0.00	0.00
NiO	0.10	0.09	0.12	0.08	0.12	0.12	0.08	0.07	0.09
Total	100.08	99.91	100.29	101.01	99.96	100.44	100.70	100.56	100.58
Cr#	0.69	0.73	0.71	0.72	0.76	0.76	0.72	0.76	0.74
Cr'	62.21	66.86	64.43	65.75	70.60	71.22	65.93	70.82	68.11
Al'	27.74	24.45	26.15	25.55	22.52	22.02	25.10	22.38	23.58
Fe^{3+}	10.05	8.69	9.42	8.70	6.88	6.76	8.97	6.80	8.31
Cations (based on 4.0 oxygens)									
Si	0.007	0.003	0.005	0.002	0.002	0.002	0.002	0.001	0.002
Ti	0.006	0.005	0.005	0.004	0.004	0.003	0.005	0.004	0.003
Al	0.550	0.487	0.520	0.509	0.449	0.439	0.500	0.446	0.470
Cr	1.234	1.331	1.281	1.310	1.407	1.421	1.313	1.412	1.358
Fe3+	0.199	0.173	0.187	0.173	0.137	0.135	0.179	0.136	0.166
Fe2+	0.413	0.413	0.363	0.408	0.320	0.376	0.387	0.395	0.388
Mn	0.008	0.008	0.007	0.007	0.007	0.008	0.008	0.009	0.008
Mg	0.571	0.570	0.618	0.582	0.669	0.612	0.602	0.594	0.601
Ca	0.004	0.007	0.007	0.000	0.000	0.000	0.000	0.000	0.000
Na	0.000	0.000	0.000	0.000	0.000	0.000	0.000	0.000	0.000
Ni	0.003	0.002	0.003	0.002	0.003	0.003	0.002	0.002	0.002
Total	2.995	2.997	2.996	2.998	2.998	2.998	2.998	2.998	2.998

	ZM2-107					B-5-7						
Sample	spot8-	spot9-	spot9-	spot10-	spot10-	spot1	spot3	spot3	spot4	spot4	spot5	spot6	spot6 sp
SiO_2	0.08	0.03	0.05	0.15	0.06	0.09	0.10	0.11	0.10	0.05	0.05	0.07	0.06
TiO_2	0.22	0.15	0.10	0.11	0.12	0.18	0.17	0.20	0.15	0.10	0.12	0.11	0.14
Al_2O_3	13.66	12.96	11.61	7.58	11.62	13.47	12.95	14.36	12.09	10.81	11.64	9.96	11.84
Cr_2O_3	51.60	55.52	56.44	60.75	56.13	50.98	52.67	50.71	54.17	57.32	56.05	59.08	57.05
Fe_2O_3	7.18	5.62	5.13	4.25	5.23	7.48	7.38	8.03	6.66	5.34	5.37	4.84	5.30
FeO	14.52	12.41	14.57	15.47	15.23	15.75	14.11	13.58	13.72	15.49	13.54	11.70	11.21
MnO	0.28	0.24	0.31	0.35	0.31	0.28	0.27	0.24	0.25	0.29	0.24	0.28	0.26
MgO	12.52	14.13	12.48	11.31	12.09	11.58	12.73	13.24	12.87	11.90	12.97	14.08	14.65
CaO	0.14	0.00	0.00	0.03	0.00	0.21	0.18	0.18	0.18	0.06	0.14	0.00	0.00
Na_2O	0.00	0.00	0.00	0.00	0.00	0.00	0.02	0.03	0.01	0.00	0.00	0.00	0.03
NiO	0.09	0.14	0.11	0.09	0.07	0.13	0.11	0.13	0.10	0.13	0.12	0.14	0.14
Total	100.31	101.20	100.79	100.09	100.86	100.17	100.70	100.79	100.29	101.48	100.24	100.25	100.68
Cr#	0.72	0.74	0.77	0.84	0.76	0.72	0.73	0.70	0.75	0.78	0.76	0.80	0.76
Cr'	65.49	69.24	71.78	79.83	71.57	65.21	66.67	63.58	68.98	73.00	71.39	75.23	71.54
Al'	25.84	24.09	22.01	14.85	22.08	25.67	24.44	26.84	22.95	20.53	22.10	18.91	22.13
Fe^{3+}	8.67	6.67	6.21	5.31	6.35	9.11	8.89	9.58	8.07	6.47	6.51	5.86	6.33
Cations (based on 4.0 oxygens)													
Si	0.003	0.001	0.001	0.005	0.002	0.003	0.003	0.003	0.003	0.002	0.002	0.002	0.002
Ti	0.005	0.004	0.002	0.003	0.003	0.004	0.004	0.005	0.004	0.002	0.003	0.003	0.003
Al	0.514	0.481	0.439	0.296	0.440	0.511	0.487	0.534	0.457	0.410	0.441	0.377	0.441
Cr	1.303	1.381	1.432	1.589	1.427	1.298	1.328	1.266	1.374	1.456	1.424	1.500	1.426
Fe3+	0.173	0.133	0.124	0.106	0.127	0.181	0.177	0.191	0.161	0.129	0.130	0.117	0.126
Fe2+	0.388	0.326	0.391	0.428	0.410	0.424	0.376	0.358	0.368	0.416	0.364	0.314	0.296
Mn	0.008	0.006	0.008	0.010	0.008	0.008	0.007	0.006	0.007	0.008	0.006	0.008	0.007
Mg	0.596	0.663	0.597	0.558	0.579	0.556	0.605	0.623	0.615	0.570	0.621	0.674	0.691
Ca	0.005	0.000	0.000	0.001	0.000	0.007	0.006	0.006	0.006	0.002	0.005	0.000	0.000
Na	0.000	0.000	0.000	0.000	0.000	0.000	0.001	0.002	0.000	0.000	0.000	0.000	0.002
Ni	0.002	0.004	0.003	0.002	0.002	0.003	0.003	0.003	0.002	0.003	0.003	0.003	0.003
Total	2.997	2.998	2.999	2.997	2.998	2.997	2.998	2.998	2.998	2.998	2.998	2.998	2.999

	B-5-7	ZM2-100A						
Sample	spot8	spot9	spot2	spot5	spot6	spot7	spot7	spot9
SiO_2	0.06	0.08	0.06	0.12	0.08	0.11	0.11	0.13
TiO_2	0.06	0.15	0.13	0.15	0.18	0.18	0.17	0.18
Al_2O_3	9.12	10.23	10.58	11.12	11.17	12.89	13.03	13.71
Cr_2O_3	59.66	57.89	57.84	55.27	54.55	52.00	52.39	50.54
Fe_2O_3	4.92	5.13	5.78	5.57	6.45	7.17	6.99	7.58
FeO	14.61	12.66	11.79	15.47	15.16	15.24	14.50	15.78
MnO	0.30	0.26	0.27	0.30	0.29	0.29	0.27	0.27
MgO	12.25	13.43	14.11	11.48	11.75	11.96	12.37	11.52
CaO	0.03	0.01	0.06	0.20	0.13	0.05	0.21	0.26
Na_2O	0.01	0.00	0.01	0.01	0.00	0.00	0.00	0.03
NiO	0.10	0.12	0.17	0.10	0.12	0.12	0.13	0.13
Total	101.12	99.95	100.82	99.78	99.89	100.03	100.18	100.13
Cr#	0.81	0.79	0.79	0.77	0.77	0.73	0.73	0.71
Cr'	76.55	74.20	73.11	71.64	70.53	66.63	66.77	64.64
Al'	17.44	19.55	19.94	21.49	21.53	24.62	24.76	26.13
Fe^{3+}	6.00	6.26	6.95	6.88	7.93	8.75	8.47	9.23
Cations (based on 4.0 oxygens)								
Si	0.002	0.003	0.002	0.004	0.003	0.004	0.004	0.004
Ti	0.001	0.004	0.003	0.004	0.004	0.004	0.004	0.004
Al	0.348	0.389	0.398	0.428	0.429	0.490	0.493	0.520
Cr	1.528	1.478	1.458	1.426	1.404	1.326	1.329	1.286
Fe3+	0.120	0.125	0.139	0.137	0.158	0.174	0.169	0.184
Fe2+	0.396	0.342	0.314	0.422	0.413	0.411	0.389	0.425
Mn	0.008	0.007	0.007	0.008	0.008	0.008	0.007	0.007
Mg	0.591	0.647	0.671	0.558	0.571	0.575	0.592	0.553
Ca	0.001	0.000	0.002	0.007	0.005	0.002	0.007	0.009
Na	0.000	0.000	0.001	0.001	0.000	0.000	0.000	0.002
Ni	0.003	0.003	0.004	0.003	0.003	0.003	0.003	0.003
Total	2.999	2.998	2.998	2.997	2.997	2.997	2.997	2.998

Table 2. Whole rock major and trace-element compositions of boninite and boninite series volcanics from northern Zambales ophiolite.

	B-5-7	B-5-8	B-6-9	B-6-10	B-7-11	ZM2-100B	ZM2-100A	ZM2-107
Longitude	119.938	119.938	119.938	119.938	119.939	119.939	119.939	119.94
Latitude	15.9905	15.9905	15.9903	15.9903	15.9904	15.991	15.991	15.9928
Unit	UV	UV	UV	UV	UV	UV	UV	UV
Occurrence	pillow lava	lapili tuff	vesicular pillow	pillow lava,	pillow lava outer	pillow lava	pillow lava	tuff breccia
SiO_2 (wt%)	57.07	56.66	57.29	56.99	56.93	57.23	58.07	54.83
TiO_2	0.25	0.25	0.26	0.25	0.25	0.25	0.25	0.23
Al_2O_3	13.24	13.31	13.43	13.54	13.05	13.29	13.37	13.25
Fe_2O_3	8.72	8.73	8.91	9.11	9.32	8.85	8.71	9.29
MnO	0.14	0.15	0.15	0.15	0.15	0.15	0.16	0.14
MgO	8.91	8.56	8.51	8.41	9.00	8.90	8.98	12.28
CaO	9.41	9.34	9.51	9.57	9.15	9.28	8.98	8.49
Na_2O	1.33	1.30	1.35	1.45	1.28	1.37	1.28	0.81
K_2O	0.29	0.35	0.34	0.28	0.33	0.33	0.31	0.44
P_2O_5	0.02	0.02	0.02	0.02	0.02	0.02	0.02	0.01
Total	99.38	98.66	99.77	99.78	99.49	99.67	100.13	99.76
LOI	3.73	3.86	3.76	1.84	4.09	4.06	4.32	7.02
TAS	And	And	And	And	And	And	And	Bas And
High-Mg classification	BON, HSB	BON, HSB	BON, HSB	BON, HSB	BON, HSB	BON, HSB	BON, HSB	BON, LSB
SiO_2 (wt%)	57.94	57.95	57.94	57.65	57.77	57.93	58.50	55.48
TiO_2	0.25	0.25	0.26	0.25	0.25	0.25	0.25	0.23
Al_2O_3	13.44	13.61	13.58	13.69	13.24	13.45	13.47	13.40
FeO*	7.97	8.03	8.11	8.29	8.51	8.07	7.90	8.45
MnO	0.14	0.15	0.15	0.15	0.15	0.15	0.16	0.15
MgO	9.05	8.75	8.61	8.51	9.13	9.00	9.05	12.42
CaO	9.55	9.55	9.62	9.68	9.29	9.39	9.05	8.59
Na_2O	1.35	1.33	1.37	1.47	1.30	1.39	1.29	0.82
K_2O	0.29	0.35	0.35	0.29	0.34	0.34	0.31	0.44
P_2O_5	0.02	0.02	0.02	0.02	0.02	0.02	0.02	0.01
Total	100.00	100.00	100.00	100.00	100.00	100.00	100.00	100.00
LOI	3.73	3.86	3.76	1.84	4.09	4.06	4.32	7.02
Mg#	0.67	0.66	0.65	0.65	0.66	0.67	0.67	0.72
Rb (µg/g)	7.56	8.44	8.16	7.63	8.19	7.87	7.58	8.32
Sr	61.7	68.7	69.7	63.3	71.3	63.3	62.6	68.6
Y	13.20	11.95	11.62	11.84	12.31	12.16	11.89	10.44
Zr	15.19	15.54	15.29	15.68	15.13	15.83	15.64	12.55
Nb	0.30	0.33	0.32	0.35	0.33	0.29	0.30	0.25

Cs	0.674	0.737	0.740	0.727	0.721	0.739	0.677	0.447
Ba	26.61	30.88	29.79	28.93	26.90	27.31	29.02	17.69
La	0.58	0.61	0.61	0.64	0.62	0.63	0.60	0.57
Ce	1.33	1.43	1.46	1.48	1.40	1.48	1.46	1.16
Pr	0.22	0.22	0.23	0.23	0.22	0.22	0.22	0.20
Nd	1.19	1.25	1.29	1.26	1.19	1.29	1.22	1.10
Sm	0.53	0.56	0.55	0.59	0.55	0.58	0.57	0.50
Eu	0.21	0.22	0.22	0.23	0.22	0.21	0.22	0.18
Gd	1.07	1.05	1.02	1.03	1.03	1.04	1.04	0.85
Tb	0.23	0.22	0.22	0.22	0.22	0.23	0.22	0.18
Dy	1.75	1.65	1.62	1.63	1.59	1.63	1.63	1.37
Ho	0.42	0.39	0.39	0.40	0.39	0.41	0.39	0.33
Er	1.36	1.26	1.24	1.24	1.23	1.25	1.21	1.02
Tm	0.21	0.19	0.19	0.19	0.21	0.20	0.20	0.16
Yb	1.50	1.41	1.39	1.39	1.40	1.39	1.41	1.17
Lu	0.24	0.24	0.23	0.22	0.23	0.23	0.23	0.19
Hf	0.53	0.55	0.57	0.54	0.53	0.56	0.53	0.42
Ta	0.025	0.026	0.026	0.027	0.024	0.026	0.025	0.023
Pb	1.70	1.69	1.70	1.83	1.66	1.75	1.79	1.65
Th	0.13	0.13	0.13	0.13	0.13	0.13	0.13	0.11
U	0.09	0.09	0.09	0.10	0.09	0.09	0.10	0.08
V	210.9	229.7	230.7	231.1	211.1	223.7	217.9	221.0
Cr	491.50	475.60	474.36	549.83	488.15	561.24	495.62	635.73
Ni	153.55	127.49	131.83	124.12	143.95	139.12	131.55	260.91
Li	5.68	5.29	4.32	8.33	7.18	7.51	11.02	10.44
Be	0.232	0.222	0.237	0.231	0.210	0.226	0.217	0.172

[1]JB-2 reference values (RV): Imai, 1995 and Jochum et al., 2016

[2]JB-3 reference values (RV): Imai, 1995 and Dulski, 2001

Unit: UV- upper volcanic unit, LV-lower volcanic unit, DC - dike complex

	B-99D	B-99C	B-100	B-82	B-89	B-90-1	B-54f	ZM2-128A
Longitude	119.937	119.937	119.937	119.952	119.95	119.95	119.95	119.945
Latitude	15.984	15.984	15.9834	15.9695	15.9725	15.973	15.9582	15.9842
Unit	UV	UV	UV	DC	DC	DC	UV	UV
Occurrence	pillow lava	pillow lava	massive flow	dike	dike	dike	pillow lava	pillow lava
SiO_2 (wt%)	55.54	53.33	55.03	54.48	53.77	54.26	51.22	49.89
TiO_2	0.36	0.28	0.43	0.32	0.35	0.33	0.32	0.24
Al_2O_3	13.87	12.94	14.43	16.52	15.16	14.05	13.93	13.30
Fe_2O_3	9.90	9.67	9.73	10.12	10.69	9.16	10.28	11.33
MnO	0.15	0.15	0.15	0.19	0.24	0.21	0.18	0.28
MgO	9.62	12.83	8.34	8.63	9.65	12.31	12.20	13.43
CaO	8.78	9.78	9.37	7.70	8.77	7.34	10.03	9.61
Na_2O	1.40	0.72	2.20	1.89	1.28	1.57	1.31	0.13
K_2O	0.32	0.25	0.23	0.26	0.14	0.32	0.18	1.70
P_2O_5	0.02	0.02	0.03	0.02	0.02	0.02	0.02	0.02
Total	99.96	99.97	99.93	100.13	100.07	99.57	99.67	99.93
LOI	2.93	4.12	2.66	4.45	3.69	4.44	5.66	9.60
TAS classification	Bas And	Bas And	Bas And	Bas And	Bas And	Bas And	Bas	Bas
High-Mg classification	BON, LSB	BON, LSB	BON, LSB	BON, LSB	BON, LSB	BON, LSB	Bon. Bas	Bon. Bas
SiO_2 (wt%)	56.12	53.87	55.62	54.97	54.31	55.00	51.92	50.50
TiO_2	0.36	0.28	0.43	0.32	0.35	0.33	0.33	0.24
Al_2O_3	14.01	13.07	14.58	16.67	15.31	14.24	14.12	13.46
FeO*	9.00	8.79	8.85	9.19	9.72	8.35	9.38	10.32
MnO	0.15	0.15	0.15	0.19	0.24	0.21	0.18	0.28
MgO	9.72	12.96	8.43	8.71	9.75	12.48	12.37	13.59
CaO	8.87	9.88	9.47	7.77	8.86	7.44	10.17	9.73
Na_2O	1.41	0.73	2.22	1.91	1.29	1.59	1.33	0.13
K_2O	0.32	0.25	0.23	0.26	0.14	0.32	0.19	1.72
P_2O_5	0.02	0.02	0.03	0.02	0.02	0.02	0.02	0.02
Total	100.00	100.00	100.00	100.00	100.00	100.00	100.00	100.00
LOI	2.93	4.12	2.66	4.45	3.69	4.44	5.66	9.60
Mg#	0.66	0.72	0.63	0.63	0.64	0.73	0.70	0.70
Rb (µg/g)	2.75	1.98	1.51	1.47		2.73	2.50	27.42
Sr	69.8	42.5	106.0	57.7		82.7	64.3	51.8
Y	17.03	13.52	13.87	12.32		11.66	21.80	6.25
Zr	15.50	13.97	17.93	13.11		14.93	13.38	10.36
Nb	0.36	0.28	0.17	0.20		0.17	0.17	0.21
Cs	0.025	0.024	0.025	0.046		0.019	0.368	0.137
Ba	29.85	16.64	21.28	10.26		99.24	32.31	49.29

La	0.76	0.58	0.53	0.35	0.44	0.58	0.27
Ce	1.49	1.30	1.57	1.02	1.22	1.10	0.69
Pr	0.25	0.21	0.28	0.18	0.22	0.27	0.10
Nd	1.47	1.23	1.81	1.19	1.37	1.75	0.56
Sm	0.63	0.56	0.82	0.60	0.66	0.81	0.29
Eu	0.27	0.20	0.35	0.20	0.26	0.37	0.13
Gd	1.30	1.08	1.39	1.09	1.15	1.68	0.60
Tb	0.26	0.22	0.28	0.23	0.23	0.34	0.14
Dy	1.90	1.63	1.97	1.72	1.68	2.46	1.00
Ho	0.47	0.40	0.45	0.41	0.38	0.60	0.24
Er	1.46	1.26	1.38	1.28	1.15	1.90	0.77
Tm	0.24	0.20	0.20	0.21	0.18	0.29	0.13
Yb	1.56	1.34	1.42	1.36	1.24	1.92	0.90
Lu	0.26	0.23	0.23	0.21	0.19	0.34	0.14
Hf	0.56	0.52	0.66	0.49	0.53	0.51	0.36
Ta	0.032	0.023	0.012	0.017	0.015	0.011	0.020
Pb	0.52	0.47	0.92	0.14	0.56	1.06	1.33
Th	0.12	0.11	0.07	0.10	0.06	0.05	0.09
U	0.09	0.08	0.04	0.06	0.07	0.04	0.19
V	280.5	260.1	292.8	260.5	237.8	251.7	292.7
Cr	570.35	717.58	382.96	145.37	726.59	712.20	1113.10
Ni	178.54	291.63	84.42	72.21	215.73	248.21	301.46
Li	5.18	5.67	2.97	4.57	6.29	11.38	54.76
Be	0.186	0.184	0.184	0.181	0.166	0.187	0.158

	ZM2-128C	B-1-1	B-1-3	B-1-4	B-72	ZM2-96-2A	B-2-5	ZM2-105A
Longitude	119.945	119.939	119.939	119.939	119.938	119.94	119.939	119.941
Latitude	15.9842	15.99	15.99	15.99	15.9745	15.9906	15.9898	15.993
Unit	UV	LV	LV	LV	LV	LV	LV	LV
Occurrence	pillow lava	glassy pillow	glassy pillow	glassy pillow	pillow lava	glassy pillow	glassy dike	glassy pillow
SiO_2 (wt%)	49.40	62.46	62.99	62.18	57.79	56.18	62.10	56.73
TiO_2	0.24	0.44	0.45	0.45	0.37	0.44	0.44	0.33
Al_2O_3	15.12	14.50	14.50	14.40	16.51	15.94	14.36	15.90
Fe_2O_3	9.81	10.20	9.86	10.41	9.79	11.28	10.52	9.80
MnO	0.26	0.15	0.14	0.15	0.16	0.17	0.14	0.15
MgO	12.74	2.38	2.48	2.43	5.08	4.92	2.54	5.46
CaO	10.78	7.29	7.16	7.25	8.71	9.68	7.15	9.84
Na_2O	0.38	2.32	2.13	2.28	1.34	1.57	2.19	1.65
K_2O	0.89	0.45	0.49	0.56	0.52	0.25	0.65	0.26
P_2O_5	0.01	0.04	0.04	0.04	0.02	0.03	0.04	0.02
Total	99.63	100.23	100.24	100.15	100.29	100.46	100.13	100.12
LOI	8.52	3.52	4.68	3.48	7.18	2.36	3.85	3.33
TAS classification	Bas	And	Dac	And	And	Bas And	And	And
High-Mg classification	Bon. Bas	LSB-series	LSB-series	LSB-series	LSB-series	LSB-series	LSB-series	LSB-series
SiO_2 (wt%)	50.08	62.96	63.46	62.74	58.19	56.56	62.68	57.22
TiO_2	0.24	0.44	0.45	0.45	0.37	0.44	0.44	0.33
Al_2O_3	15.33	14.62	14.61	14.53	16.62	16.05	14.49	16.03
FeO*	8.95	9.25	8.94	9.45	8.87	10.22	9.55	8.90
MnO	0.26	0.15	0.14	0.15	0.16	0.17	0.14	0.15
MgO	12.91	2.40	2.50	2.45	5.12	4.95	2.56	5.51
CaO	10.93	7.35	7.21	7.32	8.77	9.75	7.22	9.93
Na_2O	0.39	2.34	2.15	2.30	1.35	1.58	2.21	1.66
K_2O	0.90	0.45	0.49	0.57	0.52	0.25	0.66	0.27
P_2O_5	0.01	0.04	0.04	0.04	0.02	0.03	0.04	0.02
Total	100.00	100.00	100.00	100.00	100.00	100.00	100.00	100.00
LOI	8.52	3.52	4.68	3.48	7.18	2.36	3.85	3.33
Mg#	0.72	0.32	0.33	0.32	0.51	0.46	0.32	0.52
Rb (µg/g)	17.77	9.09	9.81	9.47	8.39	5.94	11.11	5.07
Sr	34.7	107.5	111.2	111.3	111.6	79.4	109.4	101.1
Y	6.08	19.14	19.08	19.23	15.40	14.62	18.99	12.31
Zr	10.56	29.42	29.63	30.14	20.51	17.31	29.54	18.62
Nb	0.22	0.42	0.45	0.43	0.28	0.34	0.45	0.29
Cs	0.056	0.725	0.753	0.743	0.405	0.603	0.721	0.404
Ba	28.69	41.79	42.67	41.62	23.58	28.78	39.74	24.72

La	0.18	1.05	1.08	1.08	0.76	0.58	1.06	0.64
Ce	0.63	2.62	2.62	2.64	1.69	1.47	2.56	1.60
Pr	0.07	0.40	0.40	0.41	0.28	0.24	0.40	0.24
Nd	0.46	2.32	2.32	2.29	1.66	1.42	2.22	1.45
Sm	0.25	1.05	1.07	1.00	0.75	0.72	1.01	0.63
Eu	0.12	0.39	0.38	0.39	0.30	0.29	0.38	0.26
Gd	0.53	1.80	1.77	1.83	1.36	1.28	1.73	1.12
Tb	0.12	0.36	0.37	0.37	0.27	0.28	0.37	0.23
Dy	0.94	2.61	2.62	2.61	1.95	1.98	2.61	1.71
Ho	0.23	0.61	0.61	0.63	0.47	0.49	0.62	0.40
Er	0.69	1.94	1.90	1.93	1.47	1.46	1.90	1.26
Tm	0.11	0.30	0.31	0.31	0.22	0.23	0.30	0.19
Yb	0.80	2.09	2.12	2.15	1.55	1.63	2.13	1.38
Lu	0.13	0.34	0.34	0.34	0.25	0.26	0.34	0.22
Hf	0.36	1.04	1.01	1.03	0.74	0.64	1.03	0.66
Ta	0.022	0.033	0.041	0.035	0.024	0.024	0.035	0.022
Pb	1.37	1.97	2.05	2.00	1.44	1.37	2.03	1.39
Th	0.10	0.22	0.22	0.22	0.15	0.11	0.22	0.13
U	0.12	0.14	0.14	0.14	0.09	0.08	0.14	0.09
V	275.8	285.3	265.8	292.6	287.3	355.9	285.5	273.7
Cr	901.34	4.12	3.13	4.43	19.85	28.66	4.42	43.50
Ni	295.75	7.80	8.00	8.44	28.61	28.86	8.07	36.55
Li	55.39	4.63	5.87	3.17	14.12	6.52	4.87	8.06
Be	0.149	0.405	0.385	0.409	0.284	0.249	0.380	0.292

	ZM2-105D	B-102	ZM2-141	ZM2-96-2B	ZM2-116	ZM2-148	B-79	B-28
Longitude	119.941	119.933	119.95	119.94	119.932	119.944	119.94	119.942
Latitude	15.993	15.9824	15.98	15.9906	15.9763	15.9778	15.9768	15.9646
Unit	LV	LV	LV	LV	LV	LV	LV	LV
Occurrence	glassy pillow	glassy pillow	tuff breccia	hyaloclastite	pillow lava	tuff breccia	lapili tuff	lapili tuff (overlain
SiO_2 (wt%)	55.75	56.31	56.83	56.84	54.54	56.76	57.15	57.69
TiO_2	0.44	0.34	0.32	0.43	0.30	0.34	0.34	0.39
Al_2O_3	16.04	16.33	17.17	15.91	16.31	17.25	16.26	17.15
Fe_2O_3	11.47	10.33	9.17	10.91	8.95	9.03	9.39	10.25
MnO	0.17	0.15	0.15	0.17	0.13	0.15	0.14	0.18
MgO	5.44	4.84	5.89	5.32	6.93	6.09	5.51	5.00
CaO	9.32	10.01	8.80	9.04	9.44	8.37	9.40	8.20
Na_2O	1.39	1.66	1.12	1.41	1.53	1.02	1.32	1.18
K_2O	0.34	0.28	0.74	0.26	0.89	1.05	0.71	0.71
P_2O_5	0.02	0.03	0.02	0.03	0.02	0.02	0.02	0.03
Total	100.38	100.28	100.21	100.32	99.04	100.08	100.24	100.78
LOI	4.86	1.98	8.23	4.50	3.24	9.61	6.61	9.25
TAS classification	Bas And	Bas And	And	And	Bas And	And	And	And
High-Mg classification	LSB-series	LSB-series	LSB-series	LSB-series	LSB-series	LSB-series	LSB-series	LSB-series
SiO_2 (wt%)	56.18	56.74	57.24	57.28	55.57	57.23	57.55	57.83
TiO_2	0.44	0.34	0.32	0.43	0.31	0.34	0.34	0.39
Al_2O_3	16.16	16.45	17.29	16.03	16.62	17.39	16.37	17.19
FeO*	10.40	9.37	8.31	9.89	8.21	8.19	8.51	9.25
MnO	0.17	0.15	0.15	0.17	0.13	0.15	0.14	0.18
MgO	5.48	4.88	5.93	5.36	7.06	6.14	5.55	5.01
CaO	9.39	10.09	8.86	9.11	9.62	8.44	9.47	8.22
Na_2O	1.40	1.67	1.13	1.42	1.56	1.03	1.33	1.18
K_2O	0.34	0.28	0.75	0.26	0.91	1.06	0.72	0.71
P_2O_5	0.02	0.03	0.02	0.03	0.02	0.02	0.02	0.03
Total	100.00	100.00	100.00	100.00	100.00	100.00	100.00	100.00
LOI	4.86	1.98	8.23	4.50	3.24	9.61	6.61	9.25
Mg#	0.48	0.48	0.56	0.49	0.61	0.57	0.54	0.49
Rb (µg/g)	6.60	5.65	9.67	6.14	5.11	13.90	8.09	12.48
Sr	64.5	104.9	127.9	82.3	82.8	128.6	112.1	104.4
Y	13.82	12.36	11.40	14.30	19.43	11.54	12.81	13.67
Zr	17.07	18.71	18.37	17.07	10.43	18.88	18.54	21.36
Nb	0.30	0.33	0.25	0.29	0.21	0.24	0.29	0.30
Cs	0.560	0.458	0.281	0.577	0.097	0.299	0.324	0.681
Ba	19.79	25.28	18.29	26.96	35.78	27.15	19.83	53.87

La	0.53	0.69	0.69	0.55	0.73	0.61	0.68	0.68
Ce	1.31	1.71	1.65	1.38	1.49	1.60	1.61	1.80
Pr	0.22	0.27	0.25	0.23	0.24	0.24	0.26	0.28
Nd	1.31	1.49	1.42	1.38	1.52	1.39	1.51	1.63
Sm	0.66	0.66	0.61	0.66	0.71	0.61	0.67	0.71
Eu	0.27	0.26	0.27	0.30	0.29	0.26	0.29	0.29
Gd	1.22	1.17	1.07	1.28	1.48	1.13	1.18	1.27
Tb	0.26	0.24	0.22	0.27	0.30	0.23	0.25	0.27
Dy	1.91	1.68	1.63	1.97	2.15	1.66	1.72	1.95
Ho	0.46	0.40	0.37	0.47	0.51	0.38	0.42	0.46
Er	1.39	1.23	1.18	1.47	1.59	1.19	1.25	1.40
Tm	0.22	0.20	0.18	0.24	0.23	0.19	0.20	0.22
Yb	1.60	1.38	1.31	1.63	1.53	1.31	1.38	1.55
Lu	0.27	0.23	0.21	0.26	0.25	0.21	0.23	0.25
Hf	0.63	0.64	0.63	0.63	0.40	0.65	0.64	0.73
Ta	0.022	0.023	0.022	0.023	0.019	0.020	0.026	0.024
Pb	1.38	1.35	1.35	1.46	0.53	1.40	1.23	1.43
Th	0.11	0.14	0.13	0.11	0.08	0.14	0.13	0.15
U	0.08	0.09	0.09	0.08	0.24	0.09	0.08	0.11
V	312.6	282.4	276.2	342.7	259.7	269.9	263.4	282.3
Cr	35.35	20.10	35.15	27.42	36.77	31.74	43.77	17.80
Ni	36.08	28.17	32.42	28.23	58.43	30.75	33.39	27.10
Li	11.16	6.26	15.81	9.06	15.43	24.44	8.68	20.25
Be	0.216	0.248	0.284	0.236	0.149	0.296	0.272	0.277

	B-92-2B	B-102-1	ZM2-124	ZM2-136	B-91-1	ZM2-123	ZM2-125	ZM2-135
Longitude	119.95	119.933	119.933	119.949	119.95	119.933	119.934	119.949
Latitude	15.978	15.9824	15.968	15.9798	15.9782	15.967	15.9688	15.9797
Unit	LV	LV	LV	LV	LV	LV	LV	LV
Occurrence	lapili tuff	lapili tuff (overlying	lapili tuff	lapili tuff (overlying	lapili tuff	lapili tuff	lapili tuff	lapili tuff (adjacent
SiO_2 (wt%)	59.42	57.14	57.08	57.02	59.66	57.08	56.78	56.46
TiO_2	0.43	0.32	0.35	0.33	0.43	0.33	0.33	0.33
Al_2O_3	16.05	16.28	17.04	17.00	15.93	16.50	16.32	17.15
Fe_2O_3	10.08	9.24	9.43	9.10	10.04	9.38	9.54	9.12
MnO	0.16	0.14	0.13	0.16	0.15	0.16	0.15	0.20
MgO	3.77	5.51	5.54	5.96	3.87	5.55	5.67	5.89
CaO	7.99	9.70	8.59	8.74	7.92	9.42	9.37	8.99
Na_2O	1.73	1.57	1.07	1.15	1.69	1.39	1.40	1.21
K_2O	0.65	0.26	0.80	0.77	0.69	0.56	0.56	0.71
P_2O_5	0.03	0.03	0.02	0.02	0.03	0.02	0.02	0.02
Total	100.31	100.19	100.05	100.25	100.41	100.39	100.14	100.08
LOI	6.52	3.52	9.55	8.85	6.69	6.14	6.06	8.01
TAS classification	And	And	And	And	And	And	And	Bas And
High-Mg classification	LSB-series	LSB-series	LSB-series	LSB-series	LSB-series	LSB-series	LSB-series	LSB-series
SiO_2 (wt%)	59.84	57.56	57.60	57.40	60.02	57.40	57.25	56.93
TiO_2	0.43	0.32	0.35	0.33	0.43	0.33	0.33	0.33
Al_2O_3	16.16	16.40	17.19	17.11	16.03	16.59	16.45	17.29
FeO*	9.13	8.38	8.56	8.24	9.09	8.49	8.65	8.28
MnO	0.16	0.14	0.13	0.16	0.15	0.16	0.15	0.20
MgO	3.80	5.55	5.59	6.00	3.89	5.58	5.72	5.94
CaO	8.05	9.77	8.67	8.80	7.97	9.47	9.45	9.07
Na_2O	1.74	1.58	1.08	1.16	1.70	1.40	1.41	1.22
K_2O	0.65	0.26	0.81	0.78	0.69	0.56	0.56	0.72
P_2O_5	0.03	0.03	0.02	0.02	0.03	0.02	0.02	0.02
Total	100.00	100.00	100.00	100.00	100.00	100.00	100.00	100.00
LOI	6.52	3.52	9.55	8.85	6.69	6.14	6.06	8.01
Mg#	0.43	0.54	0.54	0.56	0.43	0.54	0.54	0.56
Rb (µg/g)	9.55	5.96	10.17	10.54	11.04	8.01	7.86	10.39
Sr	108.5	106.6	84.9	124.6	111.7	103.6	127.5	153.7
Y	15.46	11.92	11.98	11.01	15.12	11.88	12.22	11.79
Zr	25.99	18.56	19.16	18.39	25.76	18.38	18.71	18.75
Nb	0.39	0.30	0.25	0.25	0.35	0.27	0.28	0.25
Cs	0.453	0.436	0.250	0.286	0.616	0.357	0.323	0.319
Ba	27.18	24.49	15.28	43.63	27.90	24.68	20.18	40.36

La	0.95	0.64	0.68	0.66	0.97	0.64	0.64	0.68
Ce	2.30	1.55	1.69	1.66	2.37	1.61	1.60	1.70
Pr	0.35	0.24	0.26	0.25	0.36	0.26	0.25	0.26
Nd	1.97	1.44	1.43	1.35	1.92	1.47	1.45	1.48
Sm	0.87	0.62	0.65	0.60	0.88	0.65	0.64	0.67
Eu	0.35	0.26	0.26	0.25	0.33	0.26	0.26	0.25
Gd	1.48	1.10	1.14	1.06	1.46	1.15	1.16	1.17
Tb	0.31	0.22	0.24	0.21	0.29	0.24	0.24	0.23
Dy	2.15	1.61	1.65	1.53	2.13	1.74	1.71	1.65
Ho	0.51	0.38	0.40	0.37	0.51	0.40	0.41	0.39
Er	1.61	1.20	1.21	1.13	1.57	1.28	1.28	1.21
Tm	0.25	0.19	0.19	0.18	0.24	0.20	0.20	0.19
Yb	1.78	1.30	1.37	1.25	1.69	1.38	1.37	1.33
Lu	0.27	0.21	0.22	0.21	0.27	0.22	0.22	0.22
Hf	0.88	0.63	0.65	0.64	0.87	0.64	0.66	0.64
Ta	0.033	0.024	0.020	0.021	0.031	0.021	0.021	0.022
Pb	1.86	1.32	1.37	1.34	1.75	1.26	1.32	1.45
Th	0.19	0.13	0.14	0.13	0.19	0.13	0.13	0.13
U	0.13	0.09	0.09	0.09	0.13	0.09	0.09	0.09
V	319.4	273.4	258.4	237.6	318.3	254.4	264.9	253.8
Cr	4.58	41.32	25.71	29.17	4.00	41.76	46.84	33.61
Ni	13.99	33.91	30.14	31.44	14.31	34.49	36.14	31.64
Li	6.64	10.35	20.62	21.69	9.91	11.91	10.58	13.93
Be	0.333	0.281	0.270	0.267	0.364	0.274	0.261	0.300

	B-47 d1	B-47 d3	B-47 d7	B-47 d4	B-97A	ZM2-120A3-54 pillow/		B-31
Longitude	119.96	119.96	119.96	119.96	119.94	119.93	119.95	119.94
Latitude	15.96	15.96	15.96	15.96	15.98	15.97	15.96	15.96
Unit	DC	DC	DC	DC	altered UV	altered UV	altered UV	altered dike cutting LV
Occurrence	dike	dike	dike, vent breccia	dike	dike?	massive lava over	glassy pillow	dike cutting
SiO_2 (wt%)	58.89	59.85	59.88	53.18	56.29	55.41	54.91	54.50
TiO_2	0.47	0.47	0.39	0.60	0.38	0.27	0.35	0.32
Al_2O_3	15.98	15.08	15.08	18.01	15.30	14.04	14.09	16.60
Fe_2O_3	8.68	8.41	10.12	10.65	8.41	9.30	9.77	8.34
MnO	0.21	0.17	0.15	0.20	0.13	0.20	0.16	0.08
MgO	4.99	5.25	6.02	6.16	7.96	10.27	13.60	7.65
CaO	9.56	9.48	7.37	9.25	7.05	6.10	5.62	10.95
Na_2O	1.60	1.63	1.41	2.21	3.60	2.94	0.60	1.26
K_2O	0.11	0.16	0.12	0.09	0.91	1.19	0.11	0.19
P_2O_5	0.03	0.03	0.03	0.04	0.03	0.02	0.01	0.02
Total	100.52	100.53	100.57	100.39	100.06	99.74	99.23	99.91
LOI	1.58	1.18	2.47	1.85	2.96	3.34	11.41	2.39
TAS classification	And	And	And	Bas And	Bas And	Bas And	Bas And	Bas And
High-Mg classification	LSB-series	LSB-series	LSB-series	TH Bas. Andesite dike	BON, LSB alt.	BON, LSB alt.	BON, LSB alt.	BON, LSB alt.
SiO_2 (wt%)	59.10	60.04	60.15	53.54	56.73	56.08	55.88	55.01
TiO_2	0.47	0.47	0.39	0.60	0.38	0.27	0.35	0.32
Al_2O_3	16.04	15.13	15.15	18.13	15.42	14.21	14.34	16.76
FeO*	7.84	7.59	9.15	9.65	7.63	8.47	8.95	7.57
MnO	0.21	0.17	0.15	0.20	0.13	0.20	0.17	0.08
MgO	5.01	5.27	6.05	6.20	8.02	10.39	13.85	7.72
CaO	9.59	9.51	7.40	9.31	7.11	6.17	5.72	11.05
Na_2O	1.61	1.64	1.42	2.23	3.63	2.98	0.61	1.27
K_2O	0.11	0.16	0.12	0.09	0.92	1.20	0.11	0.19
P_2O_5	0.03	0.03	0.03	0.04	0.03	0.02	0.01	0.02
Total	100.00	100.00	100.00	100.00	100.00	100.00	100.00	100.00
LOI	1.58	1.18	2.47	1.85	2.96	3.34	11.41	2.39
Mg#	0.53	0.55	0.54	0.53	0.65	0.69	0.73	0.65
Rb (µg/g)	0.81	0.87		0.69	7.36	13.96	3.07	2.37
Sr	93.1	65.3		103.5	82.5	62.2	65.6	69.5
Y	14.89	15.72		15.72	11.28	9.14	13.78	10.30
Zr	19.78	18.02		19.83	14.37	10.39	14.69	11.00

Nb	0.31	0.35	0.25	0.21	0.23	0.14	0.16
Cs	0.010	0.012	0.009	0.012	0.060	0.339	0.045
Ba	4.69	7.27	7.22	136.20	267.03	3.62	19.87
La	0.64	0.68	0.75	0.57	0.48	0.39	0.36
Ce	1.73	1.61	2.21	1.61	1.08	1.00	0.90
Pr	0.28	0.25	0.39	0.27	0.16	0.20	0.16
Nd	1.72	1.49	2.48	1.66	0.87	1.28	0.99
Sm	0.81	0.71	1.12	0.70	0.39	0.63	0.52
Eu	0.35	0.26	0.44	0.29	0.15	0.28	0.24
Gd	1.43	1.36	1.79	1.19	0.78	1.25	0.96
Tb	0.30	0.29	0.33	0.23	0.16	0.26	0.20
Dy	2.06	2.19	2.35	1.63	1.26	1.86	1.47
Ho	0.49	0.52	0.53	0.38	0.31	0.44	0.35
Er	1.55	1.61	1.60	1.17	0.93	1.33	1.05
Tm	0.24	0.26	0.25	0.18	0.15	0.21	0.17
Yb	1.67	1.78	1.64	1.24	1.06	1.46	1.09
Lu	0.28	0.28	0.26	0.19	0.18	0.22	0.17
Hf	0.70	0.70	0.71	0.51	0.36	0.56	0.43
Ta	0.027	0.028	0.021	0.02	0.02	0.01	0.01
Pb	0.14	0.12	0.21	0.72	1.26	1.22	1.52
Th	0.13	0.11	0.09	0.06	0.10	0.06	0.07
U	0.07	0.06	0.06	0.04	0.07	0.03	0.08
V	287.0	278.0	329.6	262.8	287.8	222.2	270.7
Cr	5.85	29.02	25.90	216.76	428.21	518.61	219.00
Ni	14.34	26.60	25.52	52.63	135.32	256.76	57.83
Li	1.44	1.27	1.37	4.52	5.59	24.70	12.09
Be	0.288	0.220	0.215	0.160	0.174	0.085	0.158

	ZM2-128B	B-30	B-64	ZM2-104	B-86-5	B-87	B-22	B-56
Longitude	119.94	119.94	119.94	119.94	119.95	119.95	119.94	119.95
Latitude	15.98	15.96	15.97	15.99	15.97	15.97	15.96	15.96
Unit	altered UV	altered UV	altered UV	altered UV	altered DC	altered DC	altered LV	altered LV
Occurrence	pillow lava	dike	lapili tuff	tuff breccia	dike	dike	clasts in glassy	sheet flow
SiO_2 (wt%)	49.41	51.90	52.20	52.94	51.62	51.43	58.84	57.22
TiO_2	0.23	0.27	0.35	0.37	0.34	0.39	0.41	0.39
Al_2O_3	14.15	16.07	18.18	16.56	17.18	15.18	17.93	18.92
Fe_2O_3	9.88	9.07	9.50	9.92	10.77	12.02	8.52	8.04
MnO	0.18	0.15	0.18	0.15	0.30	0.23	0.18	0.07
MgO	9.85	7.90	8.30	7.46	10.32	12.29	4.86	3.43
CaO	12.85	10.60	8.24	9.89	6.01	5.05	7.18	9.05
Na_2O	0.39	3.59	2.51	0.59	3.01	3.04	0.43	2.09
K_2O	2.25	0.51	1.10	2.33	0.16	0.03	1.58	0.83
P_2O_5	0.10	0.03	0.01	0.03	0.02	0.03	0.02	0.03
Total	99.29	100.09	100.57	100.24	99.73	99.69	99.95	100.07
LOI	8.52	5.61	7.14	8.96	5.19	5.31	14.85	3.79
TAS classification	Basalt	Bas And	Bas And	Bas And	Bas And	Bas And	And	And
High-Mg classification	Bon. Bas alt.	Bon. Bas alt.	Bon. Bas alt.	Bon. Bas alt.	Bon. Bas alt./	Bon. Bas alt./	LSB-series	LSB-series
SiO_2 (wt%)	50.26	52.33	52.40	53.34	52.33	52.22	59.38	57.64
TiO_2	0.23	0.27	0.35	0.37	0.34	0.40	0.41	0.39
Al_2O_3	14.39	16.20	18.25	16.69	17.41	15.41	18.09	19.06
FeO*	9.04	8.23	8.58	8.99	9.82	10.98	7.74	7.29
MnO	0.18	0.15	0.18	0.15	0.30	0.23	0.18	0.07
MgO	10.02	7.97	8.33	7.52	10.46	12.48	4.90	3.46
CaO	13.07	10.69	8.27	9.97	6.09	5.13	7.25	9.12
Na_2O	0.40	3.62	2.52	0.59	3.05	3.09	0.43	2.11
K_2O	2.29	0.52	1.10	2.35	0.16	0.03	1.59	0.84
P_2O_5	0.10	0.03	0.01	0.03	0.02	0.03	0.02	0.03
Total	100.00	100.00	100.00	100.00	100.00	100.00	100.00	100.00
LOI	8.52	5.61	7.14	8.96	5.19	5.31	14.85	3.79
Mg#	0.66	0.65	0.67	0.63	0.63	0.60	0.53	0.46
Rb (µg/g)	45.18	12.78	14.74	31.11	1.41	0.29	23.21	38.95
Sr	59.0	118.0	56.0	48.5	76.9	46.6	100.3	104.7
Y	13.61	9.18	8.40	20.12	11.60	15.37	18.14	16.40
Zr	9.33	11.90	13.44	12.46	9.72	10.37	24.82	22.48
Nb	0.19	0.20	0.22	0.18	0.14	0.13	0.30	0.29
Cs	0.273	1.832	0.160	0.210	0.033	0.007	0.618	2.503

Ba	68.20	77.54	26.38	42.98	13.52	8.57	280.61	27.20
La	0.78	0.56	0.19	1.02	0.20	0.22	0.73	0.90
Ce	0.98	1.26	0.68	1.71	0.59	0.59	2.00	1.97
Pr	0.18	0.19	0.10	0.39	0.12	0.12	0.32	0.34
Nd	1.01	1.00	0.66	2.43	0.84	0.82	1.82	2.03
Sm	0.41	0.45	0.40	1.12	0.51	0.55	0.90	0.89
Eu	0.18	0.18	0.18	0.40	0.18	0.20	0.38	0.35
Gd	0.91	0.79	0.79	2.04	1.06	1.25	1.63	1.60
Tb	0.19	0.17	0.17	0.39	0.22	0.27	0.34	0.32
Dy	1.46	1.26	1.31	2.77	1.62	2.04	2.58	2.27
Ho	0.38	0.30	0.30	0.63	0.38	0.50	0.61	0.52
Er	1.23	0.92	0.95	1.94	1.18	1.54	1.87	1.56
Tm	0.19	0.14	0.15	0.28	0.18	0.24	0.29	0.24
Yb	1.35	1.04	1.06	1.80	1.23	1.58	1.99	1.56
Lu	0.22	0.17	0.16	0.28	0.20	0.25	0.32	0.24
Hf	0.35	0.41	0.52	0.52	0.41	0.45	0.87	0.77
Ta	0.02	0.02	0.02	0.02	0.01	0.01	0.03	0.03
Pb	1.38	1.21	1.19	0.99	0.15	0.38	1.73	0.76
Th	0.09	0.09	0.10	0.09	0.06	0.06	0.17	0.13
U	0.14	0.08	0.06	0.05	0.04	0.15	0.12	0.11
V	291.6	254.8	282.5	312.7	272.9	264.4	270.1	267.6
Cr	1205.56	422.67	49.13	147.49	109.88	627.05	30.93	13.16
Ni	184.14	102.87	48.13	58.36	67.65	217.80	29.35	20.55
Li	21.49	18.98	25.87	11.82	6.73	5.42	20.68	18.10
Be	0.148	0.205	0.155	0.148	0.141	0.158	0.326	0.281

	B-74A	B-52	JB-2	JB-2[1], RV	JB-3	JB-3[2], RV
			N=2			
Longitude	119.938	119.951				
Latitude	15.9751	15.9579				
Unit	altered LV	altered LV				
Occurrence	lapili tuff	massive lava				
SiO_2 (wt%)	57.74	60.19	53.26	53.25		
TiO_2	0.35	0.40	1.17	1.19		
Al_2O_3	17.41	15.34	14.68	14.64		
Fe_2O_3	9.01	9.77	14.30	14.25		
MnO	0.14	0.11	0.22	0.22		
MgO	5.45	4.39	4.55	4.62		
CaO	8.28	5.10	9.78	9.82		
Na_2O	1.09	3.40	2.03	2.04		
K_2O	0.67	1.12	0.42	0.42		
P_2O_5	0.02	0.03	0.09	0.10		
Total	100.16	99.85				
LOI	9.73	3.49				
TAS classification	And	And				
High-Mg classification	LSB-series	LSB-series				
SiO_2 (wt%)	58.17	60.88				
TiO_2	0.35	0.40				
Al_2O_3	17.54	15.52				
FeO*	8.17	8.89				
MnO	0.14	0.11				
MgO	5.49	4.44				
CaO	8.34	5.16				
Na_2O	1.10	3.44				
K_2O	0.68	1.13				
P_2O_5	0.02	0.03				
Total	100.00	100.00				
LOI	9.73	3.49				
Mg#	0.55	0.47				
			N=3		N=3	
Rb (µg/g)	9.55	12.63	6.5	6.4	14.6	14.3
Sr	114.6	115.0	178.4	178.2	403	414
Y	13.70	17.52	25.61	23.56	27.7	24.7
Zr	19.31	26.04	47.35	48.25	95	100
Nb	0.24	0.32	0.518	0.565	2.13	*2.47*
Cs	0.320	0.422	0.8	0.8	0.9	0.87
Ba	17.30	46.52	216.8	218.1	234	234

La	0.69	0.93	2.233	2.281	8.3	8.3
Ce	1.47	2.26	6.515	6.552	21.1	20.8
Pr	0.27	0.35	1.098	1.129	3.07	3.25
Nd	1.51	2.00	6.233	6.392	15.4	15.1
Sm	0.69	0.89	2.232	2.266	4.17	4.08
Eu	0.28	0.33	0.799	0.836	1.27	1.28
Gd	1.20	1.59	3.131	3.123	4.6	4.7
Tb	0.25	0.32	0.5794	0.5863	0.738	0.714
Dy	1.79	2.35	3.896	3.868	4.5	4.44
Ho	0.43	0.56	0.857	0.863	0.9	0.9
Er	1.30	1.73	2.523	2.537	2.6	2.6
Tm	0.20	0.28	0.376	0.393	0.38	0.38
Yb	1.39	1.92	2.502	2.529	2.48	2.44
Lu	0.23	0.31	0.3884	0.3894	0.381	0.366
Hf	0.66	0.88	1.467	1.487	3	3
Ta	0.02	0.03	0.0437	0.0396	0.15	*0.15*
Pb	1.38	0.84	5.4	5.25	5.36	5.04
Th	0.14	0.19	0.2525	0.2576	1.26	1.27
U	0.08	0.14	0.1499	0.1528	0.465	0.468
V	256.2	306.4	567.8	572.4	375	*372.0*
Cr	31.99	3.31	25.51	26.65	61	*58.1*
Ni	31.69	12.60	12.53	14.77	35.7	*36.2*
Li	18.60	6.71	7.98	8.08	7.3	*7.2*
Be	0.262	0.350	0.253	0.273	0.7	*0.8*

[1]JB-2 reference values (RV): Imai, 1995 and Jochum et al., 2016

[2]JB-3 reference values (RV): Imai, 1995 and Dulski, 2001

Unit: UV- upper volcanic unit, LV-lower volcanic unit, DC - dike complex

Table 3. Major and trace element compositions of boninitic glasses and spinel-hosted melt inclusions from northern Zambales ophiolite.

Sample	ZM2-107c-4	ZM2-107c-4b	ZM2-107c-3	ZM2 100Ab-1	ZM2 100Ab-2	ZM2 100Ab-3	ZM2 100Ab-4	ZM2 100Aa-1
Type	LSB	LSB	LSB	HSB	HSB	HSB	HSB	HSB
SiO_2	52.88	53.31	51.77	54.14	51.29		55.06	55.93
SD	0.321	0.206	0.456	0.417	0.246		0.105	0.104
TiO_2	0.21	0.25	0.26	0.25	0.27		0.24	0.25
SD	0.015	0.007	0.022	0.025	0.012		0.024	0.033
Al_2O_3	14.04	14.09	13.90	14.25	13.62		14.35	14.57
SD	0.061	0.035	0.115	0.074	0.070		0.067	0.038
FeO	6.70	6.92	6.53	6.47	6.53		6.38	6.77
SD	0.037	0.125	0.114	0.079	0.179		0.047	0.182
MnO	0.12	0.10	0.18	0.13	0.10		0.13	0.14
SD	0.066	0.023	0.028	0.021	0.035		0.017	0.029
MgO	6.98	7.06	7.09	5.48	5.47		5.55	5.64
SD	0.010	0.118	0.107	0.021	0.129		0.059	0.045
CaO	11.12	11.24	11.30	10.21	10.12		10.08	10.23
SD	0.053	0.101	0.108	0.121	0.081		0.081	0.152
Na_2O	1.40	1.38	1.39	1.72	1.69		1.74	1.82
SD	0.045	0.065	0.052	0.041	0.034		0.056	0.053
K_2O	0.25	0.25	0.26	0.29	0.30		0.29	0.31
SD	0.016	0.032	0.012	0.036	0.032		0.013	0.015
H_2O (wt%)	0.998	1.255	0.823	1.129	1.151	1.201	1.119	0.918
error ($\pm1\sigma$)	0.048	0.059	0.040	0.055	0.057	0.059	0.055	0.044
Total	93.697	94.600	92.689	92.955	89.377		93.818	95.644
SiO_2	56.432	56.353	55.850	58.239	57.381		58.688	58.477
TiO_2	0.220	0.263	0.286	0.274	0.298		0.253	0.260
Al_2O_3	14.986	14.895	14.998	15.335	15.237		15.298	15.231
FeO	7.149	7.314	7.046	6.964	7.305		6.798	7.076
MnO	0.132	0.109	0.195	0.138	0.109		0.134	0.145
MgO	7.446	7.459	7.648	5.896	6.123		5.920	5.896
CaO	11.870	11.878	12.195	10.983	11.319		10.744	10.692
Na_2O	1.497	1.462	1.498	1.855	1.891		1.851	1.902
K_2O	0.269	0.266	0.284	0.316	0.336		0.314	0.322
$R_{baseline}$	6.8127	7.2343	7.1211	6.9249	7.0112	6.9852	7.0236	6.9607
ΔR	0.1476	0.1941	0.1293	0.1524	0.1577	0.1645	0.1532	0.1218
$\Delta R/R_{baseline}$	0.0217	0.0268	0.0182	0.0220	0.0225	0.0235	0.0218	0.0175

Calibration	Bas	Bas	Bas	And	And	And	And	And
H_2O (wt%)	0.998	1.255	0.823	1.129	1.151	1.201	1.119	0.918
error (±1σ)	0.048	0.059	0.040	0.055	0.057	0.059	0.055	0.044
Total	100.000	100.000	100.000	100.000	100.000		100.000	100.000
Li	7.053	6.782	7.057	8.248	7.769	8.125	8.200	8.308
B	15.094	15.103	15.162	17.127	16.054	17.365	17.685	18.599
Sc	40.548	40.636	41.763	36.375	35.991	35.331	35.898	35.712
Ti	1474.53	1478.11	1513.23	1680.33	1668.17	1649.75	1681.65	1674.67
V	270.909	268.352	273.862	238.285	234.974	235.517	237.893	244.252
Cr	252.356	248.526	253.546	82.409	84.206	83.651	95.200	91.901
Co	34.389	33.947	34.768	31.722	31.032	31.584	31.804	31.621
Ni	50.629	48.564	48.170	58.370	57.443	59.866	59.043	58.453
Rb	8.029	8.030	8.045	8.928	8.766	8.989	8.749	8.887
Sr	65.405	66.413	66.432	70.656	70.072	69.316	69.955	70.237
Y	7.943	8.156	7.955	11.555	11.447	11.084	11.129	11.036
Zr	11.926	12.149	12.183	16.305	16.005	15.872	15.826	15.509
Nb	0.216	0.237	0.244	0.287	0.278	0.276	0.276	0.289
Cs	0.747	0.738	0.736	0.887	0.852	0.864	0.876	0.894
Ba	26.396	27.065	26.677	34.036	33.611	33.567	33.817	34.119
La	0.599	0.613	0.609	0.694	0.696	0.680	0.693	0.679
Ce	1.487	1.529	1.499	1.780	1.741	1.737	1.751	1.774
Pr	0.210	0.217	0.210	0.262	0.261	0.259	0.254	0.264
Nd	1.095	1.118	1.084	1.418	1.420	1.402	1.449	1.454
Sm	0.435	0.460	0.460	0.661	0.648	0.636	0.624	0.625
Eu	0.186	0.196	0.182	0.246	0.245	0.245	0.241	0.252
Gd	0.754	0.815	0.783	1.144	1.077	1.103	1.091	1.074
Tb	0.158	0.163	0.160	0.231	0.227	0.222	0.229	0.217
Dy	1.243	1.286	1.272	1.808	1.759	1.762	1.758	1.734
Ho	0.288	0.291	0.286	0.411	0.413	0.395	0.405	0.397
Er	0.930	0.993	0.961	1.327	1.316	1.298	1.307	1.316
Tm	0.147	0.141	0.152	0.205	0.200	0.193	0.194	0.190
Yb	1.086	1.120	1.103	1.510	1.465	1.454	1.455	1.482
Lu	0.161	0.169	0.174	0.234	0.234	0.223	0.229	0.227
Hf	0.435	0.444	0.398	0.570	0.549	0.577	0.584	0.605
Ta	0.019	0.018	0.018	0.023	0.019	0.019	0.020	0.024
Pb	1.865	1.864	1.887	2.063	1.965	2.004	2.052	2.067
Th	0.118	0.117	0.117	0.140	0.139	0.146	0.144	0.145
U	0.112	0.112	0.109	0.116	0.115	0.121	0.116	0.117

Sample	ZM2 100Aa-3	ZM2 100Aa-4	B-5-8_1	B-5-8_2	B-5-8_3	B-7-11rim-1	B-7-11rim-3	B-7-11rim-4
Type	HSB	HSB	HSB	HSB	HSB	HSB	HSB	HSB
SiO_2	56.35	54.05	55.90	55.81	55.83	56.27	56.04	56.22
SD	0.178	0.264	0.129	0.187	0.227	0.333	0.391	0.061
TiO_2	0.28	0.25	0.27	0.27	0.23	0.27	0.26	0.24
SD	0.004	0.025	0.024	0.013	0.044	0.036	0.024	0.048
Al_2O_3	14.62	14.13	14.60	14.58	14.50	14.48	14.54	14.56
SD	0.120	0.133	0.094	0.172	0.070	0.022	0.101	0.020
FeO	6.71	6.53	6.83	6.69	6.68	6.74	6.87	6.95
SD	0.116	0.207	0.045	0.050	0.173	0.101	0.234	0.129
MnO	0.12	0.10	0.12	0.12	0.16	0.16	0.14	0.14
SD	0.010	0.010	0.040	0.027	0.046	0.044	0.048	0.066
MgO	5.72	5.58	5.78	5.77	5.71	5.76	5.59	5.75
SD	0.063	0.020	0.089	0.067	0.097	0.057	0.082	0.064
CaO	10.29	10.22	10.36	10.27	10.30	10.18	10.23	10.20
SD	0.124	0.055	0.106	0.095	0.070	0.033	0.094	0.120
Na_2O	1.78	1.73	1.78	1.75	1.77	1.74	1.72	1.78
SD	0.015	0.071	0.027	0.040	0.043	0.013	0.032	0.052
K_2O	0.29	0.31	0.30	0.30	0.32	0.29	0.29	0.28
SD	0.013	0.013	0.013	0.027	0.005	0.027	0.010	0.022
H_2O (wt%)		1.122	1.053	1.197	0.825	1.180	0.926	1.008
error ($\pm1\sigma$)		0.055	0.051	0.059	0.039	0.058	0.045	0.049
Total	96.165	92.895	95.925	95.558	95.500	95.881	95.679	96.114
SiO_2	58.599	58.187	58.273	58.400	58.458	58.692	58.573	58.490
TiO_2	0.287	0.268	0.276	0.280	0.246	0.280	0.276	0.251
Al_2O_3	15.203	15.213	15.219	15.263	15.187	15.099	15.197	15.152
FeO	6.981	7.025	7.124	7.002	6.991	7.030	7.181	7.232
MnO	0.121	0.112	0.125	0.124	0.166	0.168	0.144	0.143
MgO	5.951	6.010	6.022	6.035	5.974	6.006	5.847	5.982
CaO	10.705	10.998	10.799	10.751	10.785	10.612	10.688	10.609
Na_2O	1.852	1.859	1.854	1.832	1.858	1.815	1.795	1.847
K_2O	0.302	0.329	0.308	0.313	0.335	0.299	0.300	0.294
$R_{baseline}$	6.4173	6.6646	6.0875	7.0885	6.8253	7.5358	6.9782	7.1651
ΔR	0.1292	0.1457	0.1242	0.1664	0.1059	0.1741	0.1233	0.1392
$\Delta R/R_{baseline}$	0.0201	0.0219	0.0204	0.0235	0.0155	0.0231	0.0177	0.0194
Calibration	And	And	And	And	And	And	And	And

H_2O (wt%)		1.122	1.053	1.197	0.825	1.180	0.926	1.008
error (±1σ)		0.055	0.051	0.059	0.039	0.058	0.045	0.049
Total	100.000	100.000	100.000	100.000	100.000	100.000	100.000	100.000
Li	8.610	8.388	8.415	8.111	8.257	8.163	8.205	7.990
B	19.082	18.371	20.310	20.361	20.795	24.442	23.745	23.254
Sc	35.828	35.115	38.701	36.104	35.762	35.560	35.306	35.684
Ti	1712.2	1675.1	1692.0	1652.4	1665.4	1628.8	1644.4	1657.9
V	249.824	243.778	256.492	236.580	241.012	240.761	238.338	237.644
Cr	92.875	95.125	292.797	92.112	90.188	96.139	90.123	96.120
Co	32.796	31.796	36.952	31.246	31.098	31.806	30.605	30.501
Ni	59.183	58.427	83.331	54.372	53.399	57.307	54.157	53.117
Rb	9.170	8.846	8.857	8.806	8.812	8.963	8.787	8.403
Sr	71.571	69.795	70.769	69.971	70.178	68.478	69.732	71.129
Y	11.128	10.859	11.128	10.948	10.838	10.698	10.720	10.842
Zr	15.709	15.269	15.668	15.591	15.350	14.986	15.217	15.274
Nb	0.290	0.278	0.281	0.278	0.282	0.269	0.274	0.272
Cs	0.944	0.899	0.894	0.872	0.895	0.900	0.878	0.837
Ba	34.711	34.227	33.892	32.884	33.672	33.241	33.424	33.682
La	0.709	0.697	0.699	0.674	0.684	0.661	0.674	0.691
Ce	1.832	1.808	1.797	1.694	1.742	1.693	1.729	1.763
Pr	0.264	0.261	0.267	0.257	0.253	0.250	0.258	0.258
Nd	1.424	1.429	1.487	1.346	1.394	1.409	1.395	1.414
Sm	0.626	0.638	0.645	0.600	0.623	0.614	0.606	0.615
Eu	0.255	0.250	0.253	0.244	0.245	0.236	0.242	0.251
Gd	1.114	1.083	1.094	1.033	1.100	1.034	1.102	1.084
Tb	0.221	0.227	0.228	0.217	0.218	0.216	0.224	0.214
Dy	1.746	1.741	1.742	1.637	1.679	1.612	1.648	1.674
Ho	0.398	0.392	0.412	0.390	0.404	0.379	0.387	0.407
Er	1.290	1.289	1.305	1.282	1.299	1.209	1.262	1.296
Tm	0.197	0.197	0.204	0.188	0.195	0.184	0.195	0.193
Yb	1.439	1.429	1.453	1.396	1.428	1.389	1.398	1.455
Lu	0.225	0.223	0.221	0.216	0.224	0.214	0.216	0.227
Hf	0.540	0.545	0.557	0.570	0.565	0.546	0.534	0.548
Ta	0.021	0.022	0.023	0.021	0.020	0.024	0.023	0.021
Pb	2.146	2.066	2.005	2.053	2.007	2.069	2.034	2.062
Th	0.133	0.142	0.138	0.131	0.136	0.131	0.132	0.136
U	0.123	0.123	0.117	0.108	0.113	0.115	0.113	0.112

Sample	ZM-2 100Ac-1_gmass	ZM-2 100Ac-2_gmass	ZM-2 100Ac-4_gmass	B-7-11 gmass-2	B-7-11 gmass-3	ZM2-136_1	ZM2-136_2	ZM2-141_1
Type	HSB gmass	HSB gmass	HSB gmass	HSB gmass	HSB gmass	LSB-series	LSB-series	LSB-series
SiO_2	56.24	58.99	56.46	58.65	57.26	56.36	55.84	56.90
SD	0.002	0.151	0.709	0.037	0.503	0.094	0.494	0.278
TiO_2	0.28	0.27	0.29	0.28	0.27	0.34	0.33	0.35
SD	0.025	0.037	0.016	0.043	0.029	0.033	0.023	0.037
Al_2O_3	14.72	16.30	14.92	16.04	15.59	15.00	15.77	14.74
SD	0.127	0.144	0.220	0.157	0.194	0.033	1.187	0.089
FeO	6.94	5.50	6.43	6.53	6.66	8.01	7.72	8.23
SD	0.157	0.152	0.152	0.234	0.520	0.098	0.528	0.106
MnO	0.12	0.03	0.11	0.12	0.13	0.15	0.16	0.17
SD	0.029	0.018	0.031	0.024	0.032	0.058	0.018	0.046
MgO	4.89	2.49	3.97	3.04	3.23	4.77	4.60	4.45
SD	0.132	0.050	0.473	0.163	0.152	0.068	0.249	0.039
CaO	8.83	7.20	8.12	7.77	7.58	9.53	9.84	9.41
SD	0.089	0.116	0.718	0.094	0.102	0.010	0.439	0.081
Na_2O	1.45	2.04	1.64	1.89	1.54	1.97	1.93	1.97
SD	0.027	0.061	0.097	0.022	0.048	0.073	0.034	0.015
K_2O	0.26	0.37	0.28	0.35	0.28	0.26	0.25	0.27
SD	0.021	0.003	0.020	0.026	0.016	0.002	0.022	0.028
H_2O (wt%)	1.491	1.490	1.995	2.845	3.062	1.484	1.359	1.130
error ($\pm1\sigma$)	0.075	0.075	0.102	0.067	0.072	0.075	0.068	0.056
Total	93.736	93.182	92.221	94.663	92.562	96.405	96.453	96.490
SiO_2	60.002	63.306	61.218	61.958	61.864	58.460	57.897	58.974
TiO_2	0.297	0.290	0.314	0.294	0.296	0.357	0.338	0.367
Al_2O_3	15.707	17.488	16.184	16.942	16.842	15.560	16.354	15.276
FeO	7.400	5.904	6.977	6.899	7.198	8.308	7.999	8.532
MnO	0.126	0.036	0.115	0.124	0.140	0.155	0.171	0.173
MgO	5.213	2.671	4.302	3.213	3.495	4.949	4.772	4.611
CaO	9.423	7.726	8.806	8.211	8.189	9.890	10.205	9.750
Na_2O	1.551	2.184	1.781	1.991	1.668	2.046	2.004	2.041
K_2O	0.280	0.394	0.304	0.368	0.308	0.275	0.262	0.275
$R_{baseline}$	6.0336	6.0576	6.1246	5.6452	5.9514	7.2719	7.2388	7.2735
ΔR	0.1796	0.1802	0.2483	0.3696	0.4193	0.2153	0.1950	0.1602
$\Delta R/R_{baseline}$	0.0298	0.0297	0.0405	0.0655	0.0705	0.0296	0.0269	0.0220

Calibration	Rhyo	Rhyo	Rhyo	Rhyo	Rhyo	And	And	And
H_2O (wt%)	1.291	1.290	1.760	2.845	3.062	1.484	1.359	1.130
error (±1σ)	0.030	0.030	0.041	0.067	0.072	0.075	0.068	0.056
Total	100.000	100.000	100.000	100.000	100.000	100.000	100.000	100.000
Li				8.182	*1.502*	*4.556*	6.545	6.356
B				21.560	*13.771*	*11.011*	14.419	12.261
Sc				26.645	*30.036*	*24.214*	39.025	37.796
Ti				1622.068	*1196.937*	*1434.758*	2253.901	2180.955
V				182.993	*186.733*	*197.103*	314.265	291.481
Cr				39.226	*231.033*	*9.072*	15.501	8.633
Co				22.471	*26.081*	*22.344*	34.825	31.094
Ni				14.642	*64.270*	*14.079*	22.296	17.914
Rb				10.158	*5.654*	*4.360*	6.623	6.064
Sr				85.023	*45.820*	*97.583*	106.826	103.046
Y				10.498	*8.216*	*6.807*	11.333	11.155
Zr				16.799	*10.994*	*11.319*	18.763	18.573
Nb				0.312	*0.184*	*0.144*	0.238	0.225
Cs				0.997	*0.570*	*0.353*	0.575	0.524
Ba				40.007	*21.730*	*19.824*	30.878	29.518
La				0.788	*0.450*	*0.480*	0.784	0.754
Ce				1.880	*1.149*	*1.283*	2.093	1.972
Pr				0.263	*0.177*	*0.193*	0.304	0.294
Nd				1.406	*0.961*	*1.028*	1.719	1.626
Sm				0.578	*0.449*	*0.440*	0.734	0.701
Eu				0.222	*0.177*	*0.195*	0.294	0.291
Gd				0.993	*0.799*	*0.694*	1.276	1.188
Tb				0.204	*0.166*	*0.142*	0.246	0.219
Dy				1.554	*1.250*	*1.086*	1.813	1.776
Ho				0.357	*0.300*	*0.248*	0.431	0.395
Er				1.204	*0.958*	*0.792*	1.351	1.291
Tm				0.179	*0.151*	*0.118*	0.199	0.191
Yb				1.375	*1.056*	*0.856*	1.453	1.408
Lu				0.211	*0.168*	*0.133*	0.226	0.213
Hf				0.607	*0.391*	*0.402*	0.669	0.679
Ta				0.022	*0.014*	*0.010*	0.018	0.019
Pb				2.480	*1.353*	*1.134*	1.640	1.543
Th				0.155	*0.094*	*0.091*	0.153	0.139
U				0.136	*0.072*	*0.076*	0.116	0.114

Sample	ZM2-141_4	ZM2-141_5	ZM2-148_1	ZM2-148_5	spl1-MI1-1	spl1-MI3-1	spl1-MI5-1	spl1-MI8-1
Type	LSB-series	LSB-series	LSB-series	LSB-series	LSB melt inc.	LSB melt inc.	LSB melt inc.	LSB melt inc.
SiO_2	56.05	54.27	55.76	55.18	52.91	54.05	52.37	51.67
SD	0.085	0.079	0.112	0.104	0.343	0.434	0.650	0.344
TiO_2	0.32	0.29	0.33	0.36	0.16	0.15	0.16	0.16
SD	0.037	0.009	0.035	0.022	0.041	0.022	0.083	0.018
Al_2O_3	14.73	18.12	15.02	15.09	12.52	12.25	11.86	11.84
SD	0.103	0.187	0.055	0.255	0.207	0.462	0.016	0.166
FeO	7.92	6.27	7.92	7.77	7.56	5.70	6.04	6.49
SD	0.057	0.229	0.153	0.056	0.287	0.030	0.253	0.182
MnO	0.10	0.10	0.19	0.14	0.19	0.16	0.20	0.12
SD	0.053	0.063	0.033	0.022	0.056	0.033	0.066	0.015
MgO	4.64	3.64	4.80	4.75	11.64	12.24	11.49	12.04
SD	0.113	0.077	0.094	0.122	0.039	0.435	0.824	0.268
CaO	9.21	10.65	9.54	9.49	11.20	11.28	10.11	10.98
SD	0.130	0.134	0.098	0.072	0.030	0.170	0.074	0.286
Na_2O	1.97	2.08	1.85	1.93	0.45	0.63	0.58	0.46
SD	0.089	0.036	0.049	0.030	0.069	0.078	0.068	0.034
K_2O	0.27	0.21	0.28	0.28	0.12	0.16	0.18	0.11
SD	0.008	0.030	0.021	0.004	0.002	0.004	0.004	0.286
H_2O (wt%)	1.235	1.472	2.056	1.849	2.370	2.440	2.707	1.755
error ($\pm1\sigma$)	0.061	0.074	0.105	0.094	0.122	0.126	0.141	0.089
Total	95.220	95.638	95.693	94.987	96.755	96.624	92.982	93.866
SiO_2	58.864	56.750	58.274	58.088	54.685	55.943	56.324	55.043
TiO_2	0.336	0.303	0.347	0.381	0.167	0.156	0.167	0.175
Al_2O_3	15.473	18.949	15.696	15.886	12.939	12.675	12.759	12.615
FeO	8.320	6.561	8.276	8.179	7.815	5.904	6.492	6.910
MnO	0.106	0.106	0.195	0.152	0.198	0.168	0.220	0.129
MgO	4.875	3.806	5.018	4.996	12.031	12.667	12.355	12.824
CaO	9.676	11.134	9.967	9.991	11.574	11.674	10.871	11.697
Na_2O	2.064	2.171	1.931	2.033	0.466	0.653	0.625	0.491
K_2O	0.285	0.219	0.295	0.293	0.125	0.160	0.189	0.116
$R_{baseline}$	7.2048	7.1202	6.8112	6.0956	6.0778	6.1035	6.1238	7.0142
ΔR	0.1750	0.2089	0.2850	0.2280	0.2952	0.3056	0.3416	0.2484
$\Delta R/R_{baseline}$	0.0243	0.0293	0.0418	0.0374	0.0486	0.0501	0.0558	0.0354
Calibration	And	And	And	And	And	And	And	And

H_2O (wt%)	1.235	1.472	2.056	1.849	2.370	2.440	2.707	1.755
error ($\pm 1\sigma$)	0.061	0.074	0.105	0.094	0.122	0.126	0.141	0.089
Total	100.000	100.000	100.000	100.000	100.000	100.000	100.000	100.000
Li	6.342	6.792	6.417	6.463	6.546	6.292	5.000	5.135
B	11.652	12.825	13.538	13.765	12.604	11.845	9.472	10.561
Sc	38.203	40.485	36.286	37.822	55.095	50.103	40.711	46.038
Ti	#######	#######	#######	#######	876.974	950.434	752.875	810.285
V	295.140	318.073	286.469	298.777	266.279	263.997	217.595	242.322
Cr	9.534	14.838	16.817	17.852	60.516	175.236	151.652	101.162
Co	31.816	35.252	32.466	33.771	37.234	31.160	26.910	31.522
Ni	18.624	21.583	20.795	21.609	153.195	192.475	154.735	191.167
Rb	6.139	6.571	6.076	6.394	4.240	3.921	2.900	2.713
Sr	102.317	118.229	104.270	104.862	22.158	21.385	15.018	14.276
Y	11.410	11.708	10.394	10.667	6.573	6.452	5.468	5.978
Zr	19.066	19.611	17.436	18.071	3.928	4.327	3.551	3.596
Nb	0.236	0.247	0.223	0.227	0.152	0.120	0.068	0.101
Cs	0.525	0.565	0.524	0.555	0.436	0.421	0.352	0.312
Ba	30.209	31.998	28.561	29.130	14.008	12.961	9.398	8.273
La	0.764	0.798	0.703	0.728	0.291	0.266	0.209	0.223
Ce	2.004	2.115	1.881	1.931	0.631	0.594	0.492	0.444
Pr	0.306	0.309	0.283	0.284	0.079	0.078	0.065	0.063
Nd	1.681	1.756	1.525	1.595	0.424	0.436	0.282	0.326
Sm	0.726	0.739	0.675	0.681	0.235	0.217	0.161	0.178
Eu	0.294	0.301	0.278	0.277	0.082	0.094	0.067	0.075
Gd	1.219	1.219	1.117	1.128	0.403	0.483	0.368	0.503
Tb	0.241	0.245	0.209	0.217	0.097	0.095	0.089	0.093
Dy	1.823	1.831	1.624	1.698	1.017	0.901	0.780	0.921
Ho	0.411	0.424	0.376	0.382	0.219	0.240	0.218	0.196
Er	1.300	1.356	1.205	1.223	0.860	0.823	0.661	0.701
Tm	0.203	0.202	0.192	0.191	0.118	0.132	0.104	0.107
Yb	1.445	1.458	1.304	1.326	0.905	0.910	0.813	0.865
Lu	0.228	0.238	0.205	0.209	0.160	0.170	0.142	0.143
Hf	0.675	0.689	0.659	0.609	0.221	0.192	0.141	0.135
Ta	0.020	0.021	0.016	0.016	0.011	0.018	0.014	0.003
Pb	1.519	1.641	1.565	1.589	1.015	0.923	0.773	0.597
Th	0.149	0.161	0.129	0.145	0.061	0.055	0.044	0.052
U	0.116	0.112	0.101	0.109	0.047	0.042	0.045	0.029

Sample	spl2-MI1-1	spl2-MI2-1	spl2-MI3-1
Type	LSB melt inc.	LSB melt inc.	LSB melt inc.
SiO_2	52.45	52.54	52.09
SD	0.414	0.591	1.223
TiO_2	0.18	0.19	0.20
SD	0.042	0.001	0.022
Al_2O_3	11.96	11.75	11.74
SD	0.092	0.083	0.756
FeO	6.32	6.85	6.92
SD	0.262	0.078	0.090
MnO	0.15	0.13	0.17
SD	0.021	0.083	0.074
MgO	11.11	11.62	12.31
SD	0.603	0.451	0.223
CaO	9.13	9.46	9.44
SD	0.078	0.159	0.134
Na_2O	1.38	1.23	1.29
SD	0.114	0.035	0.128
K_2O	0.22	0.17	0.18
SD	0.078	0.010	0.001
H_2O (wt%)	2.669	2.828	2.608
error ($\pm1\sigma$)	0.139	0.147	0.135
Total	92.897	93.942	94.354
SiO_2	56.463	55.929	55.212
TiO_2	0.192	0.201	0.217
Al_2O_3	12.872	12.508	12.445
FeO	6.802	7.291	7.338
MnO	0.159	0.141	0.182
MgO	11.964	12.369	13.047
CaO	9.825	10.072	10.001
Na_2O	1.490	1.309	1.371
K_2O	0.233	0.181	0.188
$R_{baseline}$	5.7182	6.1933	6.8570
ΔR	0.3143	0.3615	0.3680
$\Delta R/R_{baseline}$	0.0550	0.0584	0.0537
Calibration	And	And	And

H_2O (wt%)	2.669	2.828	2.608
error (±1σ)	0.139	0.147	0.135
Total	100.000	100.000	100.000
Li	4.779	5.975	5.726
B	5.634	7.093	7.912
Sc	32.535	40.525	39.104
Ti	1181.14	1239.33	1192.31
V	170.263	191.148	185.853
Cr	105.564	87.126	86.630
Co	31.155	34.903	35.198
Ni	147.969	168.885	176.014
Rb	3.597	3.774	3.544
Sr	70.532	71.161	64.837
Y	6.688	7.411	7.218
Zr	11.025	12.118	11.838
Nb	0.118	0.115	0.119
Cs	0.304	0.293	0.296
Ba	20.275	19.547	18.096
La	0.408	0.439	0.424
Ce	1.117	1.185	1.086
Pr	0.176	0.191	0.189
Nd	1.076	1.257	1.146
Sm	0.421	0.525	0.498
Eu	0.187	0.190	0.207
Gd	0.751	0.951	0.734
Tb	0.124	0.159	0.167
Dy	0.947	1.252	1.226
Ho	0.253	0.272	0.288
Er	0.710	0.938	0.878
Tm	0.120	0.116	0.144
Yb	0.857	0.984	0.935
Lu	0.142	0.154	0.125
Hf	0.389	0.275	0.484
Ta	0.011	0.000	0.009
Pb	0.942	1.014	0.922
Th	0.057	0.102	0.072
U	0.059	0.052	0.064

Table 4 Whole-rock major and trace element compositions of Coto Block dikes along Bulsa River, eastern Zambales ophiolite

Table 4a. Major element compositions of Coto Block dikes along Bulsa River, Zambales ophiolite

Sample	ZM18-2-4	ZM18-3-2	ZM18-3-3	ZM18-3-4	ZM18-1-1	ZM18-1-2b	ZM18-1-3	ZM18-1-4
Block	Coto Block	Coto Block	Coto Block	Coto Block	Coto Block	Coto Block	Coto Block	Coto Block
Type	Gabbro	Gabbroic dike	Gabbroic dike	Gabbroic dike	Basaltic andesite	Basaltic andesite	Basaltic andesite	Andesite
Locality	Balog-balog, Bulsa	Balog-balog,	Balog-balog,	Balog-balog,	Balog-balog,	Balog-balog,	Balog-balog,	Balog-balog,
SiO_2	48.789	46.924	49.775	48.745	55.182	52.051	55.193	56.166
TiO_2	1.695	1.701	1.373	1.4	1.159	1.461	1.2	1.125
Al_2O_3	15.746	15.708	15.574	14.981	14.68	15.29	14.93	14.851
Fe_2O_3	13.166	14.784	12.283	11.739	13.287	14.745	12.488	12.553
MnO	0.179	0.2	0.187	0.187	0.109	0.123	0.101	0.137
MgO	7.332	6.847	6.793	8.239	4.432	4.346	5.258	4.992
CaO	9.255	10.644	10.599	11.713	7.514	8.737	7.228	7.033
Na_2O	2.361	2.141	2.461	1.867	2.284	2.226	2.168	1.829
K_2O	0.463	0.2	0.145	0.161	0.568	0.282	0.59	0.406
P_2O_5	0.053	0.064	0.043	0.032	0.084	0.081	0.081	0.087
LOI	1.10	0.42	0.26	0.25	1.11	0.18	1.91	1.82
Total	99.04	99.21	99.23	99.06	99.30	99.34	99.24	99.18
SiO_2	49.93	48.01	50.79	49.80	56.33	53.19	56.33	57.36
TiO_2	1.73	1.74	1.40	1.43	1.18	1.49	1.22	1.15
Al_2O_3	16.11	16.07	15.89	15.30	14.98	15.62	15.24	15.17
FeOt	12.12	13.61	11.28	10.79	12.20	13.56	11.47	11.54
MnO	0.18	0.20	0.19	0.19	0.11	0.13	0.10	0.14
MgO	7.50	7.01	6.93	8.42	4.52	4.44	5.37	5.10
CaO	9.47	10.89	10.82	11.97	7.67	8.93	7.38	7.18
Na_2O	2.42	2.19	2.51	1.91	2.33	2.27	2.21	1.87
K_2O	0.47	0.20	0.15	0.16	0.58	0.29	0.60	0.41
P_2O_5	0.05	0.07	0.04	0.03	0.09	0.08	0.08	0.09
LOI	1.10	0.42	0.26	0.25	1.11	0.18	1.91	1.82
Total	100.00	100.00	100.00	100.00	100.00	100.00	100.00	100.00

Sample	ZM18-2-1	ZM18-2-2	ZM18-3-1	ZM18-4-2	ZM18-5-1	ZM18-5-2	ZM18-5-3	ZM18-3-5
Block	Coto Block	Coto Block	Coto Block	Coto Block	Coto Block	Coto Block	Coto Block	Coto Block
Type	Basaltic andesite	Basaltic andesite	Basaltic andesite	Basaltic andesite	Basaltic andesite	Basaltic andesite	Basaltic andesite	Plagiogranite
Locality	Balog-balog, Bulsa	Balog-balog,	Balog-balog,	Balog-balog,	Balog-balog,	Balog-balog,	Balog-balog,	Balog-balog,
SiO_2	52.538	55.695	52.225	53.415	55.782	54.923	55.73	71.595
TiO_2	1.053	1.049	0.803	1.3	0.821	0.749	1.767	0.331
Al_2O_3	15.837	15.622	15.847	15.053	15.595	15.819	14.854	13.035
Fe_2O_3	14.282	9.421	11.892	15.432	12.045	11.825	13.213	4.134
MnO	0.087	0.075	0.187	0.171	0.146	0.179	0.262	0.027
MgO	5.055	6.135	5.97	4.514	5.278	6.061	3.279	1.651
CaO	8.73	8.518	9.196	6.916	6.721	7.091	6.841	6.506
Na_2O	1.574	2.05	2.772	2.353	2.035	2.141	3.229	1.478
K_2O	0.191	0.536	0.341	0.174	0.968	0.468	0.149	0.363
P_2O_5	0.076	0.073	0.063	0.089	0.07	0.059	0.125	0.06
LOI	0.71	1.28	0.58	1.03	2.39	2.07	0.57	1.30
Total	99.42	99.17	99.30	99.42	99.46	99.32	99.45	99.18
SiO_2	53.61	56.70	53.23	54.58	56.77	55.97	56.79	72.49
TiO_2	1.07	1.07	0.82	1.33	0.84	0.76	1.80	0.34
Al_2O_3	16.16	15.90	16.15	15.38	15.87	16.12	15.14	13.20
FeOt	13.11	8.63	10.91	14.19	11.03	10.84	12.12	3.77
MnO	0.09	0.08	0.19	0.17	0.15	0.18	0.27	0.03
MgO	5.16	6.25	6.09	4.61	5.37	6.18	3.34	1.67
CaO	8.91	8.67	9.37	7.07	6.84	7.23	6.97	6.59
Na_2O	1.61	2.09	2.83	2.40	2.07	2.18	3.29	1.50
K_2O	0.19	0.55	0.35	0.18	0.99	0.48	0.15	0.37
P_2O_5	0.08	0.07	0.06	0.09	0.07	0.06	0.13	0.06
LOI	0.71	1.28	0.58	1.03	2.39	2.07	0.57	1.30
Total	100.00	100.00	100.00	100.00	100.00	100.00	100.00	100.00

Sample	ZM18-4-1	ZM18-1-2g	ZM18-2-5	JB-1b	JB-1b RV[1]	NK	NK mean (n=3)
Block	Coto Block	Coto Block	Coto Block				
Type	Plagiogranite	Gabbro	Gabbro				
Locality	Balog-balog, Bulsa	Balog-balog,	Balog-balog,				
SiO_2	73.369	44.725	40.695	53.117	52.230	49.438	
TiO_2	0.197	2.949	3.86	1.264	1.290	1.813	
Al_2O_3	11.957	13.574	11.531	14.414	14.690	17.769	
Fe_2O_3	6.232	19.755	24.601	9.076	9.220	9.543	
MnO	0.024	0.195	0.221	0.145	0.150	0.196	
MgO	0.337	6.394	6.169	8.714	8.320	6.265	
CaO	2.684	9.343	9.735	9.784	9.810	8.721	
Na_2O	4.354	1.576	1.624	2.891	2.690	3.848	
K_2O	0.069	0.393	0.126	1.332	1.350	1.908	
P_2O_5	0.029	0.075	0.038	0.253	0.260	0.728	
LOI	-0.31	0.33	-0.09				
Total	99.25	98.98	98.60				
SiO_2	74.39	46.11	42.33				
TiO_2	0.20	3.04	4.02				
Al_2O_3	12.12	13.99	11.99				
FeOt	5.69	18.33	23.03				
MnO	0.02	0.20	0.23				
MgO	0.34	6.59	6.42				
CaO	2.72	9.63	10.13				
Na_2O	4.41	1.62	1.69				
K_2O	0.07	0.41	0.13				
P_2O_5	0.03	0.08	0.04				
LOI	-0.31	0.33	-0.09				
Total	100.00	100.00	100.00				

Table 4b. Trace element compositions of Coto Block dikes along Bulsa River, Zambales ophiolite

Sample	ZM18-2-4	ZM18-2-4	ZM18-3-2	ZM18-3-2	ZM18-3-2	ZM18-3-4	ZM18-3-4	ZM18-3-4
Glass #	#G102	#G103	#G110	#G111	#G112	#G116	#G117	#G118
ID	Coto dike	Coto dike	Coto dike	Coto dike	Coto dike	Coto dike	Coto dike	Coto dike
Type	Gabbro	Gabbro	Gabbroic dike	Gabbroic dike	Gabbroic dike	Gabbroic dike	Gabbroic dike	Gabbroic dike
Li	5.914	5.975	3.376	3.308	3.411	2.516	2.316	2.545
B	6.181	7.334	6.897	6.904	7.032	11.529	8.479	10.609
Sc	51.853	50.362	44.634	43.593	42.470	44.314	42.606	41.846
Ti	8649	8252	10654	10715	7492	9218	9130	9179
V	497.7	496.0	487.9	465.7	435.1	408.2	373.1	376.8
Cr	6.016	6.092	82.973	74.139	87.569	227.978	218.825	215.910
Co	57.839	56.433	41.878	40.980	40.045	48.106	44.822	47.116
Ni	8.033	6.977	45.197	44.609	42.577	86.028	78.733	83.493
Rb	3.355	3.719	1.096	0.991	1.055	0.668	0.655	0.698
Sr	156.038	160.774	162.557	153.280	160.132	128.780	124.529	133.385
Y	18.692	18.494	18.287	18.390	17.363	15.497	14.439	15.351
Zr	20.933	18.980	27.451	24.608	22.903	35.937	25.526	24.843
Nb	0.463	0.384	0.751	0.940	0.468	0.813	0.788	0.864
Cs	0.063	0.072	0.009	0.005	0.006	0.003	0.003	0.002
Ba	11.450	11.419	5.636	4.669	5.296	3.700	3.386	3.873
La	1.399	1.227	1.577	1.466	1.563	1.083	0.941	1.085
Ce	5.167	4.580	5.173	4.984	5.047	3.816	3.382	3.839
Pr	0.905	0.822	0.899	0.885	0.886	0.706	0.607	0.704
Nd	5.145	4.860	5.230	5.202	5.115	4.193	3.613	4.268
Sm	1.931	1.884	1.949	2.002	1.888	1.644	1.416	1.661
Eu	0.746	0.732	1.138	1.040	1.049	0.816	0.691	0.822
Gd	2.626	2.557	2.623	2.707	2.546	2.361	2.025	2.378
Tb	0.485	0.466	0.495	0.475	0.448	0.415	0.357	0.420
Dy	3.314	3.242	3.348	3.355	3.181	3.021	2.496	2.994
Ho	0.688	0.691	0.711	0.684	0.636	0.636	0.523	0.637
Er	2.048	2.044	2.031	2.056	1.969	1.913	1.575	1.898
Tm	0.290	0.278	0.286	0.273	0.266	0.269	0.231	0.267
Yb	2.000	1.983	1.940	1.963	1.801	1.852	1.493	1.835
Lu	0.288	0.286	0.291	0.282	0.268	0.271	0.227	0.269
Hf	0.748	0.684	0.834	0.776	0.725	1.108	0.770	0.856
Ta	0.036	0.034	0.048	0.062	0.035	0.075	0.061	0.074
Pb	0.108	0.093	0.243	0.224	0.229	0.196	0.084	0.184
Th	0.031	0.023	0.034	0.035	0.037	0.065	0.036	0.040
U	0.009	0.010	0.014	0.011	0.012	0.028	0.012	0.016

Sample	ZM18-1-1	ZM18-1-1	ZM18-1-1	ZM18-1-2bas	ZM18-1-2bas	ZM18-1-2bas	ZM18-1-3	ZM18-1-3
Glass #	#G107	#G108	#G109	#G110	#G111	#G112	#G104	#G105
ID	Coto dike	Coto dike	Coto dike	Coto dike	Coto dike	Coto dike	Coto dike	Coto dike
Type	Basaltic andesite	Basaltic andesite	Basaltic andesite	Basaltic andesite	Basaltic andesite	Basaltic andesite	Basaltic andesite	Basaltic andesite
Li	8.167	8.373	8.377	3.209	3.247	3.125	12.774	13.430
B	6.444	6.721	6.708	4.715	5.035	4.802	9.198	9.039
Sc	37.351	37.359	35.384	40.271	40.034	39.903	37.475	37.661
Ti	7683	7654	6858	9320	9200	8952	7552	8333
V	383.5	390.1	347.9	480.0	479.5	472.0	405.0	398.9
Cr	12.402	13.274	7.855	19.022	16.699	14.445	6.590	7.184
Co	33.575	34.220	32.315	42.113	41.320	41.238	30.301	31.392
Ni	7.450	7.300	5.159	14.412	12.384	11.449	4.903	5.267
Rb	2.767	2.703	3.081	1.244	1.237	1.241	3.679	3.810
Sr	154.667	151.829	156.644	155.753	155.745	157.669	147.301	145.156
Y	25.011	24.573	23.683	23.213	23.153	23.303	24.499	23.500
Zr	53.587	53.544	50.373	50.381	50.074	49.180	49.671	52.027
Nb	0.870	0.875	0.631	0.927	0.788	0.802	0.673	0.656
Cs	0.073	0.065	0.078	0.013	0.015	0.015	0.177	0.181
Ba	9.615	9.215	9.667	9.054	8.785	8.922	10.810	11.600
La	1.624	1.786	1.765	1.646	1.604	1.697	4.104	1.390
Ce	5.585	6.034	5.902	5.569	5.467	5.656	12.294	4.945
Pr	1.025	1.067	1.027	1.001	0.985	1.023	1.952	0.899
Nd	6.025	6.212	6.054	5.937	5.739	5.934	10.289	5.383
Sm	2.367	2.357	2.228	2.313	2.191	2.224	3.009	2.198
Eu	0.758	0.759	0.728	0.909	0.899	0.914	0.883	0.614
Gd	3.418	3.296	3.190	3.196	3.174	3.211	3.804	3.250
Tb	0.624	0.611	0.581	0.586	0.576	0.597	0.625	0.577
Dy	4.519	4.291	4.185	4.057	4.058	4.136	4.329	4.155
Ho	0.945	0.913	0.863	0.858	0.857	0.853	0.892	0.883
Er	2.890	2.780	2.672	2.625	2.587	2.674	2.736	2.754
Tm	0.420	0.395	0.387	0.375	0.361	0.372	0.382	0.395
Yb	2.890	2.732	2.682	2.571	2.534	2.593	2.682	2.752
Lu	0.452	0.431	0.420	0.384	0.382	0.394	0.411	0.417
Hf	1.759	1.676	1.622	1.545	1.547	1.558	1.546	1.683
Ta	0.073	0.069	0.057	0.061	0.059	0.061	0.044	0.051
Pb	0.115	0.094	0.074	0.064	0.082	0.045	0.394	0.308
Th	0.160	0.182	0.173	0.161	0.144	0.146	0.169	0.172
U	0.078	0.075	0.068	0.054	0.062	0.055	0.081	0.079

Sample	ZM18-1-3	ZM18-1-4	ZM18-1-4	ZM18-1-4	ZM18-2-1	ZM18-2-1	ZM18-2-1	ZM18-3-1
Glass #	#G106	#G110	#G111	#G112	#G116	#G117	#G118	#G107
ID	Coto dike	Coto dike	Coto dike	Coto dike	Coto dike	Coto dike	Coto dike	Coto dike
Type	Basaltic andesite	Andesite	Andesite	Andesite	Basaltic andesite	Basaltic andesite	Basaltic andesite	Basaltic andesite
Li	12.810	14.237	13.717	13.872	4.475	4.725	4.758	3.016
B	8.963	6.487	7.058	7.087	5.831	5.770	6.525	5.741
Sc	39.199	38.282	38.483	37.670	36.340	37.912	37.482	40.476
Ti	8122	8194	7993	8407	6798	7213	6944	5416
V	418.7	404.7	401.8	412.6	380.9	399.7	387.1	268.6
Cr	13.899	11.080	14.239	10.585	30.259	44.405	31.685	7.907
Co	31.938	28.715	28.425	29.386	42.579	44.622	44.582	39.691
Ni	6.737	6.724	6.544	5.783	18.888	22.411	21.105	6.531
Rb	3.415	3.510	3.173	3.166	0.905	0.847	0.962	1.279
Sr	140.583	135.940	138.412	139.812	164.199	159.131	165.045	142.938
Y	25.726	28.856	28.931	29.515	21.560	21.400	21.928	19.901
Zr	48.964	59.271	59.524	59.325	46.928	45.228	46.056	45.940
Nb	0.894	0.805	0.792	0.849	0.621	1.116	0.672	0.568
Cs	0.170	0.222	0.207	0.195	0.008	0.006	0.009	0.004
Ba	10.610	11.818	11.763	11.912	4.899	4.827	5.046	7.420
La	3.549	1.814	1.937	1.794	1.635	1.491	1.563	1.518
Ce	11.023	6.106	6.530	6.109	5.731	5.086	5.341	5.071
Pr	1.837	1.109	1.185	1.124	0.985	0.881	0.939	0.886
Nd	10.098	6.601	6.918	6.801	5.678	5.126	5.437	5.118
Sm	3.213	2.582	2.671	2.691	2.076	1.951	2.020	1.932
Eu	0.855	0.737	0.756	0.782	0.464	0.456	0.467	0.825
Gd	4.084	3.849	3.995	4.038	2.940	2.807	2.928	2.711
Tb	0.659	0.693	0.715	0.734	0.530	0.525	0.536	0.491
Dy	4.581	5.034	5.116	5.276	3.727	3.691	3.797	3.443
Ho	0.951	1.072	1.076	1.118	0.795	0.791	0.818	0.727
Er	2.939	3.285	3.306	3.445	2.447	2.378	2.468	2.224
Tm	0.405	0.475	0.481	0.489	0.346	0.343	0.351	0.305
Yb	2.829	3.207	3.268	3.355	2.430	2.380	2.459	2.165
Lu	0.443	0.483	0.493	0.505	0.389	0.377	0.388	0.330
Hf	1.599	1.925	1.888	1.955	1.473	1.404	1.453	1.263
Ta	0.054	0.062	0.061	0.067	0.069	0.071	0.072	0.045
Pb	0.320	0.193	0.257	0.206	0.067	0.064	0.032	0.190
Th	0.185	0.198	0.217	0.199	0.158	0.139	0.147	0.091
U	0.090	0.082	0.087	0.092	0.067	0.067	0.061	0.063

Sample	ZM18-3-1	ZM18-3-1	ZM18-4-2	ZM18-4-2	ZM18-4-2	ZM18-5-1	ZM18-5-1	ZM18-5-1
Glass #	#G108	#G109	#G101	#G102	#G103	#G101	#G102	#G103
ID	Coto dike	Coto dike	Coto dike	Coto dike	Coto dike	Coto dike	Coto dike	Coto dike
Type	Basaltic andesite	Basaltic andesite	Basaltic andesite	Basaltic andesite	Basaltic andesite	Basaltic andesite	Basaltic andesite	Basaltic andesite
Li	3.316	3.050	3.619	3.566	3.611	8.632	10.548	10.266
B	6.261	5.976	9.608	9.828	10.189	8.722	9.314	8.397
Sc	31.137	37.511	33.706	33.631	33.061	35.728	32.528	34.743
Ti	3440	4604	7924	8405	8092	5272	4841	5790
V	224.1	263.3	482.3	471.9	458.8	318.8	283.9	320.3
Cr	5.002	4.017	10.585	13.245	11.487	21.781	20.038	16.778
Co	33.327	37.145	41.870	40.944	40.347	36.851	33.702	35.953
Ni	7.606	5.826	10.748	13.692	12.101	11.916	10.577	10.178
Rb	1.883	1.609	0.710	0.725	0.723	4.092	5.264	5.721
Sr	154.827	146.282	126.151	125.444	124.982	141.263	147.728	142.274
Y	17.554	19.328	28.701	29.049	28.865	22.922	21.647	23.033
Zr	46.184	42.647	65.816	65.851	66.855	40.988	46.764	44.649
Nb	0.377	0.442	0.817	0.915	0.877	0.451	0.395	0.451
Cs	0.006	0.004	0.003	0.001	0.004	0.036	0.043	0.046
Ba	8.444	7.586	9.199	9.050	8.954	10.189	11.247	11.345
La	1.590	1.277	2.103	2.375	2.835	1.560	1.426	1.426
Ce	5.107	4.315	7.281	7.986	9.166	5.255	4.768	4.761
Pr	0.897	0.778	1.287	1.376	1.564	0.906	0.835	0.827
Nd	5.009	4.546	7.373	7.984	8.888	5.410	4.996	5.069
Sm	1.850	1.787	2.813	2.873	3.098	2.101	1.947	2.030
Eu	0.811	0.788	1.004	1.010	1.047	0.737	0.676	0.705
Gd	2.508	2.597	4.064	4.125	4.249	3.020	2.916	3.095
Tb	0.448	0.479	0.707	0.734	0.720	0.549	0.514	0.567
Dy	3.102	3.364	5.085	5.033	5.104	3.902	3.599	3.990
Ho	0.619	0.734	1.069	1.069	1.073	0.839	0.803	0.878
Er	1.933	2.176	3.246	3.243	3.248	2.571	2.385	2.633
Tm	0.274	0.308	0.460	0.459	0.448	0.366	0.349	0.388
Yb	1.904	2.130	3.125	3.135	3.151	2.485	2.437	2.591
Lu	0.293	0.333	0.476	0.475	0.479	0.386	0.371	0.397
Hf	1.310	1.302	2.109	2.080	2.059	1.369	1.488	1.569
Ta	0.045	0.044	0.069	0.066	0.064	0.030	0.028	0.032
Pb	0.241	0.182	0.094	0.086	0.064	0.152	0.133	0.104
Th	0.088	0.085	0.143	0.154	0.165	0.130	0.150	0.147
U	0.057	0.051	0.076	0.072	0.075	0.069	0.087	0.075

Sample	GSJ JB-2	GSJ JB-2 SD	GSJ JB-2 RV[1]	GSJ JB-2 95%CL[1]	USGS BHVO-2	USGS BHVO-2	USGS BHVO-2	USGS BHVO-2_SD
Glass #	#G103				#G104	#G105	#G106	
ID	STD				STD	STD	STD	
Type	STD				STD	STD	STD	
Li	8.27	0.36	8.08	0.15	3.97	4.08	4.00	0.06
B	8.58	1.09	29.98	0.74	4.85	4.74	4.36	0.26
Sc	50.17	0.34	54.08	0.76	30.67	30.71	30.59	0.06
Ti	7038	83			16356	16327	16226	68
V	619.8	16.8	572.4	8.3	311.2	316.8	311.1	3.281
Cr	21.44	1.10	26.65	0.69	268.34	279.15	201.72	41.94
Co	41.05	2.23	37.57	0.67	43.08	43.74	44.54	0.73
Ni	15.41	1.03	14.77	0.51	106.03	106.14	109.34	1.88
Rb	6.0	0.4	6.4	0.11	8.047	8.178	7.900	0.139
Sr	180.7	0.8	178.2	1.5	401.208	402.114	399.332	1.419
Y	21.46	0.21	23.56	0.44	24.61	24.46	24.36	0.12
Zr	41.14	0.50	48.25	0.88	160.41	159.50	159.87	0.46
Nb	0.516	0.033	0.565	0.034	17.4	17.4	17.3	0.1
Cs	0.7	0.1	0.8	0.02	0.077	0.086	0.074	0.006
Ba	231.1	1.9	218.1	2.7	134.9	134.8	133.6	0.7
La	2.173	0.030	2.281	0.037	14.9	14.8	14.7	0.098
Ce	6.941	0.098	6.552	0.087	38.45	38.03	37.88	0.30
Pr	1.157	0.017	1.129	0.024	5.309	5.240	5.246	0.038
Nd	6.436	0.102	6.392	0.063	24.66	24.40	24.61	0.14
Sm	2.219	0.041	2.266	0.023	6.021	6.018	5.976	0.025
Eu	0.812	0.006	0.836	0.012	2.054	2.065	2.086	0.016
Gd	2.991	0.024	3.123	0.049	6.074	5.982	6.079	0.055
Tb	0.535	0.014	0.5863	0.0096	0.874	0.875	0.881	0.004
Dy	3.766	0.032	3.868	0.064	5.248	5.162	5.218	0.044
Ho	0.785	0.009	0.863	0.017	0.938	0.932	0.934	0.003
Er	2.371	0.028	2.537	0.039	2.466	2.477	2.465	0.007
Tm	0.339	0.008	0.393	0.012	0.311	0.311	0.316	0.003
Yb	2.393	0.019	2.529	0.034	1.950	1.943	1.960	0.009
Lu	0.359	0.006	0.3894	0.0058	0.270	0.273	0.274	0.002
Hf	1.299	0.012	1.487	0.033	4.221	4.135	4.137	0.049
Ta	0.036	0.003	0.0396	0.003	1.090	1.100	1.103	0.006
Pb	0.412	0.352	5.25	0.11	0.312	0.503	0.085	0.209
Th	0.241	0.001	0.2576	0.0048	1.208	1.183	1.162	0.023
U	0.129	0.011	0.1528	0.0028	0.396	0.388	0.340	0.031

Sample	GSJ JB-2	GSJ JB-2 SD	GSJ JB-2 RV[1]	GSJ JB-2 95%CL[1]	USGS BHVO-2	USGS BHVO-2	USGS BHVO-2	USGS BHVO-2_SD
Glass #	#G103				#G104	#G105	#G106	
ID	STD				STD	STD	STD	
Type	STD				STD	STD	STD	
Li	8.27	0.36	8.08	0.15	3.97	4.08	4.00	0.06
B	8.58	1.09	29.98	0.74	4.85	4.74	4.36	0.26
Sc	50.17	0.34	54.08	0.76	30.67	30.71	30.59	0.06
Ti	7038	83			16356	16327	16226	68
V	619.8	16.8	572.4	8.3	311.2	316.8	311.1	3.281
Cr	21.44	1.10	26.65	0.69	268.34	279.15	201.72	41.94
Co	41.05	2.23	37.57	0.67	43.08	43.74	44.54	0.73
Ni	15.41	1.03	14.77	0.51	106.03	106.14	109.34	1.88
Rb	6.0	0.4	6.4	0.11	8.047	8.178	7.900	0.139
Sr	180.7	0.8	178.2	1.5	401.208	402.114	399.332	1.419
Y	21.46	0.21	23.56	0.44	24.61	24.46	24.36	0.12
Zr	41.14	0.50	48.25	0.88	160.41	159.50	159.87	0.46
Nb	0.516	0.033	0.565	0.034	17.4	17.4	17.3	0.1
Cs	0.7	0.1	0.8	0.02	0.077	0.086	0.074	0.006
Ba	231.1	1.9	218.1	2.7	134.9	134.8	133.6	0.7
La	2.173	0.030	2.281	0.037	14.9	14.8	14.7	0.098
Ce	6.941	0.098	6.552	0.087	38.45	38.03	37.88	0.30
Pr	1.157	0.017	1.129	0.024	5.309	5.240	5.246	0.038
Nd	6.436	0.102	6.392	0.063	24.66	24.40	24.61	0.14
Sm	2.219	0.041	2.266	0.023	6.021	6.018	5.976	0.025
Eu	0.812	0.006	0.836	0.012	2.054	2.065	2.086	0.016
Gd	2.991	0.024	3.123	0.049	6.074	5.982	6.079	0.055
Tb	0.535	0.014	0.5863	0.0096	0.874	0.875	0.881	0.004
Dy	3.766	0.032	3.868	0.064	5.248	5.162	5.218	0.044
Ho	0.785	0.009	0.863	0.017	0.938	0.932	0.934	0.003
Er	2.371	0.028	2.537	0.039	2.466	2.477	2.465	0.007
Tm	0.339	0.008	0.393	0.012	0.311	0.311	0.316	0.003
Yb	2.393	0.019	2.529	0.034	1.950	1.943	1.960	0.009
Lu	0.359	0.006	0.3894	0.0058	0.270	0.273	0.274	0.002
Hf	1.299	0.012	1.487	0.033	4.221	4.135	4.137	0.049
Ta	0.036	0.003	0.0396	0.003	1.090	1.100	1.103	0.006
Pb	0.412	0.352	5.25	0.11	0.312	0.503	0.085	0.209
Th	0.241	0.001	0.2576	0.0048	1.208	1.183	1.162	0.023
U	0.129	0.011	0.1528	0.0028	0.396	0.388	0.340	0.031

Sample Glass # ID Type	USGS BHVO-2 RV[1]	USGS BHVO-2 95%CL[1]	USGS BIR-1 #G113 STD STD	USGS BIR-1 #G114 STD STD	USGS BIR-1 #G115 STD STD	USGS BIR-1_SD	USGS BIR-1 RV[1]	USGS BIR-1 95%CL[1]
Li	4.5	0.085	2.99	3.03	2.91	0.06	3.203	0.069
B	2.95	0.26	6.49	6.64	6.59	0.08	0.25	
Sc	31.83	0.34	39.40	41.88	41.50	1.33	43.21	0.59
Ti			5501	5503	5648	84		
V	318.2	2.3	297.0	310.5	319.6	11.4	320.6	2.9
Cr	287.2	3.1	271.38	375.17	334.01	52.26	392.9	3.9
Co	44.89	0.32	53.44	55.16	56.97	1.77	52.22	0.57
Ni	119.8	1.2	148.77	155.96	160.39	5.86	168.9	1.9
Rb	9.261	0.096	0.18	0.19	0.18	0.01	0.21	0.0081
Sr	394.1	1.7	115.02	111.69	113.31	1.67	108.6	0.7
Y	25.91	0.28	14.69	14.56	14.46	0.11	15.6	0.17
Zr	171.2	1.3	13.79	13.36	13.29	0.27	14.8	0.22
Nb	18.1	0.2	0.551	0.523	0.544	0.015	0.553	0.014
Cs	0.0996	0.0022	0.003	0.004	0.003	0.000	0.006	0.001
Ba	130.9	1	7.20	6.92	6.96	0.15	6.75	0.13
La	15.2	0.08	0.634	0.601	0.598	0.020	0.627	0.012
Ce	37.53	0.19	1.996	1.899	1.928	0.050	1.92	0.023
Pr	5.339	0.028	0.388	0.373	0.373	0.009	0.3723	0.0047
Nd	24.27	0.25	2.489	2.350	2.408	0.070	2.397	0.043
Sm	6.023	0.057	1.126	1.086	1.111	0.020	1.113	0.018
Eu	2.043	0.012	0.526	0.537	0.532	0.005	0.5201	0.0047
Gd	6.207	0.038	1.805	1.772	1.796	0.017	1.809	0.021
Tb	0.9392	0.006	0.346	0.342	0.339	0.003	0.3623	0.005
Dy	5.28	0.028	2.556	2.515	2.484	0.036	2.544	0.028
Ho	0.9887	0.0053	0.543	0.544	0.532	0.006	0.5718	0.0047
Er	2.511	0.014	1.673	1.642	1.629	0.022	1.68	0.015
Tm	0.3349	0.0031	0.247	0.243	0.236	0.005	0.2558	0.004
Yb	1.994	0.027	1.622	1.591	1.571	0.026	1.631	0.015
Lu	0.2754	0.0024	0.240	0.236	0.235	0.003	0.2484	0.0032
Hf	4.47	0.025	0.540	0.536	0.519	0.011	0.5822	0.0088
Ta	1.154	0.019	0.044	0.041	0.045	0.002	0.0414	0.002
Pb	1.653	0.038	0.425	0.876	0.391	0.271	3.037	0.049
Th	1.224	0.016	0.029	0.029	0.026	0.002	0.0328	0.0015
U	0.412	0.035	0.008	0.007	0.009	0.001	0.01051	0.0004

Sample	GSJ JA-2	GSJ JA-2	GSJ JA-2	GSJ JA-2_SD	GSJ JA-2 RV[1]	GSJ JA-2 95%CL[1]
Glass #	#G116	#G117	#G118			
ID	STD	STD	STD			
Type	STD	STD	STD			
Li	30.25	32.43	30.86	1.13	29.18	0.56
B	15.30	12.62	10.42	2.44	21.1	1.9
Sc	19.11	18.89	18.97	0.11	18.93	0.34
Ti	4119	4127	4267	83		
V	129.5	128.5	115.0	8.1	119.7	2.4
Cr	447.26	380.99	217.22	118.41	424.8	9.3
Co	32.58	32.85	32.11	0.38	28.33	0.97
Ni	130.09	134.29	121.45	6.54	136	2.2
Rb	75.4	75.1	68.2	4.1	69.8	1.3
Sr	242.7	243.3	247.7	2.7	245.8	3
Y	15.82	16.01	16.36	0.28	16.89	0.58
Zr	104.89	104.59	105.42	0.42	108.5	2.6
Nb	9.4	9.3	9.6	0.2	9.3	0.24
Cs	5.125	5.007	3.906	0.673	4.78	0.087
Ba	322.9	326.6	329.4	3.250	308.4	5.1
La	15.072	15.290	15.614	0.273	15.46	0.4
Ce	33.512	33.802	34.570	0.547	32.86	0.85
Pr	3.590	3.638	3.744	0.078	3.691	0.079
Nd	14.086	14.220	14.546	0.237	14.04	0.24
Sm	3.022	3.133	3.078	0.056	3.032	0.043
Eu	0.904	0.905	0.915	0.006	0.893	0.018
Gd	2.890	2.921	3.054	0.087	3.013	0.085
Tb	0.456	0.457	0.460	0.002	0.4786	0.0076
Dy	2.892	2.904	2.944	0.027	2.851	0.071
Ho	0.580	0.587	0.592	0.006	0.591	0.015
Er	1.745	1.723	1.752	0.015	1.676	0.031
Tm	0.249	0.248	0.256	0.004	0.2546	0.0065
Yb	1.597	1.681	1.657	0.043	1.645	0.036
Lu	0.241	0.249	0.247	0.004	0.2549	0.0092
Hf	2.788	2.827	2.764	0.032	2.838	0.062
Ta	0.653	0.666	0.670	0.009	0.652	0.017
Pb	13.41	6.82	3.61	4.997	18.88	0.29
Th	4.751	4.841	4.867	0.061	4.8	0.11
U	2.193	1.979	1.193	0.527	2.182	0.061

Table 5. Whole rock major and trace element compositions of lavas and dikes from the Acoje Block (Barlo, Sual and Subic localities).

Table 5a. Major element compositions of additional samples from the Acoje Block (Barlo, Sual and Subic localities),northern Zambales ophiolite

Sample	ZM18 B1-1	ZM15-11A	ZM15-11B	ZM15-11C	ZM15-11D	ZM15-11E	ZM15-11F	ZM15-12.1
Block	Acoje Block_Barlo	Acoje Block_Barlo	Acoje Block_Barlo	Acoje Block_Barlo	Acoje Block_Barlo	Acoje Block_Barlo	Acoje Block_Barlo	Acoje Block_Barlo
Type	dacite (K-Ar dated)	boninitic basalt	boninitic basalt	boninitic basalt	boninitic basalt	boninitic basalt	boninitic basalt	boninitic basalt (altered)
SiO_2	66.376	50.151	49.16	49.414	48.894	48.222	49.282	53.064
TiO_2	0.404	0.211	0.199	0.208	0.203	0.228	0.223	0.234
Al_2O_3	12.765	14.442	15.054	16.094	14.648	14.514	14.797	14.865
Fe_2O_3	8.923	9.837	9.889	9.447	9.745	10.253	10.009	9.109
MnO	0.098	0.197	0.189	0.182	0.187	0.259	0.278	0.227
MgO	1.667	12.293	11.92	11.269	11.612	13.01	13.613	10.418
CaO	6.296	9.459	10.721	10.666	9.101	10.601	11.026	6.666
Na_2O	2.147	3.067	2.513	2.289	3.346	0.477	0.449	3.464
K_2O	0.753	0.663	0.582	0.676	0.705	0.748	0.662	2.107
P_2O_5	0.084	0.016	0.019	0.016	0.018	0.016	0.014	0.02
LOI	0.37	9.89	10.46	10.10	10.29	8.88	9.15	8.61
Total	99.88	100.34	100.25	100.26	98.46	98.33	100.35	100.17
SiO_2	67.31	50.48	49.53	49.76	50.16	49.56	49.60	53.46
TiO_2	0.41	0.21	0.20	0.21	0.21	0.23	0.22	0.24
Al_2O_3	12.94	14.54	15.17	16.21	15.03	14.92	14.89	14.98
FeO	8.14	8.91	8.97	8.56	9.00	9.48	9.07	8.26
MnO	0.10	0.20	0.19	0.18	0.19	0.27	0.28	0.23
MgO	1.69	12.37	12.01	11.35	11.91	13.37	13.70	10.50
CaO	6.38	9.52	10.80	10.74	9.34	10.90	11.10	6.72
Na_2O	2.18	3.09	2.53	2.30	3.43	0.49	0.45	3.49
K_2O	0.76	0.67	0.59	0.68	0.72	0.77	0.67	2.12
P_2O_5	0.09	0.02	0.02	0.02	0.02	0.02	0.01	0.02

Sample	ZM15-12.2	ZM15-12.3	ZM15-12.4	ZM15-10	ZM15-13A	ZM15-14	ZM15-15	ZM15-16
Block	Acoje Block_Barlo	Acoje Block_Barlo	Acoje Block_Barlo	Acoje Block_Barlo	Acoje Block_Barlo	Acoje Block_Barlo	Acoje Block_Barlo	Acoje Block_Barlo
Type	boninitic basalt (altered)	boninitic basalt (altered)	boninitic basalt (altered)	LSB series	tholeiitic basalt (float) dike?	LSB series	LSB series	LSB series
SiO_2	53.631	53.617	53.454	50.383	50.787	53.667	54.627	53.691
TiO_2	0.221	0.229	0.227	0.313	0.987	0.332	0.479	0.458
Al_2O_3	15.742	15.285	15.691	21.453	16.95	15.355	17.844	17.854
Fe_2O_3	8.675	8.647	8.992	5.335	13.431	9.435	10.958	10.704
MnO	0.184	0.189	0.193	0.085	0.161	0.206	0.165	0.124
MgO	9.37	9.739	9.235	6.267	4.809	7.182	3.297	4.128
CaO	6.05	6.306	6.211	14.702	11.315	11.141	8.535	8.523
Na_2O	4.315	3.994	4.106	1.811	1.711	2.093	2.724	2.481
K_2O	1.965	2.098	2.211	0.161	0.089	0.999	1.983	2.331
P_2O_5	0.017	0.018	0.013	0.024	0.048	0.015	0.06	0.047
LOI	8.30	8.72	8.89	1.49	-0.19	5.82	0.33	1.72
Total	100.17	100.12	100.33	100.53	100.29	100.43	100.67	100.34
SiO_2	54.01	54.02	53.76	50.38	51.33	53.95	54.86	54.09
TiO_2	0.22	0.23	0.23	0.31	1.00	0.33	0.48	0.46
Al_2O_3	15.85	15.40	15.78	21.45	17.13	15.44	17.92	17.99
FeO	7.86	7.84	8.14	4.80	12.21	8.53	9.90	9.70
MnO	0.19	0.19	0.19	0.09	0.16	0.21	0.17	0.12
MgO	9.44	9.81	9.29	6.27	4.86	7.22	3.31	4.16
CaO	6.09	6.35	6.25	14.70	11.44	11.20	8.57	8.59
Na_2O	4.35	4.02	4.13	1.81	1.73	2.10	2.74	2.50
K_2O	1.98	2.11	2.22	0.16	0.09	1.00	1.99	2.35
P_2O_5	0.02	0.02	0.01	0.02	0.05	0.02	0.06	0.05

Sample	ZM15-01	ZM15-02A	ZM15-2B	ZM15-03	ZM15-04	ZM15-05	ZM15-06	ZM15-07
Block	Acoje Block_Sual SDC	Acoje Block_Sual SDC	Acoje Block_Sual SDC	Acoje Block_Sual SDC	Acoje Block_Sual SDC	Acoje Block_Sual SDC	Acoje Block_Sual SDC	Acoje Block_Sual SDC
Type	boninitic basalt	Basaltic andesite	Basaltic andesite	Basaltic andesite	Basaltic andesite	Basaltic andesite	Basalt	Gabbro, medium grained
SiO_2	49.886	55.441	55.026	51.891	54.129	54.584	51.877	45.213
TiO_2	0.322	0.576	0.585	0.953	0.973	0.533	0.495	1.309
Al_2O_3	20.111	16.36	16.221	16.29	15.342	17.575	15.936	16.423
Fe_2O_3	8.408	11.257	11.646	12.329	14.264	9.926	9.691	17.393
MnO	0.164	0.21	0.217	0.177	0.293	0.2	0.159	0.219
MgO	7.095	5.227	5.163	2.37	5.118	5.326	8.673	6.695
CaO	13.258	8.943	8.924	15.444	7.203	9.573	11.348	11.811
Na_2O	1.29	2.274	2.262	0.171	2.602	2.269	1.73	1.058
K_2O	0.128	0.19	0.175	0.037	0.287	0.339	0.364	0.088
P_2O_5	0.02	0.048	0.048	0.063	0.072	0.045	0.033	0.023
LOI	0.97	1.15	0.76	1.37	1.66	1.16	1.89	1.01
Total	100.68	100.53	100.27	99.73	100.28	100.37	100.31	100.23
SiO_2	49.97	55.78	55.53	52.69	54.76	54.93	52.22	45.91
TiO_2	0.32	0.58	0.59	0.97	0.98	0.54	0.50	1.33
Al_2O_3	20.14	16.46	16.37	16.54	15.52	17.69	16.04	16.67
FeO	7.58	10.19	10.57	11.26	12.98	8.99	8.78	15.89
MnO	0.16	0.21	0.22	0.18	0.30	0.20	0.16	0.22
MgO	7.11	5.26	5.21	2.41	5.18	5.36	8.73	6.80
CaO	13.28	9.00	9.01	15.68	7.29	9.63	11.42	11.99
Na_2O	1.29	2.29	2.28	0.17	2.63	2.28	1.74	1.07
K_2O	0.13	0.19	0.18	0.04	0.29	0.34	0.37	0.09
P_2O_5	0.02	0.05	0.05	0.06	0.07	0.05	0.03	0.02

Sample	ZM15-08	ZM15-23	ZM15-24	ZM15-26	ZM15-28
Block	Acoje Block_Sual SDC	Acoje Block_Subic	Acoje Block_Subic	Acoje Block_Subic dikes	Acoje Block_Subic dikes
Type	boninitic basalt	Basaltic andesite	Basaltic andesite	Basaltic andesite	Basaltic andesite
SiO_2	49.511	56.241	55.919	55.089	54.148
TiO_2	0.165	1.318	1.404	0.693	0.678
Al_2O_3	15.726	16.206	15.956	15.743	15.635
Fe_2O_3	8.623	11.585	11.634	14.176	14.901
MnO	0.15	0.132	0.136	0.157	0.157
MgO	11.604	3.209	3.828	4.056	3.895
CaO	13.904	4.205	4.185	8.25	8.968
Na_2O	0.843	7.4	7.166	2.067	1.942
K_2O	0.009	0.089	0.065	0.058	0.027
P_2O_5	0.007	0.125	0.114	0.037	0.041
LOI	1.15	1.18	2.02	1.34	-0.46
Total	100.54	100.51	100.41	100.33	100.39
SiO_2	49.67	56.61	56.35	55.70	54.75
TiO_2	0.17	1.33	1.41	0.70	0.69
Al_2O_3	15.78	16.31	16.08	15.92	15.81
FeO	7.78	10.49	10.55	12.90	13.56
MnO	0.15	0.13	0.14	0.16	0.16
MgO	11.64	3.23	3.86	4.10	3.94
CaO	13.95	4.23	4.22	8.34	9.07
Na_2O	0.85	7.45	7.22	2.09	1.96
K_2O	0.01	0.09	0.07	0.06	0.03
P_2O_5	0.01	0.13	0.11	0.04	0.04

Sample	JB-1b	JB-1b RV[1]	JA-3	JA-3 RV[1]	JA-2	JA-2 RV[1]
Block Type						
SiO_2	52.708	52.230	62.402	62.330	57.696	57.710
TiO_2	1.270	1.290	0.696	0.700	0.698	0.680
Al_2O_3	14.383	14.690	15.818	15.570	15.957	15.760
Fe2O3	9.002	9.220	6.700	6.610	6.378	6.350
MnO	0.145	0.150	0.107	0.100	0.109	0.110
MgO	8.594	8.320	3.760	3.720	7.443	7.770
CaO	9.760	9.810	6.295	6.250	6.301	6.430
Na_2O	2.666	2.690	3.130	3.190	3.197	3.180
K_2O	1.332	1.350	1.443	1.410	1.868	1.850
P_2O_5	0.261	0.260	0.117	0.120	0.163	0.150
LOI						
Total						

SiO2
TiO2
Al2O3
FeO
MnO
MgO
CaO
Na2O
K2O
P2O5

Table 5b Trace element compositions of additional samples from the Acoje Block (Barlo, Sual and Subic localities), northern Zambales ophiolite

Sample	ZM15-01	ZM15-01	ZM15-01	ZM15-2A	ZM15-2A	ZM15-04	ZM15-04	ZM15-04
Glass #	#G101	#G102	#G103	#G105	#G106	#G107	#G108	#G109
ID	Acoje_Sual dike	Acoje_Sual dike	Acoje_Sual dike	Acoje_Sual dike	Acoje_Sual dike	Acoje_Sual dike	Acoje_Sual dike	Acoje_Sual dike
Li	2.382	2.363	2.465	2.984	2.857	3.156	3.090	2.973
B	10.348	9.645	9.928	6.190	6.047	5.500	5.590	5.214
Sc	35.786	39.052	34.703	36.104	36.531	36.729	40.859	41.548
Ti	1743.360	1665.040	1609.793	3437.671	3465.843	4800.303	5433.576	5209.378
V	171.710	180.690	169.629	292.297	295.016	431.943	474.704	478.213
Cr	68.811	70.935	72.852	42.619	47.468	9.556	12.200	19.405
Co	35.138	36.015	36.204	34.998	33.232	37.281	39.219	39.727
Ni	31.285	32.064	31.496	23.583	24.665	19.359	20.724	22.591
Rb	0.900	0.846	0.969	0.749	0.836	1.517	1.480	1.370
Sr	111.829	107.060	111.377	101.947	103.651	105.225	100.484	99.317
Y	7.415	7.936	7.358	15.344	14.940	20.586	22.642	21.698
Zr	9.825	12.216	15.982	24.859	26.317	34.627	41.121	41.368
Nb	0.107	0.087	0.088	0.221	0.290	0.318	0.369	0.636
Cs	0.007	0.007	0.007	0.003	0.003	0.031	0.027	0.028
Ba	5.186	4.974	5.349	9.593	9.845	8.968	8.851	8.485
La	0.362	0.372	0.350	1.087	0.784	1.548	1.845	1.972
Ce	1.310	1.407	1.260	3.179	2.465	4.969	5.837	6.051
Pr	0.253	0.258	0.240	0.556	0.459	0.890	1.028	1.033
Nd	1.520	1.600	1.445	3.232	2.752	5.238	6.001	5.882
Sm	0.660	0.679	0.620	1.309	1.207	2.099	2.269	2.185
Eu	0.346	0.339	0.342	0.520	0.499	0.824	0.880	0.835
Gd	0.961	1.022	0.913	1.925	1.852	2.887	3.280	3.090
Tb	0.175	0.184	0.170	0.358	0.347	0.504	0.558	0.538
Dy	1.293	1.399	1.222	2.573	2.522	3.538	3.952	3.767
Ho	0.285	0.297	0.274	0.558	0.549	0.755	0.861	0.809
Er	0.885	0.900	0.853	1.751	1.745	2.267	2.576	2.485
Tm	0.128	0.137	0.128	0.259	0.256	0.321	0.354	0.347
Yb	0.868	0.903	0.856	1.758	1.769	2.209	2.502	2.421
Lu	0.129	0.141	0.130	0.270	0.274	0.339	0.386	0.368
Hf	0.340	0.419	0.473	0.816	0.920	1.147	1.363	1.367
Ta	0.018	0.017	0.014	0.016	0.020	0.018	0.028	0.033
Pb	0.286	0.234	0.278	0.367	0.381	0.198	0.193	0.173
Th	0.042	0.048	0.040	0.150	0.115	0.130	0.182	0.144
U	0.019	0.029	0.030	0.080	0.076	0.065	0.081	0.076

Sample	ZM15-05	ZM15-05	ZM15-05	ZM15-06	ZM15-06	ZM15-06	ZM15-07	ZM15-07
Glass #	#G110	#G111	#G112	#G113	#G114	#G115	#G116	#G117
ID	Acoje_Sual dike	Acoje_Sual dike	Acoje_Sual dike	Acoje_Sual dike	Acoje_Sual dike	Acoje_Sual dike	Acoje_Sual dike	Acoje_Sual dike
Li	4.694	5.056	4.683	4.284	4.053	4.325	1.935	2.106
B	5.909	7.139	6.499	5.214	6.082	5.470	7.050	7.094
Sc	33.174	27.126	36.888	39.862	40.088	40.086	48.144	56.462
Ti	3046.322	2808.972	3229.536	3077.161	3571.529	3200.053	6385.998	6643.206
V	268.453	227.061	287.552	285.757	300.470	294.673	564.684	672.572
Cr	54.595	41.834	67.774	154.452	135.092	155.378	8.232	6.800
Co	32.703	27.757	33.316	43.312	49.056	44.308	65.893	72.167
Ni	25.911	21.817	26.894	57.090	66.122	60.128	7.583	8.055
Rb	1.725	2.340	1.679	1.432	1.555	1.414	0.443	0.452
Sr	112.254	122.840	109.642	89.262	92.213	89.791	97.011	93.040
Y	12.723	11.084	13.507	12.429	13.455	12.860	8.289	8.978
Zr	22.512	19.024	23.016	18.588	20.138	19.451	10.414	10.420
Nb	0.212	0.168	0.247	0.161	0.194	0.208	0.077	0.074
Cs	0.019	0.023	0.018	0.003	0.003	0.005	0.007	0.008
Ba	11.429	16.086	11.610	4.976	5.370	5.177	3.817	3.893
La	0.642	0.562	0.650	0.585	0.647	0.608	0.460	0.358
Ce	2.098	1.874	2.177	2.059	2.325	2.186	1.650	1.374
Pr	0.402	0.351	0.401	0.393	0.448	0.418	0.298	0.271
Nd	2.370	2.105	2.454	2.458	2.809	2.571	1.784	1.744
Sm	1.053	0.957	1.053	1.046	1.169	1.118	0.754	0.739
Eu	0.456	0.438	0.478	0.455	0.510	0.481	0.346	0.366
Gd	1.663	1.426	1.728	1.583	1.769	1.713	1.101	1.167
Tb	0.309	0.264	0.318	0.299	0.315	0.309	0.200	0.223
Dy	2.207	1.866	2.281	2.118	2.321	2.217	1.480	1.576
Ho	0.484	0.421	0.495	0.445	0.493	0.474	0.302	0.356
Er	1.505	1.261	1.552	1.410	1.543	1.459	0.943	1.044
Tm	0.207	0.189	0.230	0.206	0.216	0.205	0.130	0.148
Yb	1.519	1.298	1.600	1.391	1.498	1.426	0.914	1.049
Lu	0.233	0.188	0.244	0.217	0.261	0.235	0.133	0.158
Hf	0.779	0.638	0.835	0.679	0.755	0.698	0.387	0.382
Ta	0.017	0.013	0.015	0.042	0.081	0.056	0.005	0.009
Pb	0.312	0.250	0.282	0.113	0.101	0.120	0.193	0.183
Th	0.094	0.082	0.086	0.047	0.058	0.057	0.040	0.034
U	0.055	0.043	0.057	0.025	0.022	0.023	0.018	0.017

Sample	ZM15-07	ZM15-08	ZM15-08	ZM15-08	ZM15-10	ZM15-10	ZM15-10	ZM15-23
Glass #	#G118	#G101	#G102	#G103	#G101	#G102	#G103	#G104
ID	Acoje_Sual dike	Acoje_Sual dike	Acoje_Sual dike	Acoje_Sual dike	Acoje_Sual dike	Acoje_Sual dike	Acoje_Sual dike	Acoje_Subic lava
Li	1.817	0.284	0.276	0.303	3.254	3.059	3.144	2.511
B	6.993	8.093	8.100	7.874	7.067	6.882	6.906	5.710
Sc	51.664	41.826	41.984	42.474	31.336	30.224	31.480	32.269
Ti	8630.644	1095.066	1060.544	1047.302	2182.075	3069.689	2062.550	7743.957
V	853.689	181.156	182.421	180.017	135.694	147.517	135.820	355.458
Cr	8.533	277.364	297.770	286.597	141.180	141.115	160.584	17.060
Co	67.724	46.455	48.267	48.871	23.708	23.141	23.388	33.029
Ni	8.445	101.375	108.982	105.372	45.919	44.933	44.634	14.279
Rb	0.413	0.072	0.071	0.068	0.840	0.842	0.852	0.889
Sr	94.860	98.762	99.499	97.412	127.690	131.109	126.820	117.195
Y	8.622	4.180	4.317	4.195	8.568	8.230	8.625	27.964
Zr	10.349	2.500	2.260	2.243	13.269	15.129	13.304	68.256
Nb	0.082	0.081	0.079	0.074	0.196	0.286	0.183	0.743
Cs	0.007	0.002	0.002	0.002	0.015	0.017	0.016	0.009
Ba	3.827	1.332	1.341	1.333	6.019	5.914	5.840	5.988
La	0.421	0.116	0.112	0.108	0.543	0.680	0.545	1.862
Ce	1.485	0.454	0.447	0.417	1.885	2.131	1.878	6.795
Pr	0.284	0.095	0.091	0.088	0.345	0.359	0.342	1.185
Nd	1.755	0.626	0.618	0.617	2.022	2.051	2.036	6.946
Sm	0.748	0.351	0.340	0.335	0.827	0.812	0.804	2.692
Eu	0.369	0.213	0.224	0.208	0.417	0.419	0.423	0.883
Gd	1.160	0.550	0.529	0.513	1.193	1.126	1.178	3.758
Tb	0.219	0.106	0.103	0.102	0.211	0.208	0.202	0.672
Dy	1.532	0.762	0.789	0.714	1.488	1.435	1.506	4.597
Ho	0.333	0.164	0.170	0.159	0.317	0.306	0.306	0.965
Er	0.998	0.512	0.517	0.499	0.945	0.919	0.952	2.951
Tm	0.141	0.071	0.072	0.071	0.128	0.132	0.129	0.418
Yb	0.978	0.504	0.509	0.466	0.941	0.859	0.902	2.898
Lu	0.136	0.088	0.084	0.083	0.140	0.137	0.138	0.455
Hf	0.394	0.112	0.102	0.097	0.476	0.494	0.446	1.842
Ta	0.008	0.038	0.028	0.023	0.038	0.032	0.026	0.073
Pb	0.175	0.109	0.080	0.075	0.121	0.119	0.105	0.386
Th	0.035	0.006	0.005	0.004	0.039	0.047	0.040	0.118
U	0.016	0.001	0.000	0.002	0.015	0.018	0.021	0.039

Sample	ZM15-28	ZM15-28	ZM15-28
Glass #	#G113	#G114	#G115
ID	Acoje_Subic dike	Acoje_Subic dike	Acoje_Subic dike
Li	0.171	0.093	0.126
B	5.803	5.495	5.893
Sc	41.083	43.820	45.080
Ti	4468.147	4384.138	4359.133
V	455.410	480.701	492.334
Cr	9.127	18.893	9.150
Co	40.960	44.696	42.340
Ni	5.202	8.871	4.943
Rb	0.090	0.076	0.072
Sr	134.952	131.612	128.413
Y	12.297	13.490	13.491
Zr	22.748	23.508	24.998
Nb	0.280	0.437	0.265
Cs	0.002	0.002	0.001
Ba	8.403	7.553	7.576
La	0.699	0.783	0.716
Ce	2.222	2.432	2.303
Pr	0.390	0.430	0.405
Nd	2.310	2.566	2.427
Sm	1.008	1.085	1.058
Eu	0.428	0.473	0.431
Gd	1.576	1.672	1.622
Tb	0.280	0.304	0.308
Dy	2.092	2.251	2.275
Ho	0.452	0.491	0.493
Er	1.368	1.534	1.558
Tm	0.206	0.213	0.227
Yb	1.462	1.547	1.603
Lu	0.226	0.251	0.257
Hf	0.793	0.818	0.868
Ta	0.026	0.030	0.022
Pb	0.111	0.155	0.141
Th	0.116	0.127	0.134
U	0.073	0.078	0.078

Table 6. Major and trace element composition of estimated primary boninite magmas from northern Zambales ophiolite.

sample	ZM2-107	ZM2-107'	ZM2-100A	ZM2-100A'
	LSB	primary LSB est.	HSB	primary HSB est.
% olivine added		6		11
SiO_2	54.83	**54.55**	*58.07*	*56.59*
TiO_2	0.23	**0.22**	*0.25*	*0.23*
Al_2O_3	13.25	**12.60**	*13.37*	*12.05*
Fe_2O_3	9.29	**1.30**	*8.71*	*1.44*
FeO		**7.26**		*6.64*
MnO	0.14	**0.15**	*0.16*	*0.17*
MgO	12.28	**14.59**	*8.98*	*13.25*
CaO	8.49	**8.09**	*8.98*	*8.13*
Na_2O	0.81	**0.77**	*1.28*	*1.16*
K2O	0.44	**0.42**	*0.31*	*0.28*
P2O5	0.01	**0.01**	*0.02*	*0.02*
NiO	0.03	**0.05**	*0.02*	*0.05*
Fo		**91.7**		*91.8*
H_2O	1.025	**3.17**	1.093	*no constraint yet*
[1]$Fe^{3+}_{o}/\sum Fe$	0.14		*0.165*	
$K_{d\ (Fe/Mg)}$		0.317-0.326		*0.301-0.320*
T (C)		1273		
P (Gpa)		0.34		
log (fO_2)		-6.28		
[3] Li (µg/g)	10.443	**9.832**	11.022	**9.869**
V	221.0	**208.8**	217.9	**196.4**
Rb	8.316	**7.834**	7.583	**6.796**
Sr	68.556	**64.544**	62.617	**56.064**
Y	10.442	**9.845**	11.888	**10.671**
Zr	12.549	**11.818**	15.638	**14.008**
Nb	0.250	**0.236**	0.304	**0.272**
Cs	0.447	**0.421**	0.677	**0.606**
Ba	17.694	**16.659**	29.022	**25.985**
La	0.569	**0.536**	0.605	**0.542**
Ce	1.165	**1.097**	1.459	**1.306**
Pr	0.196	**0.185**	0.225	**0.201**
Nd	1.103	**1.038**	1.221	**1.094**
Sm	0.501	**0.472**	0.566	**0.507**
Eu	0.184	**0.173**	0.217	**0.194**
Gd	0.847	**0.797**	1.043	**0.934**
Tb	0.185	**0.174**	0.222	**0.199**
Dy	1.366	**1.287**	1.626	**1.457**
Ho	0.330	**0.311**	0.388	**0.348**
Er	1.019	**0.960**	1.21	**1.086**
Ti	1366	**1288**	1504	**1349**
Tm	0.165	**0.155**	0.197	**0.176**
Yb	1.169	**1.102**	1.410	**1.266**
Lu	0.190	**0.179**	0.233	**0.209**
Hf	0.417	**0.393**	0.530	**0.475**
Ta	0.023	**0.022**	0.025	**0.023**
Pb	1.653	**1.556**	1.792	**1.604**
Th	0.113	**0.106**	0.127	**0.114**
U	0.080	**0.075**	0.103	**0.092**
K	3653	**3439**	2553	**2286**

13.Appendices

Appendix 1. Structural data, field observations, and locality coordinates

Locality	DateDateDate	Long	Lat	Altitude	Location ID	Sample/ Field Notes	Rock-type/ Geochem	Dip azimuth	Dip angle	Structure type
ZM2-01	5/16/2016 11:14	119.939	15.98997	123.52	Roadside N c	**B-1-1 (pillow**	**Dacite (LSB s**	206	20	pillow flow bec
						B-1-2 (glassy margin)		277	28	pillow breccia/
						B-1-3 (pillow	**Dacite (LSB series)**			
						B-1-4 (pillow	**Dacite (LSB series)**			
ZM2-02	5/16/2016 12:28	119.9387	15.98985	122.97	Roadside N c	**B-2-5 (glass**	**Dacite (LSB s**	138	42	dike
						B-2-6 (glassy margin of dike intruding pillow breccia)				
ZM2-03	5/16/2016 0:00	119.9385	15.99032	141.35	Top of the rid	**B-6-9 (glass**	**Boninite, HSB**			
						B-6-10 (glas	**Boninite, HSB**			
		119.9381	15.99045			**B-5-7 (glass**	**Boninite, HSB**			
		119.9381	15.99045			**B-5-8 (glass**	**Boninite, HSB**			
ZM2-04	5/16/2016 13:34	119.9382	15.99036	138.26	Ridge N of M	boninite lapillistone		318	50	lapillistone be
ZM2-05	5/16/2016 14:25	119.9389	15.99044	140.04	Ridge N of M	**B-7-11 (vesi**	**Boninite, HSB**			
ZM2-06	5/16/2016 15:17	119.9301	15.99472	83.17	Below bridge	Badly weathered boninitic? pillows				
ZM2-07	5/16/2016 16:22	119.9253	15.98841	110.8	Airstrip W of	Limestone on top of ridge				
ZM2-08	5/16/2016 16:46	119.9233	15.99078	101	Airstrip W of	Limestone on top of ridge/su		0	0	
ZM2-09	5/16/2016 17:27	119.9409	15.97273	147.97	1 km S of Mt.	Altered lapillistone; Trenches digged				
		119.9388	15.97266		On the ridge	Pillow lava				
ZM2-10	5/17/2016 10:47	119.9483	15.96707	184.65	On the ridge	Lateritized dike in SDC		260	66	Lateritized dik
ZM2-11	5/17/2016 11:00	119.9486	15.96502	198.13	On the ridge	Hydrothermal alteration zone ~30 m wide				
ZM2-12	5/17/2016 11:12	119.9464	15.96409	188.48	On the ridge	B-18 (fine grained volcanics, with amygdules), Bleached al				
ZM2-13	5/17/2016 11:30	119.9446	15.96388	167.11	On the ridge	Hydrothermally altered volcanic rock				
ZM2-14	5/17/2016 11:43	119.9435	15.9641	144.74	On the plane	B-19 (basalt/dolerite),B19 (gabbronorite), pillow-fragment-b				
ZM2-15	5/17/2016 12:04	119.9432	15.96455	131.23	In creek E of	Pillow-fragment-bg. lapillituff/agglomerate				
		119.9431	15.96458			**B-22 (pillow**	**Andesite (LSB series)**			
ZM2-16	5/17/2016 12:25	119.943	15.96453	130.01	In creek E of	B-23-1 (massive lava below		33	50	pillow flow bec
ZM2-17	5/17/2016 12:49	119.9429	15.96444	123.29	In creek E of	Tuff breccia/massive lava (spatter?)				
ZM2-18	5/17/2016 12:53	119.9428	15.96457	121.96	In creek E of	B-24-1 (massive lava, spatte		205	36	massive lava (
ZM2-19	5/17/2016 13:04	119.9427	15.96459	119.64	In creek E of	Tuff breccia		138	30	massive lava (
ZM2-20	5/17/2016 13:23	119.9423	15.9647	124.69	In creek E of	Spatter in tuff breccia aggl.		180	24	spatter
		119.9422	15.9646			**B-28 (glass)**	**Andesite (LSB series)**			

Locality	DateDateDate	Long	Lat	Altitude	Location ID	Sample/Fie	Rock-type/ G	Dip azimuth	Dip angle	Structure typ
		119.9422	15.96452			B-29 (tuff breccia clasts)				
		119.9423	15.96447			**B-30 (dike?)**	**Boninite, LSB altered**			
ZM2-21	5/17/2016 14:08	119.9423	15.96438	116.29	In creek E of	**B-31 (bonini**	**Boninite, LSB**	140	36	spatter
ZM2-22	5/17/2016 15:01	119.9422	15.96432	124.22	In creek E of	Boninite dike into tuff breccia		206	86	dike
ZM2-23	5/17/2016 15:36	119.9418	15.96451	114.22	In creek E of	Tuff breccia aggl.		125	28	welded tuff br
ZM2-24	5/17/2016 16:05	119.9415	15.96471	107.76	In creek E of	B-34 (talus deposit clast with		14	50	Tuff breccia/pi
ZM2-25	5/17/2016 16:17	119.9413	15.9647	108.23	In creek E of	B-35 (boninite dike intruding pillow breccia),				Pillow breccia
		119.9413	15.9647					177	44	dike 55 cm
		119.9413	15.9647					152	44	dike 40 cm
		119.9413	15.9647					155	40	dike 30 cm
		119.9413	15.9647					173	58	dike >3 m
ZM2-26	5/17/2016 16:51	119.9409	15.96472	99.6	In creek E of	B-36 (boninite dike intruding		331	32	dike >1.5 m
ZM2-27	5/17/2016 17:11	119.9405	15.96498	87.5	In creek E of	Pillow breccia forming a fall				
ZM2-28	5/17/2016 17:34	119.9368	15.96949	111.11	On the ridge	Pillow lava		180	15	pillow flow
ZM2-29	5/17/2016 17:39	119.9374	15.97028	127.91	On the ridge	B-64D, B-64, pillow lava				
ZM2-30	5/17/2016 17:45	119.9383	15.97137	135.06	On the ridge	Pillow lava				
ZM2-31	5/17/2016 17:52	119.9399	15.97218	147.4	On the ridge	Pillow lava		304	22	pillow flow
ZM2-32	5/18/2016 10:47	119.9584	15.96154	175.86	Way down to	Gabbro cobbles				
ZM2-33	5/18/2016 11:00	119.9622	15.96297	141.57	Way down to	**B-47-dike1**	**Andesite (LSE**	325	72	Dolerite SDC-
						B-47-dike2				
						B-47-dike3	**Andesite (LSE**	176	47	Dolerite SDC-
						B-47-dike4	**Andesite (Tho**	100	58	Dolerite SDC-
						B-47-dike6		310	60	Dolerite SDC-
						B-47-7 (vent	**Andesite (LSB series)**			
								10	20	Dolerite SDC
								132	30	Dolerite SDC
								50	70	Dolerite SDC

Locality	DateDateDate	Long	Lat	Altitude	Location ID	Sample/Fie	Rock-type/ G	Dip azimuth	Dip angle	Structure typ
								340	50	Dolerite SDC
								224	60	Dolerite SDC
ZM2-34	5/18/2016 14:18	119.9541	15.95784	194.24	S of San Vice	Apyric basalt? massive lava (SDC?)				
ZM2-35	5/18/2016 14:33	119.9535	15.95737	190.61	S of San Vice	B-49-dike1, SDC		69	48	Dolerite SDC
								340	50	Dolerite SDC
ZM2-36	5/18/2016 14:47	119.9518	15.9568	184.35	S of San Vicente			151	16	Sheet flow/pill
ZM2-37	5/18/2016 15:02	119.9511	15.95717	177.52	S of San Vice	Sheet flow/pillow flow				
ZM2-38	5/18/2016 15:08	119.9507	15.95787	170.46	S of San Vice	Pillow flow, N	**Andesite (LSB series), altered**			
ZM2-39	5/18/2016 15:19	119.9505	15.95796	166.63	S of San Vice	Ropy wrinkled pahoehoe sh		41	37	Ropy wrinkled
ZM2-40	5/18/2016 15:40	119.9496	15.95824	152.34	S of San Vice	**B-54 (float),**	**Boninite, LSB**	50	44	
						B-54 (pillow	**Boninite, LSB altered**			
						B-54 (pillowB glassy margin)				
						B-54 (pillowC glassy margin)				
						B-54 (pillowD glassy margin)				
						B-54 (glassy dike margin)				
						B-54 (sheet flows on top of pillows)				
ZM2-41	5/18/2016 16:51	119.9458	15.96113	144.3	Creek SE of	Plag-phyric andesite? sheet flow				
ZM2-42	5/18/2016 17:04	119.9456	15.9612	142.59	Creek SE of	**B-56 (sheet**	**Andesite (LSE**	226	26	Basalt sheet fl
ZM2-43	5/19/2016 10:30	119.9426	15.98093	145.47	Road cut E o	Tuff breccia, weathered		127	36	Tuff breccia, v
ZM2-44	5/19/2016 11:12	119.9389	15.97204	138.1	Between Mt.	Boninitic andesite fragmenta		30	49	fragmentary p
ZM2-45	5/19/2016 11:28	119.9387	15.97232	152.06	Between Mt.	Boninitic andesite large flow		176	24	large flow lobe
ZM2-46	5/19/2016 11:35	119.9385	15.97259	161.3	Top of the bl	Cpx-bg. boninitic andesite p		196	4	pahoehoe lob
		119.9384	15.97253			B-62, B-62B, B-62 interpillows, B-62C				

Locality	DateDateDate	Long	Lat	Altitude	Location ID	Sample/Fie	Rock-type/ G	Dip azimuth	Dip angle	Structure typ
ZM2-47	5/19/2016 12:35	119.9358	15.96908	96.71	Beteen Mt. S	B-65 lapillituff				
ZM2-48	5/19/2016 12:45	119.9355	15.96959	99.34	Beteen Mt. S	Boninite lapillituff				
ZM2-49	5/19/2016 12:52	119.9356	15.9704	99.04	Beteen Mt. S	B-69, Boninitic andesite pillo		122	34	pillow flow
ZM2-50	5/19/2016 14:07	119.9359	15.97245	106.91	Beteen Mt. S	B-70, Boninitic andesite pillo		90	24	pillow flow
ZM2-51	5/19/2016 15:00	119.9364	15.97341	100.39	In a creek be	Boninitic pillow flow				
ZM2-52	5/19/2016 15:11	119.938	15.9745	111	Between Mt.	**B-72, B-72 g**	**Andesite (LSE**	296	4	pillow flow
ZM2-53	5/19/2016 15:30	119.9381	15.97513	121.03	Between Mt.	Boninitic lapillituff overlying boninite pillows of ZM2-52				
		119.9381	15.97505			**B-74A**	**Andesite (LSB series), altered**			
ZM2-54	5/19/2016 15:43	119.9387	15.97602	135.57	Between Mt.	Boninite lava?				
ZM2-55	5/19/2016 15:53	119.9396	15.9765	143.51	Between Mt.	Boninite pillow breccia				
ZM2-56	5/19/2016 16:03	119.94	15.9765	149.23	On the top of	Boninite lapillistone with drib		151	26	lapillistone wit
		119.9399	15.97647			B-78 glassy lapili				
ZM2-57	5/19/2016 16:21	119.9397	15.97679	166.47	Between Mt.	Boninitic lapillistone fall				
		119.9397	15.97675			**B-79**, B-79lava, B-79b				
ZM2-58	5/19/2016 16:46	119.9394	15.97702	165.13	Between Mt.	Sol & Caliwaen				
ZM2-59	5/19/2016 16:49	119.9395	15.97713	164.15	Between Mt.	Dike trending 126° ?				
ZM2-60	5/23/2016 10:22	119.9517	15.96949	164.2	San Vicente	Boninite lapillistone fall				
ZM2-61	5/23/2016 10:34	119.9521	15.96953	165.48	San Vicente	**B-82-1**, B-82	**Boninite, LSB**	30	40	dike swarm
ZM2-62	5/23/2016 11:53	119.9523	15.96957	165.53	San Vicente	B-83, diabase dike swarm				
	5/23/2016 12:15	119.9516	15.97058	181.05	San Vicente	diabase dike swarm				
	5/23/2016 12:18	119.9512	15.97128	168.51	San Vicente	diabase dike swarm				
ZM2-63	5/23/2016 12:35	119.9502	15.97105	147.58	San Vicente	B-86-1, B-86	**Boninitic basa**	260	50	dike swarm
	5/23/2016 14:31	119.9504	15.97168	152.11	San Vicente	**B-87, diabas**	**Boninitic basa**	250	60	dike swarm
						diabase dike swarm		240	60	dike swarm
						diabase dike swarm		266	10	dike swarm
						diabase dike swarm				
						diabase dike swarm		160	10	dike swarm

Locality	DateDateDate	Long	Lat	Altitude	Location ID	Sample/Fie	Rock-type/ G	Dip azimuth	Dip angle	Structure typ
ZM2-79	5/24/2016 14:03	119.9365	15.98339	208.77	Mt. Sol	**B-100,** mass	**Boninite, LSB**			
ZM2-80	5/24/2016 14:43	119.9347	15.98224	169.17	Mt. Sol	boninitic pyroclastics				
ZM2-81	5/24/2016 14:50	119.934	15.98222	175.22	Mt. Sol	B-101, weathered boninitic pillows				
ZM2-82	5/24/2016 15:01	119.9331	15.98236	171.03	Mt. Sol	**B-102-1,** bor	**Andesite (LSE**	290	60	boninitic pillow
						B-102-2				
						B-103-1				
						B-103-2				
						B-104-1				
ZM2-83	5/24/2016 15:43	119.9328	15.9823	169.32	Mt. Sol	boninitic pyroclastics overlyi		280	20	boninitic pillow
	5/24/2016 16:09	119.9333	15.98239	172	Mt. Sol	boninitic pyroclastics overlying pillows				
ZM2-84	5/24/2016 16:41	119.9348	15.98169	155.95	Mt. Sol	B-105, massive andesitic lava				
ZM2-85	5/24/2016 16:59	119.9359	15.9796	165.5	Mt. Sol	weathered boninitic pillows				
ZM2-86	5/24/2016 17:11	119.9387	15.97858	149.76	Mt. Sol					
ZM2-87	5/24/2016 17:19	119.9391	15.97833	151.46	Mt. Sol	B-106, massive andesitic lava				
ZM2-96	5/27/2016 11:56	119.9403	15.99062	137	north of Mt. S	ZM2-96-1 (andesitic spatter)		310	40	andesitic flows
						ZM2-96-2A (Basaltic Ande		305	20	andesitic flows
						ZM2-96-2B (Andesite (LSE		320	40	andesitic flows
						ZM2-96-3 (andesitic dike)		340	10	andesitic flows
								170	30	dike cutting an
								140	30	andesitic flows
								150	30	andesitic flows
ZM2-97	5/27/2016 12:55	119.9399	15.99073	117.21	north of Mt. S	ZM2-97 (massive andesitic l		300	40	massive ande
								310	30	
ZM2-98	5/27/2016 13:11	119.9398	15.99093	117.57	north of Mt. S	massive andesitic lava		310	50	massive ande
ZM2-99	5/27/2016 13:15	119.9396	15.99091	119.85	north of Mt. S	ZM2-99 (spatter deposit)				
ZM2-100	5/27/2016 13:29	119.9392	15.99101	111.46	north of Mt. S	**ZM2-100A, 2**	**Boninite, HSB**			
ZM2-101	5/27/2016 14:23	119.9396	15.99177	121.32	north of Mt. S	boninitic? pillows		298	40	pillows

Locality	DateDateDate	Long	Lat	Altitude	Location ID	Sample/Fie	Rock-type/ G	Dip azimuth	Dip angle	Structure typ
	5/27/2016 14:26	119.9397	15.99187	124.01	north of Mt. S	boninitic? pillows		300	40	
								310	40	
ZM2-102	5/27/2016 14:54	119.94	15.99231	127.68	north of Mt. S	ZM2-102 (glassy lapili tuff)		330	10	lapili tuff
								324	10	
ZM2-103	5/27/2016 15:11	119.9398	15.99244	131.29	north of Mt. S	ZM2-103A (glassy pillow ma		320	20	
						ZM2-103B (tuff breccia)		330	20	
ZM2-104	5/27/2016 15:42	119.9406	15.99277	138.13	north of Mt. S	**ZM2-104 (tu**	**Boninitic basalt altered**			
ZM2-105	5/27/2016 15:55	119.9411	15.99295	153.63	north of Mt. S	**ZM2-105A (f**	**Andesite (LSE**	330	20	pillows
	5/27/2016 16:40	119.9411	15.99304	162.95	north of Mt. S	ZM2-105B (fresh glassy margins)				
						ZM2-105C (fresh glassy margins)				
						ZM2-105D (f	**Basaltic Andesite (LSB series)**			
ZM2-106	5/27/2016 16:47	119.9409	15.99397	154.92	north of Mt. S	boninitic? Pillows		340	20	pillows
ZM2-107	5/27/2016 17:03	119.9399	15.99284	147.21	north of Mt. S	**ZM2-107,** tuf	**Boninite, LSB**			
ZM2-108	5/27/2016 17:37	119.943	15.9999	206.72	west, road to	coralline limestone				
	5/27/2016 17:43	119.9411	15.99891	209.03	west, road to	coralline limestone				
	5/27/2016 17:47	119.9406	15.99889	211.82	west, road to	coralline limestone				
ZM2-109	5/27/2016 18:00	119.942	16.00035	200.84	west, road to	coralline limestone		30	20	coralline limes
ZM2-110	5/28/2016 11:29	119.9359	15.97737	145.42	SSW of Mt. S	boninitic floats, relict pillow structure				
ZM2-111	5/28/2016 11:39	119.935	15.97847	136.22	SSW of Mt. S	relict pillow structure				

Locality	DateDateDate	Long	Lat	Altitude	Location ID	Sample/Fie	Rock-type/ G	Dip azimuth	Dip angle	Structure typ
ZM2-113	5/28/2016 11:53	119.934	15.97848	133.18	SSW of Mt. S	ZM2-113	pillow, elongate pil	276	35	pillows
						ZM2-113	dike	190	30	dike
								230	30	dike
								195	25	dike
ZM2-114	5/28/2016 12:50	119.9316	15.97785	169.42	SSW of Mt. S	weathered boninitic pillows		300	60	pillows
								290	70	pillows
ZM2-115	5/28/2016 13:48	119.9321	15.97647	161.89	SSW of Mt. S	andesite?				
ZM2-116	5/28/2016 13:57	119.9322	15.97631	160.16	SSW of Mt. S	**ZM2-116 (an**	**Basaltic Andesite (LSB series)**			
ZM2-117	5/28/2016 14:04	119.9322	15.97534	161.14	SSW of Mt. S	ZM2-117 (boninitic pillows)		150	50	pillows
								130	40	pillows
ZM2-118	5/28/2016 14:50	119.9305	15.97372	164.48	SSW of Mt. S	ZM2-118 (diabase floats)				
ZM2-119	5/28/2016 14:56	119.9304	15.97356	153.93	SSW of Mt. S	ZM2-119A (massive), andes		100	50	pillows and m
						ZM2-119B (glassy margin)				
ZM2-120	5/28/2016 15:32	119.9294	15.9727	136.59	SSW of Mt. S	**ZM2-120A (r**	**Boninite, LSB**	160	30	
						ZM2-120B (pillow)		160	20	
ZM2-121	5/28/2016 16:40	119.9296	15.96871	102.92	SSW of Mt. S	weathered pillow or flow?		195	40	
ZM2-122	5/28/2016 17:01	119.932	15.96899	120.96	SSW of Mt. S	boninitic pillows?				
	5/28/2016 17:07	119.9324	15.96799	103.34	SSW of Mt. S	boninitic pillows?				

Locality	DateDateDate	Long	Lat	Altitude	Location ID	Sample/Fie	Rock-type/ G	Dip azimuth	Dip angle	Structure typ
ZM2-123	5/28/2016 17:11	119.9326	15.96698	107.35	SSW of Mt. S	**ZM2-123 (bc**	**Andesite (LSB series)**			
ZM2-124	5/28/2016 17:22	119.9333	15.96796	98.97	SSW of Mt. S	**ZM2-124 (bc**	**Andesite (LSB series)**			
ZM2-125	5/28/2016 17:29	119.9336	15.96878	94.63	SSW of Mt. S	**ZM2-125** (bo	**Andesite (LSB series)**			
ZM2-125b	5/28/2016 17:37	119.9336	15.969	111.02	SSW of Mt. S	boninitic? Lapili tuff on fragmentary pillows				
ZM2-126	5/28/2016 17:48	119.934	15.96985	96.02	SSW of Mt. S	boninitic pillows?				
ZM2-127	5/28/2016 17:53	119.9351	15.9708	97.58	SSW of Mt. S	boninitic pillows?				
ZM2-128	5/29/2016 10:54	119.9449	15.98419	157.24	ZM15 travers	**ZM2-128A (t**	**Boninitic basa**	282	40	pillows
						ZM2-128B (t	**Boninitic basa**	305	30	pillows
						ZM2-128C (t	**Boninitic basa**	280	30	pillows
						ZM2-128D (boninitic pillows)				
ZM2-128A	5/29/2016 11:46	119.9449	15.98408	150.53	ZM15 travers	sand				
ZM2-128B	5/29/2016 12:47	119.9451	15.98384	154.85	ZM15 travers	sand				
ZM2-128C	5/29/2016 13:46	119.9448	15.98335	154.59	ZM15 travers	sand				
ZM2-128D	5/29/2016 13:50	119.9443	15.98406	153.95	ZM15 travers	sand				
ZM2-129	5/29/2016 13:07	119.9446	15.98448	155.98	ZM15 travers	boninitic pillows		280	45	pillows
								280	30	pillows
ZM2-130	5/29/2016 13:28	119.9448	15.98392	153.86	ZM15 travers	boninitic pillows		48	30	pillows
								20	40	pillows

Locality	DateDateDate	Long	Lat	Altitude	Location ID	Sample/Fie	Rock-type/ G	Dip azimuth	Dip angle	Structure typ
ZM2-137	5/29/2016 17:08	119.9491	15.97989	122.75	ZM15 travers	ZM2-137 (sheet flow), spatte		70	50	
								72	40	
ZM2-138	5/29/2016 17:25	119.9492	15.97986	120.98	ZM15 travers	ZM2-138 (blocky lava sheet		80	25	
ZM2-139	5/29/2016 17:30	119.9494	15.98	120.81	ZM15 travers	tuff breccia overlain by lapili	tuff			
ZM2-140	5/29/2016 17:34	119.9497	15.98003	120.21	ZM15 travers	tuff breccia overlain by lapili	tuff			
ZM2-141	5/29/2016 17:36	119.95	15.97993	116.47	ZM15 travers	**ZM2-141 (tu**	**Andesite (LSE**	30	20	
ZM2-142	5/29/2016 18:10	119.9491	15.98153	132.58	ZM15 travers	sand, boninitic pillows		30	40	
ZM2-142	5/29/2016 18:10	119.9491	15.98153	132.58	ZM15 travers	sand				
ZM2-145	5/29/2016 18:33	119.9488	15.98189	139.9	ZM15 traverse					
	5/29/2016 18:44	119.9481	15.98231	146.59	ZM15 travers	boninitic pillows				
ZM2-146	5/29/2016 18:48	119.9469	15.98238	154.95	ZM15 travers	boninitic pillows		20	20	
	5/30/2016 11:31	119.9385	16.00843	108.64	west, road to	limestone				
ZM2-147	5/30/2016 12:00	119.9447	15.97754	152.19	south of ZM1	ZM2-147 (andesitic tuff breccia)				
ZM2-148	5/30/2016 12:12	119.9439	15.97781	155.67	south of ZM1	**ZM2-148 (tu**	**Andesite (LSE**	30	35	
	5/30/2016 12:18	119.9432	15.97804	149.39	south of ZM1	andesitic tuff breccia		320	30	
	5/30/2016 12:26	119.9427	15.97743	141.54	south of ZM1	andesitic tuff breccia				
ZM2-149	5/30/2016 12:38	119.942	15.98776	146.26	south of ZM1	ZM2-149 (buff colored clays		70	30	
								55	38	

Locality	DateDateDate	Long	Lat	Altitude	Location ID	Sample/Fie	Rock-type/ G	Dip azimuth	Dip angle	Structure typ
ZM2-150	5/30/2016 12:46	119.942	15.98801	150.42	south of ZM1	ZM2-150 (vfg sandstone/cla		70	20	
								60	30	
ZM2-151	5/30/2016 12:53	119.9429	15.98799	146.55	south of ZM1	claystone		68	10	
ZM2-152	5/30/2016 12:58	119.9446	15.98762	144.29	south of ZM1	claystone		35	10	
ZM2-153	5/30/2016 13:05	119.9457	15.98723	141.03	south of ZM1	boninitic pillows		80	30	
ZM2-154	5/30/2016 13:15	119.9476	15.98731	131.8	south of ZM1	boninitic pillows				
ZM2-155	5/30/2016 13:45	119.9461	15.99316	154.29	west, road to	claystone				
ZM2-156	5/30/2016 14:31	119.9454	15.99354	186.43	west, road to	ZM2-156 (andesitic tuff brec		290	50	
	5/30/2016 15:13	119.9455	15.9933	175.95	west, road to	andesitic tuff breccia		290	70	
								310	70	
ZM2-157	5/30/2016 15:27	119.9261	15.9949	108.04	road to Dasol	limestone		280	10	

Appendix 2. Zambales Geochem DB

	Acoje Block_Barlo														
Sample	Barlo 7	LUZ152	LUZ163A	LUZ159	LUZ160C	ZO-293	ZO-298	Z298	LUZ28C	ZO-302	LUZ160A	Barlo 10E	ZO-301	LUZ28D	LUZ354A
Type	LSB, pillo	LSB, dike	LSB dike	LSB dike	LSB, pillo	LSB, pillo	LSB, pillo	LSB	Bon. Bas	Bon. Bas	Bon. Bas	Bas. And	Dacite	altered Lł	altered Lł
Locality	Balincag	Balincaguin	River	Balincag	Balincag	Balincag	Balincaguin	River	Barlo Min	Balincag	Balincag	Balincag	Balincag	Barlo Mine	
Referenc	RAT01	HKEV83/	HKEV83/	HKEV83/	HKEV83/	GPY90	GPY90	Pearce et	HKEV83/	GPY90	HKEV83/	RAT01	GPY90	HKEV83/	HKEV83/
SiO_2	51.6	54.02	52.81	55.13	53.49	53.97	53.4	52.99	50.42	51.64	50.88	52.6	66.03	53.91	56.07
TiO_2	0.28	0.44	0.24	0.34	0.22	0.3	0.34	0.34	0.25	0.4	0.36	0.35	0.63	0.26	0.28
Al_2O_3	13.95	16.37	13.94	16.72	13.67	14.08	16.3	16.18	14.06	16.99	16.03	16.4	14.86	13.74	16.31
Fe_2O_3	8							8.8				7.95			
FeO		9.32	8.74	8.04	8.49	7.99	8.06		9.29	8.88	8.21		6.35	8.32	8.17
MnO	0.1	0.21	0.22	0.27	0.23	0.18	0.18	0.18	0.33	0.26	0.22	0.08	0.13	0.12	0.16
MgO	9.25	7.94	14.06	7.77	13.08	11.77	10.72	10.64	15.88	10.52	9.96	6.15	4.52	9.94	8.79
CaO	9.65	8.11	7.76	7.84	7.76	9.52	9.33	9.26	8.72	10.23	10.76	9.5	4.33	10.22	4.06
Na_2O	1.09	1.63	1.44	2.45	2.01	1.77	0.9	0.89	0.65	0.44	0.64	1.35	2.96	1.16	5.67
K_2O	0.18	0.6	0.37	0.58	0.7	0.36	0.71	0.7	0.38	0.56	0.47	0.14	0.12	2.17	0.03
P_2O_5	0.03	0.04	0.05	0.02	0.02	0.02	0.02	0.02	0.02	0.02	0.18	0.03	0.04		0.1
LOI	5.88											5.32			
Total	94.13	98.68	99.63	99.16	99.67	99.96	99.96	100	100	99.94	97.71	94.55	99.97	99.84	99.64
SiO_2	55.29	54.74	53.01	55.60	53.67	53.99	53.42	53.46	50.42	51.67	52.07	56.10	66.05	54.00	56.27
TiO_2	0.30	0.45	0.24	0.34	0.22	0.30	0.34	0.34	0.25	0.40	0.37	0.37	0.63	0.26	0.28
Al_2O_3	14.95	16.59	13.99	16.86	13.72	14.09	16.31	16.32	14.06	17.00	16.41	17.49	14.86	13.76	16.37
FeO	7.71	9.44	8.77	8.11	8.52	7.99	8.06	7.99	9.29	8.89	8.40	7.63	6.35	8.33	8.20
MnO	0.11	0.21	0.22	0.27	0.23	0.18	0.18	0.18	0.33	0.26	0.23	0.09	0.13	0.12	0.16
MgO	9.91	8.05	14.11	7.84	13.12	11.77	10.72	10.73	15.88	10.53	10.19	6.56	4.52	9.96	8.82
CaO	10.34	8.22	7.79	7.91	7.79	9.52	9.33	9.34	8.72	10.24	11.01	10.13	4.33	10.24	4.07
Na_2O	1.17	1.65	1.45	2.47	2.02	1.77	0.90	0.90	0.65	0.44	0.65	1.44	2.96	1.16	5.69
K_2O	0.19	0.61	0.37	0.58	0.70	0.36	0.71	0.71	0.38	0.56	0.48	0.15	0.12	2.17	0.03
P_2O_5	0.03	0.04	0.05	0.02	0.02	0.02	0.02	0.02	0.02	0.02	0.18	0.03	0.04	0.00	0.10
Total	100.00	100.00	100.00	100.00	100.00	100.00	100.00	100.00	100.00	100.00	100.00	100.00	100.00	100.00	100.00
V	260	235	269	240	240	250	265	265	220	289	232	286	233	235	280
Ti_ppm	1799	2673	1444	2056	1323	1799	2039	2056	1499	2399	2209	2238	3778	1561	1685

		Acoje Block_Barlo						Coto Block mantle dikes							
ZO-303	Sample	ZO-304	ZO-292	ZO-295	ZO-297	Barlo 11	Barlo 12	C-2	C-8	C-12	LUZ209A	LUZ209Y	LUZ209Z	LUZ215M	LUZ399A
altered Lł	Type	altered Lł	altered Ba	altered An	altered An	altered Ba	altered Ba	Bas. Andesite, lower unit							
Barlo Min	Locality	Balincag	Balincag	Balincag	Barlo Min	SW of Ba	SW of Ba	Coto area	Coto area	Coto area	Coto area	Coto area	Coto area	Coto area	Coto area
GPY90	Referenc	GPY90	GPY90	GPY90	GPY90	RAT01	RAT01	EVNS91	EVNS91	EVNS91	EVNS91	EVNS91	EVNS91	EVNS91	EVNS91
57.78	SiO_2	58.45	55.27	57.32	57.2	52.75	53.2	55.69	53.54	53.50	54.89	53.10	49.49	54.12	52.37
0.4	TiO_2	0.33	0.35	0.43	0.37	0.34	0.32	0.78	0.73	1.09	1.17	0.60	0.47	0.94	0.86
17.07	Al_2O_3	15.68	16.83	15.81	16.21	15.8	15.4	15.63	16.34	15.20	15.83	16.41	15.39	17.02	16.27
	Fe_2O_3					9.13	8.8								
8.12	FeO	7.15	8.56	9.19	7.62			10.30	10.37	11.09	10.73	7.50	6.78	10.22	9.90
0.16	MnO	0.16	0.16	0.16	0.15	0.17	0.16	0.18	0.19	0.19	0.15	0.19	0.21	0.13	0.18
8.05	MgO	7.77	7.03	5.31	7.04	6.7	6.51	4.22	4.72	4.19	4.10	7.37	10.66	4.23	5.31
3.03	CaO	5.9	5.86	7.32	7.58	6.85	5.52	8.84	9.46	8.60	8.39	10.42	14.31	9.42	7.28
5.17	Na_2O	4.34	4.83	4.33	3.12	2.8	3.81	2.65	2.53	2.68	2.49	3.21	1.44	3.23	3.97
0.35	K_2O	0.15	1.03	0.06	0.63	1.52	2.06	0.03	0.12	0.13	0.12	0.28	0.05	0.15	0.21
0.02	P_2O_5	0.02	0.02	0.02	0.03	0.03	0.03	0.08	0.07	0.07	0.09	0.21	0.04	0.08	0.14
	LOI					3.54	3.85								
100.15	Total	99.95	99.94	99.95	99.95	96.09	95.81	98.40	98.07	96.74	97.96	99.29	98.84	99.54	96.49
57.69	SiO_2	58.48	55.30	57.35	57.23	55.42	56.04	56.59	54.59	55.31	56.03	53.48	50.07	54.37	54.28
0.40	TiO_2	0.33	0.35	0.43	0.37	0.36	0.34	0.79	0.74	1.13	1.19	0.60	0.48	0.94	0.89
17.04	Al_2O_3	15.69	16.84	15.82	16.22	16.60	16.22	15.88	16.66	15.71	16.16	16.53	15.57	17.10	16.86
8.11	FeO	7.15	8.57	9.19	7.62	8.63	8.34	10.47	10.58	11.46	10.96	7.56	6.86	10.27	10.26
0.16	MnO	0.16	0.16	0.16	0.15	0.18	0.17	0.18	0.19	0.20	0.15	0.19	0.21	0.13	0.19
8.04	MgO	7.77	7.03	5.31	7.04	7.04	6.86	4.29	4.81	4.33	4.19	7.42	10.78	4.25	5.50
3.03	CaO	5.90	5.86	7.32	7.58	7.20	5.81	8.98	9.65	8.89	8.56	10.49	14.48	9.46	7.54
5.16	Na_2O	4.34	4.83	4.33	3.12	2.94	4.01	2.69	2.58	2.77	2.54	3.23	1.46	3.24	4.11
0.35	K_2O	0.15	1.03	0.06	0.63	1.60	2.17	0.03	0.12	0.13	0.12	0.28	0.05	0.15	0.22
0.02	P_2O_5	0.02	0.02	0.02	0.03	0.03	0.03	0.08	0.07	0.07	0.09	0.21	0.04	0.08	0.15
100.00	Total	100.00	100.00	100.00	100.00	100.00	100.00	100.00	100.00	100.00	100.00	100.00	100.00	100.00	100.00
224	V	224	267	329	210	285	275	337	365	356	424	282	229	386	370
2394	Ti_ppm	1979	2100	2579	2219	2142	2021	4752	4462	6755	7160	3623	2851	5661	5343

			Coto Block mantle dikes													
LUZ252	LUZ254	Sample	LUZ256B	LUZ259D	LUZ666F	LUZ666K	LUZ670C	LUZ675	ZO-40	ZO-42	ZO-43	ZO-48	ZO-72	ZO-76	ZO-78
Botolan	Botolan	Type	Botolan	Botolan	Botolan	Botolan	Botolan	Botolan	Diabase,	Diabase,	Diabase,	Diabase,	Diabase,	Microgab	Microgab
EVNS91	EVNS91	Locality	EVNS91	EVNS91	EVNS91	EVNS91	EVNS91	EVNS91	Hayden F	Hayden F	Hayden F	Hayden F	South La	South La	South La
		Referenc							GPY90	GPY90	GPY90	GPY90	GPY90	GPY90	GPY90
52.86	52.97	SiO_2	52.53	50.74	55.87	56.52	50.28	51.38	54.02	51.73	55.36	45.71	53.10	51.51	54.07
0.98	0.95	TiO_2	0.70	1.62	0.34	0.71	0.75	0.82	0.69	1.36	1.35	0.53	0.79	0.25	0.69
17.52	16.25	Al_2O_3	15.97	15.21	15.23	14.50	14.80	16.70	16.01	16.38	14.65	13.49	16.77	12.51	16.89
		Fe_2O_3													
8.44	10.06	FeO	7.58	8.86	7.37	5.84	8.82	9.06	8.85	11.71	12.75	8.61	10.13	8.19	9.36
0.10	0.14	MnO	0.16	0.18	0.14	0.14	0.16	0.17	0.15	0.19	0.20	0.34	0.15	0.12	0.15
5.19	6.32	MgO	6.77	6.65	7.93	7.44	10.48	6.73	6.42	5.16	4.66	19.83	5.44	16.66	5.53
10.04	9.71	CaO	9.97	9.58	11.32	8.75	11.14	10.67	9.92	9.41	7.03	11.36	9.03	9.76	8.86
4.41	2.55	Na_2O	3.06	4.39	2.27	4.91	2.61	3.46	3.68	3.79	3.72	0.00	4.36	0.87	4.25
0.05	0.67	K_2O	0.36	0.10	0.02	0.17	0.06	0.11	0.15	0.15	0.16	0.06	0.11	0.06	0.10
0.12	0.13	P_2O_5	0.20	0.20	0.04	0.07	0.07	0.08	0.05	0.07	0.07	0.04	0.05	0.02	0.05
		LOI													
99.71	99.75	Total	97.30	97.53	100.53	99.05	99.17	99.18	99.94	99.95	99.95	99.97	99.93	99.95	99.95
53.01	53.10	SiO_2	53.99	52.02	55.58	57.06	50.70	51.80	54.05	51.76	55.39	45.72	53.14	51.54	54.10
0.98	0.95	TiO_2	0.72	1.66	0.34	0.72	0.76	0.83	0.69	1.36	1.35	0.53	0.79	0.25	0.69
17.57	16.29	Al_2O_3	16.41	15.59	15.15	14.64	14.92	16.84	16.02	16.39	14.66	13.49	16.78	12.52	16.90
8.46	10.09	FeO	7.79	9.09	7.33	5.90	8.89	9.14	8.86	11.72	12.76	8.61	10.14	8.19	9.36
0.10	0.14	MnO	0.16	0.18	0.14	0.14	0.16	0.17	0.15	0.19	0.20	0.34	0.15	0.12	0.15
5.21	6.34	MgO	6.96	6.82	7.89	7.51	10.57	6.79	6.42	5.16	4.66	19.84	5.44	16.67	5.53
10.07	9.73	CaO	10.25	9.82	11.26	8.83	11.23	10.76	9.93	9.41	7.03	11.36	9.04	9.76	8.86
4.42	2.56	Na_2O	3.15	4.50	2.26	4.96	2.63	3.49	3.68	3.79	3.72	0.00	4.36	0.87	4.25
0.05	0.67	K_2O	0.37	0.10	0.02	0.17	0.06	0.11	0.15	0.15	0.16	0.06	0.11	0.06	0.10
0.12	0.13	P_2O_5	0.21	0.21	0.04	0.07	0.07	0.08	0.05	0.07	0.07	0.04	0.05	0.02	0.05
100.00	100.00	Total	100.00	100.00	100.00	100.00	100.00	100.00	100.00	100.00	100.00	100.00	100.00	100.00	100.00
367	423	V	306	287	219	220	272	274	289	414	416	211	351	185	320
5892	5710	Ti_ppm	4313	9958	2028	4297	4534	4956	4139	8157	8097	3178	4739	1499	4139

			Coto Block mantle dikes												
ZO-80	ZO-87	ZO-93	Sample	ZO-94	ZO-114	ZO-115	ZO-128	ZO-134	ZO-135	ZO-138	ZO-141	ZO-145	ZO-155	ZO-74	ZO-417
Microgab	Diabase,	Diabase,	Type	Diabase,	Diabase,	Diabase,	Microgab	Diabase,	Diabase,	Microgab	Diabase	Microgab	Microgab	Basalt, di	Diabase,
South La	South La	South La	Locality	South La	Level 55(	Western	Dalayap	Level 70(	909 orebo	909 orebo	83-91ft, D	137ft, DD	DDH-1871,	Coto M	Bucao Ri
GPY90	GPY90	GPY90	Referenc	GPY90	GPY90	GPY90	GPY90	GPY90	GPY90	GPY90	GPY90	GPY90	GPY90	GPY90	GPY90
47.33	52.52	56.72	SiO_2	57.06	52.91	57.99	51.69	54.13	50.44	51.44	55.45	55.66	55.60	45.24	52.10
0.29	0.91	0.95	TiO_2	0.87	0.86	0.92	0.51	0.68	0.94	0.73	0.75	0.77	0.87	0.30	0.38
13.66	17.82	15.87	Al_2O_3	16.04	16.75	15.93	17.04	15.59	15.37	16.51	14.45	16.62	16.16	10.78	14.11
			Fe_2O_3												
8.06	9.81	11.20	FeO	11.03	11.15	10.01	7.29	9.15	10.43	8.95	7.97	10.26	10.54	8.97	5.65
0.14	0.15	0.13	MnO	0.16	0.18	0.16	0.13	0.16	0.18	0.15	0.13	0.15	0.16	0.27	0.07
13.57	4.24	3.84	MgO	3.66	5.21	3.53	8.73	6.57	6.35	7.94	7.85	4.83	5.02	19.44	12.22
16.83	10.62	8.72	CaO	8.42	7.98	8.32	12.39	9.53	13.29	11.12	8.84	5.59	8.33	14.37	14.41
0.00	3.69	2.31	Na_2O	2.51	4.66	2.89	1.84	3.95	2.70	2.90	4.31	5.74	3.01	0.51	0.93
0.05	0.11	0.16	K_2O	0.13	0.20	0.13	0.31	0.14	0.18	0.15	0.14	0.28	0.22	0.05	0.06
0.02	0.09	0.06	P_2O_5	0.07	0.05	0.07	0.03	0.05	0.08	0.05	0.06	0.05	0.05	0.02	0.03
			LOI												
99.95	99.96	99.96	Total	99.95	99.95	99.95	99.96	99.95	99.96	99.94	99.95	99.95	99.96	99.95	99.96
47.35	52.54	56.74	SiO_2	57.09	52.94	58.02	51.71	54.16	50.46	51.47	55.48	55.69	55.62	45.26	52.12
0.29	0.91	0.95	TiO_2	0.87	0.86	0.92	0.51	0.68	0.94	0.73	0.75	0.77	0.87	0.30	0.38
13.67	17.83	15.88	Al_2O_3	16.05	16.76	15.94	17.05	15.60	15.38	16.52	14.46	16.63	16.17	10.79	14.12
8.06	9.81	11.20	FeO	11.04	11.16	10.02	7.29	9.15	10.43	8.96	7.97	10.27	10.54	8.97	5.65
0.14	0.15	0.13	MnO	0.16	0.18	0.16	0.13	0.16	0.18	0.15	0.13	0.15	0.16	0.27	0.07
13.58	4.24	3.84	MgO	3.66	5.21	3.53	8.73	6.57	6.35	7.94	7.85	4.83	5.02	19.45	12.22
16.84	10.62	8.72	CaO	8.42	7.98	8.32	12.39	9.53	13.30	11.13	8.84	5.59	8.33	14.38	14.42
0.00	3.69	2.31	Na_2O	2.51	4.66	2.89	1.84	3.95	2.70	2.90	4.31	5.74	3.01	0.51	0.93
0.05	0.11	0.16	K_2O	0.13	0.20	0.13	0.31	0.14	0.18	0.15	0.14	0.28	0.22	0.05	0.06
0.02	0.09	0.06	P_2O_5	0.07	0.05	0.07	0.03	0.05	0.08	0.05	0.06	0.05	0.05	0.02	0.03
100.00	100.00	100.00	Total	100.00	100.00	100.00	100.00	100.00	100.00	100.00	100.00	100.00	100.00	100.00	100.00
236	338	476	V	351	401	297	245	295	329	292	247	348	388	199	197
1739	5458	5698	Ti_ppm	5218	5158	5518	3059	4079	5638	4379	4498	4618	5218	1799	2279

					Coto Block_east side										
ZO-423 Diabase, Bucao Ri GPY90	ZO-424 Diabase, Bucao Ri GPY90	ZO-425 Diabase, Bucao Ri GPY90	ZO-427 Diabase, Bucao Ri GPY90	Sample Type Locality Referenc	LUZ116-(Diabase (Camiling HKEV83	LUZ112 Diabase (Moriones HKEV83	LUZ118C Diabase (Camiling HKEV83	LUZ116-I Diabase (Camiling HKEV83	EG-12 Diabase, Camiling, GEAR89	EG-60 Diabase, Camiling, GEAR89	EG-17A Diabase, Camiling, GEAR89	EG-21 Basalt, D Camiling, GEAR89	EG-26 Basalt, Di Camiling, GEAR89	EG-27 Diabase, Camiling, GEAR89	EG-29 Basalt, Di Camiling, GEAR89
54.04	54.10	51.55	52.31	SiO_2	50.87	51.39	52.9	50.15	47.26	50.03	57.76	58.06	52.12	51.77	53.01
0.67	0.79	0.72	0.36	TiO_2	0.91	0.59	1.47	0.98	3.24	1.5	1.23	1.25	1.35	1.09	0.9
16.83	16.89	17.60	13.09	Al_2O_3	15.93	16.71	15.97	16.47	14.82	15.23	15.36	15.93	16.25	16.28	17.65
				Fe_2O_3											
8.17	9.64	9.26	8.49	FeO	8.94	8.27	10.87	8.58	13.31	10.75	7.86	11.08	9.75	8.33	9.68
0.15	0.15	0.15	0.15	MnO	0.21	0.22	0.36	0.19	0.18	0.14	0.07	0.12	0.13	0.13	0.22
6.89	5.73	7.36	12.55	MgO	8.15	8.56	5.48	9.12	8.83	7.11	6.17	5.43	7.87	9.45	6.5
10.43	7.74	10.10	11.08	CaO	11.91	9.54	9.41	12.19	10.42	11.58	6.76	4.2	7.72	10.73	6.76
2.64	4.72	2.96	1.80	Na_2O	1.83	1.64	3.09	1.62	1.7	2.93	4.74	2.82	3.63	2.37	4.48
0.09	0.14	0.20	0.10	K_2O	0.01	0.97	0.05	0.22	0.19	0.05	1.08	0.19	0.56	0.31	0.02
0.05	0.06	0.06	0.03	P_2O_5		0.17	0.17	0.09					0.11	0.08	
				LOI											
99.96	99.96	99.96	99.96	Total											
54.06	54.12	51.57	52.33	SiO_2	51.51	52.41	53.02	50.35	47.28	50.37	57.17	58.60	52.39	51.49	53.43
0.67	0.79	0.72	0.36	TiO_2	0.92	0.60	1.47	0.98	3.24	1.51	1.22	1.26	1.36	1.08	0.91
16.84	16.90	17.61	13.10	Al_2O_3	16.13	17.04	16.01	16.53	14.83	15.33	15.20	16.08	16.33	16.19	17.79
8.17	9.64	9.26	8.49	FeO	9.05	8.43	10.90	8.61	13.32	10.82	7.78	11.18	9.80	8.29	9.76
0.15	0.15	0.15	0.15	MnO	0.21	0.22	0.36	0.19	0.18	0.14	0.07	0.12	0.13	0.13	0.22
6.89	5.73	7.36	12.56	MgO	8.25	8.73	5.49	9.16	8.83	7.16	6.11	5.48	7.91	9.40	6.55
10.43	7.74	10.10	11.08	CaO	12.06	9.73	9.43	12.24	10.43	11.66	6.69	4.24	7.76	10.67	6.81
2.64	4.72	2.96	1.80	Na_2O	1.85	1.67	3.10	1.63	1.70	2.95	4.69	2.85	3.65	2.36	4.52
0.09	0.14	0.20	0.10	K_2O	0.01	0.99	0.05	0.22	0.19	0.05	1.07	0.19	0.56	0.31	0.02
0.05	0.06	0.06	0.03	P_2O_5	0.00	0.17	0.17	0.09	0.00	0.00	0.00	0.00	0.11	0.08	0.00
100.00	100.00	100.00	100.00	Total	100	100	100	100	100	100	100	100	100	100	100
264	319	290	223	V	240	220	340	220							
4018	4738	4318	2159	Ti_ppm	5524	3607	8833	5898							

					Coto Block_east side										
EG-34 Diabase, Camiling, GEAR89	EG-35 Diabase, Camiling, GEAR89	EG-36 Basalt, Di Camiling, GEAR89	EG-37 Basalt, Di Camiling, GEAR89	EG-62 Diabase, Camiling, GEAR89	Sample Type Locality Referenc	EG-64 Basalt, Di Camiling, GEAR89	EG-06 Basalt, Ba Camiling, GEAR89	EG-31 Basalt, Ba Camiling, GEAR89	EG-44 Basaltic t Camiling, GEAR89	EG-49 Basalt, Ba Camiling, GEAR89	EG-50 Basaltic t Camiling, GEAR89	EG-68 Basalt, Ba Camiling, GEAR89	RK-16A Basalt, Ba Camiling, GEAR89	LUZ423F dike Moriones GEAR89	LUZ616A dike and Bulsu GEAR89
52.94	50.62	41.33	59.03	51.4	SiO_2	51.94	51.67	60.59	46.8	50.95	41.84	55.85	54.45	50.98	50.89
0.72	0.73	0.92	1.23	0.95	TiO_2	1.06	0.97	1.21	0.15	0.56	0.36	0.64	1.46	1.01	1.57
17.5	18.41	21.08	15.08	16.29	Al_2O_3	17.38	16.07	16.63	21.93	16.26	15.35	16.55	19.14	19.88	14.69
					Fe_2O_3										
8.78	8.29	18.86	8.97	8.93	FeO	11.06	11.64	9.11	3.03	9.09	6.65	8.16	8.32	7.44	11.51
0.15	0.16	0.21	0.09	0.17	MnO	0.24	0.23	0.22	2.34	0.24	0.2	0.21	0.2	0.17	0.21
7.83	9.5	13.14	3.79	9.05	MgO	6.16	5.88	8.05	1.15	9.62	3.97	8.02	1.19	6.44	7.6
7.18	10.25	1.18	10.05	10.51	CaO	8.95	6.91	1	16.92	8.85	25.37	4.91	8	12.34	9.53
3.7	1.78	3.1	0.48	2.47	Na_2O	2.87	3.88	4.08	7.58	3.75	5.13	5.39	4.5	1.97	3.63
0.54	0.36	0.04		0.42	K_2O	0.06	1.83	0.01	1	0.22	1.55	0.06	1.51	0.31	0.16
0.13			0.15	0.13	P_2O_5		0.35		0.13	0.11	0.14		0.3	0.2	0.16
					LOI										
					Total										
53.22	50.57	41.39	59.70	51.24	SiO_2	52.09	51.97	60.05	46.32	51.13	41.61	55.97	54.96	50.61	50.92
0.72	0.73	0.92	1.24	0.95	TiO_2	1.06	0.98	1.20	0.15	0.56	0.36	0.64	1.47	1.00	1.57
17.59	18.39	21.11	15.25	16.24	Al_2O_3	17.43	16.16	16.48	21.71	16.32	15.26	16.58	19.32	19.73	14.70
8.83	8.28	18.89	9.07	8.90	FeO	11.09	11.71	9.03	3.00	9.12	6.61	8.18	8.40	7.39	11.52
0.15	0.16	0.21	0.09	0.17	MnO	0.24	0.23	0.22	2.32	0.24	0.20	0.21	0.20	0.17	0.21
7.87	9.49	13.16	3.83	9.02	MgO	6.18	5.91	7.98	1.14	9.65	3.95	8.04	1.20	6.39	7.60
7.22	10.24	1.18	10.16	10.48	CaO	8.98	6.95	0.99	16.75	8.88	25.23	4.92	8.08	12.25	9.53
3.72	1.78	3.10	0.49	2.46	Na_2O	2.88	3.90	4.04	7.50	3.76	5.10	5.40	4.54	1.96	3.63
0.54	0.36	0.04	0.00	0.42	K_2O	0.06	1.84	0.01	0.99	0.22	1.54	0.06	1.52	0.31	0.16
0.13	0.00	0.00	0.15	0.13	P_2O_5	0.00	0.35	0.00	0.13	0.11	0.14	0.00	0.30	0.20	0.16
100	100	100	100	100	Total	100	100	100	100	100	100	100	100	100	100
					V									249	284
					Ti_ppm									6010	9417

ZO-174	ZO-176	ZO-178	ZO-184
basalt, pil	Basalt	Basalt	Diabase
Moriones	Moriones	Barrio Ma	Sitio, Ubc
GPY90	GPY90	GPY90	GPY90
64.01	56.3	55.86	57.82
0.84	1.44	1.19	1.18
14.28	14.8	16.06	15.93
10.91	14.09	17.15	9.23
0.14	0.17	0.07	0.15
4.36	8.02	4.61	8.17
2.33	4.98	4.08	4.05
2.98	0.01	0.71	3.29
0.06	0.05	0.14	0.05
0.06	0.1	0.07	0.07
64.03	56.32	55.89	57.85
0.84	1.44	1.19	1.18
14.28	14.81	16.07	15.94
10.91	14.10	17.16	9.24
0.14	0.17	0.07	0.15
4.36	8.02	4.61	8.17
2.33	4.98	4.08	4.05
2.98	0.01	0.71	3.29
0.06	0.05	0.14	0.05
0.06	0.10	0.07	0.07
100	100	100	100
238	412	429	314
5037	8636	7138	

	Acoje Block_Subic														
Sample	ZO-1	ZO-2	ZO-3	ZO-6	ZO-8	ZO-9	ZO-13	ZO-400	ZO-401	ZO-402	ZO-403	ZO-404	ZO-405	ZO-406	ZO-409
Type	Basalt br	Basalt sill	Basalt di	Basalt di	Diabase (	Augite ba	Diabase	Pillow ba	Pillow ba	Diabase (	Diabase (	Diabase (	Diabase (	Pillow ba	Diabase (
Locality	Baretto, (	Baretto, (	Baretto, (	Kale, Sut	Baretto, (	Baretto, (	Calapacu	Subic Be	Subic Be	Subic Be	Subic Be	Subic Be	Subic Be	Subic Be	Subic Be
Referenc	GPY90	GPY90	GPY90	GPY90	GPY90	GPY90	GPY90	GPY90	GPY90	GPY90	GPY90	GPY90	GPY90	GPY90	GPY90
SiO_2	62.27	51.24	58.84	57.44	53.99	48.82	51.85	55.01	55.63	57.12	55.84	76.59	76.27	55.78	66.72
TiO_2	0.75	0.62	1.07	1.36	1.52	0.65	0.52	0.99	0.98	0.79	0.4	0.22	0.22	0.99	0.6
Al_2O_3	14.76	11.63	15.56	15.33	15.4	10.58	15.09	15.87	16.13	17.29	16.85	12.1	12.32	16.11	14.74
Fe_2O_3															
FeO	10.26	10.52	9.22	10.35	11.89	10.76	8.2	10.46	9.77	10.74	8.93	3.65	3.66	9.68	7.89
MnO	0.12	0.17	0.17	0.19	0.16	0.18	0.18	0.17	0.16	0.16	0.14	0.08	0.09	0.15	0.11
MgO	3.35	8.92	5.22	4.57	4.53	14.41	9.82	7.64	6.72	3.53	7.23	0.6	0.48	5.48	1.8
CaO	2.04	12.07	3.43	4.31	6.17	11.67	12.79	3.26	3.65	2.36	5.78	0.27	0.26	4.85	1.39
Na_2O	6.26	2.05	6.22	6.21	6.08	0.87	1.36	6.26	6.63	7.8	4.19	6.3	6.32	6.66	6.51
K_2O	0.08	2.36	0.12	0.1	0.11	1.57	0.08	0.22	0.23	0.1	0.56	0.11	0.28	0.17	0.1
P_2O_5	0.06	0.36	0.08	0.1	0.09	0.45	0.04	0.08	0.06	0.07	0.03	0.04	0.04	0.08	0.08
LOI															
Total															
SiO_2	62.30	51.27	58.88	57.46	54.02	48.84	51.89	55.03	55.65	57.14	55.87	76.62	76.32	55.81	66.76
TiO_2	0.75	0.62	1.07	1.36	1.52	0.65	0.52	0.99	0.98	0.79	0.40	0.22	0.22	0.99	0.60
Al_2O_3	14.77	11.64	15.57	15.34	15.41	10.58	15.10	15.88	16.14	17.30	16.86	12.10	12.33	16.12	14.75
FeO	10.27	10.53	9.23	10.35	11.90	10.76	8.21	10.46	9.77	10.74	8.93	3.65	3.66	9.68	7.89
MnO	0.12	0.17	0.17	0.19	0.16	0.18	0.18	0.17	0.16	0.16	0.14	0.08	0.09	0.15	0.11
MgO	3.35	8.93	5.22	4.57	4.53	14.42	9.83	7.64	6.72	3.53	7.23	0.60	0.48	5.48	1.80
CaO	2.04	12.08	3.43	4.31	6.17	11.67	12.80	3.26	3.65	2.36	5.78	0.27	0.26	4.85	1.39
Na_2O	6.26	2.05	6.22	6.21	6.08	0.87	1.36	6.26	6.63	7.80	4.19	6.30	6.32	6.66	6.51
K_2O	0.08	2.36	0.12	0.10	0.11	1.57	0.08	0.22	0.23	0.10	0.56	0.11	0.28	0.17	0.10
P_2O_5	0.06	0.36	0.08	0.10	0.09	0.45	0.04	0.08	0.06	0.07	0.03	0.04	0.04	0.08	0.08
Total															
V	330	329	297	323	437	284	228	300	299	307	230			303	
Ti_ppm	4498	3719	6419	8156	9118	3898	3120	5937	5877	4738	2399	1319	1320	5938	3599

		Acoje Block_Subic														
ZO-410	Sample	ZO-411	ZO-412	ZO-413	ZO-414	SBFZ-60	SBFZ-61	SBFZ-62	SBFZ-10	SBFZ-10	SBFZ-10	SBFZ-10	SBFZ-11	SBFZ-11	SBFZ-11	SBFZ-11
Pillow ba	Type	Pillow ba	Ankarami	Ankarami	Ankarami	Diabase	Diabase	Diabase	Diabase,	Ferrobas	Diabase	Diabase	Diabase	Island	Ferrobas	Diabase
Subic Be	Locality	Subic Be	Subic Be	Subic Be	Subic Be	Beach area	Subic-Ol	Subic-Ol	Pamana	Pamana	Pamana	Pamana	Pamana	Island	Mayanga	Mayanga
GPY90	Referenc	GPY90	GPY90	GPY90	GPY90	GPY97	GPY97	GPY97	GPY97	GPY97	GPY97	GPY97	GPY97	GPY97	GPY97	GPY97
59.17	SiO_2	57.29	51.75	51.54	50.4	47.96	48.8	47.14	50.77	52.13	50.03	50.25	41.21	49.64	48.69	
0.97	TiO_2	1	0.88	0.9	0.91	0.47	0.34	0.4	0.34	1.21	0.43	0.36	0.31	1.2	1.01	
15.42	Al_2O_3	16.62	15.94	15.69	16.15	13.42	13.73	13.87	14.95	16.19	17.09	16.4	18.71	15.07	15.56	
	Fe_2O_3					12.7	10.1	13.06	9.8	10.13	11.66	10.7	10.01	11.26	9.89	
8.09	FeO	9.07	9.24	9.58	9.81											
0.16	MnO	0.15	0.16	0.18	0.19	0.27	0.24	0.29	0.21	0.18	0.27	0.25	0.2	0.22	0.22	
4.4	MgO	4.79	6.02	7.25	7.46	9.07	10.51	9.85	9.39	5.54	7.33	8.95	4.81	7.03	7.19	
4.56	CaO	3.55	10.15	9.07	9.84	11.79	12.95	12.62	8.79	8.9	8.26	7.4	20.28	9.51	10.92	
6.92	Na_2O	7.26	3.87	3.33	2.84	1.91	1.49	1.39	3.37	4.2	1.84	2.1	0.03	3.35	2.75	
0.18	K_2O	0.14	1.57	2.05	1.98	0.15	0.07	0.03	0.29	0.22	0.4	0.36	0	0.31	0.14	
0.08	P_2O_5	0.08	0.37	0.37	0.38	0.05	0.05	0.04	0.04	0.13	0.04	0.04	0.05	0.1	0.1	
	LOI															
	Total															
59.20	SiO_2	57.32	51.78	51.56	50.42	49.69	50.17	48.41	52.36	53.29	52.02	52.49	43.56	51.41	51.00	
0.97	TiO_2	1.00	0.88	0.90	0.91	0.49	0.35	0.41	0.35	1.24	0.45	0.38	0.33	1.24	1.06	
15.43	Al_2O_3	16.63	15.95	15.70	16.16	13.90	14.12	14.24	15.42	16.55	17.77	17.13	19.78	15.61	16.30	
8.09	FeO	9.07	9.24	9.58	9.81	11.84	9.34	12.07	9.09	9.32	10.91	10.06	9.52	10.49	9.32	
0.16	MnO	0.15	0.16	0.18	0.19	0.28	0.25	0.30	0.22	0.18	0.28	0.26	0.21	0.23	0.23	
4.40	MgO	4.79	6.02	7.25	7.46	9.40	10.81	10.11	9.68	5.66	7.62	9.35	5.08	7.28	7.53	
4.56	CaO	3.55	10.16	9.07	9.84	12.22	13.31	12.96	9.06	9.10	8.59	7.73	21.44	9.85	11.44	
6.92	Na_2O	7.26	3.87	3.33	2.84	1.98	1.53	1.43	3.48	4.29	1.91	2.19	0.03	3.47	2.88	
0.18	K_2O	0.14	1.57	2.05	1.98	0.16	0.07	0.03	0.30	0.22	0.42	0.38	0.00	0.32	0.15	
0.08	P_2O_5	0.08	0.37	0.37	0.38	0.05	0.05	0.04	0.04	0.13	0.04	0.04	0.05	0.10	0.10	
	Total															
	V	253	268	273	295											
5818	Ti_ppm	5998	5278	5398	5458											

			Acoje Block_Subic				Acoje Block_Sual								
SBFZ-11	Z008	Sample	PH98-1	PH98-2	PH98-26	PH98-27	LUZ129B	LUZ130A	LUZ634N	LUZ634C	LUZ632C	LUZ516E	LUZ516B	LUZ516H	LUZ516J
Diabase	dike	Type	Basalt, di	Basalt, di	Basalt, pi	Basalt, pi	Diabase	Diabase	lower pill	Dike	Dike	Dike	Dike	upper pill	Dike
Mayanga	Baretto, C	Locality	Kale Bea	Kale Bea	Olongapo	Olongapo									
GPY97	Pearce et	Referenc	RAT01	RAT01	RAT01	RAT01	HKEV83	HKEV83	EVNS91	EVNS91	EVNS91	EVNS91	EVNS91	EVNS91	EVNS91
49.88	52.69	SiO_2	49.5	51.4	53.4	51.7	51.28	54.14	54.19	52.59	55.65	62	54.71	55.56	54.02
0.91	1.48	TiO_2	0.59	0.6	1.15	1.43	0.51	0.56	0.63	0.91	1.01	0.91	0.99	0.99	0.45
15.94	15.03	Al_2O_3	12.4	12.8	15.6	14.5	16.33	18.02	13.72	16.97	15.73	13.3	14.67	14.93	15.89
9.87	11.6	Fe_2O_3	10.25	10.55	11.05	11.85			7.74	12.52	13.53	10.83	12.03	12	9.45
		FeO					8.92	8.81							
0.22	0.16	MnO	0.18	0.18	0.18	0.18	0.17	0.17	0.28	0.2	0.18	0.12	0.19	0.17	0.18
7.89	4.42	MgO	9.15	7	5.62	5.65	7.64	6.31	11.35	5.5	5.02	2.86	3.95	4.48	7.51
11.36	6.02	CaO	9.6	8.2	3.67	2.25	11.52	9.26	6.73	4.77	6.82	3.56	6.1	3.67	5.06
2.44	5.93	Na_2O	2.8	3.64	4.29	3.76	2.95	2.26	4.97	6.01	2.45	5.4	4.45	5.37	4.02
0.16	0.11	K_2O	2.33	2.69	0.27	2.57		0.26	0.03	0.02	0.12	1.9	1.12	2.69	3.45
0.08	0.09	P_2O_5	0.33	0.48	0.1	0.13	0.62	0.03	0.08	0.08	0.07	0.09	0.11	0.09	0.05
	2.41	LOI	2.69	2.35	4.33	5.18									
		Total													
51.02	54.68	SiO_2	51.51	53.27	56.67	55.69	51.31	54.24	54.77	53.49	56.09	62.07	56.34	56.26	54.49
0.93	1.54	TiO_2	0.61	0.62	1.22	1.54	0.51	0.56	0.64	0.93	1.02	0.91	1.02	1.00	0.45
16.31	15.60	Al_2O_3	12.90	13.27	16.56	15.62	16.34	18.05	13.87	17.26	15.85	13.32	15.11	15.12	16.03
9.08	10.83	FeO	9.60	9.84	10.55	11.49	8.93	8.83	7.04	11.46	12.27	9.76	11.15	10.93	8.58
0.23	0.17	MnO	0.19	0.19	0.19	0.19	0.17	0.17	0.28	0.20	0.18	0.12	0.20	0.17	0.18
8.07	4.59	MgO	9.52	7.26	5.96	6.09	7.64	6.32	11.47	5.59	5.06	2.86	4.07	4.54	7.58
11.62	6.25	CaO	9.99	8.50	3.90	2.42	11.53	9.28	6.80	4.85	6.87	3.56	6.28	3.72	5.10
2.50	6.15	Na_2O	2.91	3.77	4.55	4.05	2.95	2.26	5.02	6.11	2.47	5.41	4.58	5.44	4.06
0.16	0.11	K_2O	2.42	2.79	0.29	2.77	0.00	0.26	0.03	0.02	0.12	1.90	1.15	2.72	3.48
0.08	0.09	P_2O_5	0.34	0.50	0.11	0.14	0.62	0.03	0.08	0.08	0.07	0.09	0.11	0.09	0.05
		Total													
		V	280	280	300	340	270	245	195	388	375	316	440	349	261
	9207	Ti_ppm	3680	3728	7317	9235	3059	3363	3817	5549	6102	5462	6111	6010	2721

				Acoje Block, Sual				
LUZ516D	LUZ627C	LUZ660A	Sample	LUZ123A	PH98-18	PH98-19	PH98-20	PH98-22
Dike	Dike	Dike	Type	Microgab	Dacite di	Diabase (	Diabase (	Diabase dike
			Locality		Tobuan, !	Tobuan, !	Tobuan, !	Tobuan, Sual
EVNS91	EVNS91	EVNS91	Referenc	EVNS91	RAT01	RAT01	RAT01	RAT01
52.9	55.24	58.23	SiO_2	51.99	68	44	49	51.5
0.4	0.81	0.44	TiO_2	0.21	0.48	1.29	0.37	0.82
16.08	15.81	16.14	Al_2O_3	13.46	13.6	16.7	19.3	15.5
8	10.33	8.33	Fe_2O_3	9.9	6.5	17.2	7.8	11.6
			FeO					
0.18	0.12	0.17	MnO	0.23	0.11	0.19	0.16	0.2
9.41	4.76	5.58	MgO	12.98	1.03	6.54	7.15	5.3
7.34	9.94	9.11	CaO	11.21	4.05	11.28	13.1	8.75
4.15	2.42	1.61	Na_2O	0.86	4.2	1.03	1.28	1.92
1.28	0.27	0.13	K_2O	0.04	0.03	0.07	0.08	0.17
0.06	0.08	0.05	P_2O_5	0.02	0.15	0.05	0.03	0.07
			LOI		1.73	1.33	1.54	3.42
			Total					
53.44	55.94	58.84	SiO_2	52.04	69.74	45.54	50.26	54.40
0.40	0.82	0.44	TiO_2	0.21	0.49	1.34	0.38	0.87
16.24	16.01	16.31	Al_2O_3	13.47	13.95	17.28	19.80	16.37
7.27	9.41	7.57	FeO	8.92	6.00	16.02	7.20	11.03
0.18	0.12	0.17	MnO	0.23	0.11	0.20	0.16	0.21
9.51	4.82	5.64	MgO	12.99	1.06	6.77	7.33	5.60
7.41	10.07	9.21	CaO	11.22	4.15	11.67	13.44	9.24
4.19	2.45	1.63	Na_2O	0.86	4.31	1.07	1.31	2.03
1.29	0.27	0.13	K_2O	0.04	0.03	0.07	0.08	0.18
0.06	0.08	0.05	P_2O_5	0.02	0.15	0.05	0.03	0.07
			Total					
233	389	197	V	165	3	846	224	
2422	4918	2666	Ti_ppm	1260	2951	8004	2275	

Appendix 3. Raw FT-IR reflectance spectra of Zambales boninitic glasses